Impact of the Hydrodynamical Scheme on High Resolution Simulations of Structure Formation

Frederick Felix Groth

München 2024

Impact of the Hydrodynamical Scheme on High Resolution Simulations of Structure Formation

Frederick Felix Groth

Dissertation
an der Fakultät für Physik
der Ludwig–Maximilians–Universität
München

vorgelegt von
Frederick Felix Groth
aus Berlin

München, den 02.10.2024

Erstgutachter: Prof. Dr. Klaus Dolag
Zweitgutachter: Prof. Dr. Volker Springel
Tag der mündlichen Prüfung: 29.11.2024

Zusammenfassung

Das Intra-Cluster-Medium (ICM) von Galaxienhaufen ist eine hochgradig dynamische Umgebung. Sie ist geprägt von Verschmelzungen und räumlich großskaligen Bewegungen von Sub-Strukturen. Kleine räumliche Skalen werden von Turbulenz dominiert, die über eine turbulente Kaskade mit den großen Skalen verbunden sind. Sowohl Beobachtungen als auch Simulationen sagen voraus, dass die typischen Geschwindigkeiten dieser Turbulenz im Unterschallbereich liegen. Dies stellt numerische Herausforderungen für die Berechnung der turbulenten Kaskade dar und erfordert eine sorgfältige numerische Behandlung der Hydrodynamik.

Viele verschiedene numerische Methoden wurden entwickelt und auf dieses spezifische Problem angewandt. Sie lassen sich nach ihrem Diskretisierungsansatz in gitterbasierte Volumendiskretisierungsmethoden wie stationäre und bewegliche Gitter und Massendiskretisierungsmethoden wie Smoothed Particle Hydrodynamics (SPH) unterteilen. In jüngerer Zeit wurde die Meshless Finite Mass (MFM) Methode entwickelt. Das Gas wird hierbei nach Masse diskretisiert. Zusätzlich werden Flüsse zwischen den Nachbarn berechnet, sodass die Vorteile von SPH mit denen gitterbasierten Methoden kombiniert werden.

In dieser Arbeit stellen wir eine neue Implementierung von MFM in dem kosmologischen Simulationscode OpenGadget3 vor. Sie basiert auf der Implementierung im Gandalf-Code, mit verschiedenen Ergänzungen und Erweiterungen, um kosmologische Anwendungen zu ermöglichen. Ein Hauptziel ist die Anwendung auf Unterschallturbulenz in dem ICM von Galaxienhaufen und ein detaillierter und fairer Vergleich mit anderen hydrodynamischen Methoden.

Diese Arbeit ist wie folgt aufgebaut: In Teil I geben wir eine allgemeine Einführung in die relevante Physik und Numerik, einschließlich der MFM-Methode.

Darauf folgen in Teil II einige weitere Details zur Implementierung in OpenGadget3 und diverse Tests, um die Fähigkeiten der verschiedenen Methoden zu analysieren. Mit einer Vielzahl von Testfällen, die von idealisierten Tests bis hin zu komplexeren kosmologischen Anwendungen reichen, können wir verschiedene Aspekte der hydrodynamischen Lösungsmethoden untersuchen. Dies ermöglicht es, die Leistung unserer neuen MFM-Implementierung im Detail zu testen und erlaubt auch einen Vergleich mit anderen Methoden. Wir achten darauf, einheitliche Parameter-Einstellungen für die Tests zu verwenden, um einen fairen Vergleich zwischen den Methoden ohne nachträgliche Anpassungen zu ermöglichen. MFM bietet mehrere Vorteile gegenüber dem zuvor implementierten SPH, einschließlich einer verbesserten Entwicklung von Mischungsinstabilitäten und einem verbesserten Konvergenzverhalten. Da weniger Nachbarn in den Berechnungen benötigt werden, ergibt sich eine effektiv höhere Auflösung bei ähnlichem

Rechenaufwand. MFM zeigt hervorragende Leistungen bei der Anwendung auf das Problem der Unterschallturbulenz, und liefert auch vielversprechende Ergebnisse in nicht-radiativen kosmologischen Simulationen.

Darüber hinaus stellen wir Erweiterungen von MFM über die reine Hydrodynamik hinaus vor, einschließlich einer vorläufigen Implementierung der Magneto-Hydrodynamik und der Kopplung an numerische Modelle für physikalische Prozesse unterhalb der Auflösungsgrenze. Einige zusätzliche Verbesserungen des OpenGadget3-Codes werden ebenfalls zusammengefasst.

In Teil III analysieren wir, über idealisierte Tests hinausgehend, den turbulenten Druck im ICM, einschließlich eines Vergleichs hydrodynamischer Lösungsmethoden und Analysemethoden.

Der turbulente Duck wird mit drei verschiedenen Ansätzen ermittelt: indirekt (I) über die Abweichung vom hydrostatischen Gleichgewicht und direkter auf Grundlage der (II) solenoidalen oder (III) multi-skalig gefilterten Geschwindigkeit. Simulationen mit MFM führen im Allgemeinen zu einem erhöhten Turbulenzdruck im ICM von Galaxienhaufen, insbesondere bei Untersuchung mit geschwindigkeitsbasierten Methoden. Auch bei Galaxienhaufen kurz nach einer Verschmelzung wird, im Vergleich zu ruhigeren Systemen, eine erhöhte Turbulenz festgestellt. Der Anteil des nicht-thermischen Drucks am Gesamtdruck reicht von wenigen Prozent bei ruhigen Systemen bis zu $\approx 13\%$ bei aktiven Haufen in der zentralen Region. Er nimmt in Richtung der äußeren Bereiche zu. Es zeigt sich eine Abhängigkeit von der Analysemethode, die zur Gewinnung von Informationen über die Turbulenz verwendet wird, wobei geschwindigkeitsbasierte Ansätze die direktesten Ergebnisse liefern. Die theoretische Untersuchung der turbulenten Linienverbreiterung ermöglicht einen zusätzlichen Vergleich mit spektralen Beobachtungen.

Ergänzend wenden wir die Multiskalen-Filteranalyse auf simulierte Galaxienhaufens des lokalen Universums an, was wiederum einen direkten Vergleich mit Beobachtungen ermöglicht. Die Ergebnisbandbreiten der daraus ermittelten Druckanteile stimmen mit unserer vorherigen Studie sowie mit Beobachtungen überein.

In Teil IV ordnen wir unsere Ergebnisse ein und geben einige Ausblicke auf mögliche zukünftige Projekte und Weiterentwicklungen. Dazu gehören die Kopplung der MFM-Implementierung an bisher nicht eingebundene physikalische Modelle für Prozesse unterhalb der Auflösungsgrenze in OpenGadget3, außerdem mögliche numerische Verbesserungen und eine Erweiterung der Studie über turbulenten Druck unter Einbeziehung von Rückkopplungsprozessen durch Sterne und supermassereiche Schwarze Löcher. Weiterhin geben wir einen Ausblick auf die Relevanz dieser Arbeit im Zusammenhang mit laufenden und kommenden XRISM-Beobachtungen. Zusätzliches Material befindet sich im Anhang.

Abstract

The Intra Cluster Medium (ICM) of Galaxy Clusters (GCs) is a highly dynamic environment. It is shaped by mergers and bulk motions on large scales. Small scales are dominated by turbulence, connected to large scales via a turbulent cascade. Both observations and simulations predict this turbulence to be subsonic. This poses numerical challenges for calculating the turbulent cascade and requires careful numerical treatment of hydrodynamics.

Many different numerical methods have been developed and applied to this specific problem. They can be divided according to their discretization approach into grid-based volume-discretization methods, such as stationary and moving meshes, and mass-discretization methods such as Smoothed Particle Hydrodynamics (SPH). More recently, Meshless Finite Mass (MFM) has been developed. The gas is discretized by mass, but fluxes between neighbors are calculated, thus combining the advantages of SPH with grid-based methods.

In this work, we present a new implementation of MFM in the cosmological simulation code OpenGadget3. It is based on the implementation in the Gandalf code but has been extended to allow for cosmological applications. One main goal is the application to subsonic turbulence in the ICM of GCs and a detailed and fair comparison with other hydrodynamical methods.

This work is structured as follows: In Part I we will give a general introduction to the relevant physics and numerics, including the MFM method.

This is followed by some more details on the implementation in OpenGadget3 and an extensive test suite to analyze the capabilities of the different methods in Part II. Using a variety of test problems ranging from more idealized tests to more complex cosmological applications, we can probe different aspects of the hydrodynamical solver. It allows to test the performance of our new MFM implementation in great detail, and also provides a comparison to other methods. We make sure to use a consistent setup throughout the tests, to have a fair comparison between the methods without further tuning. MFM has several advantages over the previously implemented SPH, including improved development of mixing instabilities and improved convergence behavior. Requiring fewer neighbors in the calculations leads to an effectively higher resolution at similar computational costs. MFM performs exceptionally well when applied to the problem of subsonic turbulence and also shows promising results in non-radiative cosmological simulations.

In addition, we present extensions of MFM beyond pure hydrodynamics including a preliminary Magneto Hydrodynamics (MHD) implementation and coupling to physical sub-resolution models. Some additional improvements of the OpenGadget3 code are summarized.

Going beyond idealized tests, in Part III we analyze the turbulent pressure support in the ICM, including a comparison of hydro-solvers and analysis methods.

The turbulence pressure is obtained using three different approaches, more indirectly based on (i) the deviation from hydrostatic equilibrium (HE) and more directly based on the (ii) solenoidal or (iii) multi-scale filtered velocity. MFM generally leads to more turbulent pressure support detected in the ICM of galaxy clusters, in particular when studied with velocity-based methods. Increased turbulence is also found for GCs that underwent a recent merger compared to more relaxed systems. The non-thermal to total pressure fraction ranges from a few percent for relaxed systems up to $\approx 13\%$ for active clusters in the central region with a general increase towards the outskirts. Some dependence is found on the analysis method used to extract information on turbulence, where velocity-based approaches give the most direct results. Studying the turbulent line broadening allows for an additional comparison to observations.

We apply the multi-scale filtering analysis to simulated local universe clusters, allowing a direct comparison to observations. The turbulent pressure fractions are consistent with our previous study and also with observed fractions.

We conclude our findings and present some perspectives on possible future improvements in Part IV. This includes coupling of the MFM solver to remaining subgrid descriptions in OpenGadget3, possible numerical improvements, and a possible extension of the turbulent pressure study including feedback processes. We also give some outlook on the relevance of this work in light of the ongoing and upcoming XRISM observations. Some additional material is provided in the Appendix.

Contents

List of Acronyms

AGN Active Galactic Nucleus

AMR Adaptive Mesh Refinement

BH black hole

CMB Cosmic Microwave Background

CR Cosmic Ray

DM Dark Matter

GC Galaxy Cluster

HE hydrostatic equilibrium

IC initial condition

ICM Intra Cluster Medium

ISM Interstellar Medium

LSS Large Scale Structure

MFM Meshless Finite Mass

MFV Meshless Finite Volume

MHD Magneto Hydrodynamics

NFW Navarro, Frenk & White

SN Supernova

SPH Smoothed Particle Hydrodynamics

SZ Sunyaev-Zeldovich

Part I

Introduction

1 | Cosmology

1.1 Cosmological Background Evolution

Cosmology describes the evolution of the Universe as a whole with its Large Scale Structure (LSS). Observations reveal that the Universe is homogeneous and isotropic on large scales greater than 100 Mpc, visible, e.g., in the map of galaxies as tracers of the LSS shown in Fig. 1.1. This fact is also called the cosmological principle.

A mathematical description of the whole Universe under this assumption can be provided in the framework of general relativity (Einstein, 1916). The field equation describes the space-time geometry in terms of the Einstein tensor

$$\mathbf{G}_{\mu\nu} = \frac{8\pi G}{c^4}\mathbf{T}_{\mu\nu} - \Lambda \mathbf{g}_{\mu\nu} \tag{1.1}$$

depending on the energy momentum tensor $\mathbf{T}_{\mu\nu}$, cosmological constant Λ and metric tensor $\mathbf{g}_{\mu\nu}$. G is the Newtonian gravitational constant, and c is the speed of light.

The underlying metric has first been described by Friedmann (1922, 1924); Lemaître (1931, 1933) and was later extended by Robertson (1935, 1936b,a); Walker (1937) who have proven its properties more strictly. It is called Friedmann-Lemaître-Robertson-Walker metric, with the metric tensor combining both space and time-like distances

$$\begin{aligned} \mathrm{d}s^2 =& \mathbf{g}_{\mu\nu}\mathrm{d}\boldsymbol{x}^\mu \mathrm{d}\boldsymbol{x}^\nu & (1.2)\\ =& a^2 \mathrm{d}s_3^2 - c^2\mathrm{d}t^2. & (1.3) \end{aligned}$$

The scale factor a describes the change in cosmological distances with time due to the cosmological background evolution $R(t) = a(t)R_0$. In our Universe, a is growing with time and thus is often used as a time variable. The term $\mathrm{d}s_3$ contains the underlying spatial geometry.

Two main equations describe the evolution of the Universe. The first Friedmann-Lemaître equation

$$\frac{\dot{a}^2}{a^2} = \frac{8\pi G\rho}{3} + \frac{\Lambda c^2}{3} - \frac{kc^2}{a^2} \tag{1.4}$$

describes the expansion rate of the Universe depending on gravity, the cosmological constant, and curvature parameter is $k \in \{-1, 0, 1\}$. If space is hyperbolic, then the curvature parameter $k = -1$, if it is flat $k = 0$, and for a spherical space $k = 1$.

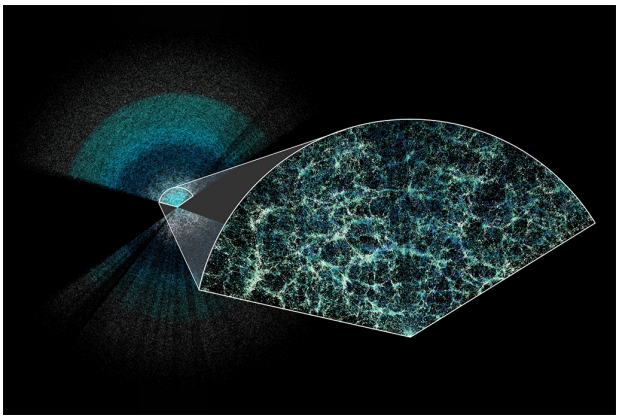

Figure 1.1: Map of galaxies as tracers of the Universe's large-scale structure observed by DESI. Credit: Claire Lamman/DESI collaboration; custom colormap package by cmastro (Biron, 2024).

The expansion rate can be expressed in terms of the Hubble function $H = \frac{\dot{a}}{a}$. Equation (1.4) can be rewritten by replacing all contributions to the expansion rate in terms of the density parameters being the ratio of actual to critical density $\Omega = \rho/\rho_{\text{crit}}$, where

$$\rho_{\text{crit}} = \frac{3H^2(t)}{8\pi G}, \tag{1.5}$$

and their corresponding evolution with scale factor

$$\frac{H^2}{H_0^2} = \Omega_{0,\text{r}} a^{-4} + \Omega_{0,\text{m}} a^{-3} + \Omega_{0,k} a^{-2} + \Omega_{0,\Lambda}. \tag{1.6}$$

The matter density is split into contributions of radiation and other relativistic matter $\Omega_{0,\text{r}}$ and non-relativistic matter $\Omega_{0,\text{m}}$. The third term $\Omega_{0,k}$ contains the curvature, and $\Omega_{0,\Lambda}$ the cosmological constant, all evaluated at the current time indicated by the subscript 0. For convenience, we set the expansion factor at the current time $a_0 = 1$. Energy conservation enforces the sum of all density contributions to be unity

$$1 = \Omega_{0,\text{r}} + \Omega_{0,\text{m}} + \Omega_{0,k} + \Omega_{0,\Lambda}. \tag{1.7}$$

The second Friedmann-Lemaître equation

$$\frac{\ddot{a}}{a} = -\frac{4\pi G}{3}\left(\rho + \frac{3p}{c^2}\right) + \frac{\Lambda c^2}{3} \tag{1.8}$$

describes the acceleration of the expansion. Also the pressure p acts gravitationally in general relativity.

This background evolution leads to a shift between the emitted wavelength λ_e of light and the wavelength at which it is observed today λ_0 depending on the scale factor of the Universe at the time of emission

$$\frac{1}{1+z} = \frac{\lambda_e}{\lambda_0} = a_e. \tag{1.9}$$

Thus, the redshift can be used as a tracer for the expansion of the Universe. The notion that the Universe expands, first suggested by Lemaître (1927), was later given observational support by Hubble (1929). He studied the redshift z of galaxies, interpreted in terms of the recession velocity $v_r = zc$[1], and found a linearly increasing velocity with distance r

$$v_r = H_0 \cdot r. \tag{1.10}$$

The Hubble parameter H_0 is the one from Eqn. (1.6). It is often expressed via the dimensionless parameter

$$h = \frac{H_0}{100\ \mathrm{km/s/Mpc}}. \tag{1.11}$$

Different measurements confirmed this trend of expansion and refined the value of the Hubble parameter. Later observations by Riess et al. (2001) showed that the Universe is expanding at an accelerated rate.

Tracing back this evolution of an expanding Universe predicts that the Universe must have been denser and hotter at earlier times, called "big bang" scenario. The early radiation field from the initially hot plasma is still present, but cooled down with expansion. After theoretical speculations by Alpher & Herman (1948); Alpher et al. (1948) and predictions by Doroshkevich & Novikov (1964), it was first observed by Penzias & Wilson (1965). Due to the low temperature of only ≈ 2.73 K today, the spectrum peaks in the microwave regime and is thus called Cosmic Microwave Background (CMB). Its temperature is almost constant, with relative deviations of only 10^{-5}. This very strong homogeneity imposes that the different regions had to be in causal contact which is achieved by an initial rapid expansion phase called inflation. Quantum fluctuations that started on very small scales are enlarged in size, and imprinted on large scales, visible in the CMB.

By ongoing gravitational collapse, these fluctuations lead to the formation of the LSS. An approximation for the initial collapse in the linear regime has been developed by Zel'dovich (1970a) connecting comoving Lagrangian coordinates to Eulerian coordinates at later time. Overdensities grow with time and quickly become non-linear.

The initial overdense regions will collapse into halos with continuously increasing densities. As it takes shorter for smaller halos to collapse, the collapse will happen bottom-up. During this "hierarchical structure formation", halos will accrete and merge. On large scales, the initial overdensities lead to the formation of sheets and filaments connecting the nodes hosting galaxy groups and clusters. In the largest overdensities, several clusters can even form superclusters. The initial underdensities will evacuate, forming comparatively emptier regions, the so-called voids.

A prescription for the structure formation in terms of the mass function of objects has been found by Press & Schechter (1974). The number of objects in a given mass range is

$$M \frac{\mathrm{d}n}{\mathrm{d}M} = \frac{1}{\sqrt{\pi}} \frac{\bar{\rho}}{M} \left(\frac{M}{M^*} \right)^{1/2} e^{-M/M^*} \tag{1.12}$$

[1]Strictly speaking this equation is only true in the linear regime for nearby galaxies.

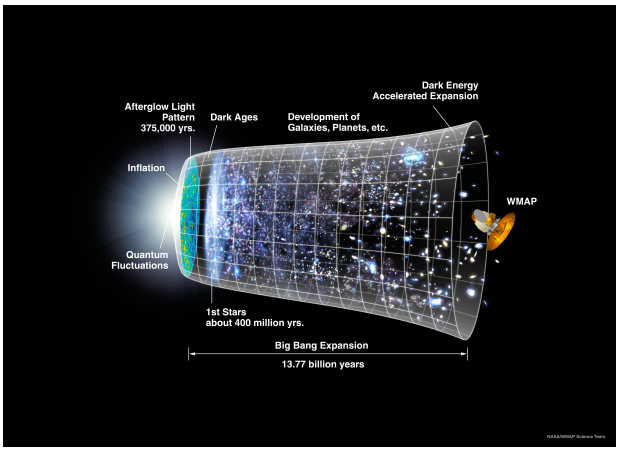

Figure 1.2: Evolution of the Universe from the "big bang" to the current Universe. After the emission of the CMB, hierarchical structure formation leads to the formation of stars, galaxies, and the LSS. Illustration taken from `https://map.gsfc.nasa.gov/media/060915/index.html`, last accessed August 16th, 2024

for a scale-free initial power spectrum as it is found in our Universe. The mass M^* is the upper cut-off mass below which structures can form. Cosmological simulations that we will describe later in Sec. 4 can give additional insight into this highly non-linear collapse beyond simplified models. On the other hand, simulations have to be informed of the large-scale cosmological evolution. This can either be done by explicitly adding evolutionary terms due to the Hubble expansion or by choosing an appropriate unit system as described in Sec. 3.8.

An illustration of this evolution from the "big bang" to the current Universe is shown in Fig. 1.2. After an initial inflation phase, the CMB is visible as "afterglow light pattern". After the dark ages, the first light is emitted by stars. Hierarchical structure formation then continues, leading to the formation of galaxies and ultimately Galaxy Clusters (GCs) and the LSS.

Overall, this cosmological model has been a great success in describing the large-scale evolution of the Universe. Due to many different measurements, we have very good constraints on the relevant parameters, see the next section for details. The model is based on the assumptions of cold Dark Matter (DM) (CDM) and the existence of a cosmological constant Λ, summarized as ΛCDM model.

1.1.1 The Cosmological Parameters

The cosmological background evolution can be fully described by the density parameters $\Omega_{0,\mathrm{r}}$ for radiation, $\Omega_{0,\mathrm{m}}$ for non-relativistic matter, $\Omega_{0,k}$ for the spatial geometry and $\Omega_{0,\Lambda}$ for the cosmological constant in combination with the Hubble function at the current time H_0. Information on the initial perturbations is contained in the parameter σ_8. It describes the amplitude of clustering at a reference scale of 8 Mpch^{-1}.

The non-relativistic matter contains not only baryons but also DM. This is evident from the CMB and also more local observations. In the CMB, the initial fluctuations are smeared out

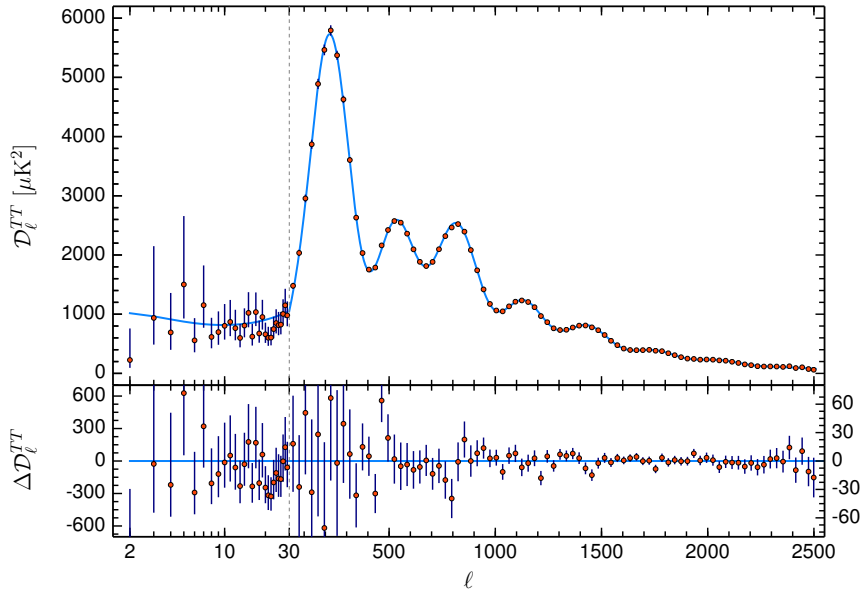

Figure 1.3: Temperature power spectrum of the CMB measured by Planck Collaboration et al. (2020). The fit is for the best cosmological model with parameters $\Omega_\Lambda = 0.6889 \pm 0.0056$, $\Omega_\mathrm{m} = 0.3111 \pm 0.0056$, $\Omega_\mathrm{b}h^2 = 0.02242 \pm 0.00014$, $\Omega_\mathrm{dm}h^2 = 0.11933 \pm 0.00091$, and $\sigma_8 = 0.8102 \pm 0.0060$.

by baryons. An additional, only gravitationally interacting mass budget in the form of DM is necessary to preserve the fluctuations and lead to later collapse. In GCs Zwicky (1933) discovered that the visible baryonic matter cannot account for the gravitational potential needed to explain galaxy velocities. Similarly, the rotation curves of galaxies show a missing mass budget.

DM is most likely cold, meaning it has low velocities, and interacts only gravitationally. Some freedom is still present in the parameters. Possible alternatives include fuzzy DM described by condensation of an ultra-light scalar field, warm DM with partly higher velocities, or self-interacting DM, which is not fully collisionless. Although the general existence of DM is required to explain various observations, it is still unclear what it consists of (compare Arbey & Mahmoudi, 2021, for a review). Potential candidates are primordial black holes (BHs) or weakly interacting massive particles (WIMPs) beyond the Standard Model of particle physics. Even modifications to Einstein's theory of gravity could be a possibility, though they often struggle with specific observations. Overall, the presence of DM implies that a full description of the content of the Universe has to include baryons $\Omega_{0,\mathrm{b}}$ and cold DM $\Omega_{0,\mathrm{DM}}$ separately.

At the current day several methods are used to constrain the cosmological parameters. The main method used for constraining them all together is based on high-resolution measurements of the CMB. These measurements have been continuously refined, starting with the COBE space mission (Boggess et al., 1992) over the WMAP telescope (Komatsu et al., 2011), until the more recent Planck satellite (Planck Collaboration et al., 2014, 2020). All cosmological parameters are derived from the temperature power spectrum via a model fit. The most recent Planck Collaboration et al. (2020) measurement including the fit is shown in Fig. 1.3. Cosmological

parameters can be derived with great accuracy but also depend on the model used for obtaining the fit.

The results obtained by Planck Collaboration et al. (2020) are widely used e.g. as the foundation for simulations. They find a Hubble parameter $H_0 = (67.66 \pm 0.42)$ km/s/Mpc, density parameters $\Omega_\Lambda = 0.6889 \pm 0.0056$, $\Omega_\mathrm{m} = 0.3111 \pm 0.0056$, $\Omega_\mathrm{b}h^2 = 0.02242 \pm 0.00014$, $\Omega_\mathrm{dm}h^2 = 0.11933 \pm 0.00091$, and $\sigma_8 = 0.8102 \pm 0.0060$. The curvature parameter imposes an almost perfectly flat Universe $\Omega_k \approx 0$. As the radiation content decreases strongly with increasing scale factor, it is much lower than the matter content and can be neglected.

An alternative method to obtain the cosmological parameters is via measurements at later times studying the LSS, in particular using galaxies as tracers. Different all-sky or large-area surveys provide the large datasets necessary to perform the relevant analysis, several of them are ongoing. Recent constraints can be obtained from the Dark Energy Spectroscopic Instrument (DESI; DESI Collaboration et al., 2024), the extended Baryon Oscillation Spectroscopic Survey (eBOSS) within the Sloan Digital Sky Survey (SDSS; Alam et al., 2021), and the Dark Energy Survey (DES; DES Collaboration et al., 2022). They find a matter content and Hubble parameter consistent with CMB measurements.

Nevertheless, there is some tension with respect to the value of σ_8. Also the Hubble parameter varies significantly between different observational methods. We want to address these tensions in the following section.

1.1.2 Tensions

Comparisons between different observational approaches reveal some tensions. The Hubble parameter is significantly different between direct measurements using the distance ladder ($H_0 \approx (74.03 \pm 1.42)$ km/s/Mpc, Riess et al., 2019) and CMB measurements ($H_0 \approx (67.66 \pm 0.42)$ km/s/Mpc, Planck Collaboration et al., 2020) by more than 4σ, known as Hubble tension (compare, e.g., Valentino et al., 2021, for a review). Local measurements generally predict a higher expansion rate than CMB-based values. Many models going beyond ΛCDM have been proposed to reduce the tension, including dynamic dark energy, primordial magnetic fields, and modified gravity, which can reduce the tension but are highly degenerate with the additional physics. In addition, the CMB measurement is strongly model-dependent.

Also the amplitude of clustering σ_8 at scales of 8 Mpch^{-1} differs between different measurements. The results by Planck Collaboration et al. (2020) suggest $\sigma_8 = 0.8102 \pm 0.0060$. More local measurements, e.g., by DES Collaboration et al. (2022) in contrast, suggest a smaller value of $\sigma_8 = 0.741^{+0.034}_{-0.042}$. In general, there is a dependence on the redshift at which the measurement is obtained (Abdalla et al., 2022). Sánchez (2020) showed that differences in σ_8 are closely related to differences in the Hubble parameter. Instead, the clustering should be measured at a physical scale of 12 Mpc not to probe different scales depending on h.

Comparisons of observations to theoretical models also show a cusp-core and missing satellite problem. The former describes the observation of halos with flat central DM profiles (“cores”), while only cusp profiles are expected following the Navarro, Frenk & White (NFW) profile obtained from N-body simulations (compare,e.g., Del Popolo & Le Delliou, 2021). The latter is related to the number of small subhalos. Observations in the local group find fewer satellite

galaxies than predicted by the DM clustering (Bullock, 2013). As these "missing" galaxies are very faint, a strong selection bias can affect the interpretation of the data.

Solutions to these two small-scale tensions include alternative DM models such as self-interacting DM and modified Newtonian dynamics (MOND). In addition, baryonic effects are among the possible solutions to alleviate the tensions. Feedback processes by Active Galactic Nuclei (AGNs) can significantly alter the structure on small scales in the center of galaxies. Thus, a sophisticated understanding of baryonic processes is important to understand if resolving these tensions requires any additional physics. Overall, the origin of the different tensions is still unclear and under debate.

1.2 Galaxy Clusters and the Intra Cluster Medium

GCs are the largest gravitationally bound and virialized structures in the Universe. In this chapter, we will describe some of their main properties and processes relevant for the formation and structure of GCs. For a more detailed review refer to, e.g., Kravtsov & Borgani (2012) which we use as our main reference for this chapter. Overall, both cosmology and baryonic physics are relevant to describe them. On one hand, they are embedded in the LSS, located at the nodes, connected via filaments, and impacted by the cosmological background evolution. On the other hand, baryonic physics can significantly impact the structure of their gas and even couple back to the DM.

1.2.1 Observations

Observations in different wavelength bands give insight into the properties of GCs. Optical imaging focuses on the bright stellar component. As mentioned in Sec. 1.1, several finished and ongoing all-sky and large-area surveys have collected vast amounts of data. Famous more historic catalogs from optical surveys include those by Abell (1958) and Zwicky et al. (1968). GCs are detected as overdensities of galaxies. A possible definition of a GC from these observations is based on the number of galaxies in a specific brightness range contained within the overdensity, called richness. This definition is not unique but varies between different catalogs. If spectroscopic data are available, these can be used to remove foreground and background contaminations of galaxies at different redshifts. In addition, they give insight into the velocities of galaxies, thus making it possible to study the cluster potential and obtain the cluster mass.

Lensing is an alternative way to measure the cluster potential. The light of background galaxies traveling through the cluster gets distorted and deflected due to the gravity of the cluster. In the weak lensing regime further away from the cluster center images of galaxies get deformed. These deformations can be studied by statistical analysis of the shape and orientation of a large number of galaxies. In the strong lensing regime background galaxies even produce multiple images. The modeling of the cluster potential relies on many assumptions and resulting mass estimates can be prone to significant errors. More details on how to obtain mass estimates from lensing observations within clusters can be found in the review by Hoekstra et al. (2013).

The hot and diffuse Intra Cluster Medium (ICM) can be observed in X-ray via thermal Bremsstrahlung. A more detailed overview can be found in the reviews by Sarazin (1986); Böhringer & Werner (2010). Assuming hydrostatic equilibrium (HE), the cluster potential can be derived from the gas temperature. Several processes which we will discuss later in this section will lead to deviations from HE, summarized in the term hydrostatic bias. Fluctuations in the intensity can be translated into pressure fluctuations and therefore are tracers of turbulence.

More direct insight into turbulent velocities and gas dynamics can be obtained by using spectroscopic velocity information, e.g. by Hitomi (Hitomi Collaboration et al., 2016, 2018), XMM-Newton (den Herder et al., 2001), or XRISM (Sato et al., 2023).

An alternative method to observe GCs is via the Sunyaev-Zeldovich (SZ) effect (Zeldovich & Sunyaev, 1969; Sunyaev & Zeldovich, 1972) in the CMB maps. Low energy photons of the CMB gain energy by inverse Compton scattering with the hot ICM electrons. Overall, this effect shifts the spectrum towards higher frequencies, resulting in a non black body spectrum. The SZ effect is directly proportional to the surface density for a simple temperature structure, such that it can be used as an alternative mass measure. As it is independent of redshift, its interpretation is independent of any distance estimates of the cluster. The scattering with the thermal electrons is called the thermal SZ effect, while the contribution of gas and bulk motions is called the kinetic SZ effect. The latter is smaller by a factor of $10 - 20$ than the thermal effect and shows a different impact in the spectrum. Very precise CMB measurements are necessary to study this effect, which are, however, available with modern observations.

Finally, radio observations focus on the relativistic non-thermal electrons in the cluster called Cosmic Rays (CRs) that radiate via synchrotron radiation. They are relatively short lived, such that the radio emission is contained in a region close to where they have been excited to relativistic energies. Acceleration happens mainly within shocks, which thus appear bright in radio, called radio relics. In the center, electrons can be re-accelerated and stabilized against cooling by turbulence, visible as diffuse and faint radio halo in the center of GCs. Overall, this observation can give additional insight into the gas dynamics of the cluster.

Most information can be obtained if different observations are combined. An example of a multi-wavelength observation in the GC Abell 1033 is shown in Fig.1.4. Different wavelengths are shown in different colors. Optical data shows the stellar component within the galaxies. X-ray traces the diffuse, hot ICM. Radio emission is present in radio galaxies (labeled WAT and HT), a re-accelerated radio galaxy tail (GReET), and the radio relic (S).

1.2.2 Basic Properties

As described in Sec. 1.1, clusters form via hierarchical structure formation. This process is not finished, but GCs are still forming and growing in mass to this day. Clusters can accrete quasi-spherically, smoothly along the filaments, or more rapidly via mergers with other clusters. Such massive mergers are among the most energetic phenomena in the Universe. Violent relaxation as a collective gravitational effect enables them to still reach a relaxed state and the cluster to be close to virialization. The virial condition in dynamical equilibrium can be expressed as

$$0 = 2E_{\mathrm{kin}} + E_{\mathrm{pot}} - E_{\mathrm{s}}. \tag{1.13}$$

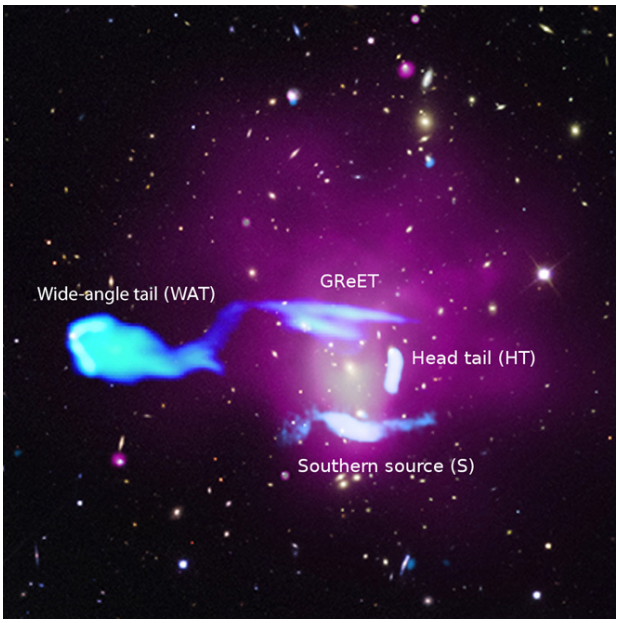

Figure 1.4: Multi-wavelength observation of Abell 1033 by de Gasperin et al. (2017). Optical data from the Sloan Digital Sky Survey (SDSS) in the background, X-ray from Chandra in purple, and radio from the Low-Frequency Array (LOFAR) in blue. The size of the region is around 1 Mpc^2

In addition to the kinetic energy E_{kin} and the gravitational potential energy E_{pot}, it includes the energy from the surface pressure E_{s}.

As the density continuously decreases further away from the center and there is no sharp boundary, different definitions are possible for the mass of a GC. Simulations allow for a very direct mass measurement but require an identification of particles belonging to the cluster. The Friends of Friends (FoF) method is commonly used in simulations. Two particles closer than a given linking length belong to the same group ("friends"). All friends of friends are also taken as members of the same group, resulting in a full list of member particles. The main advantage is that the method is simple, depends only on a single parameter, and no shape has to be assumed. The main caveats are that it cannot easily be used in observations and close-by halos are potentially joined together.

Alternatively, the center is defined by the minimum potential. The size is given by the radius within which the mean density exceeds a specific density. Common choices include multiples of 200, 500, or 2500 of the mean or critical density of the Universe ($R_{200/500/2500\mathrm{m/c}}$). This definition relies on the assumption of spherical symmetry but can be used in simulations and observations.

There is no unique definition for the lower mass limit of GCs. A commonly used lower threshold is $M_{200\mathrm{c}} = 10^{14}\mathrm{M}_{\odot}$, as used in the TNG-Cluster project (Nelson et al., 2024). Clusters with up to $10^{14.5}\mathrm{M}_{\odot}$ are considered low-mass clusters. Intermediate mass clusters have up to $10^{15}\mathrm{M}_{\odot}$, and everything above is considered high mass. Structures with lower masses between

$10^{13-14}\mathrm{M}_\odot$ are called galaxy groups.

GCs consist mainly of DM, hot volume filling gas called ICM, and several 100 to 1000s of galaxies. In the center, most clusters host a large elliptical galaxy, called the brightest cluster galaxy (BCG). The mass ratio between baryons and DM within GCs is close to the cosmological mass ratio. Deviations can occur as the collapse involves more physics than gravity, in particular feedback processes, causing a reduced baryon fraction. Feedback becomes less significant at higher masses, leading to an increase in baryon content with cluster mass. Overall, DM makes up the majority of the mass content at $\approx 84 - 90\%$. Baryons in the form of hot gas make up $\approx 10 - 15\%$. Galaxies with the stars inside them contribute only by $\approx 1 - 5\%$ to the total mass.

Navarro et al. (1997) found from DM-only simulations that the DM density profile of GCs in particular and halos in general can be well approximated by

$$\rho(r) = \rho_\mathrm{c} \frac{\delta_c}{\frac{r}{r_s}\left(1 + \frac{r}{r_s}\right)^2} \tag{1.14}$$

with scale radius r_s, critical density of the Universe ρ_c and the characteristic density parameter

$$\delta_c = \frac{200}{3} \frac{c^3}{\ln(1+c) - \frac{c}{1+c}} \tag{1.15}$$

containing information on the concentration $c = R_{200}/r_s$. Using the initials of the authors' names, this is also called NFW profile. They also found that the concentration increases with decreasing mass.

Adding the baryonic component, it couples back to the underlying DM component. The effects on the DM potential are mainly important in the cluster center at $r < R_{2500}$. Cooling and condensation lead to a deeper central gas potential, resulting in the contraction of the DM and increasing the central concentration. Stellar and AGN feedback processes can mitigate this effect (van Daalen et al., 2011). If the received kinetic energy is large enough or the heating is sufficiently strong, increasing the temperature above the escape temperature, gas outflows can occur. Thus, baryonic effects can explain the tensions between the concentrations of N-body simulations and observations (e.g., Fedeli, 2012).

Global gas motions are excited due to mergers and accretion along filaments. After a major merger, the baryonic component can be significantly perturbed and offset with respect to the global potential, which is dominated by the DM, leading to a "sloshing" motion of gas. Turbulence will be excited, as we will discuss in Sec. 1.2.4. Accretion also affects the thermodynamical properties of the gas. Kinetic energy is converted into thermal energy via adiabatic compression and shocks. Accretion shocks form at the virial radius from the smooth accretion. These strong, external shocks have Mach numbers $\mathcal{M} > 30$. Weak internal shocks with $\mathcal{M} \lesssim 2-3$ form within the pre-heated gas of filaments and accreting groups. Additional strong shocks can be present after a major merger.

Infalling galaxies will lose gas by "ram pressure stripping" with the hot ICM. Substructures lead to significant clumping of the gas, especially in the outskirts. When analyzing X-ray emission that scales with ρ^2_gas, this can result in significant bias. The clumpiness depends on a variety

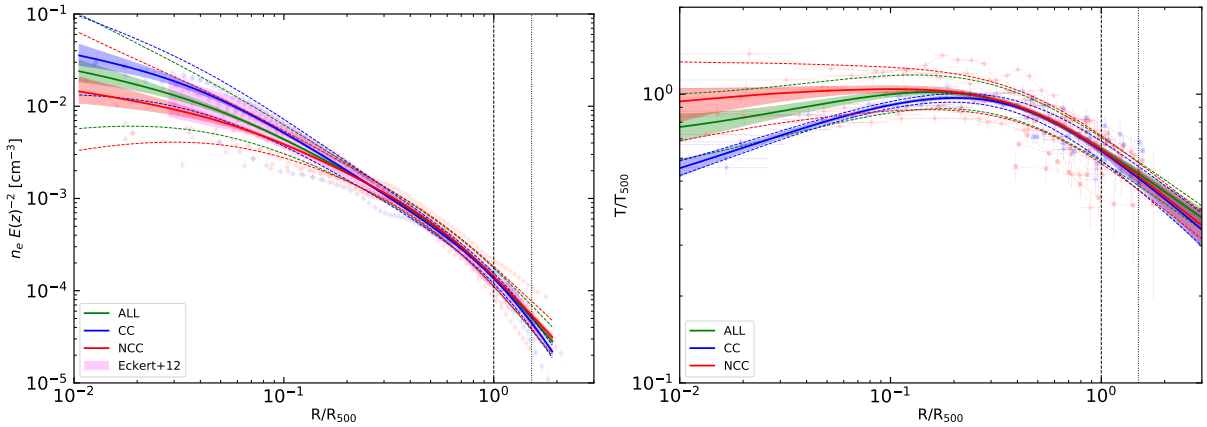

Figure 1.5: Radial density (left) and temperature (right) profile of X-COP clusters (plots by Ghirardini et al., 2019). Individual cluster data are in the background, the lines represent functional fits. Clusters are divided between cool-core (blue) and non cool-core (red), the total average is shown in green.

of uncertain processes including feedback and conduction, which we will discuss in more detail below.

Depending on the central slope of the temperature profile, clusters can be divided into cool-core and non-cool-core clusters as shown in Fig. 1.5. Cool-core clusters show a lower temperature in the core than farther out, which requires that the cooling time is shorter than the age of the cluster. Thus, the presence of a cool core is closely related to the presence of cooling flows. It is found that the central thermodynamic properties are closely correlated with the global cluster properties. Cool-core clusters tend to be more symmetrical and regular, while non-cool-core clusters are more asymmetric and have more substructure. An explanation is the different merger history, where non-cool-core clusters are expected to have had a recent merger, while cool-core clusters tend to be more relaxed. An additional anti-correlation of the metallicity with (pseudo-) entropy, an alternative tracer for cool-coreness, is found. Cool-core clusters appear to not only be cooler in the center and have a higher central gas density, but are on average also more metal rich (Rasia et al., 2015; Ettori et al., 2015; Biffi et al., 2017).

1.2.3 Plasmaphysics in the Intra Cluster Medium

A variety of hydrodynamical processes are important to understand the structure and evolution of the ICM. In this section, we want to briefly review the most important processes, including corresponding length- and timescales. A more detailed description can be found in the review by Sarazin (1986), which we use as a main reference here and follow their structure.

Depending on the cluster mass, the central gas density is around 10^{-3} – 10^{-1} cm^{-3} and decreases with radius. The temperature of the hot volume-filling ICM varies less as shown in the radial profiles in Fig. 1.5 so that the ICM is close to isothermal. It has a temperature around 10^{7} – 10^{8} K, which is close to the virial temperature of the halo. As metal enrichment happens

mainly by stars forming more in the central region, the metallicity is higher in the center. The entropy increases towards the outskirts.

At such high temperatures, the ICM is fully ionized and the free electrons radiate in X-rays, most dominantly in the continuum via thermal Bremsstrahlung. Metals, in particular iron, contribute by line emission. The total X-ray luminosity is $10^{43} - 10^{45}$ erg/s. The related cooling timescale due to the emission of Bremsstrahlung is

$$t_{\rm cool} = 8.5 \cdot 10^{10} \left(\frac{n_p}{10^{-3}\ {\rm cm}^{-3}}\right)^{-1} \left(\frac{T_g}{10^8\ {\rm K}}\right)^{1/2}\ {\rm yr} \tag{1.16}$$

which is mostly longer than the Hubble time. In the cluster center where the density is the highest, it can be shorter thus leading to to cooling flows and the presence of cool cores. Cold gas can be accreted onto the central galaxy. Cooling can also be effective in dense clumps in substructures outside the cluster core. Colder, low-entropy gas is removed from the hot ICM phase and replaced by higher entropy gas from the outskirts. Simulations find that the overall entropy even increases, which can be seen from the entropy profile in Fig. 1.6. Observed clusters show a diversity in central entropy profiles, but on average tend to be more flat than predicted by non-radiative simulation. To be consistent with observations, cooling and star formation are necessary. If only cooling was included, simulations predict much too high star formation rates. This emphasizes the necessity of an additional heating term to balance cooling. Heating is provided by Supernova (SN) and AGN feedback. In addition, the gas is heated by dynamical friction of galaxies moving inside the cluster environments, gravitational heating from accretion, and CRs.

Information on a possible deviation from HE propagates through the cluster at the speed of sound. The sound crossing time through the cluster is

$$t_s = 6.6 \cdot 10^8 \left(\frac{T_g}{10^8\ {\rm K}}\right)^{-1/2} \left(\frac{D}{\rm Mpc}\right)\ {\rm yr}, \tag{1.17}$$

which is shorter than the cluster age. If no other dynamical processes, heating or cooling act on shorter timescales, GCs are in HE. Different processes which lead to deviations from HE will be discussed in Sec. 1.2.4. In spherical symmetry, the HE equation becomes

$$\nabla P = -\rho_g \nabla \Phi. \tag{1.18}$$

The main length scale describing transport processes within the plasma is the mean free path of an electron (Spitzer, 1956)

$$\lambda_{\rm mfp} = \frac{3^{3/2}\,(k_B T_e)^2}{4\pi^{1/2} n_e e^4 \ln \Lambda} \tag{1.19}$$

$$\approx 23 \left(\frac{T_g}{10^8\ {\rm K}}\right)^2 \left(\frac{n_e}{10^{-3}\ {\rm cm}^{-3}}\right)^{-1}\ {\rm kpc}. \tag{1.20}$$

The Coulomb logarithm

$$\ln \Lambda = 37.8 + \ln\left(\left(\frac{T_e}{10^8\ {\rm K}}\right)\left(\frac{n_e}{10^{-3}\ {\rm cm}^{-3}}\right)^{-1/2}\right) \tag{1.21}$$

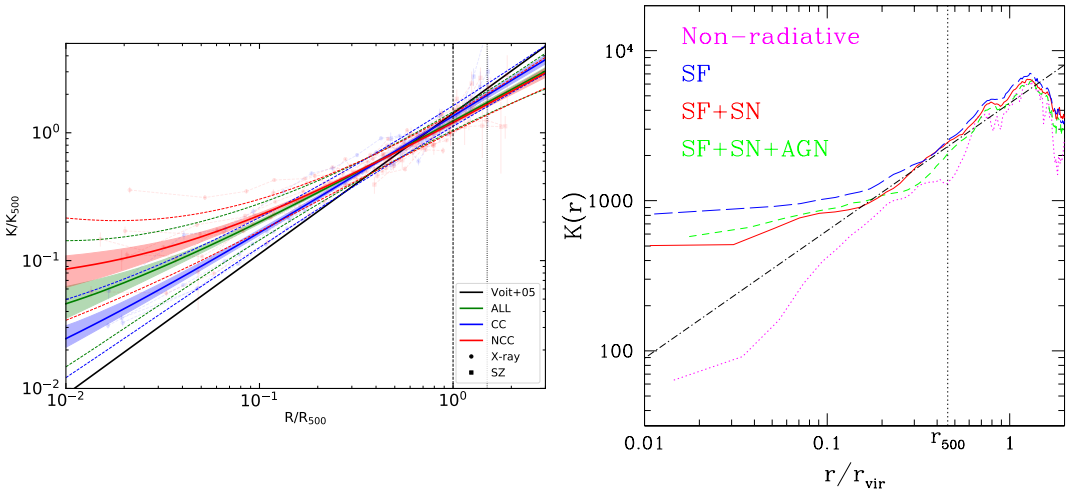

Figure 1.6: Radial entropy profiles. Left: observed X-COP clusters (plot by Ghirardini et al., 2019), data in the background, fits with functional forms for cool-core (blue) and non cool-core (red) clusters, all clusters (green). Black line is the pure gravitational collapse prediction (Voit et al., 2005). Right: simulated GC in units of keV cm^2 without cooling (magenta dotted), with cooling and star formation (long-dashed blue), also including SN feedback (continuous red), and with additional AGN feedback (short-dashed green) (plot by Kravtsov & Borgani, 2012).

describes the limits of impact parameters for interactions. The mean free path is shorter than macroscopic cluster length scales, such that the plasma can be treated with the hydrodynamical equations described in Sec. 2.1 as a collisional fluid. It is of a similar size as galaxies, such that in galaxy ICM interactions the plasma would behave collisionlessly, which would pose problems to simulations.

The Reynolds number of the ICM in the classical, collisional view is

$$\mathrm{Re} = \frac{L v_L}{\nu_{\mathrm{visc}}} = 3\mathcal{M}\left(\frac{l}{\lambda_i}\right) \tag{1.22}$$

$$= 52\left(\frac{v_L}{10^3\ \mathrm{km/s}}\right)\left(\frac{L}{300\ \mathrm{kpc}}\right)\left(\frac{n}{10^{-3}\ \mathrm{cm}^{-3}}\right)\left(\frac{k_B T}{8\ \mathrm{keV}}\right)^{-5/2}\left(\frac{\log\Lambda}{40}\right) \tag{1.23}$$

with eddy size L, the typical root-mean-square velocity at that scale v_L, and viscosity ν_{visc}. We will describe the concept behind this number in more detail in Sec. 2.4. Under typical ICM conditions, the Reynolds number is $\mathrm{Re} \lesssim 10^2$ implying that the flow should be mostly laminar. However, turbulence is detected in the ICM. Thus, it is necessary to go beyond this idealized picture.

Observations indicate the presence of magnetic fields in the ICM. They have a typical field strength B of a few μG (Carilli & Taylor, 2002; Bonafede et al., 2011b, 2013). Their origin and initial field strength are still under discussion (compare Kulsrud & Zweibel, 2008, for a review). Their growth can be described by a turbulent dynamo (Zel'dovich, 1970b; Vazza et al., 2018b;

Steinwandel et al., 2024a). Magnetic field lines are stretched, twisted, and folded, leading to initially exponential growth and saturation of the field strength at later times (compare also the review by Donnert et al., 2018).

Magnetic fields affect the movement of electrons, forcing them to gyrate around the magnetic field lines. The gyroradius

$$r_{\rm g} = \frac{3.1 \cdot 10^8}{Z} \left(\frac{T_g}{10^8\ {\rm K}}\right)^{1/2} \left(\frac{m}{m_e}\right)^{1/2} \left(\frac{B}{1\ \mu{\rm G}}\right)^{-1}\ {\rm cm} \tag{1.24}$$

is much smaller than $\lambda_{\rm mfp}$, thus suppressing any transport processes by electrons perpendicular to the magnetic field.

The typical Alfvén velocity is

$$v_a = \frac{B}{\sqrt{4\pi\rho}} \tag{1.25}$$

$$= 69 \left(\frac{B}{1\ \mu{\rm G}}\right) \left(\frac{n_{\rm th}}{10^{-3}\ {\rm cm}^{-3}}\right)^{-1/2} \frac{\rm km}{\rm s}. \tag{1.26}$$

Large-scale motions are super-Alfvénic, such that the magnetic field is not dynamically important, but the field topology is determined by the fluid motion. As the velocity decreases towards smaller scales along the turbulent cascade, it becomes sub-Alfvénic. The Alfvén-scale describes this transition scale at which magnetic fields become important and is on the order of

$$l_{\rm A} = 100 \left(\frac{B}{1\ \mu{\rm G}}\right)^3 \left(\frac{L_0}{300\ {\rm kpc}}\right) \left(\frac{v_L}{10^3\ {\rm km/s}}\right)^{-3} \left(\frac{n_{\rm th}}{10^{-3}\ {\rm cm}^{-3}}\right)^{3/2}\ {\rm pc} \tag{1.27}$$

implying that the collisionality can be satisfied down to this scale mediated by magnetic fields rather than the mean free path in Eqn. (1.20). The effective Reynolds number is at least a few 1000.

Additional insight can be gained from kinetic calculations. Micro-instabilities grow from magnetic field fluctuations at the Lamor scale, leading to the "firehose" and "mirror" instability. They provide a source for collisionality on much smaller scales down to the Lamor radius of protons. The effective Reynolds number is thus even larger ${\rm Re} \approx 10^{19}$ (compare Donnert et al., 2018).

Overall, the ICM can be considered collisional at all resolved scales in simulations such that the plasma can be described as an ideal fluid by the Magneto Hydrodynamics (MHD) equations. Nevertheless, there are deviations from this idealized description motivated by observations and kinetic calculations, such as viscosity and conductivity, which have been summarized in the review by Sarazin (1986).

In order to have a well-defined temperature, the protons and electrons must both follow a Maxwellian distribution. The relevant timescale for electrons to equilibrate by collisions is

$$t_{\rm eq}^{ee} = \frac{3 m_e^{1/2} \left(k_B T_e\right)^{3/2}}{4\pi^{1/2} n_e e^4 \ln \Lambda} \tag{1.28}$$

$$\approx 3.3 \cdot 10^3 \left(\frac{T_e}{10^8\ {\rm K}}\right)^{3/2} \left(\frac{n_e}{10^{-3}\ {\rm cm}^{-3}}\right)^{-1}\ {\rm yr}. \tag{1.29}$$

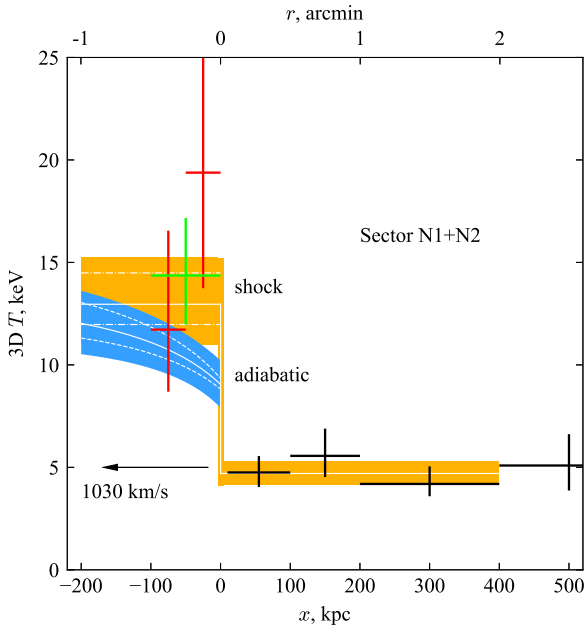

Figure 1.7: Temperature measured in a shock compared to two different model profiles for instant-equilibration (yellow) and adiabatic compression followed by Coulomb equilibration (blue). Different colored data denote different binnings. The error bars in the position mark the radial range of measurements, temperature errors are 1σ uncertainty ranges (Wang et al., 2018).

As protons are more massive, their equilibration timescale scales as $t_{\rm eq}^{pp} = \left(m_p/m_e\right)^{1/2} t_{\rm eq}^{ee} \approx 43 t_{\rm eq}^{ee}$. The equilibration timescales are shorter than most evolutionary timescales, hence both electrons and protons individually follow a Maxwellian distribution. The equipartition timescale between protons and electrons is even longer $t_{\rm eq}^{pe} = \left(m_p/m_e\right) t_{\rm eq}^{ee} \approx 1870 t_{\rm eq}^{ee}$. It is still shorter than typical evolutionary timescales, such that a single temperature for the gas can be defined. Different measurements in shocks such as the one by Wang et al. (2018) shown in Fig. 1.7 confirm that even on the very short scales relevant in shocks instant equilibration can be assumed.

Thermal conduction leads to a heat flux along temperature gradients

$$Q = -\kappa \nabla T_e \tag{1.30}$$

depending on the thermal conductivity κ. The conductivity κ itself depends only weakly on density, but very strongly on the temperature. Thus, this process is only efficient in the cluster center, and its efficiency rapidly decreases with radius. Within the center, the conduction timescale is

$$t_{\rm cond} = 3.3 \cdot 10^8 \left(\frac{n_0}{10^{-3}\ {\rm cm}^{-3}}\right) \left(\frac{T_e}{10^8\ {\rm K}}\right)^{-5/2} \left(\frac{r_c}{0.25\ {\rm Mpc}}\right)^2 \left(\frac{\ln \Lambda}{40}\right)\ {\rm yr} \tag{1.31}$$

with the cluster core radius r_c, defined as radius at which the projected galaxy density decreases by a factor of two compared to the central value. Already at $2r_c$, the conduction timescale is

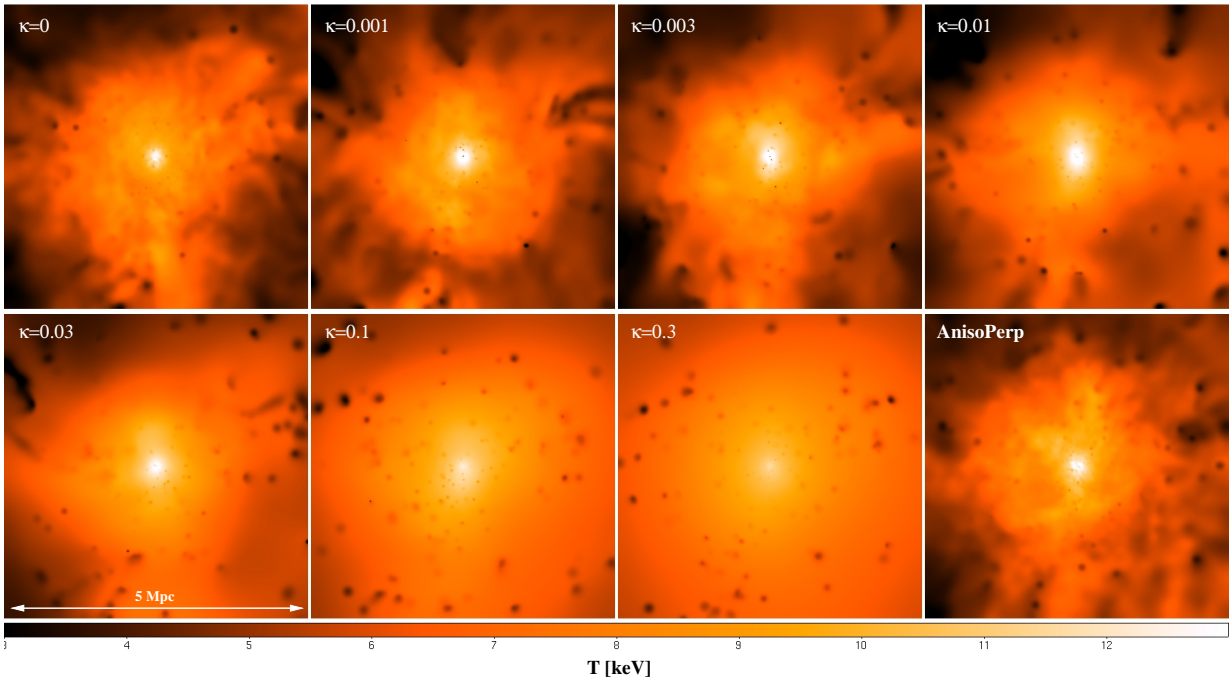

Figure 1.8: Effect of thermal conduction shown by Arth et al. (2014). Different panels show different levels of suppression and an additional model for anisotropic conduction depending on the magnetic field strength.

longer by a factor of ≈ 100. Conduction transports energy to larger radii, leading to cooling in the center and heating in the outskirts. The effect of conduction on the cluster temperature can be seen in Fig. 1.8. Conduction smears out any temperature fluctuations, homogenizing the temperature. Magnetic fields suppress transport perpendicular to the field direction and make conduction anisotropic. It proceeds at full efficiency in the direction along the magnetic field lines, causing them to become approximately isothermal. As the magnetic correlation length $l_B \approx 20$ kpc is similar to the mean free path, conduction is suppressed in the direction perpendicular to the magnetic field by a factor of at least $1/3$. This leads to an effective insulation perpendicular to the magnetic fields and strongly reduces mixing.

Viscosity acts against shear flows, converting kinetic energy into thermal energy. The dynamic viscosity coefficient is

$$\eta = 5500 \left(\frac{T_e}{10^8 \text{ K}} \right)^{5/2} \left(\frac{\ln \Lambda}{40} \right)^{-1} . \tag{1.32}$$

Zhuravleva et al. (2019) found from the observed density fluctuations in X-rays that this value is suppressed. The effective viscosity is several orders of magnitude smaller, indicating enhanced collisionality due to instabilities or anisotropic behavior due to magnetic fields.

Metals are redistributed and smeared out by metal diffusion. In addition, heavy metals tend to sink towards the center. Mixing by convection occurs if the temperature gradient is steep enough

compared to the density gradient and the cluster gas is unstable against the convective instability. Due to the short mixing timescale, this is rarely the case except, e.g., for rising AGN bubbles.

1.2.4 Turbulence and Non-Thermal Pressure in the ICM[2]

The ICM of GCs is a very dynamic environment and is shaped by mergers, global gas motions, and turbulence (Carilli & Taylor, 2002; Kravtsov & Borgani, 2012). These processes act on different scales. Mergers and bulk motions directly impact the gas dynamics on large scales. Small scales, in contrast, are dominated by turbulent motions (compare also the reviews by Subramanian et al., 2006; Schekochihin & Cowley, 2006, for a more detailed summary on turbulence in the ICM).

All of these gas motions can be described as different pressure terms contributing to the total pressure in the ICM. Besides gas motions, magnetic fields can also produce additional magnetic pressure. In combination, the aforementioned two contributions are often summarized as non-thermal pressure opposed to the thermal pressure of the gas.

In this work, we will refer to the pressure due to small-scale turbulent motions as the turbulent pressure. The entirety of pressures except for the thermal, including turbulence, bulk motions, and possibly magnetic fields will be called non-thermal pressure.

There are a plethora of numerical and observational programs that are specifically targeted to understand the origin of the structure of the ICM. Turbulence is injected on large scales in merger shocks, after which it decays and cascades down to smaller scales (Roettiger & Burns, 1999; Subramanian et al., 2006; Mohapatra et al., 2020, 2021). Both simulations and observations find that ICM turbulence is subsonic, with typical velocities of a few 100 km/s (den Herder et al., 2001; Hitomi Collaboration et al., 2016, 2018). For a sound speed of the order of $c_s = 1000$ km/s, this results in a volume filling turbulent Mach number between $\mathcal{M} = 0.2$ and 0.5, depending on the position within the clusters. While global measurements of turbulence in GCs can be understood within the context of the classical theory of subsonic turbulence which is supported by observations (e.g. the results by Hitomi Collaboration et al., 2016, 2018), our understanding of its origin and dissipation scales still lacks a solid base.

Various X-ray observations provide insight into ICM properties and aim to analyze ICM turbulence. Schuecker et al. (2004) quantify turbulence based on pressure fluctuations in the Coma cluster. A map of the pressure in the central region is shown in Fig. 1.9 where fluctuations and turbulent eddies are visible. They find that turbulence is well described by a Kolmogorov power spectrum, with an upper limit of the turbulent pressure of 10% of the total pressure. Similarly, Zhuravleva et al. (2019) study density fluctuations from X-ray observations and quantify viscosity in the ICM. They derive velocities up to around a few 100 km/s, closely following the expected Kolmogorov scaling for subsonic turbulence.

Exploiting spectroscopically resolved lines to derive velocities, Hitomi Collaboration et al. (2016, 2018) perform detailed measurements in the Perseus cluster, yielding velocities between 100 – 200 km/s and a turbulent pressure support of only 4% compared to the total pressure. This value is at the lower end compared to many other results cited in this work. As Perseus also shows a cool core, it is often classified as relaxed in the center where the turbulence is measured,

[2]Part of this section has been published by Groth et al. (2024).

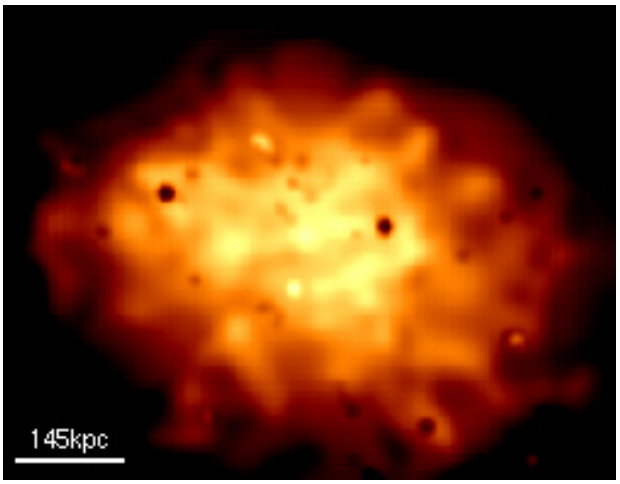

Figure 1.9: Pressure fluctuations in the central regions of the Coma cluster by Schuecker et al. (2004). Turbulent eddies have sizes between 20 kpc and 145 kpc.

despite the cluster showing sloshing motions and an AGN. As this is a single system, it is unclear from the aforementioned work if there is any dependence on the dynamical state. The result is still consistent with the upper limits of the spectroscopic measurements by XMM-Newton (den Herder et al., 2001) of 200 − 600 km/s.

An alternative method is used by Eckert et al. (2019). For the X-COP sample, they quantify the non-thermal pressure based on the deviation from HE and find values between 2% and 15%, depending on radius and cluster.

Different observations indicate that the amount of turbulence should depend on the dynamical state of the system. One indirect tracer of turbulence is the existence of a radio halo, which requires turbulent re-acceleration. Cassano et al. (2010); Cuciti et al. (2015, 2021) found that merging systems typically host such a radio halo, while relaxed systems do not.

Alternative insight can be gained from simulations of cosmological boxes or zoom-in regions with adequate resolution. One main advantage is the access to the velocity data for every resolution element in the simulation. Nevertheless, it remains difficult to extract turbulence directly, as this requires a good estimate of the bulk flow.

Based on the velocity dispersion, Lau et al. (2009) find a turbulent pressure support between 6 – 15%, increasing with radius, in relaxed systems and higher values between 9 – 24% in unrelaxed systems. Using a slightly different approach, i.e. separating the smooth gas component from clumps, and computing median instead of mean properties, Zhuravleva et al. (2013) find consistent results. They find increased root-mean-square (rms) velocities in active clusters of $\approx 0.7\, c_s$ in units of the sound speed, compared to $\approx 0.4\, c_s$ in relaxed clusters.

In a series of papers, Vazza et al. (2009, 2012, 2017, 2018a) explore turbulence in GCs simulated with the ENZO code (Bryan et al., 2014) featuring Adaptive Mesh Refinement (AMR) (Berger & Colella, 1989). They introduce the multi-scale filtering technique, which decomposes the total velocity into bulk and turbulent motions, predicting a turbulent pressure support around 10%. In addition, they show a strong dependence on whether a constant or variable filtering

length is used. Such a dependence is expected because the filtering length allows to focus on motions only on the length scales defined by the size of turbulent eddies, ignoring any bulk motions on larger scales that can increase the kinetic energy budget.

Biffi et al. (2016) use a modern Smoothed Particle Hydrodynamics (SPH) implementation with a high-resolution shock-capturing method and a high-resolution entropy-increasing diffusion scheme (also known as artificial viscosity and conduction), with an additional stabilization of the method against the tensile instability using a high-order kernel for their simulations. They find overall high devitations from HE around $10 - 20\%$, with a higher deviation for more disturbed systems. This is slightly higher than other values from previously quoted references in this section, but still consistent. In addition, not all of this deviation from HE will be attributed to turbulence, instead this is only an upper limit.

A direct comparison between simulations and observations has been made by Sayers et al. (2021). Using the "Clump3d" method, they combine several observations to de-project the cluster and derive a non-thermal pressure based on the deviation from HE. Even when analyzed with the same method, simulations and observations show a significant disagreement in the non-thermal pressure fraction. It reaches $\approx 13\%$ for simulations, while it is consistent with zero for observations. In addition, Sayers et al. (2021) find no dependence on the dynamical state.

Overall, the interpretation of the non-thermal pressure depends on the analysis method. Many strategies based on the deviation from HE include the effect of bulk motions, magnetic fields, cooling flows, turbulence, and everything not attributed to the thermal origin. Magnetic dynamo theory and numerical simulations predict a magnetic pressure of $20 - 40\%$ compared to the turbulent pressure (Subramanian et al., 2006). The ratio of thermal pressure to magnetic pressure is often summarized in the parameter β. Typical values are on the order of $\beta \approx 10^2$. The volume-averaged magnetic pressure is small and $\lesssim 5\%$ (compare, e.g., the review by Kravtsov & Borgani, 2012). The non-thermal pressure support by relativistic CRs is even lower. Non-detections of energetic γ rays provide an upper limit of $\lesssim 10^{-2}$ (compare, e.g., the review by Ruszkowski & Pfrommer, 2023). Also rotational patterns can affect the non-thermal pressure support (Biffi et al., 2011). This makes the comparison between different results depend on subtleties and motivates the need for more robust methods. More direct methods such as the multi-scale-filtering technique return instead the actual turbulent pressure, filtering out motions on larger scales.

2 | (Magneto-)Hydrodynamics

As discussed in Sec. 1.2.3 the ICM can at first order be described as an ideal fluid, which is incompressible and described entirely by velocity, density, and isotropic pressure, implicitly assuming that no deviations such as viscosity or heat conduction are present. At the resolution considered, the gas contains a large number of particles (atoms/ions) and behaves collisionally. Many books describe the governing equations and processes in detail (Landau & Lifshitz, 1959; Feldmeier, 2019). Here, we want to give a brief overview of the governing equations. We will also discuss shocks and turbulence in more detail as these hydrodynamical processes are especially relevant to this work.

2.1 Basic Hydrodynamical Equations[1]

The evolution of any ideal fluid is described by three main equations. In this chapter, we write them in the Eulerian formulation (compare, e.g., Clarke & Carswell, 2007). Mass conservation leads to the continuity equation in differential form

$$\frac{\partial \rho}{\partial t} + \nabla \cdot (\rho \boldsymbol{v}) = 0 \tag{2.1}$$

where ρ is the fluid density and $\boldsymbol{v}$ the velocity. The second equation is an equation of motion (Euler's equation), corresponding to Newton's second law

$$\frac{\partial (\rho \boldsymbol{v})}{\partial t} + \nabla \cdot (\rho \boldsymbol{v} \otimes \boldsymbol{v}) = -\nabla P + \rho \boldsymbol{a}. \tag{2.2}$$

The pressure P and external accelerations $\boldsymbol{a}$ lead to momentum changes. In the remainder of this chapter, we will neglect any external forces $\boldsymbol{a}$, as they will be treated independently of hydrodynamics by operator splitting in our numerical framework.

Finally, energy conservation is ensured by the first law of thermodynamics and leads to the governing equation

$$\frac{\partial (\rho e)}{\partial t} + \nabla \cdot ((\rho e + p)\, \boldsymbol{v}) = 0. \tag{2.3}$$

[1]This section has been published by Groth et al. (2023). Some extensions have been added.

The energy density

$$e = u + \frac{1}{2}\boldsymbol{v}^2 \tag{2.4}$$

consists of the internal energy density u and the kinetic energy of the fluid.

Within an inertial frame of reference, all these equations can be combined into

$$\frac{\partial \boldsymbol{U}}{\partial t} + \nabla \cdot (\mathbf{F} - \boldsymbol{v}_{\text{frame}} \otimes \boldsymbol{U}) = \boldsymbol{S} \tag{2.5}$$

with outer product $\otimes$ and, for pure hydrodynamics, field vector

$$\boldsymbol{U} = \begin{pmatrix} \rho \\ \rho \boldsymbol{v} \\ \rho e \end{pmatrix}, \tag{2.6}$$

flux

$$\mathbf{F} = \begin{pmatrix} \rho \boldsymbol{v} \\ \rho \boldsymbol{v} \otimes \boldsymbol{v} + P\mathbb{1} \\ (\rho e + P)\, \boldsymbol{v} \end{pmatrix}, \tag{2.7}$$

and vanishing source terms $\boldsymbol{S} = \mathbf{0}$.

In total, Eqn. (2.5) provides 5 constraints for 6 variables: fluid density ρ, energy density e, pressure P, and the three components of the velocity $\boldsymbol{v}$. The missing constraint is provided by an equation of state, connecting the pressure to the internal energy density u. For an ideal gas it takes the form

$$P = (\gamma - 1)\, \rho u \tag{2.8}$$

where the adiabatic index γ amounts to $5/3$ if the gas is monoatomic.

Several derived properties are used in calculations. The temperature is directly related to the internal energy

$$T = \frac{\mu}{k_{\text{B}}} (\gamma - 1)\, u \tag{2.9}$$

where μ is the mean molecular weight and k_{B} the Boltzmann constant. In the idealized case without any heat exchange, the fluid motion is adiabatic. This implies that the entropy remains constant and the equation of state is adiabatic. In simulations, the entropic function

$$A = \frac{(\gamma - 1)\, u}{\rho^{\gamma - 1}} \tag{2.10}$$

is used as a proxy for the entropy and the two quantities are closely related. Adiabatic soundwaves propagate at the speed of sound

$$c_s = \sqrt{\gamma \frac{P}{\rho}} = \sqrt{\gamma\, (\gamma - 1)\, u}. \tag{2.11}$$

which is the relevant speed for the propagation of (small and linear) perturbations.

2.2 Magnetic Fields

The presence of magnetic fields complicates the picture. Ideal MHD relies on the assumption that the magnetic field is constrained to move with the fluid. This is even true for almost neutral fluids and thus especially for the mostly ionized plasma in astrophysical environments.

Additional terms in the momentum and energy equation are present describing the impact of the magnetic field $\boldsymbol{B}$. In addition, the induction equation describes the evolution of the magnetic field itself. In astrophysical environments, the electric conductivity is very high, such that the diffusive terms in the induction equation can be neglected. All equations below are written in units where the magnetic vacuum permeability is $\mu_0 = 1$.

The field vector and flux tensor in Eqn. 2.5 become (e.g., Gaburov & Nitadori, 2011)

$$\boldsymbol{U} = \begin{pmatrix} \rho \\ \rho \boldsymbol{v} \\ \rho e \\ \boldsymbol{B} \end{pmatrix}, \tag{2.12}$$

$$\mathbf{F} = \begin{pmatrix} \rho \boldsymbol{v} \\ \rho \boldsymbol{v} \otimes \boldsymbol{v} + p - \boldsymbol{B} \otimes \boldsymbol{B} \\ \rho e \boldsymbol{v} + p \boldsymbol{v} - \boldsymbol{B} \left(\boldsymbol{v} \cdot \boldsymbol{B} \right) \\ \boldsymbol{v} \otimes \boldsymbol{B} - \boldsymbol{B} \otimes \boldsymbol{v} \end{pmatrix}. \tag{2.13}$$

Source terms $\boldsymbol{S} = 0$ vanish. Most importantly, magnetic fields introduce cross-terms among the dimensions.

Three different speeds classify the propagation of waves for the different modes. The first characteristic velocity is the Alfvén velocity

$$v_{\mathrm{A}} = \frac{B}{\sqrt{\rho}}. \tag{2.14}$$

In addition, fast and slow magnetosonic waves propagate with speeds

$$c_{\mathrm{ms,f/s}} = \sqrt{0.5 \left(c_{\mathrm{ms}}^2 \pm \sqrt{c_{\mathrm{ms}}^4 - 4 v_{A,\perp}^2 c_s^2} \right)}, \tag{2.15}$$

$$c_{\mathrm{ms}} = \sqrt{v_{\mathrm{A}}^2 + c_s^2}, \tag{2.16}$$

where $v_{A,\perp}$ depends on the magnetic field perpendicular to the direction of propagation $B_\perp$.

2.3 Shocks

A shock is a strong, non-linear perturbation of the fluid. It propagates faster than the speed of sound, such that the fluid ahead of the perturbation cannot adjust. Sudden changes lead to

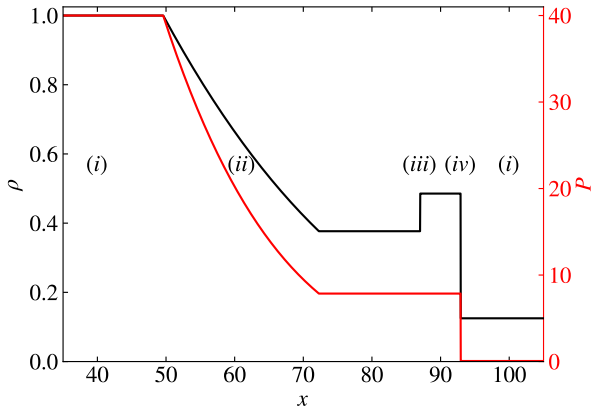

Figure 2.1: Density and pressure structure of a shock tube with Mach number $\mathcal{M} = 10$ at time $t = 2.5$. The numbers indicate (*i*) the unperturbed left state, (*ii*) the rarefaction fan, (*iii*) the contact discontinuity, (*iv*) the shock front, (*v*) the unperturbed right state.

discontinuities in the hydrodynamical properties. The propagation speed v is often expressed in terms of the sound speed in form of the Mach number

$$\mathcal{M} = \frac{v}{c_s}. \tag{2.17}$$

The jumps must satisfy the Rankine-Hugoniot jump conditions, which are derived from the conservation equations (2.1)-(2.3). The density, internal energy, and pressure jumps are

$$\frac{\rho_2}{\rho_1} = \frac{u_1}{u_2} = \frac{(\gamma+1)\,p_2 + (\gamma-1)\,p_1}{(\gamma+1)\,p_1 + (\gamma-1)\,p_2} = \frac{(\gamma+1)\,\mathcal{M}^2}{(\gamma-1)\,\mathcal{M}^2+2}, \tag{2.18}$$

$$\frac{P_2}{P_1} = \frac{2\gamma\mathcal{M}^2 - (\gamma-1)}{\gamma+1} \tag{2.19}$$

which, for a strong shock with $P_2 \gg P_1$, reduces to

$$\frac{\rho_2}{\rho_1} \to \frac{\gamma+1}{\gamma-1}. \tag{2.20}$$

For $\gamma = 5/3$ the jump is limited to a factor of 4.

Depending on the geometry, the general properties of the evolution of the shock can be characterized. Linear shocks are often referred to as “shock tubes” based on the experimental setup. The fluid is initialized with two distinct states on the left and right sides of a separating barrier, which is removed to allow the two fluid states to interact. A shock then starts to propagate, leading to a very characteristic structure shown in Fig. 2.1. As discussed above, the height of the jumps depends on the Mach number, but the general features are consistent and independent of the Mach number. The leftmost (*i*) and rightmost (*v*) states did not interact yet, keeping information of the initial fluid states. The left fluid expands in the rarefaction fan (*ii*), followed by the contact discontinuity (*iii*), where the density changes, but the pressure and also velocity do not. Thus, it

separates the two initial fluids. At the shock front (*iv*) kinetic energy is dissipated into thermal energy, and the entropy increases. This setup is closely related to the Riemann problem, which is discussed in Sec. 3.6.

Spherical propagation results in a blast wave of initially very high Mach number. Thus, the jump condition Eqn. (2.20) holds. The propagation can be described by a self-similar solution derived by Sedov (1946, 1959). It depends only on the energy inside the shock E and the density of the ambient medium ρ_0. In astrophysical environments, the geometry applies to SN explosions.

Magnetic fields complicate the picture, as they lead to the split-up into fast and slow magnetosonic waves. Thus, the shock structure becomes even more complex and depends on the magnetic field strength and orientation.

A more detailed description of the main properties of shocks and hydrodynamics in general in the astrophysical context has been provided by Clarke & Carswell (2007). In principle, the ICM is collisionless on the small scales relevant within shocks. The buildup of jumps relies on magneto-hydrodynamical instabilities, most importantly the Weibel instability (Weibel, 1959). The plasma is weakly magnetized, including initial magnetic field perturbations. The Lorentz force leads to the formation of a current sheath and the growth of the instability. Eventually, particles pile up perpendicular to the shock front, leading to a behavior identical to collisional shocks (Medvedev & Loeb, 1999).

2.4 Turbulence

An important quantity to describe a flow is the Reynolds number

$$\mathrm{Re} = \frac{lv}{\nu_{\mathrm{visc}}} \tag{2.21}$$

with kinematic viscosity ν_{visc}, characteristic length scale l, and velocity v. The Reynolds number describes the ratio between the viscous and dynamical timescale, thus containing information on the importance of viscosity. A flow at a low Reynolds number is smooth and laminar, while it typically is turbulent for a very large Reynolds number. The critical Reynolds number that separates these two regimes can be found from experiments and simulations and is on the order of $\mathrm{Re}_{\mathrm{crit}} \approx 10^{3-4}$.

Turbulence in general is characterized by a non-zero vorticity. The precise amount of vorticity depends on the driving process and significantly impacts the density structure (Federrath et al., 2008, 2009, 2010).

For subsonic turbulence, the energy is contained in soundwaves. A phenomenological description has been found by Kolmogorov (1941); Obukhov (1962). Energy is inserted into the system on large scales l at rate ϵ and transported to smaller scales via a turbulent cascade until the energy is dissipated on small scales due to viscous forces ("dissipation range"). The characteristic turbulent velocity v_λ of turbulent eddies at spatial scale/size λ can be described by the Kolmogorov-Obukhov law

$$v_\lambda = v_l \left(\frac{\lambda}{l}\right)^{1/3} . \tag{2.22}$$

The resulting kinetic energy is often studied in Fourier space. The energy power spectrum scales with wavenumber $k = 2\pi/\lambda$ according to

$$E(k) \sim \epsilon^{2/3} k^{-5/3} \tag{2.23}$$

between the external scale l of energy injection and the internal scale λ_0 below which kinetic energy is dissipated. Most of the energy is contained at large scales. Experiments and simulations show a bottleneck effect close to the dissipation range, where a pile-up of energy occurs (Falkovich, 1994).

This Kolmogorov theory has been a great success in describing subsonic turbulence in many systems, but relies on several assumptions, including self-similarity among different scales, which implies scale-invariant statistics. These assumptions are not always satisfied, especially in supersonic turbulence. For supersonic flows, energy is dissipated in shocks. The power spectrum of the energy cascade follows the Burgers (1948) law

$$E(k) \sim k^{-2} \tag{2.24}$$

with a different slope than the Kolmogorov cascade.

A more detailed understanding of turbulence and its density structure requires experiments and numerical simulations. Padoan et al. (1997); Passot & Vázquez-Semadeni (1998) found that the density perturbations are related to the Mach number

$$\frac{\sigma_\rho}{\rho_0} = b\mathcal{M} \tag{2.25}$$

where b varies between 0.25 and 1 for different simulations, and also depends on the mixture of solenoidal and compressive driving modes (compare Federrath et al., 2008, and references therein) and stratification (Mohapatra et al., 2021).

More recently, progress has been made in the understanding of MHD-turbulence. Here, we want to focus on the early, basic results. More details can be found in the review by Schekochihin (2022). The energy transfer in the turbulent cascade is affected by the presence of magnetic fields. Kraichnan (1965) found that the power spectrum scales as

$$E(k) \sim (\epsilon v_\mathrm{A})^{1/2} k^{-2/3}. \tag{2.26}$$

For strong magnetic fields, the energy transport becomes anisotropic (Goldreich & Sridhar, 1995). Thus, the Kolmogorov scaling holds for $k_\perp$ perpendicular to the magnetic field. Along the magnetic field, the velocity at a certain scale satisfies

$$v_{l_\parallel} \sim \left(\frac{\epsilon l_\parallel}{v_\mathrm{A}}\right)^{1/2}. \tag{2.27}$$

3 | Numerical Methods[1]

Solving the system of differential equations describing the evolution of the gas requires discretizing them. In the temporal dimension a sufficiently small timestep Δt is introduced. The spatial discretization can be obtained using various approaches.

Historically, there exist different methods to solve the hydrodynamical equations in the comoving/cosmological context. Hereby, one has the option to discretize the hydrodynamic equations by mass or volume. The former leads to the concept of "Lagrangian" (particle-based) codes and the concept of SPH, and the more recent Meshless Finite Mass (MFM) and Meshless Finite Volume (MFV). The latter gives rise to the concept of "Eulerian" (grid-based) codes and the Godunov finite volume approach.

Mesh codes exist in two flavors: either as a stationary mesh, possibly with AMR, as implemented e.g. in ZEUS (Stone & Norman, 1992), TVD (Ryu et al., 1993, 1998), ENZO (Bryan et al., 1995, 2014), FLASH (Fryxell et al., 2000), RAMSES (Teyssier, 2002), ATHENA (Stone et al., 2008), and ATHENA++ (Stone et al., 2020) or as a moving mesh as in AREPO (Springel, 2010; Weinberger et al., 2020) and SHADOWFAX (Vandenbroucke & De Rijcke, 2016). The latter has the advantage of being Pseudo-Lagrangian. A moving mesh is invariant to boosts, but each individual resolution element is not fully Lagrangian due to the choice of the frame velocity of the interfaces and the resulting presence of mass fluxes. While mesh codes as well as MFM employ a Godunov-method and calculate fluxes between neighbors (Godunov, 1959), SPH directly retrieves the hydrodynamical fluid vectors from the kernel density estimation that is obtained by adopting a weighted sum over a certain (typically non-constant) number of neighbors.

Popular SPH codes include GADGET in the different versions including GADGET-1 (Springel et al., 2001), GADGET-2 (Springel, 2005), and GADGET-4 (Springel et al., 2021), PHANTOM (Lodato & Price, 2010; Price et al., 2018) and GASOLINE (Wadsley et al., 2004, 2017). An improved SPH scheme with non-standard enhancements has been implemented in MAGMA2 (Rosswog, 2020).

MFM has been implemented in e.g. GIZMO (Hopkins, 2015), GANDALF (Hubber et al., 2018), GADGET-3 (Steinwandel et al., 2020), and PKDGRAV-3 (Alonso Asensio et al., 2023).

For gravitational forces of DM or stars, most codes employ a mass discretization, with different options for computationally more efficient calculations. In OPENGADGET3, it is solved using the TreePM method.

In this chapter, we want to give a brief overview of the different numerical methods. The time discretization strategy is described in Sec. 3.1. In Sec. 3.2, we describe the solution strategies for gravitational interactions as used in OPENGADGET3. We continue with the main hydrodynamical

[1]The introductory part of this section has been published by Groth et al. (2023). Some details have been added.

solvers in Sects. 3.3 to 3.7. For MFM and SPH, we will focus on the details relevant to the implementation in OpenGadget3. Finally, in Sec. 3.8 we give a brief overview on how to take into account the cosmological expansion. Where applicable, we focus on the implementation in OpenGadget3.

3.1 Integrator and Timestepping[2]

For the time integration, we employ a Leapfrog scheme in kick-drift-kick (KDK) form to achieve second order accuracy (compare, e.g., Hernquist & Katz, 1989) in the implementation following Verlet (1967); Springel (2005). This integrator is symplectic and thus ensures good energy conservation, while it requires only a single force calculation per timestep.

Starting from values at timestep number n, velocities $\boldsymbol{v}$ are updated in a first half-step kick. It is followed by drifting the positions $\boldsymbol{r}$, and another, second half-step kick:

$$\boldsymbol{v}^{n+1/2} = \boldsymbol{v}^{n} + \frac{1}{2}\boldsymbol{a}^{\tilde{n}}\Delta t, \tag{3.1}$$

$$\boldsymbol{r}^{n+1} = \boldsymbol{r}^{n} + \boldsymbol{v}^{n+1/2}\Delta t, \tag{3.2}$$

$$\boldsymbol{v}^{n+1} = \boldsymbol{v}^{n+1/2} + \frac{1}{2}\boldsymbol{a}^{\widetilde{n+1}}\Delta t. \tag{3.3}$$

The acceleration $\boldsymbol{a}^{\tilde{n}} = \boldsymbol{a}^{\tilde{n}}_{\mathrm{hydro}} + \boldsymbol{a}^{n}_{\mathrm{grav}}$ consists of hydrodynamical accelerations $\boldsymbol{a}_{\mathrm{hydro}}$ and gravitational accelerations $\boldsymbol{a}_{\mathrm{grav}}$. Following the operator splitting approach, they are calculated separately. Gravity and hydrodynamical accelerations are evaluated between the drift and the second half-kick. Gravitational interactions depend only on the position, and can thus be calculated at timestep n. While in traditional SPH, entropy remains unchanged, allowing also for the calculation of hydrodynamical forces at timestep n, modern SPH incorporates entropy evolution and introduces velocity dependence for the viscous terms and artificial conductivity. Thus, we use predicted values based on the changes calculated during the previous timestep, updated at the drift. The dependence of the predicted variables is indicated by $\tilde{n}$.

For SPH, the entropic function

$$A = (\gamma - 1)U/\rho^{\gamma-1} \tag{3.4}$$

is integrated in two half-steps at the kicks

$$A^{n+1/2} = A^{n} + \frac{1}{2}\left(\frac{\mathrm{d}A}{\mathrm{d}t}\right)^{\tilde{n}}_{\mathrm{hydro}}\Delta t, \tag{3.5}$$

$$A^{n+1} = A^{n+1/2} + \frac{1}{2}\left(\frac{\mathrm{d}A}{\mathrm{d}t}\right)^{\widetilde{n+1}}_{\mathrm{hydro}}\Delta t. \tag{3.6}$$

[2]This section was taken from Groth et al. (2023) and was extended.

OpenGadget3 uses hierarchical timestepping to ensure synchronization, while allowing adaptive timesteps, depending on different timestep limiters. The main ones are a limiter for gravity, a Courant-like timestep criterion (Springel, 2005) and a limiter based on the velocity divergence:

$$\Delta t_i^{\text{grav}} = \frac{2 C_{\text{int accuracy}} a \epsilon_i}{\left| a^{-3\gamma+2} \boldsymbol{a}_{\text{hydro}} + a^{-2} \boldsymbol{a}_{\text{grav}} \right|}, \tag{3.7}$$

$$\Delta t_i^{\text{Courant}} = \frac{C_{\text{Courant}} a h_i}{a^{3(1-\gamma)/2} c_{\text{max},i}}, \tag{3.8}$$

$$\Delta t_i^{\nabla \cdot \boldsymbol{v}} = \frac{1.5}{\left| a^{-2} \nabla \cdot \boldsymbol{v} \right|} \tag{3.9}$$

where $c_{\text{max},i}$ is the maximum signal velocity over the neighbors, h_i the smoothing length, ϵ_i the gravitational softening, and $C_{\text{Courant}} = 0.15$, $C_{\text{int accuracy}} = 0.05$ are free parameters. The velocity divergence timestep is limited to go down two timebins to avoid small timesteps due to purely numerical artifacts. Timesteps are chosen as the largest timestep that fulfills $\Delta t_i = 2^{-n} \Delta t_{\text{global}} \leq \min\left(\Delta t_i^{\text{grav}}, \Delta t_i^{\text{Courant}}, \Delta t_i^{\nabla \cdot \boldsymbol{v}}\right)$ with timebin $n \in \mathbb{N}_0$.

Each particle has an individual timestep, which formally breaks the symplectic nature of the integrator, but allows to take into account the large dynamic range of cosmological systems. The integration is still a series of kicks, drift, and kick. The system progresses by the smallest global timestep. Accelerations are calculated only for active particles, which are in synchronization with the current timestep, while they are not modified for inactive particles located on a smaller time bin, corresponding to larger timesteps. Thus, the kick of velocities uses the individual timestep of each particle. Drifts are performed for every particle. More details can be found in the Gadget-2 paper (Springel et al., 2005).

For strong shocks, large differences can occur between the timesteps of close-by particles. This is avoided by a wake-up scheme, described in more detail by Pakmor (2010); Pakmor et al. (2012); Beck et al. (2016b). OpenGadget3 uses a criterion based on the signal velocity. If for any neighbor j, the signal velocity varies strongly $c_{\text{max},i} > f_w c_j$ with tolerance factor $f_w = 3$, wake-up is triggered. In this case, the neighboring particle is considered active and moved to a shorter timestep, such that synchronization is still ensured. While this scheme will break conservation, it works reasonably well and avoids numerical errors in strong shocks.

3.2 Gravity Solver – TreePM[3]

The accurate treatment of gravity is of great importance for cosmological simulations (Springel, 2010). In principle, it can be solved accurately by a direct summation, which is, however, computationally expensive ($O\left(N^2\right)$). Instead, we follow the much more efficient combined Oct-Tree-Particle Mesh (PM) approach (Xu, 1995; Bode et al., 2000; Springel, 2005, 2010; Springel et al., 2021) that scales as $O\left(N \log N\right)$. OpenGadget3 mainly follows the implementation in Gadget-2, which has been extensively described by Springel (2005). In the following, we briefly

[3]This section has been published by Groth et al. (2023). Some additions and adjustments have been made.

review the main concept. The potential is split into short-range and long-range contributions. Short-range forces are calculated following the oct-tree algorithm, while long-range forces are calculated using a particle mesh.

The idea of a tree algorithm has been proposed by Appel (1985) and Barnes & Hut (1986). Nodes of an oct-tree are constructed by splitting the domain into a sequence of cubes. Force contributions from nodes of mass m_i and size l_i are calculated if the nodes satisfy a relative opening angle criterion

$$\frac{Gm_i}{r^2}\left(\frac{l_i}{r}\right)^2 \leq \alpha_{\text{force acc}}\,|\boldsymbol{a}_{\text{old}}| \tag{3.10}$$

$$\vee\,|r_k - c_k| \leq 0.6l \quad k \in \{x, y, z\} \tag{3.11}$$

with the geometrical center of the node $\boldsymbol{c}$ and free parameter $\alpha_{\text{force acc}} = 0.005$. For numerical reasons to keep the equation linear with respect to adding and removing particles from nodes, only the monopole contributions are taken into account. The implementation in GADGET has been described by Springel et al. (2001). The total gravitational acceleration of particle i from other nodes/particles j with mass m_j at location $\boldsymbol{r}_{ij}$ relative to particle i and with (gravitational) softening length ϵ_j is given by

$$\boldsymbol{a}_{\text{grav},i} = G\sum_{j}^{N_{\text{tot}}} \boldsymbol{r}_{ij} \begin{cases} \frac{m_j}{r_{ij}^3} & \text{if } r_{ij} > \epsilon_j \\ \frac{m_j}{\epsilon_j^3}\text{Corr}(r_{ij}/\epsilon_j) & \text{if } r_{ij} \leq \epsilon_j, \end{cases} \tag{3.12}$$

with total number of particles and nodes N_{tot}. Corr is a correction term, taking into account the softening. G is the gravitational constant.

For the particle mesh (Eastwood & Hockney, 1974), all particles are assigned to grid-cells, such that a discrete Fourier-transformation can be calculated, with the gravitational potential Φ_k in Fourier space at wavenumber k being calculated as

$$-k^2\Phi_k = 4\pi G\rho_k. \tag{3.13}$$

Corrections for short-range truncation as well as periodic boundaries are applied by multiplications in Fourier space. The gravitational potential in real space is calculated as inverse Fourier-transform, and is interpolated to the original particle positions to finally obtain gravitational accelerations. OPENGADGET3 uses the more modern FFTW3 ("Fastest Fourier Transform in the West") library (Frigo & Johnson, 2005) instead of FFTW2 for the implementation of the Fourier transform.

A second mesh at higher resolution can be used in zoom-in simulations which have a very large dynamic range. The position of this high-resolution mesh is adjusted to include all particles in the high-resolution region of interest, defined by their particle type. The size is typically increased by a factor of 1.1 to reduce the necessary refactoring of the mesh.

3.3 Smoothed Particle Hydrodynamics[4]

Originally developed by Gingold & Monaghan (1977); Lucy (1977) for stellar physics, SPH is nowadays widely used in cosmological contexts. Reviews on the main properties, advantages, and challenges have been written by Price (2012b); Rosswog (2015).

For SPH, the domain is decomposed into a finite number of "particles". The physical quantities at each point are represented by contributions of close-by (neighboring) particles weighted by a kernel $\mathcal{W}_i(r_i, h_i)$, depending on the distance r_i from particle i, and its smoothing length h_i. The kernel has to be continuous, radially symmetric, have compact support, and fulfill the limit $\lim_{h\to 0} \mathcal{W} = \delta$, but otherwise can be chosen arbitrarily. OpenGadget3 offers the choice between different commonly used kernels, including a cubic spline (Monaghan & Lattanzio, 1985), quintic spline (Morris, 1996), or a Wendland C2/C4/C6 kernel (Wendland, 1995; Dehnen & Aly, 2012). A large neighbor number is preferred to reduce E_0 errors, in combination with a high-order Wendland kernel having a non-negative kernel Fourier transform to stabilize against the pairing and tensile instability. The effective volume of each particle is well approximated by $V_i^{-1} = \mathcal{W}(r_i, h_i)$, such that the density follows as

$$\rho(\boldsymbol{r}_i) = \sum_{j\in\mathrm{Ngb}} m_j \mathcal{W}\left(\left|\boldsymbol{r}_i - \boldsymbol{r}_j\right|, h_i\right), \tag{3.14}$$

summing over the neighboring particles (Ngb). We allow for adaptive smoothing, automatically increasing resolution in high-density regions compared to low-density ones. Smoothing length and effective neighbor number N_{Ngb} are related to the density via:

$$\frac{4\pi}{3}\rho_i h_i^3 = \bar{m} N_{\mathrm{Ngb}} \tag{3.15}$$

with mean neighbor mass $\bar{m}$. As Eqns. (3.14) and (3.15) are coupled for fixed neighbor number, one solves for smoothing length and density iteratively via finding roots. Quantities other than the density, labeled with X, are approximated via

$$X(\boldsymbol{r}_0) \approx \sum_{i\in\mathrm{Ngb}} \frac{X_i}{\rho_i} \mathcal{W}(|\boldsymbol{r}_0 - \boldsymbol{r}_i|, h_i) m_i. \tag{3.16}$$

Different formulations of the hydrodynamical acceleration can be derived. In OpenGadget3 the fully conservative formulation for the hydrodynamical acceleration (Springel & Hernquist, 2002)

$$\boldsymbol{a}_{\mathrm{hydro},i} = -\sum_{j\in\mathrm{Ngb}} m_j \left(f_i \frac{P_i}{\rho_i^2} \nabla_i \mathcal{W}_{ij}(h_i) + f_j \frac{P_j}{\rho_j^2} \nabla_i \mathcal{W}_{ij}(h_j) \right), \tag{3.17}$$

$$f_i = \left(1 + \frac{h_i}{3\rho_i}\frac{\partial \rho_i}{\partial h_i}\right)^{-1} \tag{3.18}$$

[4]This section has been published by Groth et al. (2023). Some additions and adjustments have been made.

is utilized. Instead of calculating gradients of physical quantities, all spatial derivatives are expressed by gradients of the kernel function. Traditional SPH has problems dealing with shocks, as well as reproducing mixing instabilities (Morris, 1996; Agertz et al., 2007). By construction, SPH does have zero dissipation, even in shocks where it is required physically. Artificial viscosity adds the necessary dissipation. In addition, SPH suppresses mixing at contact discontinuities. This issue can be resolved by adding an artificial conductivity term. In OpenGadget3, time and spatial dependent artificial viscosity (Beck et al., 2016b) and artificial conductivity (Price, 2008) are utilized, minimizing their impact in regions where they are not desired. Gradients entering the calculations are computed second order to increase accuracy.

One main advantage of the mass discretization approach in SPH is that the formulation is fully Lagrangian. In addition, the resolution directly follows the mass, increasing it in regions of high density, which are typically of great interest.

3.4 Stationary Grid

The most intuitive discretization of space uses a fixed Cartesian grid. This allows for easy implementation, including direct coupling to the PM gravity solver, as the density is already assigned onto a grid. Although this simple algorithm can be easily implemented and parallelized, it has a very limited dynamical range. Only the global resolution can be increased, while regions of interest might only cover a small fraction of the computational domain.

This disadvantage can be circumvented by using AMR (Berger & Oliger, 1984; Berger & Colella, 1989), increasing resolution only in regions of special interest. Regions that should increase or decrease resolution are identified automatically based on different criteria. Common choices for such regions are high-density environments, leading to an effective spatial resolution similar to mass-based discretizations such as SPH. Alternative refinement criteria are possible, making the method very flexible for specific scientific questions.

Typically, the cell size is halved for each additional refinement level, leading to a factor 8 higher resolution in three dimensions. To avoid strong numerical artifacts from refinement, the resolution levels are gradually increased, ensuring that transitions do not exceed a single level at a time and leaving a buffer layer of intermediate resolution where applicable. Conservation between interfaces of different resolutions has to be enforced to avoid numerical reflections.

There are two main flavors on how to realize the higher-resolution regions. The first method originally used is based on nested grids (“patches”). Alternatively, refinement can be done on a cell-by-cell basis. This allows the geometry to follow the flow closely but requires more data management than the patch-based method. The mesh structure is typically stored in form of a tree, as also used in particle methods. For each of the approaches, a corresponding gravity solver has been designed, the AP3M N-body solver (Couchman, 1991) for the former and the ART N-body solver (Kravtsov et al., 1997) for the latter.

The general algorithm to compute changes in hydrodynamical quantities on any grid consists of three steps. Gradients are calculated between neighboring cells, such that face values can be extrapolated. Slope-limiting constraints are applied in the face interpolation to avoid numerical artifacts. Possibly, an additional half-timestep interpolation can be added. Finally, fluxes are

calculated at all faces simultaneously using a Riemann solver.

For each spatial direction, the quantities $\boldsymbol{U} = (\rho, \rho\boldsymbol{v}, \rho e)$ are updated. For the one-dimensional case in x-direction, the change due to the fluxes is:

$$\Delta \boldsymbol{U}_i^n = -\frac{\Delta t}{\Delta x}\left(\mathbf{F}_{i+1/2}^{n+1/2} - \mathbf{F}_{i-1/2}^{n+1/2}\right). \tag{3.19}$$

Advection terms in the fluxes occur for the Eulerian formulation of the hydrodynamical equations. This can lead to problems especially if high velocity flows relative to the grid are present, and makes this method not Galilei-invariant. In addition, cosmological simulations have difficulty with the refinement at early times, leading to a lack of small halos at late times (O'Shea et al., 2005; Heitmann et al., 2008). Grid-alignment effects can occur depending on the grid- and flow geometry. The main advantage of grid-based approaches over SPH is that the hydrodynamical evolution does not rely on additional artificial viscosity or conductivity terms, as the fluxes are calculated using a Riemann solver. Grid codes can deal with shocks and mixing instabilities very well.

An alternative approach to adaptive refinement for stationary flows with pre-known geometry is non-cartesian unstructured meshes (Xu, 1997) used especially in engineering (compare Mavriplis, 1997, for a review). Regions of interest can be taken care of when constructing the mesh before the simulation. Convergence cannot only be improved by adjusting the resolution but also by using higher-order Godunov methods. Examples of such methods are Weighted Essentially Non-Oscillatory (WENO) methods (Liu et al., 1994) or Discontinuous Galerkin approaches (Cockburn & Shu, 1998), which use higher order stencils to describe the fluid state within each cell.

3.5 Moving Mesh

A moving mesh aims to combine ideas of SPH and grid-based methods to circumvent some of their main disadvantages.

A first, non-cosmological implementation has been provided by the FLAME code (Whitehurst, 1995). First steps towards cosmological applications have been taken by Gnedin (1995); Pen (1998). Their method was based on the continuous deformation of a cartesian grid, and was thus limited by the allowed grid deformation. A more flexible method is used within the AREPO code, which is also suited to cosmological applications and has been presented and described in detail by Springel (2010).

It is based on an unstructured mesh with a Voronoi cell structure, similar to stationary unstructured meshes used in engineering. This mesh is constructed via the topologically dual Delauney tesselation. Numerically, this is one of the most expensive and complex parts. Different algorithms exist, where the AREPO code uses an incremental insertion according to the Bowyer-Watson algorithm (Bowyer, 1981; Watson, 1981). The algorithm starts with a valid Delauney tessellation of a subset of points. Additional points are inserted consecutively, while repairing the mesh locally. Compared to other algorithms, this is faster and can be implemented for parallel execution. For random order of insertions, a scaling $O\,(N \log N)$ is reached (de Berg et al., 2008).

For each cell, the center of mass, the cell volume, interface areas, and face centers are returned, which can be used for the calculations of hydrodynamical fluxes. The steps following the mesh generation are almost identical to a stationary grid. One main advantage is that fluxes can be calculated in the rest frame of the interfaces. The cells move with the local velocity of the fluid, making the scheme Lagrangian. The resolution increases in regions of high density as for SPH. Thus, this method combines the advantages of the Lagrangian character from SPH and improved mixing and no necessity for artificial conductivity or viscosity of grid-based approaches.

As mass fluxes can still occur, the cells do not correspond to a mass discretization but still a spatial one. In contrast to mass-based discretizations, a moving mesh cannot deal with vacuum boundaries, but only periodic or reflective boundaries via ghost cells posing some challenges to the design of zoom-in regions and making the re-use of initial conditions (ICs) designed for SPH not trivial even though the data structure in general is the same.

Some additions to the basic algorithm are made to improve numerical stability. Mesh regularization avoids strongly deformed cells and reduces numerical noise. To this end, the mesh generating point is moved closer to the cell center of mass every timestep, making the cells rounder and more isotropic. To further reduce numerical noise small faces are ignored as neighbors.

Cells can be refined (splitting) or de-refined (merging) if they received or lost a large fraction of their initial mass. An additional energy-entropy switch is used within very cold flows, as we will describe in Sec. 3.7.2 for MFM.

3.6 Riemann Solvers

The Riemann problem is a specific initial-value problem described by conservation laws and piecewise constant ICs with a discontinuity. A numerical method to solve such a problem is a Riemann solver. The main application is the evolution of a (discretized) fluid. Hydrodynamical methods based on calculating fluxes from a Riemann solver are called Godunov methods (Godunov, 1959). They include grid-based methods and new meshless methods such as MFM or MFV.

In the following, we briefly review the main concepts of Riemann solvers and describe the main solvers that are used for computational fluid dynamics. An extensive description of different Riemann solvers has been provided in the book by Toro (2009), which we will refer to frequently in this chapter.

There exists no exact closed-form solution to the fluid equations (2.5). Thus, iterative or approximate solutions must be used. The ICs for the Riemann problem are fully described by fluid density, pressure, and velocity on each of the two sides of an interface. They are very similar to those of a shock-tube problem, with the generalization of non-zero velocities. Thus, also the structure of the solution is similar. Three waves will emerge, separating constant states in between. An illustration is shown in Fig. 3.1. Each of the left and right waves can be a shock or a rarefaction fan. The central wave is the contact discontinuity. The outermost states are identical to the initial states. The central "star" states have to be constructed by the Riemann solver. The relevant wave speeds are the eigenvalues of the Riemann problem.

The frame velocity is compared to these wave speeds. The flux must be calculated depending

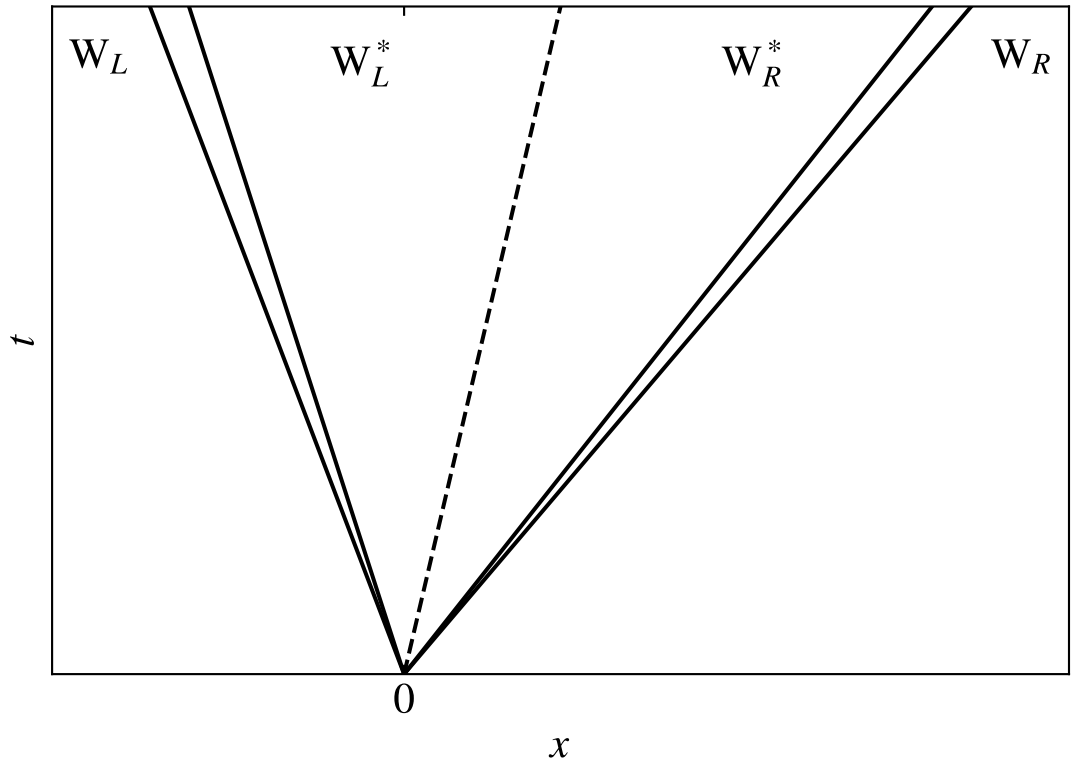

Figure 3.1: Wave structure of the solution to the Riemann problem based on Fig. 4.1 by Toro (2009). The left, central, and right lines indicate the three waves associated with the eigenvalues of the Riemann problem, separating the otherwise constant states. The split-up of the left and right waves (solid lines) indicates that either can be a shock or rarefaction wave. The central wave (dashed line) is associated with the contact discontinuity.

on where the frame velocity lies in the wave structure. Suppose that the frame velocity is slower than the left speed. In that case, fluxes are calculated based on the left state according to Eqn. (2.7). Similarly, fluxes are calculated from the right state if the frame velocity is larger than the right wavespeed. The flux calculation in the central "star" state is a central ingredient in the Riemann solver and depends on the estimate of the star state.

An exact, iterative Riemann solver has been presented by Godunov (1959) with an implementation described by Toro (2009). While this solver has a very low numerical diffusivity, it is computationally expensive. Up to 8 iterations are used until the desired accuracy is reached.

Alternative approximate Riemann solvers predict the star states emerging from the wave structure and initial states. The HLL solver (Harten et al., 1983; Toro, 2009) includes only the left and right wave, but omits the central contact discontinuity. Thus, it has a very high numerical diffusivity and fails to fully capture the shock structure. Including the missing contact discontinuity and shear waves leads to the HLLC solver (Toro et al., 1994; Toro, 2009).

The exact solution to the linearized equations leads to the Roe Riemann solver (Roe, 1981). Several extensions have been suggested to improve this solver, including an entropy fix, which is relevant in the rarefaction fans. An alternative extension to the HLL solver based on the integral form of the fluid equations is the HLLE solver (Einfeldt, 1988). The wave speeds and the intermediate solution with the central state is found using the Roe linearization.

If magnetic fields are included, the shock structure and thus the structure of the Riemann solution becomes more complex. Wave speeds depend on the relative orientation of the magnetic field. The left and right waves split into a fast magnetosonic and slow Alfvén wave. A Riemann solver designed to capture these five waves is the HLLD solver described by Miyoshi & Kusano (2005).

Overall, different wave speed estimates are possible based on the interpretation of each wave as shock or contact discontinuity. Many more Riemann solvers and variations of the previously mentioned ones based on different wave speed estimates and constructions of the central states have been published and used.

3.7 Meshless Finite Mass[5]

As a second, newly implemented option in OpenGadget3, the hydrodynamical equations can be discretized and solved following the MFM approach. This method conceptually combines SPH with a moving mesh, calculating fluxes between neighboring particles in a scheme otherwise similar to SPH, including weighting by a kernel. Thus, it combines the advantages of both methods. In contrast to SPH, the domain associated to a particle is not spherical, but rather corresponds to a smoothed Voronoi tesselation (Hopkins, 2015).

[5]This section including subsections has been published by Groth et al. (2023). Some additions and adjustments have been made.

3.7.1 MFM Discretization

Mathematically, Eqn. (2.5) is discretized by multiplying with a partition function

$$\psi_i = \frac{1}{\sum_{j\in\mathrm{Ngb}} \mathcal{W}_j}\mathcal{W}_i \tag{3.20}$$

where $\mathcal{W}_k = \mathcal{W}(|r - r_k|, h_k)$ and integrating over the volume. A more detailed derivation has been provided by Lanson & Vila (2008a); Gaburov & Nitadori (2011). In this work, we only focus on the key results relevant for the implementation. For every particle i changes in the quantities $\boldsymbol{U}_i = (\rho_i, \rho_i v_i, \rho_i e_i)$ are given by source terms $\boldsymbol{S}_i$, which vanish for pure hydrodynamics, and pairwise fluxes $\mathbf{F}_{ij}$ with the neighbors j

$$\frac{\mathrm{d}}{\mathrm{d}t}\left(V_i \boldsymbol{U}_i\right)^{\tilde{n}} + \sum_{j\in\mathrm{Ngb}} \left(\mathbf{F}_{ij}^{\tilde{n}} \cdot \boldsymbol{A}_{ij}^{\mathrm{eff},n}\right) = \boldsymbol{S}_i^{\tilde{n}} V_i^n. \tag{3.21}$$

Calculating pairwise fluxes automatically ensures mass, momentum, and energy conservation of the system. The effective interface area $\boldsymbol{A}_{ij}^{\mathrm{eff}}$ depends on the partition function and effective volume V_i,

$$\boldsymbol{A}_{ij}^{\mathrm{eff}} = V_i \tilde{\boldsymbol{\psi}}_j - V_j \tilde{\boldsymbol{\psi}}_i, \tag{3.22}$$

where

$$\tilde{\psi}_j^{\alpha}(\boldsymbol{x}_i) = B_i^{\alpha\beta}(\boldsymbol{x}_j - \boldsymbol{x}_i)^{\beta}\psi_j(\boldsymbol{x}_i) \tag{3.23}$$

with Einstein summation convention over β in Eqn. (3.23). The matrix $\mathbf{B}$ is chosen in order to be second order accurate (Lanson & Vila, 2008a)

$$\mathbf{B}_i = \mathbf{E}_i^{-1}, \tag{3.24}$$

$$E_i^{\alpha\beta} = \sum_{j\in\mathrm{Ngb}} (\boldsymbol{x}_j - \boldsymbol{x}_i)^{\alpha}(\boldsymbol{x}_j - \boldsymbol{x}_i)^{\beta}\psi_j(\boldsymbol{x}_i). \tag{3.25}$$

Also the effective volume depends on the integrated partition function and can be expressed in terms of the number density n_i:

$$V_i = \int \psi_i \approx n_i^{-1}. \tag{3.26}$$

For highly unisotropic particle arrangements, the matrix $\mathbf{E}$ can become ill-conditioned, preventing an accurate numerical matrix inversion. As described by Hopkins (2015) we use the condition number $N_{\mathrm{cond},i} = N_{\mathrm{dimensions}}^{-1}\sqrt{\left|\left|\mathbf{E}_i^{-1}\right|\right| \, ||\mathbf{E}_i||}$ as a measure of how well-conditioned the matrix is. For $N_{\mathrm{cond},i} > 100$ gradients are calculated only first order in an SPH-like way.

For the calculation of $\tilde{\psi}_i$ the matrix $\mathbf{B}_i$ is still required. In rare cases, it can happen that the matrix is not only ill-conditioned but not invertible at all. In these cases, a correction is added to the trace repeatedly

$$\mathbf{E}_i^{\alpha\alpha}{}_{\text{corr}} = \mathbf{E}_i^{\alpha\alpha} + c_i^n \tag{3.27}$$

$$c_i^0 = \text{Sign}(\text{tr}\mathbf{E}_i) \cdot \max \begin{cases} 10^{-15} \\ \frac{1.05|\text{tr}\mathbf{E}_i|}{10^4 N_{\text{dimensions}}} \end{cases} \tag{3.28}$$

$$c_i^{n+1} = 1.2 c_i^n \tag{3.29}$$

until the determinant becomes greater than 10^{-30} and the resulting matrix can be inverted.

Most importantly, no tessellation has to be calculated explicitly, as it would be necessary for a moving mesh, but an SPH-like neighbor search is used, drastically reducing the computational costs compared to the mesh reconstruction.

In contrast to SPH, for which the mass density is estimated according to Eqn. (3.15), for MFM the number density n_i is estimated together with the smoothing length in an iterative process, solving

$$n(\boldsymbol{r}_i) = \sum_{j \in \text{Ngb}} \mathcal{W}\left(\left|\boldsymbol{r}_i - \boldsymbol{r}_j\right|, h_i\right), \tag{3.30}$$

$$\frac{4\pi}{3} n_i h_i^3 = N_{\text{Ngb}}. \tag{3.31}$$

Also for MFM, N_{Ngb} corresponds to the effective neighbor number.

The flux in Eqn. (3.21) is calculated numerically using a Riemann solver, where we use an exact Riemann solver, following the implementation by Toro (2009) with a tolerance of 10^{-4}, and a maximum of 8 iterations. Alternatively, we implemented the Riemann solver that provides an exact solution to the linearized system of equations (Roe-solver, Roe, 1981), as well as the two most common flavors of a Harten-Lax-van-Leer solver (HLL) and HLLC (Toro, 2009). For all these, the exact Riemann solver is used as fallback in case the faster, approximate solver fails. The effect of the choice of the solver is discussed in more detail in Sec. 5.4.

The Riemann solver requires knowledge about velocity, density, and pressure values at the interfaces, summarized in the primitive fluid vector

$$\boldsymbol{W} = \begin{pmatrix} \rho \\ \boldsymbol{v} \\ P \end{pmatrix}. \tag{3.32}$$

In principle, values at the particle center can be used directly, following a zeroth order interpolation. While such a scheme would be stable, it is only first order accurate and very diffusive (Godunov, 1959; Barth & Jespersen, 1989). To this end, we follow a two-step approach, as illustrated in Fig. 3.2, similar to what is usually done for grid-based methods and in other MFM implementations. In a first step, gradients of the primitive fluid vector are calculated using a

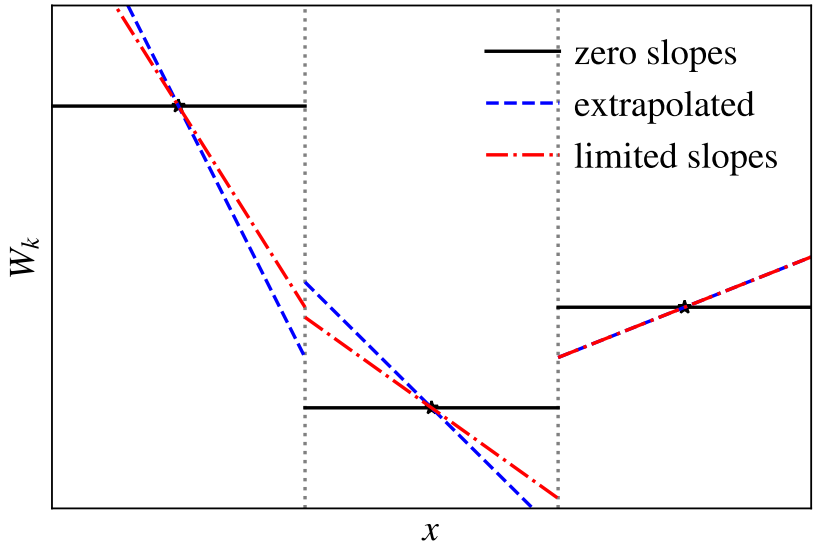

Figure 3.2: Sketch of extrapolation from central particle/cell values to face values. Using the central values corresponds to a zeroth order interpolation, leading to a first order scheme (black solid lines). It can be extended to be second order by extrapolating using a slope defined by neighboring particles/cells (blue dashed line), which however can lead to over-/undershooting at the faces (see left face) or even negative densities/pressures (see right face). This issue can be solved by limiting the slopes using different procedures (red dash-dot line). See text for further details.

second-order accurate matrix gradient estimator

$$(\nabla \otimes \boldsymbol{W})_i^\alpha = \sum_{j \in \mathrm{Ngb}} \left(\boldsymbol{W}_j - \boldsymbol{W}_i\right) \tilde{\psi}_j^\alpha(\boldsymbol{x}_i). \tag{3.33}$$

The position and velocity of the face are estimated via

$$\mathrm{d}\boldsymbol{r}_{ij}^{\mathrm{frame}} = \mathrm{d}\boldsymbol{r}_{ij} s_i, \tag{3.34}$$

$$\boldsymbol{v}_{ij}^{\mathrm{frame}} = s_j \boldsymbol{v}_j + s_i \boldsymbol{v}_i, \tag{3.35}$$

where we set

$$s_i = \frac{h_i}{h_i + h_j} \tag{3.36}$$

to be second order accurate instead of $s_i = 1/2$ for a first-order accurate interpolation.

By choosing the reference frame corresponding to the rest-frame of the interface, the scheme becomes Lagrangian. In MFM, also the boundaries are assumed to deform in a Lagrangian way, eliminating mass fluxes between neighbors. As the actual face velocity and deformation do not exactly correspond to the one assumed during a timestep, second order errors are introduced (Hopkins, 2015). An alternative is allowing for mass fluxes using the MFV method, which, however, also is only second order accurate. In addition, it has been shown that MFV can run into problems by draining the mass for particles accelerated into low density environments in cosmological simulations (Alonso Asensio et al., 2023). For this reason, we do not use this scheme here but focus on the MFM method. An additional advantage of MFM and finite volume schemes in general over SPH is that no additional dissipation terms are necessary.

The face values are extrapolated according to

$$\boldsymbol{W}_i^{\mathrm{frame}} = \boldsymbol{W}_i + \mathrm{d}\boldsymbol{r}_i^{\mathrm{frame}} \cdot \nabla \otimes \boldsymbol{W}_i. \tag{3.37}$$

To avoid over- or undershooting or even unphysical, negative densities or pressures when strong gradients are present in the fluid, these gradients are reduced by a factor $\nabla W_{i,k} \rightarrow \alpha_{i,k} \nabla W_{i,k}$, $0 \leq \alpha_{i,k} \leq 1$ in a second step in the face interpolation where $\alpha_{i,k}$ can be different for each particle i and component k. We implement different options for such a slope-limiter, including a total variation diminishing (TVD) one (Duffell & MacFadyen, 2011), the one from Arepo (Springel, 2010) originally presented by Barth & Jespersen (1989), the scalar limiter from the GANDALF code (Hubber et al., 2018), and the one used in the gizmo code (Hopkins, 2015), described further in Sec. 5.3. In addition, the pairwise limiter according to the gizmo code can be used.

In a third, final step the Riemann solver is used to calculate fluxes, which can then be converted to hydrodynamical acceleration and energy changes.[6] All these steps are only applied to particles that currently reside in an active time bin. While this workflow is computationally convenient, it

[6] As the Riemann solver requires physical units instead of (co-moving) code units, variables have to be converted accordingly (compare also Hopkins, 2015, App. H5). As flux calculations are done at the interface, no Hubble expansion has to be taken into account for the momentum changes.

makes the scheme less exact, as old gradients are used for the flux calculation. Nevertheless, the scheme still performs accurately enough in practical applications, as argued by Hopkins (2015).

In addition, in our implementation fluxes are updated only for the active particle, which breaks conservation. This could be improved by updating fluxes for both particles and only considering neighbors on lower time bins. As we found no significant disadvantage for practical applications, we kept the computationally more convenient version.

3.7.2 Energy-Entropy Switch

While the Riemann solver outputs total energy changes, the rest of the code requires internal energies. Total energy itself is never used in the code. The total energy change can straightforwardly be converted into internal energy change starting from Eqn. (26) of Gaburov & Nitadori (2011), rewriting it as a difference equation, as we have small but finite timesteps

$$\left(\frac{\mathrm{d}U}{\mathrm{d}t}\right)^n = \left(\frac{\mathrm{d}E_\mathrm{tot}}{\mathrm{d}t}\right)^n - \left(\frac{\mathrm{d}}{\mathrm{d}t}\left(\frac{1}{2}m\boldsymbol{v}^2\right)\right)^n \tag{3.38}$$

$$\approx \left(\frac{\mathrm{d}E_\mathrm{tot}}{\mathrm{d}t}\right)^n - \frac{1}{2}m^n\left(\frac{(\boldsymbol{v}+\mathrm{d}\boldsymbol{v})^2-\boldsymbol{v}^2}{\mathrm{d}t}\right)^n \tag{3.39}$$

$$\approx \left(\frac{\mathrm{d}E_\mathrm{tot}}{\mathrm{d}t}\right)^n - m^n\left(\boldsymbol{v}^n + \frac{1}{2}\left(\frac{\mathrm{d}\boldsymbol{v}}{\mathrm{d}t}\right)^n \Delta t^n\right)\cdot\left(\frac{\mathrm{d}\boldsymbol{v}}{\mathrm{d}t}\right)^n. \tag{3.40}$$

The velocity change can be calculated directly from the momentum change returned by the Riemann solver, as for MFM the mass is kept constant. Thus, both time derivatives of total energy and velocity can be obtained from the Riemann solver output. We introduce the additional term $\frac{1}{2}\left(\frac{\mathrm{d}\boldsymbol{v}}{\mathrm{d}t}\right)^n \Delta t^n$ in the bracket, which is a second order correction and improves the accuracy in the discretized equation, which is a result of discrete timesteps. While this transformation from total to internal energy does not conserve total energy to machine precision, it increases the precision in the evolution of the internal energy itself. For very cold flows, the internal energy evolution is still dominated by numerical errors. This is avoided by assuming purely adiabatic changes in these rare cases. We follow the idea of the implementation in the GIZMO code, where the switch is only active for specific test problems such as the Zeldovich pancake. If active, internal energy

$$U_{\mathrm{est},i} = U_i + \mathrm{d}U_i \tag{3.41}$$

is compared to potential and/or kinetic energy

$$E_{\mathrm{pot},i} = m_i a_\mathrm{grav}\cdot 0.5 h_i, \tag{3.42}$$

$$E_{\mathrm{kin},i} = 0.5 m_i \max_{j\in\mathrm{Ngb}}\left(\boldsymbol{v}_j - \boldsymbol{v}_i\right)^2. \tag{3.43}$$

If the internal energy is small enough compared to other energy contributions

$$U_{\mathrm{est},i} < \alpha_1 E_{\mathrm{pot},i} + \alpha_2 E_{\mathrm{kin},i} \tag{3.44}$$

in physical units, the new internal energy for particle i is instead calculated assuming adiabatic expansion or contraction. The parameters $\alpha_{1/2}$ have to be tuned to only affect the evolution of particles where necessary. We provide a comparison between different values in Sec. 5.2.8.

The internal energy is updated similarly to the entropy for SPH in two half-steps at the kicks, following a second-order time integration similar to the entropy in SPH

$$U^{n+1/2} = U^n + \frac{1}{2}\left(\frac{\mathrm{d}U}{\mathrm{d}t}\right)^{\tilde{n}} \Delta t, \tag{3.45}$$

$$U^{n+1} = U^{n+1/2} + \frac{1}{2}\left(\frac{\mathrm{d}U}{\mathrm{d}t}\right)^{\widetilde{n+1}} \Delta t. \tag{3.46}$$

For cosmological simulations, additional adiabatic contributions due to the Hubble flow are added.

3.8 Equations in an Expanding Universe[7]

In a cosmological context, the expansion of the universe has to be taken into account. One possibility is to re-write Eqn. (2.5) for an expanding universe with scale factor a, accounting for these effects, as realized e.g. in GADGET-1 (Springel et al., 2001):

$$\frac{\partial \boldsymbol{v}}{\partial t} + \frac{1}{a}(\boldsymbol{v}\cdot\nabla)\,\boldsymbol{v} + \frac{\dot{a}}{a}\boldsymbol{v} = -\frac{1}{a\rho}\nabla P - \frac{1}{a}\nabla\Phi, \tag{3.47}$$

$$\frac{\partial \rho}{\partial t} + \frac{3\dot{a}}{a}\rho + \frac{1}{a}\nabla\cdot(\rho\boldsymbol{v}) = 0, \tag{3.48}$$

$$\frac{\partial}{\partial t}(\rho u) + \frac{1}{a}\vec{v}\cdot\nabla(\rho u) = -(\rho u + P)\left(\frac{1}{a}\nabla\cdot\boldsymbol{v} + 3\frac{\dot{a}}{a}\right). \tag{3.49}$$

In OPENGADGET3 we follow a different approach, and do calculations using the so called super-co-moving coordinates, as first introduced by Martel & Shapiro (1998). Code units (denoted by subscript c) are related to physical units (p) via

$$x_c = a^{-1}x_p, \tag{3.50}$$

$$\rho_c = a^3\rho_p, \tag{3.51}$$

$$v_c = a v_p, \tag{3.52}$$

$$P_c = a^{3\gamma}P_p, \tag{3.53}$$

$$u_c = a^{3(\gamma-1)}u_p, \tag{3.54}$$

such that Eqn. (2.5) keeps the same form when written in code units except for an additional contribution in the energy and momentum evolution due to the Hubble expansion. The additional

[7]This section has been published by Groth et al. (2023). Some additions and adjustments have been made.

internal energy contribution due to the comoving integration is

$$\left.\frac{\mathrm{d}u}{\mathrm{d}t}\right|_{\text{comoving}} = -3\,(\gamma-1)\,H(t)u(t). \tag{3.55}$$

As we use peculiar velocities, the explicit dependence on the Hubble flow for momentum is absorbed into the choice of units.

4 | Cosmological Simulations

To simulate cosmological environments, different approaches are possible. They all are a compromise between computational cost, resolution, and the amount of physics that can be included. In this chapter, we describe a few commonly used approaches for cosmological simulations, including cosmological boxes, zoom-in simulations, and isolated systems.

4.1 Cosmological Boxes

Cosmological boxes are a statistical representation of a possible universe. They include the full information on the cosmological background evolution. Thus, they can be used to study the impact of cosmology and LSS on structure formation. In addition, cosmological boxes allow for good statistics without selection bias. In the low-mass end, the information is limited by the resolution. On the high-mass end, the number of structures and mass of the most massive structure depends on the computational volume covered by the simulation. The largest mode of the power spectrum corresponds to the size of the box, and is imprinted in the LSS.

The ICs for the cosmological boxes are constructed at early times when the LSS can be described by linear evolution, possibly with higher-order corrections. The initial redshift is constrained by the particle displacement that must not exceed the inter-particle distance. The higher the resolution, the earlier the simulation has to begin. The spectrum of the primordial power spectrum is then sampled and Fourier-transformed to obtain the particle displacement. Frequencies are constrained from the CMB, but usually the phases are not. Thus, the actual ICs depend on the realization of the initial density power spectrum and the seeds of the random number generators used for the construction. N-GenIC (Springel et al., 2005; Angulo et al., 2012) is a code to generate such ICs. An improved version using second-order Lagrangian theory instead of the first-order Zeldovich approximation has been described by Crocce et al. (2006).

The first simulations have been purely N-body and contained only DM, but no baryonic component, as the latter is computationally much more expensive. The impact of the underlying cosmology can be studied by varying cosmological parameters. Even though neglecting small-scale baryonic effects, these simulations gave the first insight into the non-linear collapse and structure formation from a theoretical perspective. Even today, large DM-only simulations are used as the foundation for creating zoom-in simulations or to boost the resolution and box size. With increasing computational power, gas with hydrodynamical interactions can also be included. Subgrid models can be used to add additional physics below the resolution limit such as cooling,

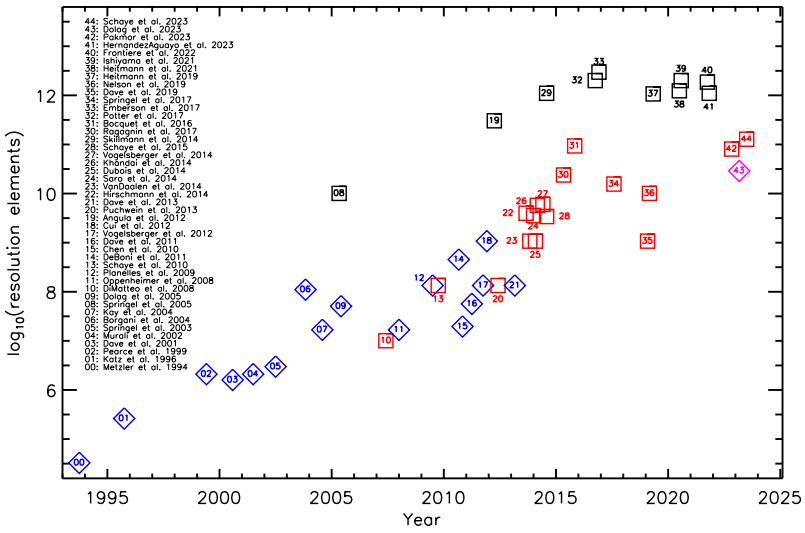

Figure 4.1: Evolution of the number of resolution elements over time (Valentini & Dolag, in prep.). The different colors denote different types of simulations: recent N-body simulations (black), hydrodynamical simulations including cooling and star formation (blue), with additional AGN feedback (red), also including magnetic fields and spectral CRs (pink). With increasing computational power, the number of resolution elements increases roughly exponentially over the first decades. Growth slows down as more physics is included instead.

star formation, SN, and AGN feedback.

The evolution of the number of resolution elements used for different simulations is shown in Fig. 4.1, starting with the first hydrodynamical simulations, including subgrid models for cooling and star formation (blue). During the first decade, the number of resolution elements increased almost exponentially. Additional models such as AGN-feedback (red) and even spectral CRs (pink) have been included more recently. DM-only simulations (black) allow to boost the number of resolution elements by more than an order of magnitude. Overall, the number of resolution elements increased several orders of magnitude over the last few decades, allowing to run much larger boxes and to achieve much higher resolution.

Many simulations of cosmological boxes are among the largest simulations that have been run. All main hydrodynamical methods described in Sec. 3 have been used for calculation. The Magneticum simulation (Dolag et al., 2016) has been run with SPH. A moving mesh has been used for the simulation of IllustrisTNG (Marinacci et al., 2018; Naiman et al., 2018; Nelson et al., 2018; Pillepich et al., 2018; Springel et al., 2018) and IllustrisTNG50 (Nelson et al., 2019; Pillepich et al., 2019) while a stationary grid with AMR has been used for Horizon-AGN (Dubois et al., 2014). Simba (Davé et al., 2019) has been simulated with MFM. In addition to the hydrodynamical method, the simulations differ in the subgrid descriptions. Different feedback processes depend on the parametrization approach and the scaling relations used for tuning parameters. This can significantly alter star formation and galaxy evolution histories.

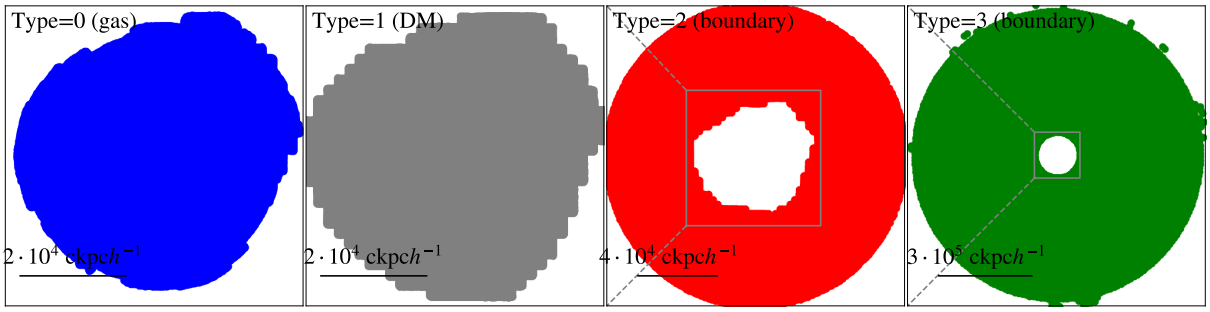

Figure 4.2: IC of the Dianoga region g55 in a central slice of 10^4 ckpch^{-1}. The different panels and colors denote different particle types. From left to right: gas particles (type 0, blue), DM (type 1, gray), and boundary particles (type 2, red, and type 3, green). The scale is different between the different types to show the distribution more clearly. Gas and DM particles cover roughly the same region in the center. They are surrounded by boundary particles of type 2, which themselves are surrounded by boundary particles of type 3. The holes left in the center are clearly visible for both boundary particle types. Even though not shown here, type 3 particles cover the full domain.

With increasing quality and amounts of observational data, constrained simulations are possible. These simulations have several advantages over unconstrained ones. In particular, they can be used to perform one-to-one comparisons with observed GCs such as Virgo, Coma, and Perseus. Nevertheless, the generation of ICs is more complex. There exist two main approaches to translate observational constraints into constraints on the ICs. The first is based on the observed galaxy density. While much data is available for this method, it suffers from severe biases that have to be dealt with. The second approach is based on galaxy velocities, which are much more difficult to observe but also reduce biases after a complex data preparation process (Sorce, 2018; Sorce & Tempel, 2018). Unconstrained regions are filled with random data according to the CMB power spectrum, similar to unconstrained boxes. Overall, this approach typically leads to massive objects or objects in specific environments being well-constrained. Less massive objects are only weakly constrained (Hernández-Martínez et al., 2024). Also further away from the center (which is set by the location of your own Galaxy) the amount of constraints decreases with less observational data available. A recent example is the SLOW simulation (Dolag et al., 2023).

4.2 Zoom-In Simulations

Zoom-in simulations are designed to focus on specific systems while keeping the information on the environment and cosmological background evolution. This information is of great importance for simulating GCs, which are embedded in the LSS of the universe, but also to understand the evolution of galaxies in specific environments.

ICs are constructed starting from a cosmological box, which is typically DM-only. Here, we focus on the construction of the Dianoga regions (Bonafede et al., 2011a) which are used in this work. An example of one of their regions is shown in Fig. 4.2. Particles belonging to

the object of interest have to be selected. The selection is performed using a friends-of-friends algorithm at redshift zero. Other methods or even a selection further in the future are possible (Seidel et al. in prep.). The positions of all particles that end up within $5 - 7R_{\rm vir}$ are traced back to the desired initial redshift. The resulting volume is extended to be convex and have no holes. It specifies the region of interest for the simulation and is up-sampled in resolution. Further out, the resolution is down-sampled compared to the parent box. This allows to keep the information on the environment and LSS, while reducing computational costs. A buffer region at intermediate resolution, which is the same as for the parent box, is kept between the high- and low-resolution regions. If the resolution of the zoom-region is much higher than that of the parent box, strong jumps in resolution occur at the interface area. Another approach used for creating the SLOW zoom-in regions relies on a more gradual increase, adding several layers in between (Seidel et al. in prep.). The up-sampled region is perturbed with the same primordial power spectrum as the original box, keeping the amplitudes and phases as in the parent box while adding additional small-scale modes. Gas can be added on top of the DM, even if not present in the parent simulation.

The initial redshift has to be adjusted to stay within the Zel'dovich (1970a) approximation. As the resolution is typically higher than in the parent simulation, also the initial redshift has to be higher. Several codes exist to create the ICs, among them the ZIC code (Tormen et al., 1997) used for the Dianoga zoom-in regions used in this work, or the ginnungagap code[1] used for creating the SLOW zoom-regions (Seidel et al. in prep.).

Massive low-resolution particles entering the high-resolution domain during the evolution can pose a challenge to these simulations. This contamination by boundary particles can lead to spurious clumping and has to be avoided. They are either removed from the ICs in an iterative process from DM-only simulations or a large enough buffer region has to be left by choosing an overall larger high-resolution volume. The Dianoga regions, which we use in this work, follow the first approach, leading to a very low contamination. No boundary particles enter within $5 - 6R_{\rm vir}$.

Overall, using zoom-in simulations instead of cosmological boxes significantly reduces the computational costs as the volume of interest is much smaller. Alternatively, it allows to push the resolution to much lower masses and to add more complex physics. Larger sets of GCs at high resolution compared to an equivalent cosmological box can be simulated. Nevertheless, statistics have to be done carefully to not have selection effects based on the regions chosen. In addition, these zoom-in regions can be used to test physical subgrid descriptions more efficiently, as less runtime is required.

Examples of ICs for zoom-in simulations are the Dianoga regions (Bonafede et al., 2011a) and the Music clusters (Sembolini et al., 2013, 2014; Biffi et al., 2014). The latter are extracted from the MultiDark cosmological simulation (Prada et al., 2012). More recently, the technique of zoom-ins has been used to run the TNG cluster simulation (Nelson et al., 2024). Several zoom-in regions have been simulated with the IllustrisTNG model at high resolution. The resulting data was collected in a similar format as for cosmological boxes to allow easy processing.

Similarly to GCs, also Milky Way-like or dwarf galaxies can be simulated using the zoom-in technique. An example are the simulations of the Aquarius Project by Springel et al. (2008).

[1]Published at `https://code.google.com/archive/p/ginnungagap/`.

4.3 Isolated Systems

An alternative approach to choosing ICs for simulations is isolated systems. Gradations in complexity versus simplification are possible, ranging from isolated systems in stratified environments to more idealized systems that completely neglect environmental effects. Typically, the evolution of the cosmological background is also not taken into account. The influence of environment and cosmology plays a significant role after several Gyr, but can be neglected over a limited timespan that depends on the object and environment of interest.

One of the pioneering simulations performed by Toomre & Toomre (1972) falls into this category. They focused on two interacting and merging spiral galaxies, laying the foundation for all modern simulations.

Overall, idealized simulations of isolated systems allow for a more clean study of the effect of individual physical processes. The most prominent use is in parameter studies covering a large parameter space. Different works study idealized galaxy mergers, varying infall parameters. One application is the formation pathway of dwarf galaxies via tidal dwarfs. Bournaud & Duc (2006) neglect the environment in their study in favor of a large set of parameters, running in total 96 N-body simulations. Ivleva et al. (2024) refine the study, taking into account the cluster potential. Stripping in the cluster potential enhances the number of dwarfs of possible tidal origin, emphasizing the necessity of considering the environment, even if only in an idealized way.

Idealized simulations are also popular testbeds for sub-resolution models. Neglecting coupling to the environment allows for a clearer study of the direct effects of feedback models. The setup and its parameters can be chosen to test specific aspects of the model. Also subgrid models in OpenGadget3 have been tested this way, e.g. the MUPPI star formation model (Murante et al., 2010) and the spin evolution of supermassive BHs (Sala et al., 2024).

Neglecting the larger scales allows for drastically boosting the resolution of simulations, especially for low-mass dwarf galaxies. Recently, this has been used to refine up to individual stars down to $1M_{\odot}$, thus allowing for completely new feedback models resolving individual SNe (Deng et al., 2024). The galaxy properties can be studied on very small scales, where the multi-phase character of the Interstellar Medium (ISM) arises self-consistently. In addition, mixing processes such as metal diffusion can be studied in more detail, such as in the work by Steinwandel et al. (2024b).

Part II

Meshless Finite Mass in OpenGadget3

5 | Hydrodynamics with Meshless Finite Mass[1]

Turbulence plays a key role in a variety of astrophysical systems at all scales, ranging from stellar structure, star-formation in the ISM all the way up to the ICM. It leads to enhanced small-scale mixing and contributes to the global pressure of a system. While being mostly supersonic in the ISM, turbulence is mainly subsonic in the ICM (compare, e.g. Schuecker et al., 2004, for observations on the Coma cluster). A theoretical framework for subsonic turbulence has been provided by Kolmogorov (1941), assuming isotropy. Simulations are an essential tool to better understand physical properties of astrophysical turbulence as well as its influence on local observables such as star formation in the ISM or its contribution to heating in the ICM.

Different hydrodynamical methods such as a stationary mesh with AMR, a moving mesh, and SPH have been developed to solve the hydrodynamical equations in cosmological contexts, presented in Sec. 3. All of them can be used for computations of turbulence, with earlier calculations primarily carried out in the supersonic regime, relevant in the ISM for regulating star formation. Many results have been obtained assuming driven turbulence in which an energy input at large scales is provided during the whole simulation. In contrast to driven turbulence, we expect decaying turbulence to be present in GCs. Turbulence is injected at large scales for example due to the collapse of LSS and subsequent merger activity (Roettiger & Burns, 1999; Subramanian et al., 2006), after which energy is transported down to the smaller scales ("turbulent cascade") on which it is dissipated (generally below the resolution scale of any given code).

In the series of papers by Federrath et al. (2008, 2009, 2010), they have used a stationary grid code to calculate turbulent boxes with driven turbulence. They found that the choice of the driving scheme plays an important role in determining properties of the resulting turbulence, leading to significant differences in the density statistics. Their results suggest a different mixture of driving-mechanisms for different star forming regions. Overall, they found good agreement with observations as well as other results, independent of the driving-mechanism employed. More recently, Federrath et al. (2021) increased the resolution to even resolve the sonic scale, starting from supersonic turbulence with a resolution of $\sim 10000^3$ cells.

Kitsionas et al. (2009) and Price & Federrath (2010) also compared the performance of different implementations of SPH and hydro schemes with a stationary mesh, and find good agreement between these two methods at high Mach numbers. Mesh codes are more efficient to

[1]This section has been published by Groth et al. (2023). Some adjustments have been made.

obtain volumetric statistics such as the power spectrum, while SPH recovers the high-density tail better due to automatically adapting the resolution.

While all these methods work well in the supersonic turbulent regime, they have problems dealing with subsonic turbulence. Going to smaller Mach numbers ($\mathcal{M}$) Padoan et al. (2007) showed that SPH performs sub-optimum when compared to finite volume methods. Based on this work, Bauer & Springel (2012) studied the capabilities of SPH for subsonic turbulence at $\mathcal{M} = 0.3$. They found that classic (vanilla) SPH fails in reproducing the expected velocity power spectrum as well as the dissipation range. Reasons are mainly the artificial viscosity scheme used and velocity noise introduced by the kernel. These results raised the general question of whether SPH can deal with subsonic turbulence to begin with.

An answer has been provided by Price (2012a) who showed that these limitations are not intrinsic to SPH, but rather a consequence of some SPH setups adopted to study subsonic turbulence. In contrast to what previous studies reported, SPH can capture the expected power spectrum by using more modern formulations of SPH that are able to reduce artificial viscosity in subsonic regimes.

The role of subsonic turbulence in GCs has been analyzed both from observational and theoretical perspectives. Simulations of turbulence in the ICM have been carried out mostly using grid codes (Vazza et al., 2009, 2018a; Mohapatra et al., 2021, 2022; Iapichino & Niemeyer, 2008; Iapichino et al., 2017). Miniati (2014, 2015) found a lack of turbulent energy at small scales depending on the refinement technique. In addition, they discussed the importance of microphysics for the evolution of turbulence. A possible improvement for modeling turbulence has been presented by Maier et al. (2009) combining AMR with large eddy simulations. Simulations by Dolag et al. (2005b) have shown that also SPH can model turbulence in GCs when properly reducing artificial viscosity.

In addition to the impact on gas dynamics, turbulence is responsible for amplifying magnetic fields through a turbulent dynamo. Simulations by Schekochihin et al. (2001, 2004) and Steinwandel et al. (2021) have focused on this turbulent dynamo, analyzing its growth. Another work of Kritsuk et al. (2020) has focused again on turbulent boxes with stochastic forcing, comparing different hydrodynamical methods and finding reasonably good convergence but significant differences in computational costs.

More recently, Sayers et al. (2021) have compared simulated clusters to observed ones. Especially, there should be a difference depending on the dynamical state, with more relaxed clusters showing less turbulence. Simulations, however, do not always find such a difference. Thus, it is important to accurately capture the turbulent cascade and the decay in turbulent energy. While the latter would require including additional microphysics such as viscosity, the former also depends on the hydro-scheme.

We use MFM as an alternative, newer method to the aforementioned ones to study subsonic turbulence. MFM combines ideas of SPH with those of a moving mesh and thus aims at solving several of their individual issues. The development of MFM goes back to first ideas presented by Vila (1999) and Godunov SPH (Inutsuka, 2002; Cha & Whitworth, 2003), which was still unstable, and to a Meshless Finite Element Method suggested by Idelsohn et al. (2003), until the nowadays used version first formulated by Lanson & Vila (2008a,b). We present a new implementation in the GADGET derivative OPENGADGET3, originally based on that in the code

GANDALF, where the skeleton of the MFM implementation has been originally taken from its code base and then adjusted. Several extensions allow its use in cosmological simulations compared to the implementation in GANDALF that is focused on star and planet formation. This allows for a stable baseline framework for applications on scales of star and planet formation that we extend into the cosmological integration framework of OpenGadget3, which is a rebase of Gadget-2 with the ability to be compiled with C++ compilers, and making vast use of templating. It comes with modules containing state-of-the-art physics and sub-resolution models, as for instance: self-interacting DM (Fischer et al., 2022), MHD (Dolag & Stasyszyn, 2009; Stasyszyn et al., 2013), thermal conduction (Arth et al., 2014), CRs (Böss et al., 2023), star formation and stellar/BH feedback according to the *Magneticum*-model (Springel & Hernquist, 2003; Tornatore et al., 2003, 2004, 2007; Hirschmann et al., 2014; Steinborn et al., 2015; Dolag, 2015) or with the MUPPI (MUlti Phase Particle Integrator) extension for non-equilibrium star formation (Murante et al., 2010, 2015; Valentini et al., 2017, 2020), as well as models describing the BH spin evolution (Sala et al., 2024) and dynamical friction (Damiano et al., 2024). These extensions have initially been coupled only to the SPH hydro-solver. The coupling to MFM is described later in Sec. 6.3.

To make use of modern computer architectures, OpenGadget3 includes a hybrid MPI-OpenMP parallelization. In addition, calculations of gravity, density, SPH hydro-force, and thermal conduction can be carried out on GPUs. These modules requiring most of the runtime (Ragagnin et al., 2020) GPU offloading can be useful for some applications, leading to a speed up by a factor of a few (2-4, depending on the exact application). The long-term goal is to have a fully publicly available updated Gadget version for OpenMP and OpenACC.

Before the introduction of the paper by Groth et al. (2024) the code was solving the hydrodynamical equations using modern SPH as formulated by Springel & Hernquist (2002), including modern, time-dependent artificial viscosity (Beck et al., 2016b) and conduction (Price, 2008). With the new implementation of MFM as a modern meshless method, we can combine advantages both of this method and efforts previously made to optimize the pre-existing code base. This also involves a treatment in order to evolve strong shocks for which we need the timestep limiter to be non-local which is ensured by a wakeup scheme (Saitoh & Makino, 2009; Pakmor, 2010; Pakmor et al., 2012). OpenGadget3 closely follows the implementation described by Beck et al. (2016b).

A main goal of this chapter is to use MFM to study decaying, subsonic turbulence, as present in GCs. To this end, we present additional details of the new implementation in the cosmological simulation code OpenGadget3 as an alternative hydro-solver to the currently implemented SPH. The main equations and main implementation details have already been described in Sec. 3.7.

This chapter is structured as follows. We first describe additional details of the MFM implementation in OpenGadget3 in Sec. 5.1. In Sec. 5.2, we use a suite of test cases, each probing specific aspects and properties of the code, to validate the performance of our MFM implementation. All settings are kept exactly the same between test cases, independent of the individual test case, without further tuning. We continue with an analysis of decaying subsonic turbulence with our new implementation presented in Sec. 5.2.6. In all cases, comparisons between different codes and methods are provided, including MFM and SPH in OpenGadget3, MFM in gizmo, and a moving and stationary mesh in the publicly available Arepo version. We

analyze the effect of specific numerical parameters in Sec. 5.2.8. Additional material such as the formulation of the slope-limiters and a comparison of the Riemann solvers implemented are presented in Sec. 5.3 and 5.4, respectively. Differences in the convergence bahvior with AREPO are discussed in Sec. 5.5. Our main findings are discussed in Sec. 5.6.

5.1 Specifics of MFM Implementation in OPENGADGET3

5.1.1 Switching between SPH and MFM in OPENGADGET3

To substitute SPH with MFM, the general code structure does not have to be altered. Mainly, the SPH specific force calculation has to be replaced by the three steps of the MFM calculation, consisting of gradient calculations, slope-limiting, and the actual flux calculation. As the Riemann solver both requires and outputs physical quantities, while the rest of the code deals with code units, these units have to be converted according to Eqn. (3.50) to (3.54) just before the flux calculation. At all places, where results of that calculation, including the hydrodynamical acceleration, are used, they first have to be converted back to physical units.

Also, MFM calculates internal energy changes following the output of the Riemann solver, while in SPH the entropy is evolved.

5.1.2 Differences to Previous Implementations of MFM

While the general concept of MFM with respect to the implementations introduced in GIZMO and GANDALF stays the same, there are several differences compared to these previously made implementations. Our implementation is based on the one in GANDALF, which is originally intended to be well suited for star and planet formation. We expand this implementation by including co-moving integration and other extensions such as an energy-entropy switch to be used for cosmological applications. In addition, we change the time integration scheme from a second-order accurate MUSCL-Hancock to a second-order accurate Leapfrog KDK, consistent with SPH in OPENGADGET3.

The main difference of OPENGADGET3 compared to GIZMO is that fluxes are by default calculated using an iterative, exact Riemann solver compared to an approximate HLLC Riemann solver used in GIZMO, with an exact Riemann solver only used as fallback.

In comparison to PKDGRAV-3 (Alonso Asensio et al., 2023), the energy-entropy switch and the implementation of how to deal with anisotropic particle distributions are different and more similar to GIZMO.

In addition, there are a few minor differences such as the second-order correction in Eqn. (3.40). We also made the pairwise limiter Lagrangian, as described in Sec. 5.3, which was independently done also in PKDGRAV-3. The convergence of the density calculation is slightly different between the codes. We follow the same implementation as for SPH in OPENGADGET3, just replacing the mass density with the number density. Finally, our implementation employs a hybrid MPI-OpenMP parallelization as done for other modules of OPENGADGET3.

5.2 Test Cases

We use several test cases to probe the ability of the different hydro-methods to accurately follow gas evolution. Only few tests have an analytical solution, including soundwaves and different shocks. Also a set of MHD waves with analytical solution has been presented by Berlok (2022), which could be used for tests of later MHD extensions. Many other tests can be used for a more qualitative analysis. All of them explore specific numerical aspects important for cosmological simulations.

We use these tests to compare our new MFM implementation in OpenGadget3 to SPH in OpenGadget3, MFM in the public gizmo[2] version and the publicly available version of the moving mesh code Arepo[3].

5.2.1 Settings

We aim for a fair comparison of the different codes throughout this chapter but adopt a general setting for slope limiters, Riemann-solvers (MFM) as well as the artificial diffusion terms (SPH) that one would adopt in cosmological simulations. While this leads to overall good performance of all solvers on almost all test cases, there are a few test problems (e.g. the square test in Sec 5.2.3) for which this is not working ideal and we will discuss this in detail in the remainder of the chapter. If not otherwise mentioned, we assume an ideal gas with $\gamma = 5/3$ and all code operate on adaptive time steps for all tests (i.e. we never force a small constant time step to improve the accuracy of the results).

MFM is used with a cubic spline kernel and 32 (24) neighbors in 3d (2d). The slope limiter from gizmo in combination with their pairwise limiter, both as presented in Sec. 5.3, is used. Consistent settings are chosen between OpenGadget3 and gizmo. For SPH, a Wendland C6 kernel, including bias correction (Dehnen & Aly, 2012), with 295 (64) neighbors in 3d (2d) is used. The modern, time-dependent artificial viscosity scheme of Beck et al. (2016b) and artificial conductivity (Price, 2008) are included. For Arepo we use additional mesh regularization based on the center of mass, and the "roundness" of the cells. An overview of all settings is made publicly available[4]. If not otherwise stated, the ICs are created with equal particle masses. In most cases, particles are arranged in a (perturbed) regular grid in order to reduce noise introduced by the initial particle distribution.

5.2.2 Stability

Soundwave

As a first test we adopt a sinusoidal soundwave with density $\rho = 1$ and small perturbation amplitude $\Delta\rho = 10^{-4}$ in a box of length 1 in x-direction and 0.75 in y/z-direction. The particles are arranged in a perturbed hexagonal close packed (hpc) grid with varying resolution. The

[2]Obtained from `https://bitbucket.org/phopkins/gizmo-public/src/master/` February 2021
[3]Obtained from `https://gitlab.mpcdf.mpg.de/vrs/arepo` June 2021
[4]`https://github.com/fgroth/hydro_tests`

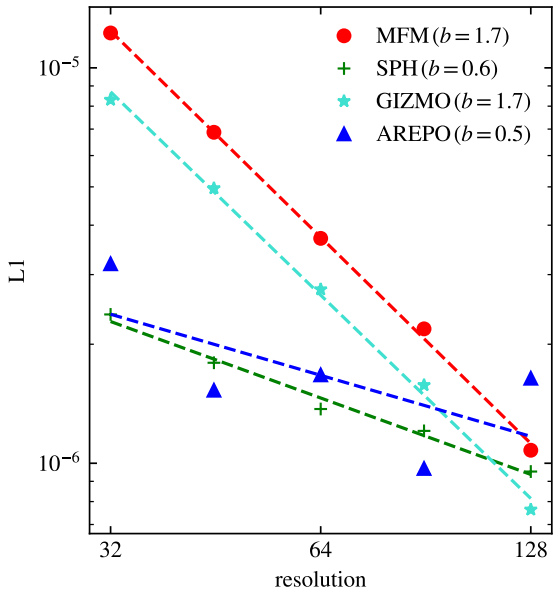

Figure 5.1: L1 norm for the soundwave at different resolutions. The order of convergence b is obtained from a fit. While MFM in both implementations shows between first and second order convergence, SPH and the moving mesh have a convergence even below first order.

number of particles is ranging from $64^3 \cdot 0.75^2$ up to $128^3 \cdot 0.75^2$. In the following, we will define the resolution by the number of particles per unit-length in x direction. We adopt a wavenumber $k = 2\pi$ and a speed of sound $c_s = 2/3$. For this test there is an analytic solution $\rho(x,t) = \rho_0 + \Delta\rho \sin(k(x + c_s t))$, which makes this test well suited to perform a convergence analysis. For this purpose, we measure the L1 error norm $\frac{1}{N_{\text{tot}}} \sum_i^{N_{\text{tot}}} |\rho_i - \rho(x,t)|$, shown in Fig. 5.1. All methods are able to evolve the soundwave, while the accuracy as well as the precise convergence behavior differ among the codes. We observe a similar convergence between the MFM implementation in GIZMO and OpenGadget3 being between first and second order. While theoretically second order convergence would be expected, the slope-limiter reduces the order of convergence, as discussed by Alonso Asensio et al. (2023). The convergence for SPH in OpenGadget3 and the Arepo code are similar, but even below first order. For Arepo, the main reasons for this low-order convergence are the mesh regularization, which introduces small numerical noise, and the fact that faces which contribute by less than 10^{-5} to the total face area are neglected (R. Pakmor, 2023, priv. comm.). The convergence can be improved by fixing these two points, as shown in Sec. 5.5, leading to a similar convergence as for MFM much closer to second order. Nevertheless, these changes would make the code more unstable in cosmological simulations.

In order to get a more detailed analysis, we split the error between errors in the position, in the amplitude, and scatter as shown in Fig. 5.2. A sinusoidal soundwave is fit to the density distribution, such that the offset and amplitude differences to the expected wave are obtained. The remaining deviations, mostly being scatter, are then quantified by an L1-norm.

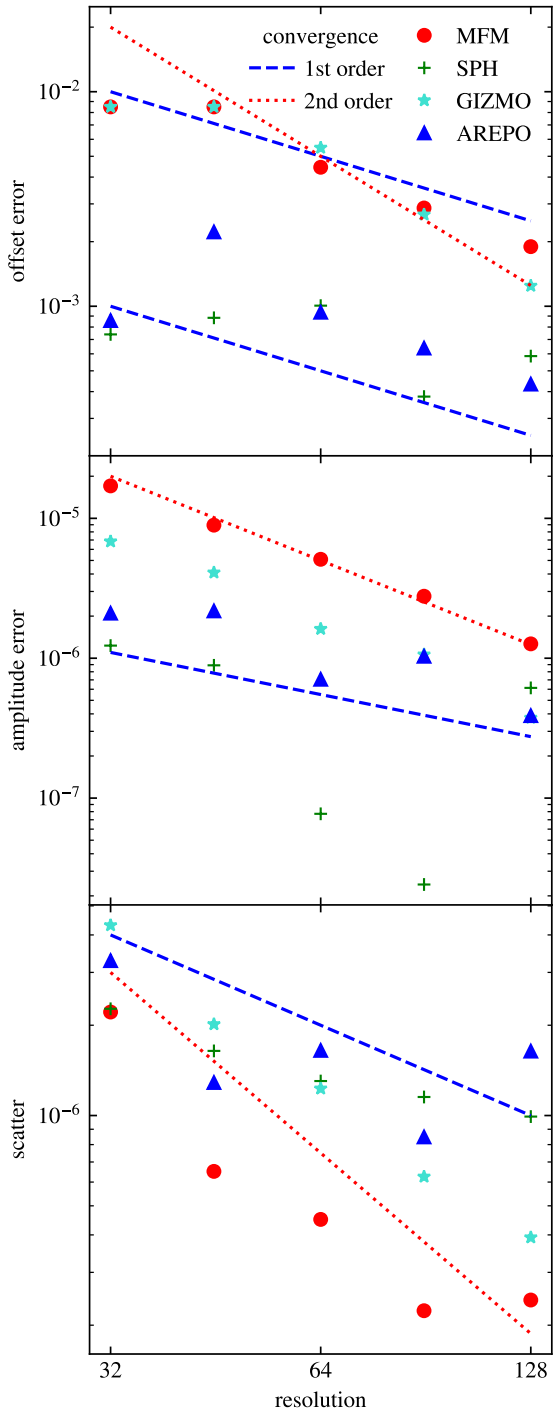

Figure 5.2: Offset-, amplitude- and scatter-errors of the density of a soundwave at $t = \frac{2}{c_s}$ calculated with MFM and SPH in OpenGadget3, MFM in GIZMO and a moving mesh in Arepo at different resolutions. The scatter converges second order for all methods, while other errors show different convergence behavior. MFM shows between first and second order convergence for all error components.

Deviations from the expected sound speed are related to dispersion errors, and will lead to an offset compared to the analytical solution. This offset error is shown in the upper panel. We observe for MFM in both implementations the convergence to be between first and second order, consistent between both codes. For SPH and Arepo, the overall error is roughly one order of magnitude smaller at the lowest resolution, but having a convergence even worse than first order. For SPH, this trend can be explained by low-order errors, which are prominent for traditional SPH, and still partly left for modern SPH.

The error in the amplitude, shown in the middle panel, is related to numerical diffusion. As we see also in other tests, the Riemann solver and the slope-limiter introduce numerical diffusivity for MFM, which thus has the largest error. Differences between the different MFM implementations can be explained by different Riemann solvers used. SPH and Arepo show much lower errors. The convergence behavior, however, is again better for MFM compared to the other methods. In both implementations, it is roughly second order, while for the other methods it appears to be approximately first order.

Finally, it is worth to note that the resulting soundwave does not have perfect sinusoidal shape but shows scatter in the amplitude. This is mainly a result of the smoothing length/density iteration and the threshold chosen for the value to be taken as converged. We quantify this error by the L1 error norm, shown in the bottom panel of Fig. 5.2. All methods show roughly second order convergence, while the amplitude of the error is different. Differences between MFM and SPH in OpenGadget3 can be explained by the different kernels used, while other codes have differences in the iteration and treat parameters for convergence slightly differently. The large error for Arepo, even at higher resolution makes the values for the other errors more uncertain. In addition to the errors already mentioned, the soundwave deforms and steepens up due to non-linear terms in the evolution. This non-linearity will lead to an additional, small but constant term in the scatter error in the bottom panel of Fig. 5.2. A reduction could be achieved by reducing the amplitude, which would also make scatter errors more significant or the convergence more expensive. As non-linear contributions are expected to become important when $L1 \approx (\Delta\rho/\rho)^2 = 10^{-8}$ in our setup, this term will not be relevant for the resolutions considered.

Kepler Disk

The Kepler disk is an important test case for cosmological simulations, allowing to study the ability of the code to conserve angular momentum and maintain stable orbits over time. Especially, the effect of viscosity can be analyzed. To this end, we initialize a two-dimensional box sufficiently large to contain all particles. The ICs are taken from Hopkins (2015) and are initialized with 48240 gas particles with equal masses, arranged in a grid-like structure and setup with vanishing pressure of $P = 10^{-6}$. The gas surface density distribution is given via:

$$\Sigma = 0.01 + \begin{cases} (r/0.5)^3 & \text{if } r < 0.5 \\ 1 & \text{if } 0.5 \leq r \leq 2 \\ (1 + (r-2)/0.1)^{-3} & \text{if } 2 < r. \end{cases} \tag{5.1}$$

For the Arepo run, we adopt a low density mesh with vanishing pressure at a resolution of 16 particles per unit length distributed around the disk as well as inside the central hole of the disk.

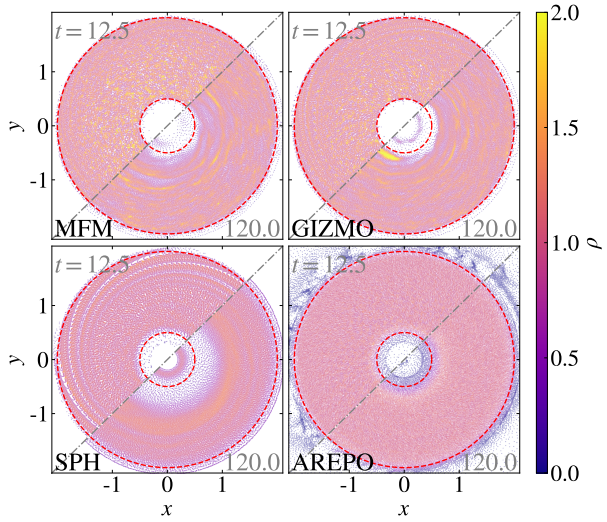

Figure 5.3: Evolution of the Kepler disk using different hydro-methods. Surface density at two times per method: $t = 12.5$ (upper left) and $t = 120$ (lower right). In general, all methods are able to evolve a stable disk. Initial perturbation introduced by the ICs, however, evolves differently for the different methods.

We adopt an external potential $\Phi = -(r^2 + \epsilon^2)^{-1/2}$ with resulting gravitational acceleration of the form

$$\boldsymbol{g} = -\boldsymbol{r} \begin{cases} \left(\frac{(r/0.35)^2}{(\boldsymbol{r}^2)^{1.5}} - \frac{(0.35-r)/0.35}{(\boldsymbol{r}^2)^{1.5}} \right) & \text{if } r \leq 0.35 \\ \left(\frac{1}{(\boldsymbol{r}^2)^{1.5}} \right) & \text{if } 0.35 < r < 2.1 \\ \left(\frac{1+(r-2.1)/0.1}{(\boldsymbol{r}^2)^{1.5}} \right) & \text{if } 2.1 \leq r. \end{cases} \tag{5.2}$$

We follow the evolution of the disk until $t = 120$, corresponding to ≈ 20 orbits at $r = 1$. The resulting density at $t = 120$ and $t = 12.5$ is shown in Fig. 5.2.2. Initially, all methods produce spirals as a result of perturbations in the ICs. While for more traditional SPH with Balsara viscosity switch (Balsara, 1998) these lead to a destruction of the disk after only a few orbits, consistent with the results of Beck et al. (2016b), the modern SPH implementation in OpenGadget3 with the improved viscosity scheme of Beck et al. (2016b) drastically increases the stability of the disk. While the inner and outer region still show some decay, the main part of the disk is stable for the whole evolution considered. For MFM the disk remains stable for more than 20 orbits. We observe that the inner and outer parts of the disk degrade much less compared to SPH. The initial perturbations are diffused throughout the disk, which shows slightly larger perturbations in the main part compared to the SPH calculation. Both, our implementation and the one in GIZMO, show qualitatively similar results. The Arepo run turns out to produce the most stable disk. Only a slight degeneration at the boundaries can be observed. Further studies would be needed to analyze whether this is a numerical effect or due to interaction with the ambient

medium not present in the other calculations.

5.2.3 Tests for Fluid Mixing Instabilities

Mixing occurs in a variety of cosmological situations, most prominently during ram-pressure-stripping. To this end, we analyze the ability of the different codes and methods to evolve such mixing instabilities.

Rayleigh-Taylor Instability

One popular fluid-mixing test is the Rayleigh-Taylor instability. It can be used to explore how well the code can describe unstable, growing modes. The setup we use is taken from Hopkins (2015). The calculations are performed in a two-dimensional periodic box with side lengths 1, populated with 65536 particles where the particles at $y < 0.1$ and $y > 0.9$ are fixed as boundary conditions. In contrast to the other codes, for Arepo the boundary particles are not fixed but instead a reflective boundary condition is used.

A fluid of high density ($\rho = 2$) is placed on top of a low-density medium ($\rho = 1$) in HE. For this test case, we take $\gamma = 1.4$, as for a diatomic gas, such as molecular hydrogen, and apply the constant gravitational acceleration:

$$\boldsymbol{a}_{\mathrm{grav}} = -0.5\hat{y}. \tag{5.3}$$

To allow the instability to grow, a small velocity perturbation at the phase boundary is introduced (for more details see Hopkins, 2015).

In Fig. 5.4 we show that all methods are perfectly able to evolve the instability. A major difference between the different methods is the presence of asymmetries and secondary instabilities. While these can be seen clearly for MFM, both in OpenGadget3 and gizmo, and are also present in the Arepo calculation where they appear more symmetric, we find that they are absent from the SPH calculation, due to the smoothing over the larger kernel and the effectively lower spatial resolution (e.g. Marin-Gilabert et al., 2022, for a more detailed discussion of the occurrence of secondary instabilities and their physical meaning). The results of Arepo indicate the sharpest boundary and highest density in the tip, followed by MFM. The particles close to the boundary for Arepo still show a clear imprint of the initial grid-like particle distribution. We note that the numerical diffusivity within modern SPH causes the boundary of the instability to have a shallower gradient and smears out initial asymmetries. In addition, the effective spatial resolution is lower by a factor of ≈ 2 compared to MFM due to the larger neighbor number and thus SPH reaches a much lower density in the tip of the instability.

Kelvin-Helmholtz Instability

Similar to the Rayleigh-Taylor instability, also the Kelvin-Helmholtz instability is a famous example for fluid mixing. Again, we use the setup provided by Hopkins (2015). Two fluids of densities $\rho_1 = 1$ and $\rho_2 = 2$ in HE are initialized in a 2d periodic box, with initial velocities $\boldsymbol{v}_1 = 0.5\hat{x}$, $\boldsymbol{v}_2 = -0.5\hat{x}$ and a small perturbation following McNally et al. (2012). The setup

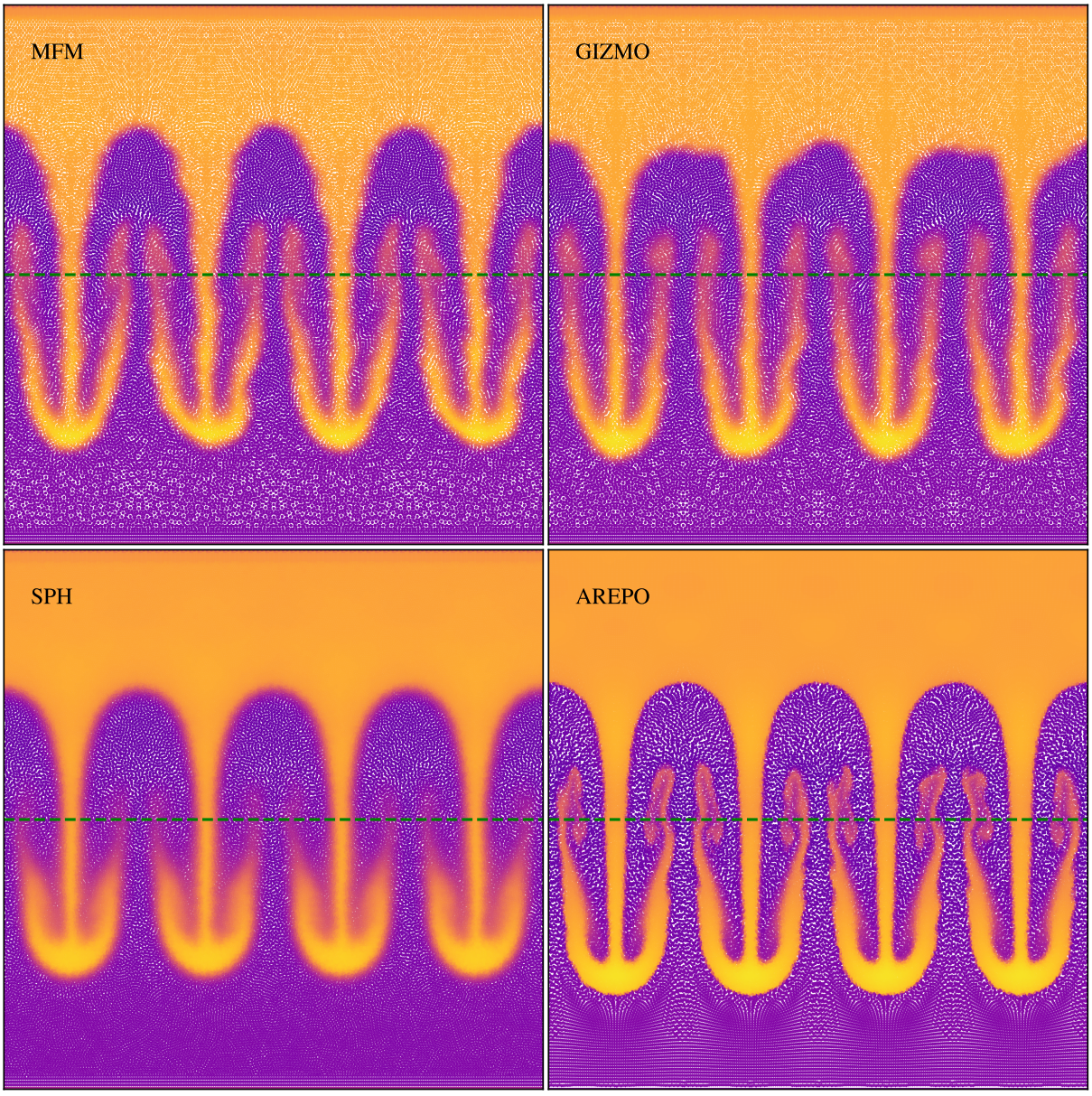

Figure 5.4: Rayleigh-Taylor instability at time $t = 3.6$. Comparison between the different hydro-methods. Vertical line marks the initial position of the phase boundary. Differences are mainly the presence or absence of secondary instabilities.

includes in total 774144 particles. At time $t = 2.5$ corresponding to $\approx 1.2\tau_{\mathrm{KH}}$ in units of the Kelvin-Helmholtz timescale $\tau_{\mathrm{KH}} = \frac{\lambda}{\Delta v_x}\frac{\rho_1+\rho_2}{\sqrt{\rho_1\rho_2}}$ (compare, e.g., Junk et al., 2010), the instability has produced a roll for all methods, as shown in Fig. 5.5.

Differences are present in the inner structure of the roll. Overall, the qualitative results are very similar to those for the Rayleigh-Taylor instability. SPH is smoothing the roll, showing no secondary instabilities and evolving more smoothly towards later times. Compared to that, MFM in both implementations shows a clear separation between the higher-density roll and the less dense medium, with the presence of secondary instabilities. A more detailed analysis of the Kelvin-Helmholtz instability, also using our new MFM implementation, has been done by Marin-Gilabert et al. (2022). They also show that the secondary instabilities can be avoided by using a higher neighbor number in combination with a higher-order kernel. This will increase the intrinsic viscosity and prevent mixing in form of secondary instabilities. Also Arepo shows secondary instabilities, present especially inside the roll. When present, these perturbations will finally dominate the evolution over the build-up of the roll for $t \gtrsim 3$.

Hydrostatic Square

As both aforementioned fluid-mixing tests contain sharp boundaries that deform due to instabilities, the understanding of the evolution of such boundaries without perturbations imprinted in the ICs is important. The Hydrostatic Square tests this behavior, as it is well suited to study the stability of edges related to numerical surface tension. Similar tests have been performed e.g. by Hess & Springel (2010) and Hopkins (2013, 2015).

We set up a two-dimensional box of size $L = 1$ with periodic boundary conditions. It is filled with 7168 gas particles with equal masses, arranged in two regular grids, one grid for the ambient medium (ρ_a=1, $P_a = 2.5$) and one for the square with side-length $L/2$ with increased density $\rho_s = 4$ in HE ($P_s = P_a$). In Fig. 5.6, we compare the resulting density distribution at time $t = 10$, evolved with the different methods. As the ICs are set in HE, we would expect no changes to occur. This ideal state is only achieved using the moving mesh code Arepo. Theoretically, we would expect the same to be true for MFM, as shown by Hopkins (2015). They use, however, a strongly idealized setup compared to ours. Especially, they use a regular grid for all particles, and increased particle masses within the square. For our setup, the gradient estimate at the boundary does not conserve linear gradients. Instead, it is biased by the inhomogeneous particle distribution due to two separate grids, especially in combination with the slope-limiter. A more detailed analysis of the effect of the slope limiter is provided in Sec. 5.2.8, where we have shown that the amount of surface tension and resulting deformation of the square strongly depends on the slope-limiter. We observe, using both our MFM implementation and gizmo, that for MFM the edges of the square start to deform, followed by some numerical instability, which leads to a more asymmetric deformation. Increasing the resolution by a factor of 4, as shown in Fig. 5.7, this instability occurs slower and the square preserves its shape much better. Also using SPH, the square deforms. As expected, it becomes more circular, caused by numerical errors, which behave as surface tension (compare, e.g., Price, 2008). For traditional SPH, these errors should be low-order. We observe, however, that this effect can be drastically reduced by increasing the resolution, as shown in Fig. 5.7 indicating that modern SPH implementations, as used in

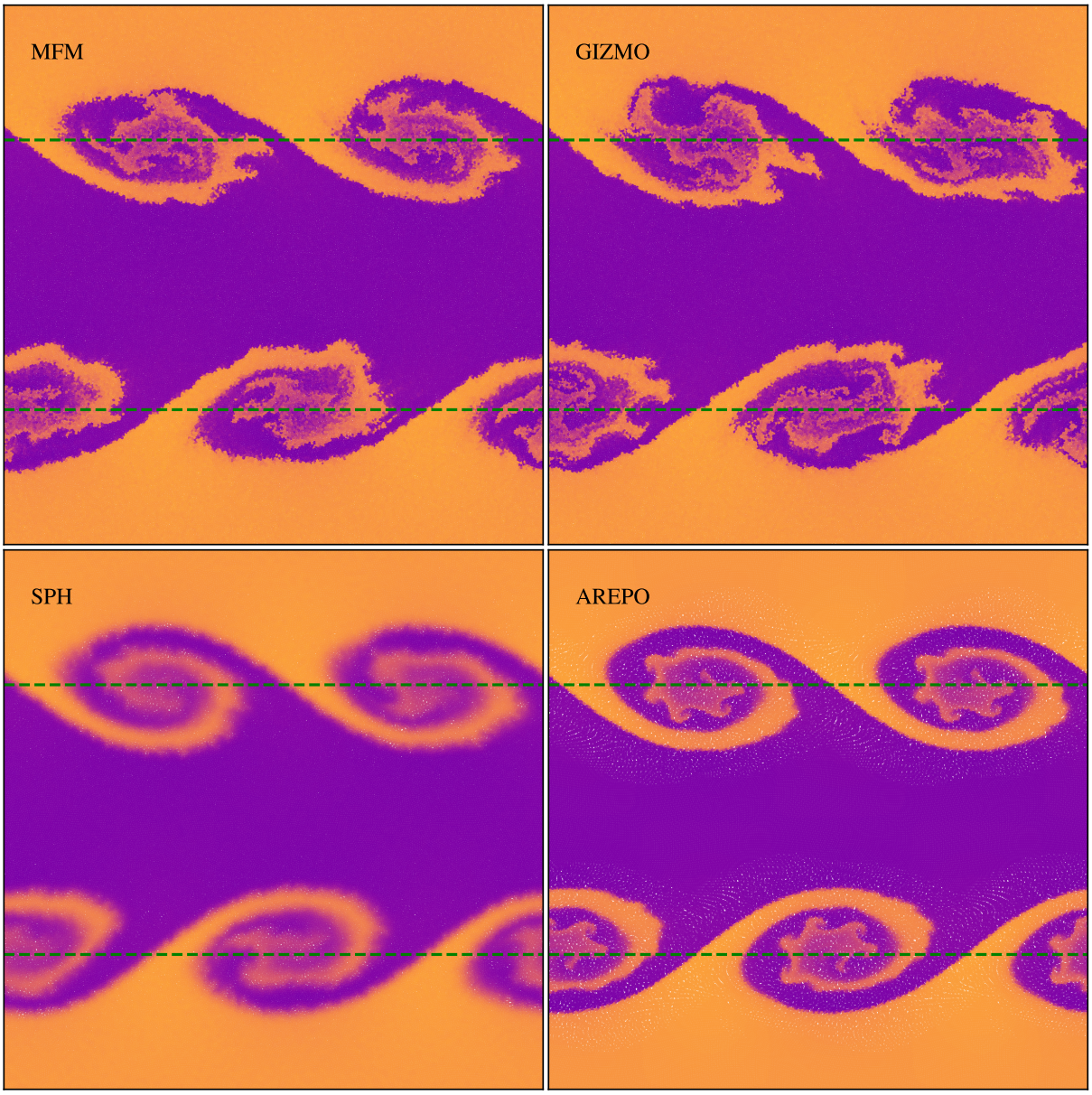

Figure 5.5: Build-up of a 2d Kelvin-Helmholtz instability at $t = 2.5$ comparing different methods. Horizontal dashed lines mark the initial position of the phase boundary. All methods produce the roll, but with differences in their inner structure.

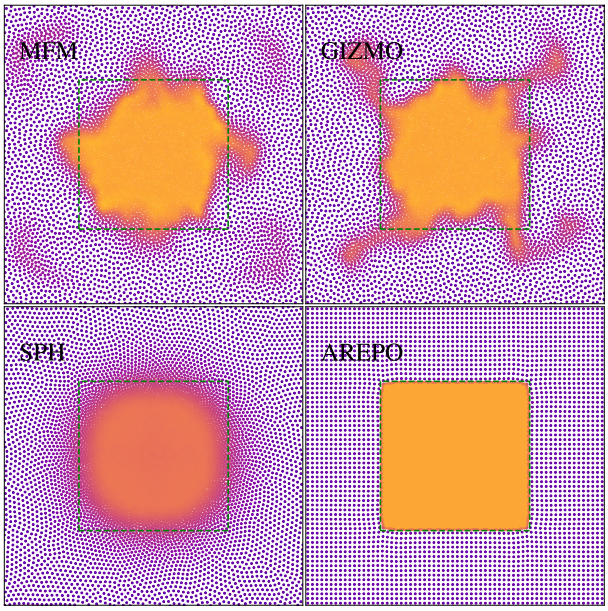

Figure 5.6: Density of the hydrostatic square evolved until $t = 10$ using different methods. The initial location of the high density "square" region is overplotted as contour. Only AREPO is able to keep the initial square shape, while other methods lead to deformation of the square.

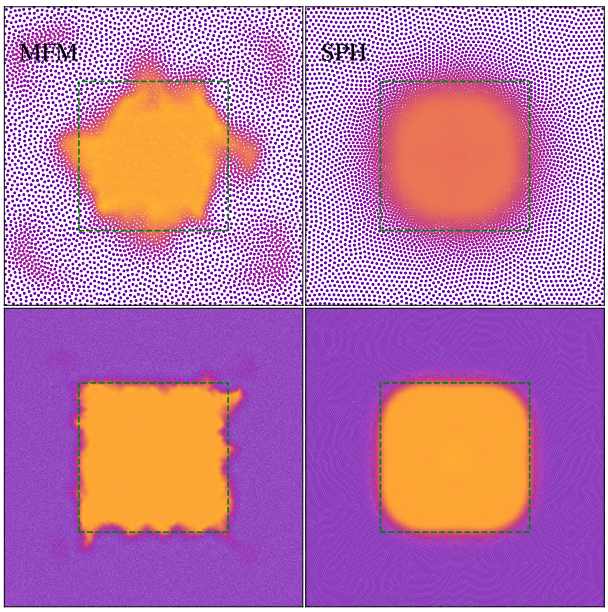

Figure 5.7: Hydrostatic Square at $t = 10$. Comparison of MFM and SPH at two different resolutions, Top: 7168 particles, Bottom: 114688 particles (increase in resolution by factor 4). Both, MFM and SPH, show convergence of the shape of the square.

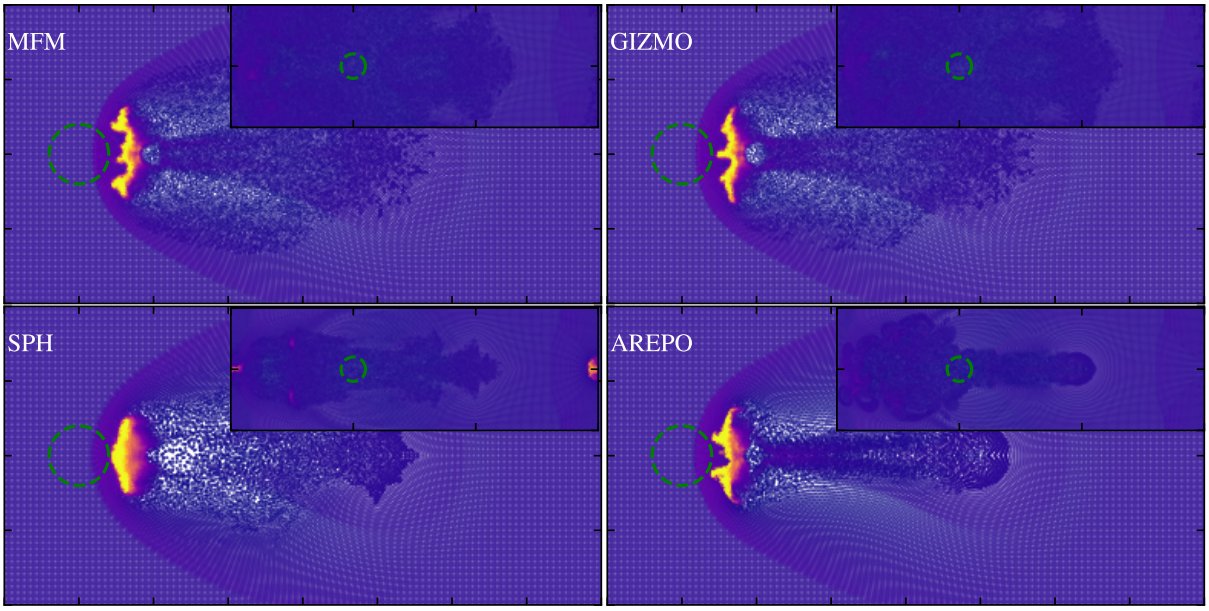

Figure 5.8: Blob at $t = \tau_{\rm KH}$ and $t = 4\tau_{\rm KH}$ as small insertion comparing different hydro-methods. At the earlier time, SPH leads to much less deformation due to less instabilities building up, while MFM in both implementations as well as Arepo agree qualitatively. At late time, MFM and Arepo are fully mixed, while SPH still has some structure remaining.

OpenGadget3, reduce low-order errors and improve convergence. Overall, for this specific test surface tension for SPH, but also for MFM can be observed. A moving mesh performs best, preserving the situation perfectly. MFM at later times shows some numerical errors leading to a more asymmetric deformation, which converge away with increasing resolution.

The "Blob" Test

A more complex problem is the blob test. It is designed to mimic ram-pressure stripping by an interplay of the evolution of shocks and fluid-mixing instabilities. We use the setup described by Hopkins (2015) (compare also Agertz et al., 2007). A three-dimensional box with side-length 2000 in x and y-direction and 6000 in z-direction is populated with 9641651 particles. A cloud of higher density $\rho_{\rm cloud} = 10\rho_{\rm wind}$ is placed into a wind tunnel with supersonic flow at $\mathcal{M} = 2.7$ and density $\rho_{\rm wind} = 2.6 \cdot 10^{-8}$. Both phases are set up in pressure equilibrium.

The resulting density in a slice through the cloud at $t = \tau_{KH}$ and $t = 4\tau_{\rm KH}$ is shown in Fig. 5.8. In front of the cloud, a bow shock forms. At the Kelvin-Helmholtz timescale $\tau_{\rm KH} = 2$, the cloud has developed instabilities. These are much more pronounced for MFM and Arepo, while for SPH the cloud deforms, without showing instabilities. The precise form of the cloud differs between our MFM implementation, that in gizmo and the moving mesh code Arepo. Nevertheless, the cloud mass, defined by the particles obeying $\rho > 0.64\rho_{{\rm cloud},i}$ and $u < 0.9u_{{\rm amb},i}$, is very similar for all methods until τ_{KH}, shown in Fig. 5.9. As expected, the MFM calculations line up with the calculations done by Hopkins (2015). The periodic bumps are a result of the

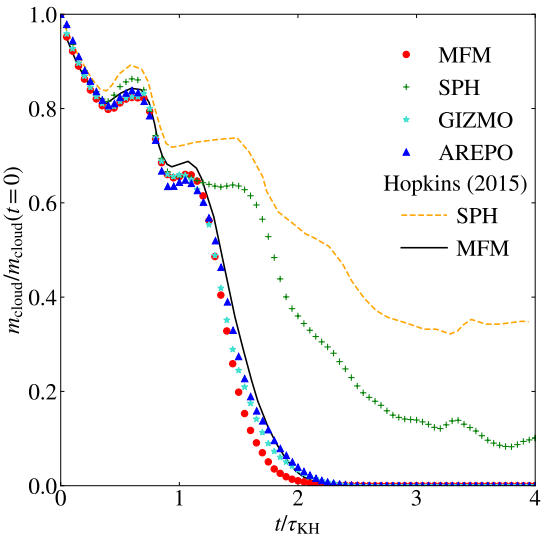

Figure 5.9: Decay of the cloud fraction surviving for the different methods. In the background, comparison lines of the results by Hopkins (2015) for MFM (black, solid) and (traditional) SPH (orange dashed) are shown. MFM and Arepo agree very well, while SPH shows less mixing.

self-interaction of the shock due to the choice of boundary conditions.

At later times the evolution strongly deviates. While for MFM as well as a moving mesh secondary instabilities build up and lead to a disruption of the cloud, it is more stable in SPH. Compared to the more traditional SPH results of Hopkins (2015), however, we find the blob to decay stronger, as modern SPH with time-dependent artificial viscosity and conductivity is able to evolve instabilities much better, thus allowing for more mixing.

5.2.4 Tests for Shock-Capturing

Sod Shock-Tubes

Another important capability of the code is to capture strong shocks of (arbitrarily) large Mach numbers. We begin testing this on a simple Sod shock-tube based on the setup of Sod (1978). The test is performed in a three dimensional periodic box of size L_x=140, $L_y = L_z = 1$ with two fluids of different density and pressure ($\rho_1 = 1, P_1 = 1$; $\rho_2 = 1/8, P_2 = 0.1$ for $\gamma = 1.4$) that are initialized in a glass-like configuration of in total 216090 particles. When the two phases start interacting, a shock begins to move to the right. In Fig. 5.10, we show the resulting structure at $t = 2.5$ for the MFM calculations at different Mach numbers and compare them to the analytic solution. The expected profiles are matched very well, for all the Mach numbers adopted in this work, ranging from a very low $\mathcal{M} = 1.5$ shock to a strong $\mathcal{M} = 100$ shock. This ability is directly connected to the accuracy of the Riemann solver. For higher Mach numbers, increasing peaks in velocity and entropy at the shock front are present as a result of the non-TVD slope-limiting

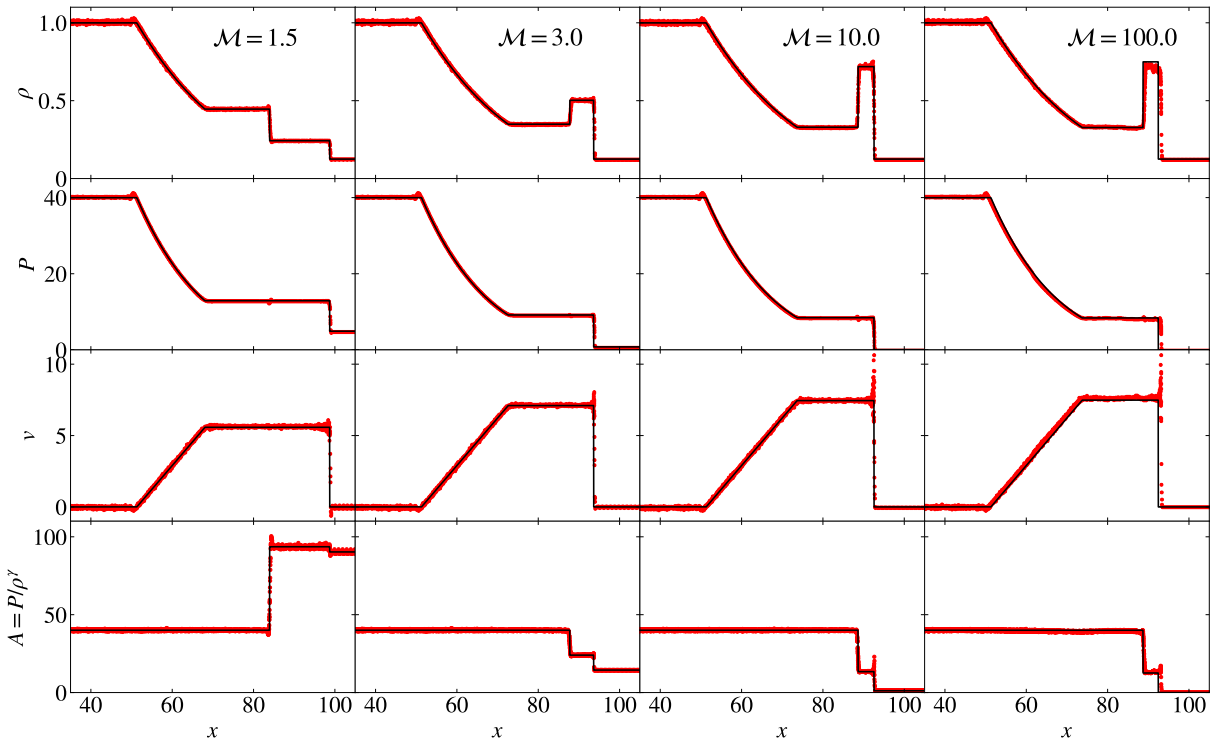

Figure 5.10: Density, pressure, velocity, and entropy profile of the shock tube at $t = 2.5$ calculated with our MFM implementation, comparison between different Mach numbers. MFM is able to reproduce the general structure of the shocks. Artifacts of surface tension introduced by the slope-limiter are visible at higher Mach numbers. The scatter is a result of the choice of ICs.

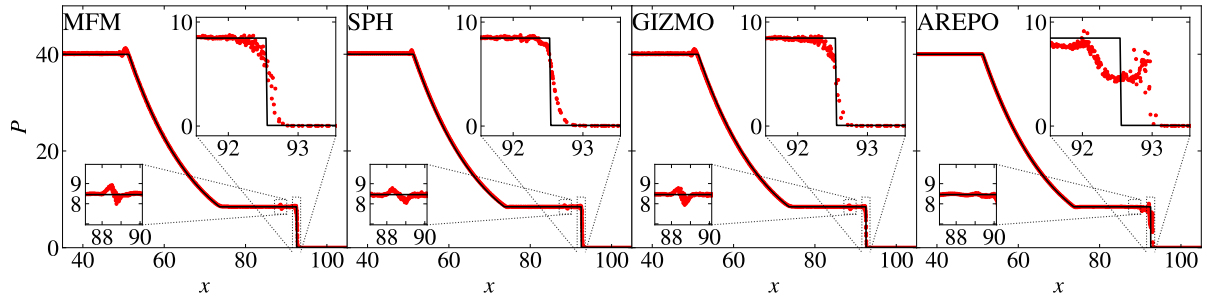

Figure 5.11: Pressure profile of the $\mathcal{M} = 10$ shock tube at $t = 2.5$, comparison between different hydro-methods. The different codes show different amounts of surface tension and also slight differences in the position of the shock front due to different timestepping

procedure, which has also been reported by Hopkins (2015). We note that this peak and nearby oscillations would be even larger if no limiter was used, and can be avoided even better by using a TVD-limiter, which has more disadvantages in other cases. With increasing Mach number, a sufficiently small timestep becomes more important. The scatter in velocity for the high $\mathcal{M} = 100$ shock, as well as the small offset in the position of the shock front converge away with decreasing timesteps.

The scatter in density present at all Mach numbers is a result of the choice of the ICs, which are set up in a glass-like configuration and designed for a higher neighbor number. It does not converge for low neighbor numbers, as chosen for MFM. The pressure profile shows the typical bump at the rarefaction fan, as well as the pressure blip at the contact discontinuity, shown in more detail in Fig. 5.11 for the intermediate $\mathcal{M} = 10$ shock. This indicates the presence of surface tension-like error terms, introduced by the slope limiter. As discussed in Sec. 5.2.3 on the example of the hydrostatic square, these terms are present for SPH and both MFM implementations, but not for Arepo, manifesting also in the presence or absence of the pressure blip for the different methods. The shock front is captured equally well for MFM and SPH, though less smoothed out for MFM due to the lower neighbor number. Arepo poorly captures the behavior at the shock front. Especially, it has troubles in the mesh reconstruction in this strongly anisotropic region, which leads to a shift in the position of the shockfront and to the oscillatory behavior in the shocked region. It could be improved using a static mesh, which would remove other advantages of this method, however.

Sedov-Taylor Blastwave

This very strong, radially symmetric shock has first been introduced by Sedov (1946, 1959). Besides the capability to deal with jumps, Saitoh & Makino (2009) describe how it can be used to analyze the timestep limiter and shows the need for the limiting to be non-local, as provided by the wakeup scheme. The test has become a popular benchmark for SN blast wave evolution in recent years (e.g. Kim & Ostriker, 2015; Steinwandel et al., 2020).

As ICs, we set up a regular grid with 64^3 particles and density $\rho = 1$. While almost all particles exhibit a vanishing pressure $P_a = 10^{-6}$, energy of $U = 10$ is distributed equally into

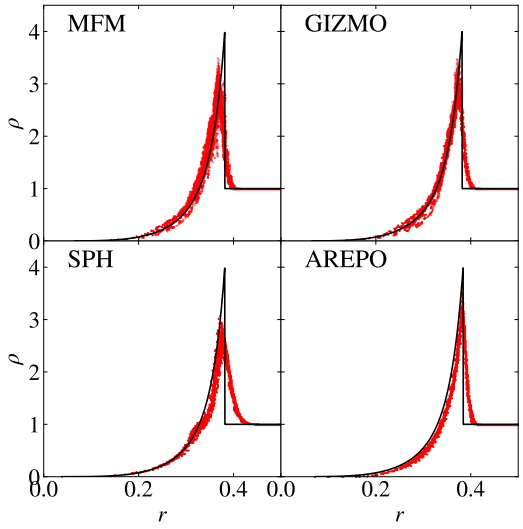

Figure 5.12: Sedov blast at $t = 0.02$. Comparison between different methods. The analytical solution (Sedov, 1946; Taylor, 1950; von Neumann, 1961) is shown as reference. The main difference is the height of the peak, which is reduced due to smoothing of the jump.

the eight central particles. A shock with very high $\mathcal{M}_i \gtrsim 2 \cdot 10^4$ arises, and quickly moves outwards.The radial density distribution is shown in Fig. 5.12.

All methods are able to capture the shock, though slightly smoothing it, thus underestimating the height of the density-peak. SPH shows the strongest smoothing, followed by the two MFM implementations. Arepo is able to reproduce the height of the peak best.

The position of the peak is similar for all methods, with minor differences. While Arepo and gizmo's MFM implementation predict the peak position correctly, MFM and SPH in OpenGadget3 lag slightly behind, which results in a more accurate position of the low-density side of the shock. This position strongly depends on the precise timestep settings, indicating differences in the timestepping between the codes.

5.2.5 Including Self-Gravity

In cosmological contexts, not only hydrodynamical forces, but also gravitational accelerations are of great importance. Gravity dominates the evolution on large scales due to its long-range character. It can lead to collapse of clouds, e.g. in the ISM for star formation, or balance thermal pressure and lead to HE, such as in the global structure of galaxies or GCs. Thus, we analyze the interplay between hydrodynamical forces and gravity in the following.

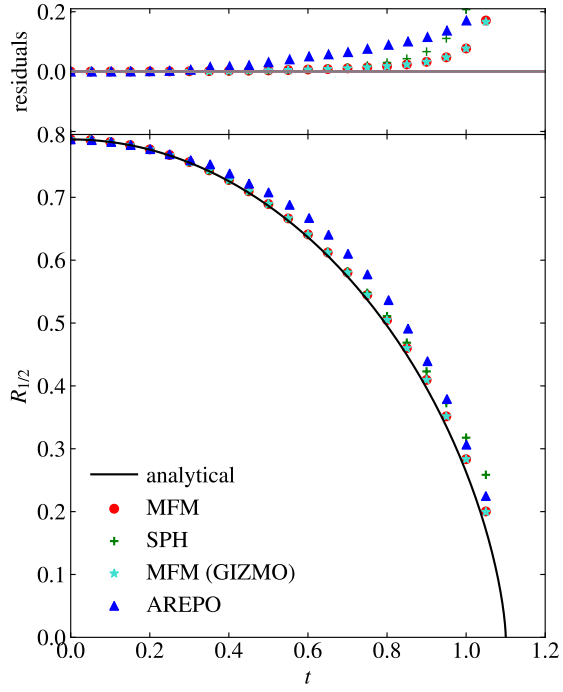

Figure 5.13: Evolution of the half-mass radius for the gravitational freefall test. All methods agree at early time, but deviate from the expected solution at later times when hydrodynamical contributions become more important.

Gravitational Freefall

As a first test including self-gravity, we simulate a collapsing sphere. The ICs are set up on a regular grid of 20^3 particles and cut out a sphere of radius 1, which has a total mass of $M_{\text{sphere}} = 1$ and a negligible pressure of $P = 10^{-6}$. For the Arepo run, we fill the region not occupied by the sphere with low mass, low energy particles at resolution of only 8 particles per unit length, arranged in a regular grid, in order to improve the mesh reconstruction at the boundary. We follow the evolution of the half-mass radius, to not be influenced by boundary effects as for the full radius, shown in Fig. 5.13. Comparing to the analytic solution for a purely gravitational freefall

$$t(r) = \arccos\left(\sqrt{\frac{r}{r_0}} + \sqrt{\frac{r}{r_0}}\sqrt{1 - \frac{r}{r_0}}\right) \cdot \frac{2}{\pi}\sqrt{\frac{3\pi}{32\rho_0}}, \tag{5.4}$$

all methods agree at early times. At late times, pressure and thus effects of the hydro-scheme become more relevant, and deviations are visible. For all methods additional pressure contributions lead to an increase in radius as it would be expected. As the initial pressure is small, only a small

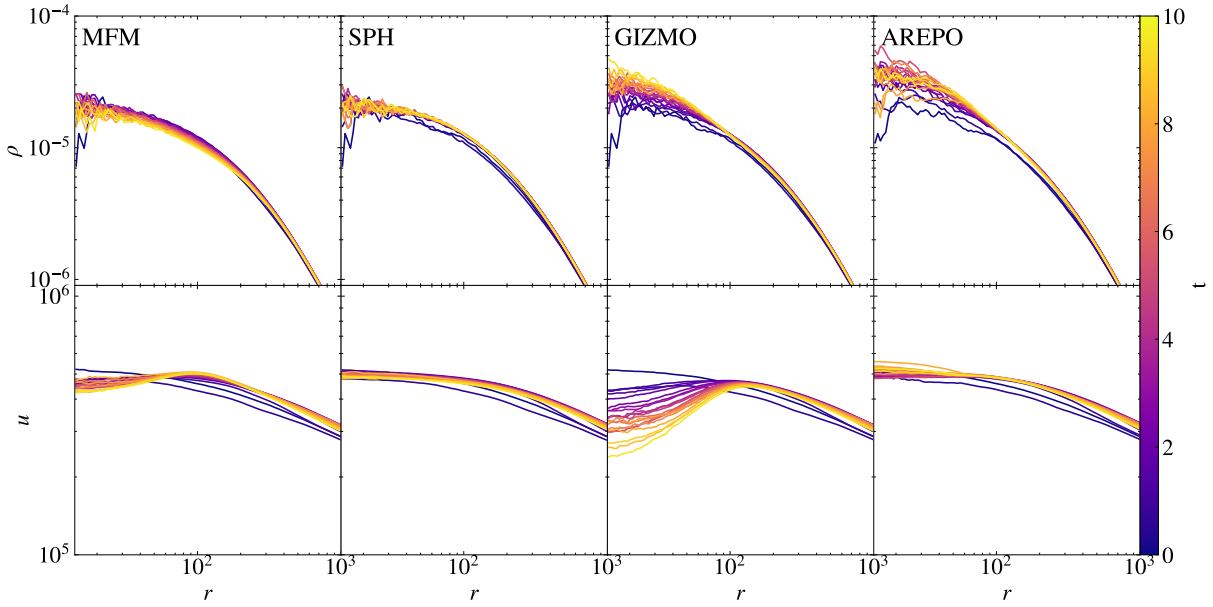

Figure 5.14: Evolution of gas density (top) and internal energy radial profiles (bottom) for the hydrostatic sphere for approximately 10 dynamical times until $t = 10$, colored by the time. Calculated using different hydro-methods. MFM shows a slightly larger numerical diffusivity, but overall still preserves the density profile.

deviation is expected. MFM lies closest to the ideal solution with both implementations being indistinguishable. The moving mesh code Arepo overestimates the radius already at early times, which can be explained by poor treatment of the non-periodic boundary conditions. While gravity is calculated in a non-periodic way, the mesh construction for the hydro-calculation requires the box to be treated periodically, which is not the case for all other methods. Including the low mass cells at the boundary already decreased the error by a factor of 2 and it could be further decreased by enlarging the box. SPH lies in between the other methods except at very late times, when the deviation strongly increases due to over-smoothing.

Hydrostatic Sphere

In cosmological contexts, e.g. for the ICM, the ability of the code to preserve HE against gravity is of great importance. To test this, we calculate a hydrostatic sphere as a second test including self-gravity. It is also the first test including DM as second, only gravitationally interacting particle type. The ICs have been created following Viola et al. (2008). 88088 DM particles are setup following an NFW profile (Navarro et al., 1997), populated with 95156 gas particles in HE. The corresponding density and internal energy profiles at different times are shown in Fig. 5.14. After a short relaxation period, happening on a timescale approximately corresponding to the dynamical time $t_{\mathrm{freefall}} \approx 1$ at $r = 10^2$, we expect the gas to keep HE. SPH as well as our MFM implementation show the lowest deformation in density. MFM in gizmo, as well as Arepo show a slightly stronger increase in density, especially in the central region. While the density is only

an indirect tracer of (numerical) diffusivity, the internal energy profile is more directly affected by it. Thus, it can give even more insight into the convergence over time.

For SPH, we observe a stable situation to be reached within one freefall time, and only minor changes to the initial profile. The same is true for MFM in OpenGadget3, where changes in internal energy are only marginally larger compared to SPH. For Arepo, changes compared to the initial profile are similar to the MFM result, as the ICs were designed assuming SPH. After a similar timescale for this relaxation, also for this method a stable situation is reached. For MFM in gizmo, in contrast, an impact of the numerical diffusivity can be observed. Resulting mixing in the central region leads to a decrease in internal energy, leading to the observed increase in central density. Differences between the MFM implementations are results of the different Riemann solvers in combination with fine differences in the implementation. Also in previous implementations of ours we observed a similar change as for gizmo. Over very long timescales, the sphere would tend to become isothermal for MFM. Despite these findings, the effect on the density profile is quite small for all methods over the timescale considered.

Zeldovich Pancake

The Zeldovich pancake is the first problem to test our implementation of co-moving integration. In addition, it is well suited to show effects of very high $\mathcal{M}$ flows, shocks, highly anisotropic particle arrangements, and also very low internal energies. It has been introduced by Zel'dovich (1970a). We start our calculation at $z_i = 100$, setting up a single Fourier mode density perturbation. During the linear growth until the caustic formation at $z_c = 1$, the evolution can be described by

$$x = x_i - \frac{1+z_c}{1+z}\frac{\sin(kx_i)}{k} \tag{5.5}$$

$$\rho = \frac{\rho_0}{1 - \frac{1+z_c}{1+z}\cos(kx_i)} \tag{5.6}$$

$$\boldsymbol{v}_{\mathrm{pec}} = -H_0 \frac{1+z_c}{\sqrt{1+z}\frac{\sin(kx_i)}{k}}\hat{\boldsymbol{x}} \tag{5.7}$$

$$T = T_i \left(\frac{1+z_c}{1+z}\right)^2 \left(\frac{\rho(x,z)}{\rho_0}\right)^{2/3} \tag{5.8}$$

starting from the unperturbed position x_i. ρ_c is the critical density, $H_0 = h_0 \cdot 100\,\mathrm{km\,s^{-1}\,Mpc^{-1}}$ the Hubble parameter (today) with $h_0 = 1$, and $T_i = 100$ K the initial temperature, such that pressure forces are negligible. The wavenumber $k = 2\pi/(64\ h_0^{-1}\,\mathrm{Mpc})$ corresponds to the first-order soundwave. We use the ICs provided by Hopkins (2015), with a resolution of 32^3 particles. After the linear growth, an accretion shock forms close to the center. As the scale factor increases, the background density decreases strongly and the background temperature decreases adiabatically. This causes a huge temperature contrast of ≈ 10 orders of magnitude between the shocked region and the background. Due to the very low internal energy compared to other energy contributions $U \lesssim 10^{-3} E_{\mathrm{kin}}$ and $U \lesssim 10^{-2} E_{\mathrm{pot}}$ in physical units, the evolution can be strongly dominated by numerical errors. Thus, the implementation of the energy-entropy switch described in Sec. 3.7.2 is important. The precise limits, when the switch is supposed to be active, are related to the

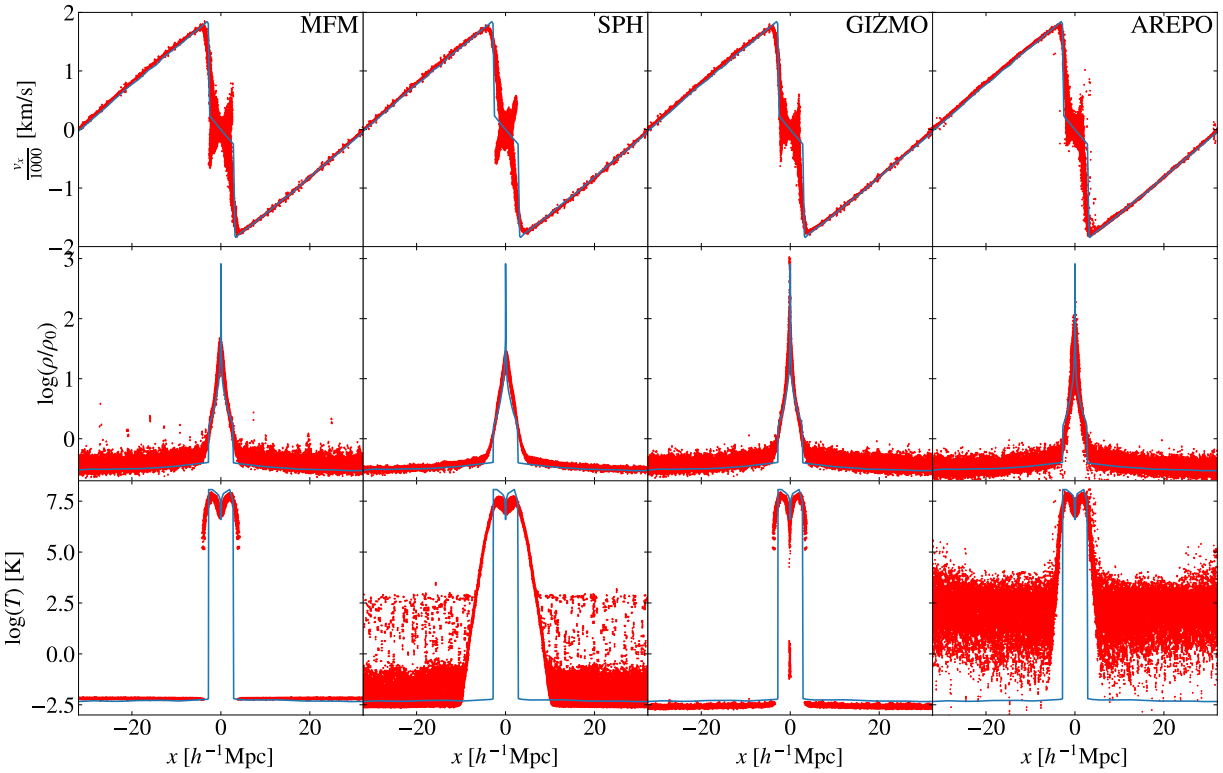

Figure 5.15: Zeldovich pancake at $z = 0$ for different hydro-methods. As a comparison, a high resolution 1d simulation of Hopkins (2015) is shown. While velocity and density profiles agree between the methods, strong deviations can be seen for the temperature profile. MFM performs best due to the energy-entropy switch employed.

numerical accuracy and details of the implementation such as the precision of the Riemann solver. The effect of the limits chosen on the evolution of the Zeldovich pancake is described further in Sec. 5.2.8.

The resulting structure at $z = 0$ is shown in Fig. 5.15. Again, we compare the performance of the different hydro-methods. The energy-entropy switch is included for MFM in OpenGadget3 if $U < 0.01 E_{\mathrm{pot}}$, corresponding also to the value implemented in GIZMO. For Arepo, we had to use additional mesh regularization to avoid too irregular cell shapes in the highly anisotropically compressed shock region and allow the code to run until the end. All methods agree with the peculiar velocity profile with only slight differences. Compared to Hopkins (2015) we find that all methods seem to have a too low viscosity and show particle over- or under-shooting compared to the predicted velocity profile, as a result of a punch-through of some particles in the high $\mathcal{M}$ shock. One difference between the methods is the height of the density peak. This is the lowest for SPH, which can be explained by the larger kernel for SPH, leading to stronger smoothing, compared to MFM. Thus, MFM in OpenGadget3 is able to resolve the central region better and has a slightly higher peak. The Arepo run shows an even higher peak, contrarily to what Hopkins (2015) found. Compared to the expected profile, all these methods over-smooth the

central region. The GIZMO code captures the density profile best, reaching the highest central peak. Most difficult for all methods is to capture the temperature structure with its very strong contrasts. Both MFM implementations work very well, as the energy-entropy switch suppresses any numerical noise in the low-energy background and allows a clear jump between shocked and unshocked regions. Slight differences in the implementation of the energy-entropy switch between OPENGADGET3 and GIZMO, as well as a lower temperature in the central region in general result in more particles in the center being treated with the switch for GIZMO, resulting in a larger number of cold particles. This difference can also explain the different heights of the density peak. As we will show in Sec. 5.2.8, a less aggressive switch will result in a higher density peak. As no analytical solution exists for this test, is it unclear if this behavior is wanted. The jump for SPH is more strongly smoothed in comparison to the other methods. In addition, amplified initial (numerical) noise causes a large scatter of several orders of magnitude in the very cold background. For AREPO, we find that this behavior is much more drastic, and the background is dominated entirely by numerical noise. To properly resolve it, some energy-entropy switch would be required also in AREPO, which does not seem to be implemented in the public version.

Nifty Cluster

Finally, we apply our newly implemented method to more complex, cosmological cases. As an example, we re-simulate a cluster from the MUSIC-2 sample (Prada et al., 2012; Sembolini et al., 2013, 2014; Biffi et al., 2014), analyzed in detail with different codes by a collaboration formed during a nifty workshop (Sembolini et al., 2016), thus called nifty cluster in the following. The cluster has a mass $M_{200c} = 10^{15}$ $M_\odot$ with resolution $m_{DM} = 9.01 \cdot 10^8 h^{-1} M_\odot$ for DM and $m_{gas} = 1.9 \cdot 10^8 h^{-1} M_\odot$ for gas particles. The background cosmology has parameters $\Omega_M = 0.27, \Omega_b = 0.0469, \Omega_\Lambda = 0.73, \sigma_8 = 0.82, n = 0.95, h = 0.7$ (Komatsu et al., 2011). The projected surface density at $z = 0$ is shown in Fig. 5.16, where the cluster center and virial radius are obtained using SUBFIND (Springel et al., 2001; Dolag et al., 2009).

We compare MFM to SPH with a different amount of artificial conductivity, ranging from the usually used amount $\alpha_{max} = 0.25$, $\alpha_{min} = 0$ (notation following Price, 2008) over a run with physical conductivity at $1/20^{th}$ of the Spitzer value (Dolag et al., 2004), effectively corresponding to an intermediate amount, to more traditional SPH without artificial conductivity. The usual amount is chosen to mimic the behavior of Godunov methods such as MFM, which have intrinsic numerical diffusivity due to the Riemann solver and thus allow for more mixing. The structure looks very similar between MFM and SPH with standard settings. This will change, however, for different values for artificial conductivity. For reduced artificial conductivity, structures are slightly less "smeared out", while the global structure does not change.

A more quantitative analysis can be done using gas radial density, temperature, and entropy profiles shown in Fig. 5.17. As a comparison, we provide lines from the nifty paper, obtained using AREPO and GADGET3-MUSIC as an example of a more traditional SPH code, which mark the range of solutions obtained. SPH can span the whole range of possible solutions provided by Sembolini et al. (2016). By construction, traditional SPH without artificial conductivity has no mixing and thus forms low entropy cores. Subgrid mixing due to the Riemann solver for MFM and AREPO leads to mixing into the core, increasing the entropy compared to traditional SPH.

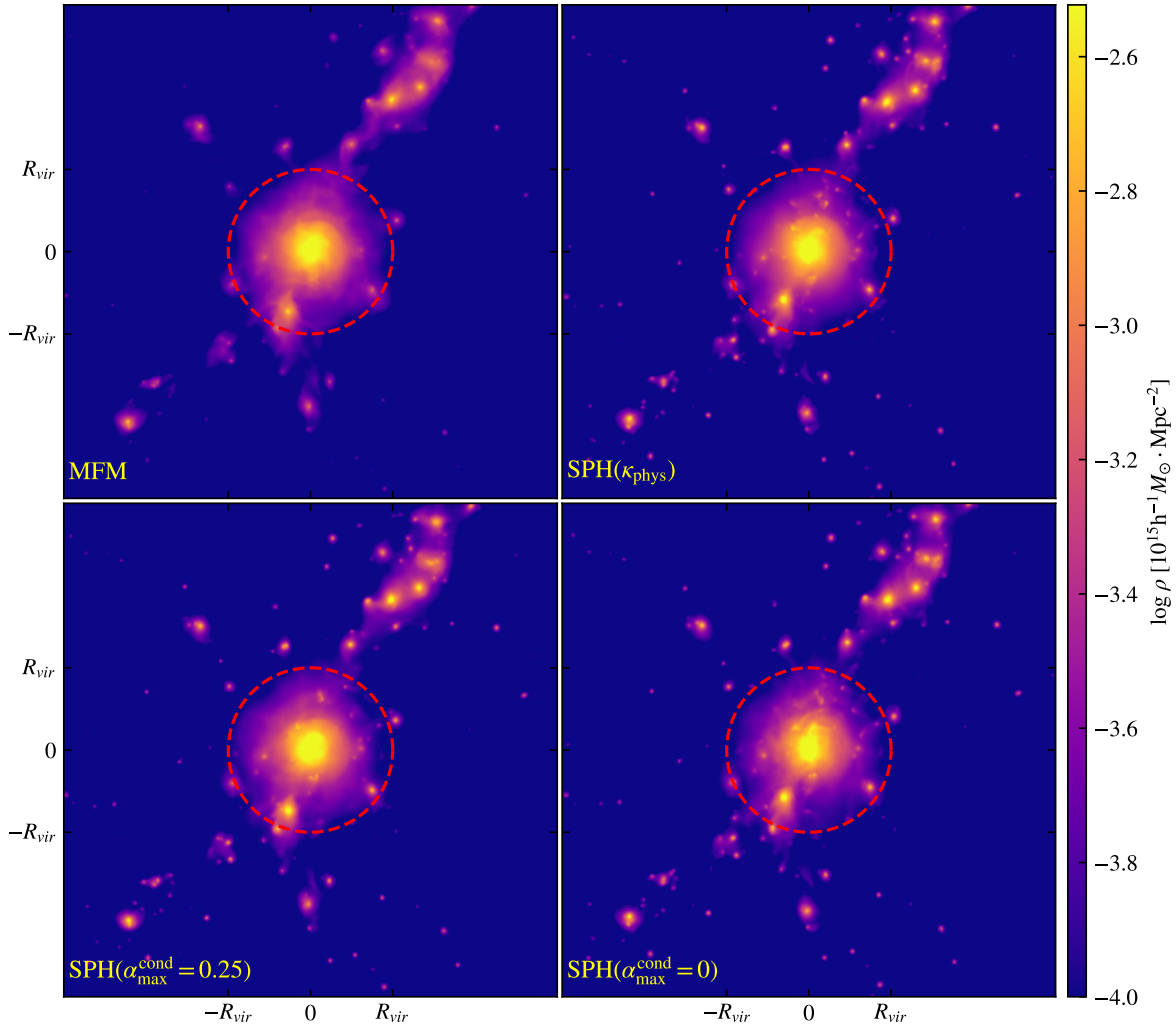

Figure 5.16: Projected surface density of the nifty cluster at $z = 0$, comparison between MFM and SPH with usual amount ($\alpha^{\mathrm{cond}}_{\mathrm{max}} = 0.25$), physical ($\kappa_{\mathrm{phys}}$), corresponding to an intermediate amount, and without artificial conductivity $\alpha^{\mathrm{cond}}_{\mathrm{max}} = 0$. The overall structure is very similar. Small sub-structures, however, appear less compact for MFM.

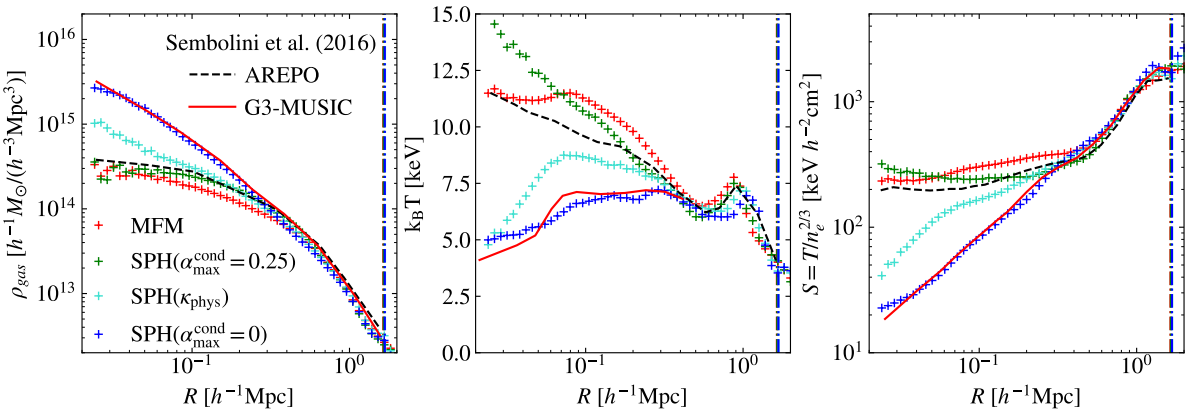

Figure 5.17: Gas density (left), temperature (middle), and entropy (right) radial profiles of the nifty cluster at $z = 0$, comparison between different hydro methods, including our MFM implementation (red plus), SPH in OpenGadget with usual (green), physical, corresponding to an intermediate value, (turquoise) and without artificial conductivity (blue). As a comparison, the Arepo (black dashed) and G3-MUSIC (traditional) SPH line (red solid) from Sembolini et al. (2016) are shown. The vertical line marks R_{200}. Our modern SPH run with sufficiently high artificial conductivity, as well as Arepo and MFM produce higher entropy cores with lower, less peaked density, while the central entropy is much lower for SPH with lower artificial conductivity.

Thus, the central density is reduced. By including artificial conductivity in SPH, it can reach the same profile as MFM, and also lie in between for effectively intermediate values by using physical conductivity.

5.2.6 Decaying Subsonic Turbulence

In many astrophysical systems, ranging from the atmosphere over the ISM up to GCs, turbulence plays a crucial role. In the ICM, we expect subsonic turbulence with a turbulent energy fraction of $X \approx 0.1$ to be excited, for instance after a merger (compare, e.g. Schuecker et al., 2004; Subramanian et al., 2006). The different hydro-schemes have problems to capture its full behavior. It has been shown that traditional SPH is not well suited to calculate sub-sonic turbulence (Bauer & Springel, 2012), but can be improved using modern SPH with more ideal settings for artificial diffusion terms (Price, 2012a). While grid-based methods produce better results, difficulties still remain for the evolution of turbulence within GCs.

To test and compare the performance of our MFM implementation, we set up a 300 kpc cubic box with varying number of particles, and seed the largest ≈ 70 modes, similar to Bauer & Springel (2012). Due to the low initial density of $\rho \approx 1.5 \cdot 10^{-6}$, gravitational acceleration can be neglected. The initial turbulent energy fraction is varied between $X_i = E_{{\rm turb},i}/E_{{\rm therm},i} = 0.3$, corresponding to a Mach number $\mathcal{M}_i \approx 0.7$ and $X_i = 0.00001$ corresponding to $\mathcal{M}_i \approx 0.004$. In addition, the resolution is varied, ranging from 64^3 up to 256^3 particles. We evolve the turbulence for 1.5 sound-crossing-times. The turbulent kinetic energy cascades down to smaller scales, forming a turbulent power spectrum. In order to analyze the velocity power spectrum, the data

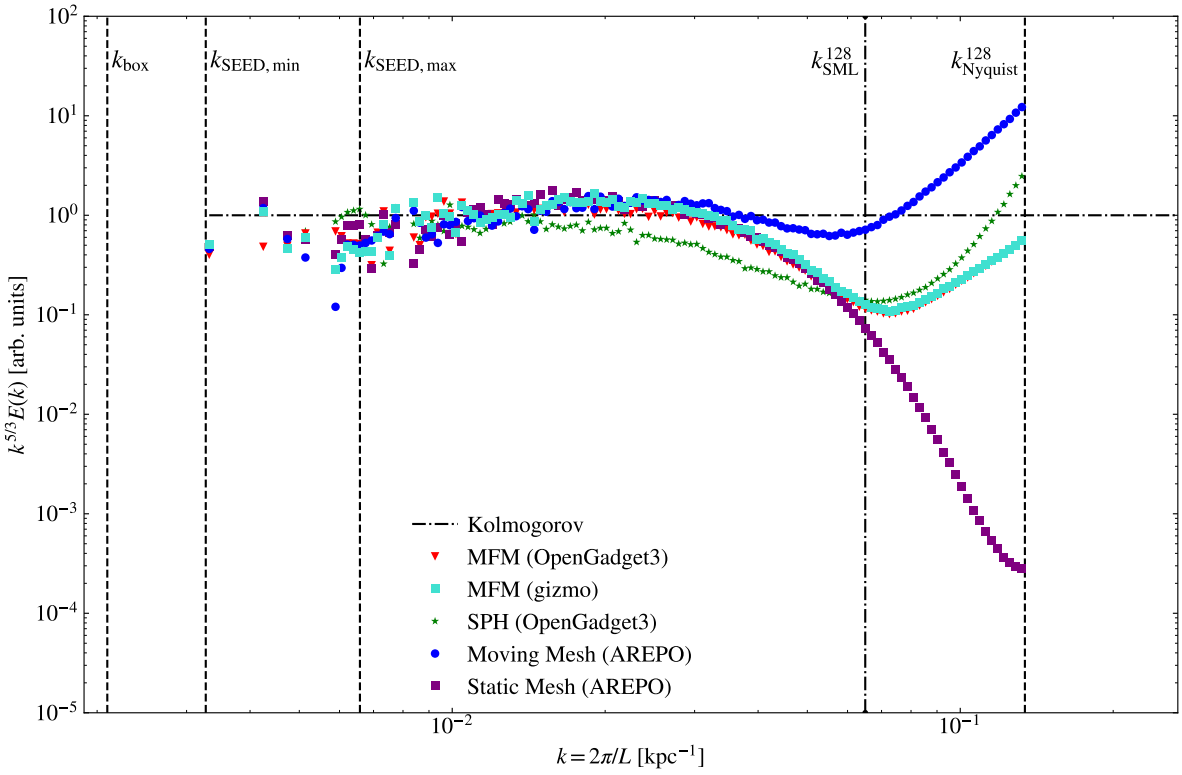

Figure 5.18: Normalized turbulent velocity power spectrum for different methods at $X_i = 0.3$ and resolution 128^3. All methods agree at large scales, but show a lack in energy at intermediate to small scales compared to the expected Kolmogorov-slope $P \sim k^{-5/3}$. Overall, all methods work very well reproducing the expected spectrum.

are binned to a grid using the code Sph2Grid[5]. From that, a power spectrum is calculated. We use a D20 sampling, to conserve energy (Cui et al., 2008). Theoretically, a Kolmogorov slope $E(k) \sim k^{-5/3}$ would be expected (Kolmogorov, 1941). In Fig. 5.18, we compare the power spectra of the different methods, normalized by the expected slope. The wavenumber k_{box} corresponds to a wavelength of the box size. Energy is seeded between $k_{\mathrm{SEED,max}}$ and $k_{\mathrm{SEED,min}}$. An estimate for the resolution limit is provided by k^{128}_{SML}, corresponding to the mean smoothing length for a Wendland C6 kernel at resolution 128^3 in plots where an SPH run is included, otherwise to the mean smoothing length for a cubic spline kernel at resolution 128^3, and $k^{128}_{\mathrm{Nyquist}}$ denoting wavenumber of the initial grid-spacing and thus the smallest length to be possibly resolved.

In contrast to many previous findings (compare, e.g., Padoan et al., 2007; Bauer & Springel, 2012; Hopkins, 2015), all methods are able to reproduce the expected Kolmogorov slope very well for such a mildly subsonic turbulence. SPH shows the strongest deviation, occurring already at intermediate scales, while for MFM in both implementations and also Arepo with moving and stationary mesh differences are present only at very small scales, approaching the resolution

[5]Developed by J. Donnert, available at `https://github.com/jdonnert/Sph2Grid`

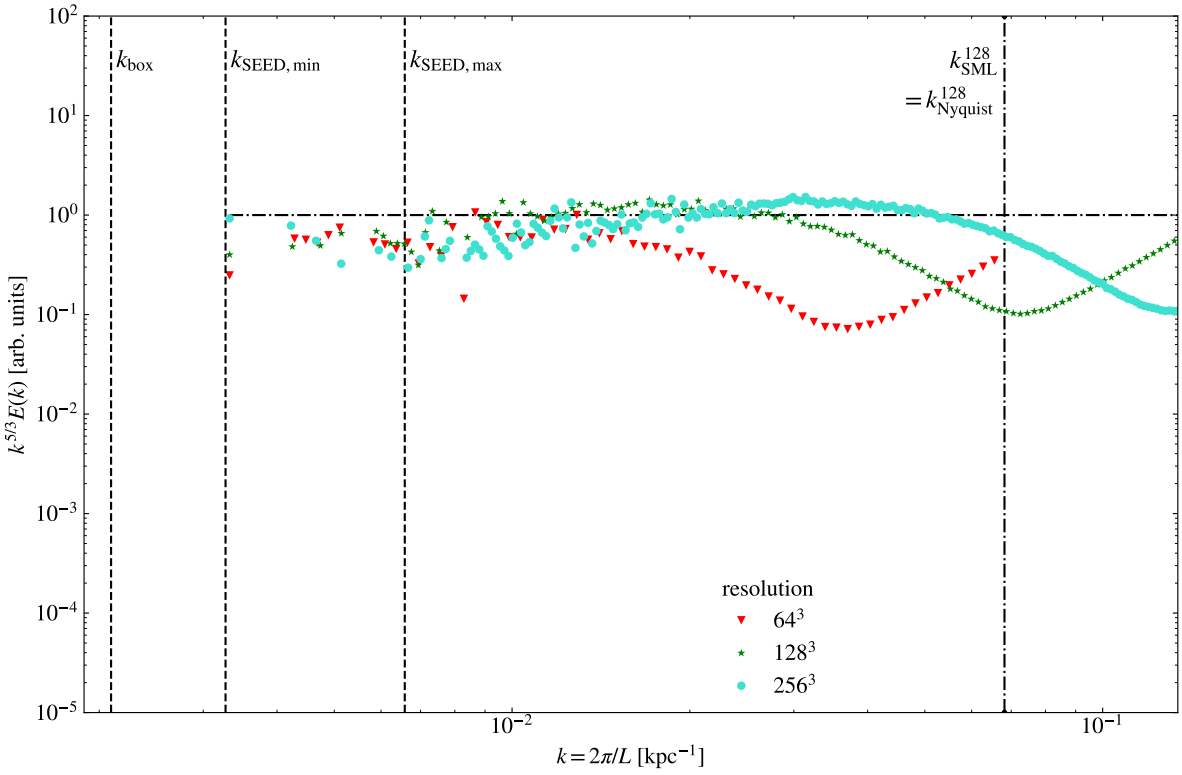

Figure 5.19: Normalized turbulent velocity power spectrum for MFM with different resolutions at $X_i = 0.3$. MFM converges fast with resolution towards the expected Kolmogorov-slope $P \sim k^{-5/3}$.

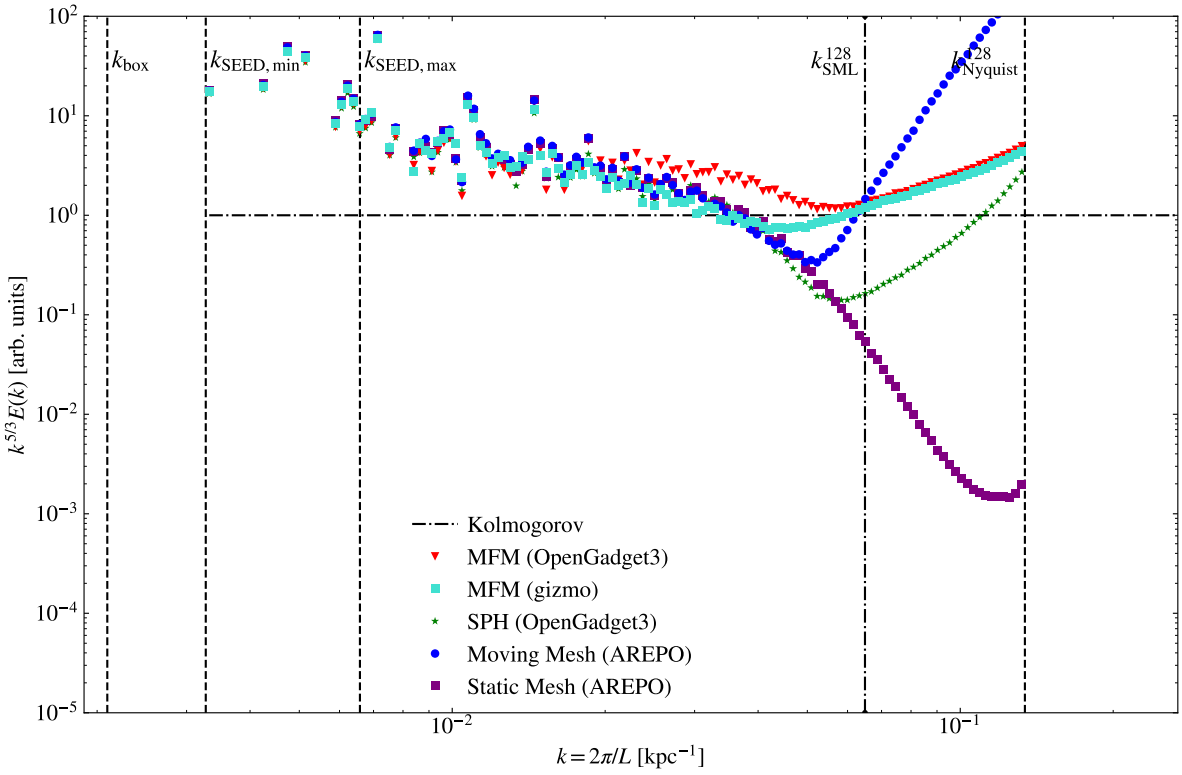

Figure 5.20: Normalized turbulent velocity power spectrum for different methods at $X_i = 0.01$ and resolution 128^3. At such low initial turbulent energy fraction, differences between the methods become more visible, where MFM works best overall reproducing the expected spectrum.

limit.

In addition, the MFM result converges quickly with resolution, shown in Fig. 5.19. As the dip moves towards smaller scales, the overall spectrum becomes even closer to the Kolmogorov one over a wider range of scales. At the highest resolution considered, it almost perfectly resembles the expected Kolmogorov slope over almost one order of magnitude of scales.

For even lower initial turbulent energy fractions, corresponding to even lower Mach numbers, more differences between the methods become visible. In Fig. 5.20, we show the resulting spectrum for an initial turbulent energy fraction of 0.01, corresponding to $\mathcal{M}_i \approx 0.1$. While all methods agree at large scales, where the energy was seeded, they show huge discrepancies at intermediate to small scales. Arepo shows deviations at the smallest scales compared to the other methods, underestimating the energy present at scales close to the resolution limit. SPH starts deviating at slightly larger scales, with a less deep dip in the power spectrum. For MFM the power spectrum shows a dip in energy at similar scales as the moving mesh code Arepo, but with a much shallower depth than in all other cases, thus being closer to the expected slope. Differences between the two MFM implementations can be attributed to different Riemann solvers used. Overall, advantages of MFM become clear for such very subsonic turbulence.

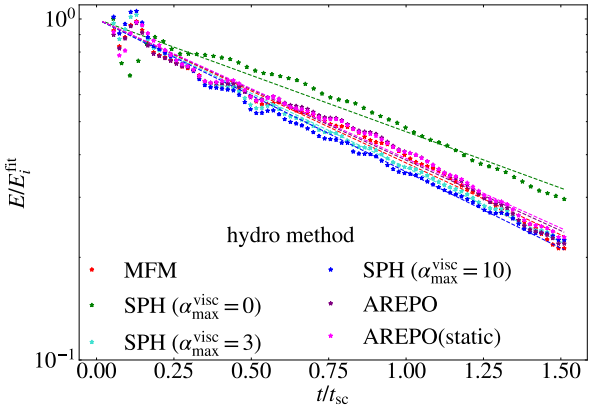

Figure 5.21: Decay time of turbulent energy for different methods at $X_i = 0.3$. For SPH, the viscosity is varied between $\alpha_{\rm max}^{\rm visc} = 10$ and $\alpha_{\rm max}^{\rm visc} = 0$, where $\alpha_{\rm max}^{\rm visc} = 3$ is the value typically used (notation following Beck et al., 2016b). Arepo has the highest decay time corresponding to the lowest numerical dissipation, while MFM and SPH at typical value of viscosity are on a similar order with a decay time of a few dynamical timescales.

While the power spectrum builds up, energy is not only transported to smaller scales, but also partly converted into internal energy. We plot this decay of kinetic, turbulent energy, here labeled with E, in Fig. 5.21, comparing the different hydro-methods. In order to better compare the slopes independent of initial turbulent energy fraction, we fit an exponential decay for each run and normalize by $E_i^{\rm fit} = E^{\rm fit}(t = 0)$. While in a physical situation the decay would depend on gas microphysics such as its viscosity, here we can use it to get an insight into the code behavior. The decay is mainly determined by numerical dissipation. In all cases, the energy shows a periodic variation, caused by the "ringing" of the initially seeded modes. The decay for SPH depends mildly on the artificial viscosity especially visible for the run excluding it. The power spectrum, in contrast, is only weakly influenced by the amount of artificial viscosity. In practical applications, it is tuned to a value of $\alpha_{\rm max}^{\rm visc} = 3$, which leads to a similar decay rate as the other methods. The exponential decay time $t_{\rm dec}$ roughly corresponds to the sound crossing time $t_{\rm sc} = L_{\rm box}/c_s$.

A comparison for the decay at different initial turbulent energy fractions, corresponding to variations in the Mach number, is shown in Fig. 5.22 for MFM and SPH. The variation between 0.3 and 0.00001 for the initial turbulent energy fraction corresponds to a range of Mach numbers from 0.7 down to below 0.004. For SPH the decay is decreasing with initial turbulent energy fraction down to $X_i = 0.01$ ($\mathcal{M} \approx 0.1$), and stays independent of the Mach number afterwards, as one would expect, so it is for Arepo. For MFM, the same initial trend can be observed. For very low initial turbulent energy fraction $X_i < 0.0001$ ($\mathcal{M} \lesssim 0.01$), however, an unphysical increase of turbulent energy occurs. At the same point also the density pdf deviates from the Gaussian shape together with the velocity power spectrum becoming strongly non-Kolmogorov, indicating the evolution is dominated by numerical artifacts for such low Mach numbers. Specifically, while we find that for this test total energy is conserved the internal energy only accounts for a small fraction, such that even evolving internal energy instead of total energy will be dominated by numerical errors. Applying an energy entropy switch could in principle alleviate this problem.

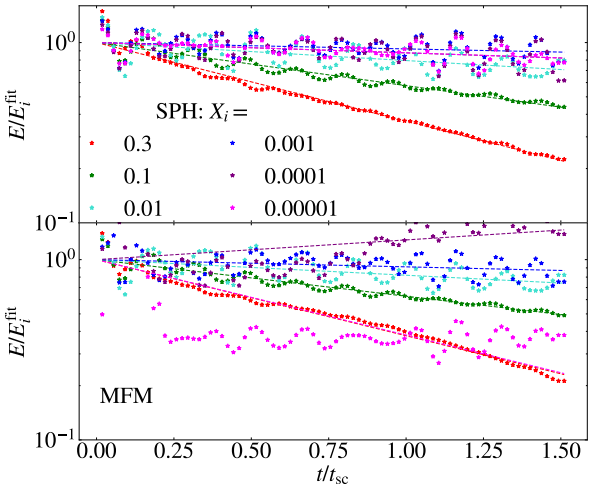

Figure 5.22: As Fig. 5.21, but for varying initial turbulent energy fractions X_i, corresponding to variations in the turbulent Mach number. The decay is consistent for all X_i for SPH, and down to $X_i = 0.003$ for MFM, when numerical artifacts lead to an unphysical increase in energy.

On the other hand, it would be unclear if this would remove other advantages for MFM in this test problem.

5.2.7 Runtime Analysis

The precise difference in wallclock runtime between MFM and SPH depends on the problem that is considered, as this can include different additional physics and might trigger different timestep-limiters. Therefore, we provide an overview of all runtimes for the tests that we have run, including the MPI and OpenMP configuration in Tab. 5.1. Overall, the computational costs for running MFM are comparable to those of SPH. For pure hydrodynamical problems the number of timesteps required increases together with the effective spatial resolution by a factor of $\lesssim 2$. It can be even larger for strong shocks due to the more strict timestep limiting at higher spatial resolution. The CPU time required per timestep is very similar between the methods. While the Riemann solver is more expensive than the calculation of hydrodynamical accelerations for SPH, and also additional neighbor loops are required for MFM, the lower neighbor number leads to a decrease in computational costs. Depending on the problem, the time required per timestep can be smaller or larger than the time required for the SPH comparison run. In combination, these effects on average lead to slightly larger total runtimes by a factor of ≈ 2 for MFM.

If gravity is included, the simulation timestep is dominated by the gravitational interactions in many cases, such that a similar number of timesteps is required, independent of the hydro-method. Also the time spent per timestep becomes even more similar, as the computation of gravitational interaction, which are calculated in the same way for MFM and SPH, are contributing as well.

If even more modules are activated, such as SUBFIND, as it is done for the nifty cluster, the runtime is mainly determined by the precise evolution. For the nifty cluster we found a slight

test	MPI	OpenMP	runtime [s]		time per timestep [s]		#steps	
			MFM	SPH	MFM	SPH	MFM	SPH
soundwave (res 128)	4	14	$4.3 \cdot 10^4$	$3.2 \cdot 10^4$	$5.3 \cdot 10^0$	$7.9 \cdot 10^0$	$8.1 \cdot 10^3$	$4.1 \cdot 10^3$
kepler disk	4	14	$4.1 \cdot 10^5$	$5.4 \cdot 10^5$	$8.1 \cdot 10^0$	$8.0 \cdot 10^0$	$5.1 \cdot 10^4$	$6.8 \cdot 10^4$
Rayleigh-Taylor instability	4	14	$8.4 \cdot 10^3$	$3.4 \cdot 10^3$	$2.6 \cdot 10^{-1}$	$1.1 \cdot 10^{-1}$	$3.2 \cdot 10^4$	$3.0 \cdot 10^4$
Kelvin-Helmholtz instability	8	12	$6.7 \cdot 10^5$	$2.9 \cdot 10^5$	$1.0 \cdot 10^1$	$8.8 \cdot 10^0$	$6.5 \cdot 10^4$	$3.2 \cdot 10^4$
Hydrostatic Square	4	14	$1.9 \cdot 10^2$	$7.1 \cdot 10^1$	$2.3 \cdot 10^{-2}$	$1.6 \cdot 10^{-2}$	$8.2 \cdot 10^3$	$4.2 \cdot 10^3$
blob test	8	12	$2.5 \cdot 10^6$	$1.5 \cdot 10^6$	$1.3 \cdot 10^2$	$1.4 \cdot 10^2$	$1.9 \cdot 10^4$	$1.1 \cdot 10^4$
shock tube ($\mathcal{M} = 10$)	4	14	$8.9 \cdot 10^3$	$1.7 \cdot 10^3$	$1.1 \cdot 10^0$	$7.7 \cdot 10^{-1}$	$8.2 \cdot 10^3$	$2.1 \cdot 10^3$
Sedov blast	4	14	$1.1 \cdot 10^2$	$1.9 \cdot 10^2$	$2.1 \cdot 10^{-1}$	$2.5 \cdot 10^{-1}$	$5.3 \cdot 10^2$	$7.8 \cdot 10^2$
gravitational freefall	4	14	$1.3 \cdot 10^1$	$1.7 \cdot 10^1$	$5.1 \cdot 10^{-2}$	$6.6 \cdot 10^{-2}$	$2.6 \cdot 10^2$	$2.7 \cdot 10^2$
hydrostatic sphere	4	14	$1.3 \cdot 10^4$	$1.9 \cdot 10^4$	$8.2 \cdot 10^{-1}$	$1.2 \cdot 10^0$	$1.6 \cdot 10^4$	$1.6 \cdot 10^4$
Zeldovich pancake	4	14	$1.6 \cdot 10^3$	$2.5 \cdot 10^3$	$1.1 \cdot 10^0$	$1.6 \cdot 10^0$	$1.5 \cdot 10^3$	$1.5 \cdot 10^3$
nifty cluster	16	28	$2.6 \cdot 10^4$	$2.3 \cdot 10^4$	$1.7 \cdot 10^0$	$1.4 \cdot 10^0$	$1.5 \cdot 10^4$	$1.6 \cdot 10^4$
turbulence (resolution 128)	8	12	$1.2 \cdot 10^5$	$4.9 \cdot 10^4$	$2.4 \cdot 10^1$	$1.6 \cdot 10^1$	$5.1 \cdot 10^3$	$3.1 \cdot 10^3$

Table 5.1: Comparison of the runtime between MFM and SPH in OpenGadget3. Different test are run with different MPI and OpenMPI configurations and also on different machines. In general, we observe an increase in runtime between MFM and SPH, varying between a factor of ≈ 2 for pure hydrodynamical tests to only a factor of 1.1 for the nifty cluster.

increase in runtime for MFM, but it can be different for other objects simulated. If even more physics was turned on, we expect differences to become even smaller.

Memory requirements are mainly defined by the size of the particle structures. As MFM holds more variables in the gas particle structure, it is larger by a factor of ≈ 2 compared to SPH. It could be improved by making more efficient use of existing SPH data and avoiding duplication which are currently still present. The total memory requirement is thus larger by a factor of $\approx 1.3 - 2$ for pure hydro problems and ≈ 1.5 for the nifty cluster. Including more physics, the difference would become negligible.

5.2.8 Effects of Numerical Parameters

The performance of the numerical methods strongly depends on the precise parameters used. Effects of neighbor number and kernel have already been analyzed in detail by various authors (compare, e.g., Dehnen & Aly, 2012; Tricco & Price, 2013; Hu et al., 2014) for SPH. To this end, we focus on two other parameters that play a major role for MFM, namely the slope-limiting scheme and the energy-entropy-switch.

Slope-Limiter

The different slope-limiting procedures, which are implemented in our code, differ not only in how aggressively they limit the slope, but also in how much numerical diffusivity they introduce. In general, different limiters are shown to produce different results for specific test-cases (com-

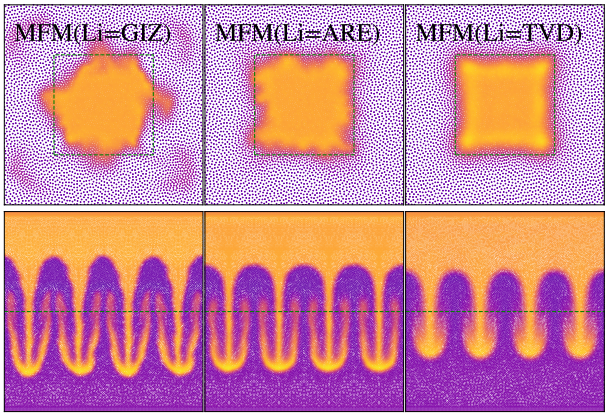

Figure 5.23: Hydrostatic square (top) and Rayleigh-Taylor instability (bottom), developed using different slope-limiters, the GIZMO limiter we usually use (left), compared to the same test, but evolved using the AREPO limiter (middle) and TVD limiter (right). Depending on the test, different slope-limiters could be preferred.

pare e.g. Barth & Jespersen, 1989; Balsara, 2004; May & Berger, 2013; Hubber et al., 2018; Alonso Asensio et al., 2023).

In the following, we compare the three cases of the limiter from GIZMO as described by Eqn. (5.14) in combination with their pariwise limiter (Eqn. (5.18/5.19)), that we usually use, the AREPO (Eqn. (5.13)) and, the TVD limiter (Eqn. (5.11)). The GIZMO and TVD limiters are the most extreme cases of the limiters implemented, with lowest and highest numerical diffusivity, respectively. The AREPO limiter lies in between. We analyze the effect on the hydrostatic square (compare also Sec. 5.2.3) and the Rayleigh-Taylor instability (Sec. 5.2.3). The results are shown in Fig. 5.23.

While for the Rayleigh-Taylor instability the much less diffusive GIZMO limiter performs best, evolving a much finer structure, this causes the strongest deformation of the hydrostatic square. The AREPO limiter is slightly more diffusive, leading to less strong secondary instabilities for the Rayleigh-Taylor instability and slightly less deformation of the square, especially at the edges. The TVD limiter has an even higher numerical diffusivity, thus strongly smooths the Rayleigh-Taylor instability, not only preventing secondary instabilities from forming, but also noticeably reducing the overall growth of the instability. The hydrostatic square, however, is preserved best, due to lower surface-tension-like errors, which also manifest in the presence of absence of the pressure-blib for shocks.

Combining the results, we show that it is not always clear which slope-limiting procedure would be the overall preferred choice. As in most cases the GIZMO limiter performs best, we chose this as our reference method.

Energy-Entropy-Switch

To avoid numerical errors to dominate the evolution of the internal energy, an energy-entropy switch as described in Sec. 3.7.2 has to be used in specific problems such as the Zeldovich

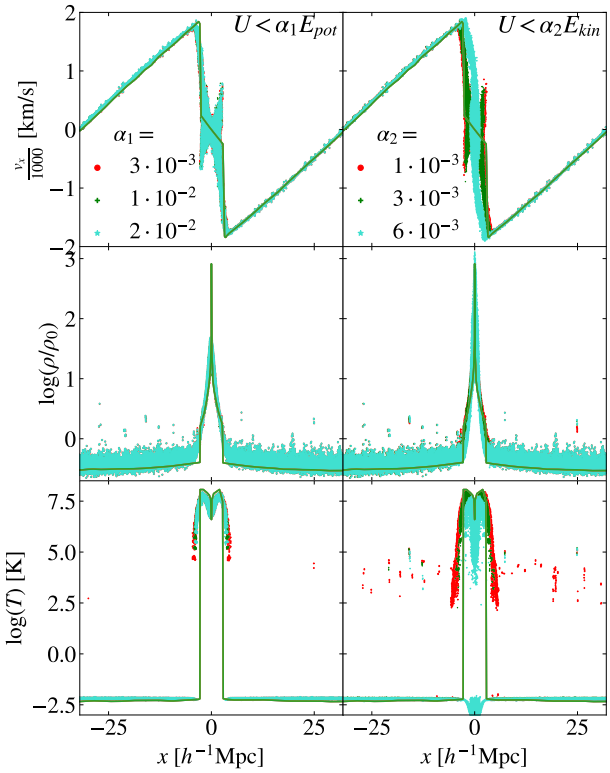

Figure 5.24: Effect of the choice of the energy-entropy switch on the Zeldovich pancake. Comparison between the switch based on kinetic and potential energy, each with three different α-values. The switch based on potential energy is much more stable.

pancake. Especially, the numerical noise should be suppressed in the very cold, unshocked region, while the shock should not be influenced at all.

The resulting structure at $z = 0$, comparing different possibilities for the switch based on potential and kinetic energy estimates (compare also Eqn. (3.44)), is shown in Fig. 5.24. We increase the tuned values ($\alpha_1 = 10^{-2}$ for the potential energy and $\alpha_2 = 3 \cdot 10^{-3}$ for kinetic energy) by a factor 2 and decrease them by a factor ≈ 3.

A more strict switch (larger α) causes less particles to be treated with the adiabatic approximation. For the kinetic energy switch, this difference causes strong variations in the temperature profiles. While for $\alpha_2 = 1 \cdot 10^{-3}$ more extended wings form and some scatter in the low-temperature background close to the peak appears, the increased value of $6 \cdot 10^{-3}$ treats even particles inside the peaked region with the adiabatic approximation and causes too low temperatures. A very fine-tuned choice of α_2 is necessary to accurately capture all particles, both the shocked ones and the low-temperature ones.

Compared to that, a variation of α_1 within the switch based on potential energy influences the temperature profile only weakly. It seems to be much more stable and should be the preferred option. We thus used $\alpha_1 = 10^{-2}$ and $\alpha_2 = 0$ for the calculations in Sec. 5.2.5.

5.3 Slope-Limiters in OpenGadget3

We implemented seven different slope-limiters and therein variants of their specific parameters in OpenGadget3. The main concept is described in Sec. 5.2.8. In general, we substitute $\nabla W_{i,k} \rightarrow \alpha_{i,k} \nabla W_{i,k}$ for each particle i and component k, when performing the face interpolation, with $\alpha_{i,k} \in [0, 1]$. In the following, we briefly describe the implemented limiters.

The simplest option is to use a zeroth order interpolation setting

$$\alpha_{i,k}^{\text{ZERO SLOPES}} = 0 \tag{5.9}$$

or to include no slope-limiter

$$\alpha_{i,k}^{\text{NULL}} = 1. \tag{5.10}$$

Alternatively, we implemented several more complex limiters. A commonly used one is a TVD scalar limiter (Duffell & MacFadyen, 2011), which is designed to produce good results especially for strong shocks. Compared to the other limiters implemented, it is the most diffusive one. It sets

$$\alpha_{i,k}^{\text{TVD SCALAR}} = \min_{j \in \text{Ngb}} \max \begin{cases} 0 \\ \min \begin{cases} 1 \\ \Delta W_{ij,k} / \mathrm{d}W_{ij,k} \end{cases} \end{cases} \tag{5.11}$$

where $\Delta \boldsymbol{W}_{ij} = \boldsymbol{W}_j - \boldsymbol{W}_i$, $\mathrm{d}\boldsymbol{W}_{ij} = \mathrm{d}\boldsymbol{r}_{ij} \cdot \nabla \otimes \boldsymbol{W}$.

An alternative is the scalar limiter which is a modified version of the Balsara (2004); Gaburov & Nitadori (2011) limiter, with relaxed constraints, as presented in the GANDALF code (Hubber et al., 2018). It looses the TVD behavior but is less diffusive. Only the extreme values are used over the neighbors in the numerator, and the maximum possible values to be reconstructed in the denominator, thus avoiding an additional neighbor loop, leading to the limiter

$$\alpha_{i,k}^{\text{SCALAR}} = \max \begin{cases} 0 \\ \min \begin{cases} 1 \\ \min \begin{cases} \frac{\Delta W_{i\,\max,k}}{|\mathrm{d}r|_{\max} |\nabla W_k|} \\ \frac{\Delta W_{i\,\min,k}}{|\mathrm{d}r|_{\max} |\nabla W_k|} \end{cases} \end{cases} \end{cases} \tag{5.12}$$

where $\Delta W_{i\,\min/\max,k} = \left| W_{i,k} - \min/\max_{j \in \text{Ngb}} W_{j,k} \right|$, and $|\mathrm{d}r|_{\max} = \max\left(\max_{j \in \text{Ngb}} \left|r_{ij}\right|, h_i\right)$. In contrast to the TVD limiter, only the global neighbor distribution is considered. Thus, values calculated from all neighbors individually for the TVD limiter are calculated in an approximate way. Finally, we implemented the limiters used both in the Arepo and gizmo code. In the Arepo code (Springel, 2010), the slope is limited using the Barth & Jespersen (1989) limiter

$$\alpha_{i,k}^{\text{Arepo}} = \min_{j \in \text{Ngb}} \begin{cases} \Delta W_{i\,\max,k} / \mathrm{d}W_{ij,k} & \text{if } \mathrm{d}W_{ij,k} > 0 \\ \Delta W_{i\,\min,k} / \mathrm{d}W_{ij,k} & \text{if } \mathrm{d}W_{ij,k} < 0 \\ 1 & \text{if } \mathrm{d}W_{ij,k} = 0. \end{cases} \tag{5.13}$$

It lies in between the TVD and scalar limiter, as only the dividend is approximated from the global neighbor distribution, while the divisor is still calculated for all neighbors individually.

In GIZMO (Hopkins, 2015) a general limiter is introduced described by

$$\alpha_{i,k}^{\text{GIZMO}} = \min \begin{cases} 1 \\ \beta_i \min \begin{cases} \frac{\mathrm{d}W_{i\,\max,k}}{0.5 h_i |\nabla W_k|} \\ \frac{\mathrm{d}W_{i\,\min,k}}{0.5 h_i |\nabla W_k|}. \end{cases} \end{cases} \tag{5.14}$$

Also this limiter has the advantage of avoiding an additional neighbor loop. The parameter β_i has to be $\beta_i > 0.5$ to ensure second order stability. A higher number corresponds to a more aggressive, less diffusive, and less stable limiter. We use the suggested value $\beta = 2$ of Hopkins (2015), which is a compromise to reduce numerical diffusivity while still working for very strong interacting shocks. While they suggest this value to be used only for particle distributions being isotropic enough based on the condition number, we use this value always as we found hardly any differences. For $\beta = 2$, this limiter is also similar to the scalar limiter with the difference that the theoretically possible distance between neighbors is defined only by the smoothing length. In addition, Hopkins (2015) provide a pairwise limiter, acting on only one specific interaction, instead of all neighbors. For this, it uses already limited slopes for the interpolation. The pairwise limiter described by Hopkins (2015) limits the already interpolated face values. The aim is to directly calculate the face value $W_{ij,k}^{\text{new}}$, starting from the extrapolated value $W_{ij,k}^{\text{frame}}$ according to Eqn. (3.37), possible already with limited gradients. If $W_{i,k} = W_{j,k}$, the face value is just chosen the same as the particle values $W_{ij,k}^{\text{new}} = W_{i,k}$. Otherwise, the values

$$\delta_1 = \psi_1 \left| W_{i,k} - W_{j,k} \right| \tag{5.15}$$

$$\delta_2 = \psi_2 \left| W_{i,k} - W_{j,k} \right| \tag{5.16}$$

are calculated. The free parameters $\psi_{1/2}$ are tuned to $\psi_1 = 0.5$, $\psi_2 = 0.25$. A simple intermediate value used later is given by

$$\bar{W}_{ij,k} = W_{i,k} + \frac{\mathrm{d}r_{ij}}{\mathrm{d}r_i^{\text{frame}}} (W_{j,k} - W_{i,k}). \tag{5.17}$$

The maximum/minimum value is $W_{\min/\max,k} = \min/\max(W_{i,k}, W_{j,k})$. Depending on how the two face values compare, the new face value is calculated: If $W_{i,k} < W_{j,k}$, then

$$W_{ij,k}^{\text{new}} = \max \begin{cases} \begin{cases} W_{\min,k} - \delta_1 & \text{if SIGN}(W_{\min,k} - \delta_1) = \text{SIGN}(W_{\min,k}) \\ \frac{W_{\min,k}}{1 + \frac{\delta_1}{|W_{\min,k}|}} & \text{else} \end{cases} \\ \min \begin{cases} W_{ij,k}^{\text{frame}} \\ \bar{W}_{ij,k} + \delta_2. \end{cases} \end{cases} \tag{5.18}$$

If $W_{i,k} \geq W_{j,k}$, then

$$W_{ij,k}^{\text{new}} = \min \begin{cases} \begin{cases} W_{\max,k} + \delta_1 & \text{if SIGN}(W_{\max,k} + \delta_1) = \text{SIGN}(W_{\max,k}) \\ \frac{W_{\max,k}}{1+\frac{\delta_1}{|W_{\max,k}|}} & \text{else} \end{cases} \\ \max \begin{cases} W_{ij,k}^{\text{frame}} \\ \bar{W}_{ij,k} - \delta_2. \end{cases} \end{cases} \tag{5.19}$$

The same limiter is applied for particle j. Finally, the GIZMO code uses a slightly different pairwise limiter. Depending on the tolerance t chosen as input parameter for the run with a typical value of 1, the parameters

$$\psi_1 = \begin{cases} 0 & t = 0 \\ 0.5 & t = 1 \\ 0.75 & t = 2 \end{cases} \tag{5.20}$$

$$\psi_2 = \begin{cases} 0 & t = 0 \\ 0.4 & t = 1 \\ 0.375 & t = 2 \end{cases} \tag{5.21}$$

are defined. To calculate $\bar{W}_{ij,k}$, the factor $\mathrm{d}r_{ij}/\mathrm{d}r_i^{\text{frame}}$ is approximated by the first order value 0.5. Except these differences, the limiter is identical to the already described one. In our implementation, we apply the limiter in the reference frame of the interface, such that the velocity is a relative velocity. This makes the limiter Lagrangian and increases the symmetry between different directions within symmetric flows such as in the Zeldovich pancake.

5.4 Effect of the Riemann Solver

In OpenGadget3 we use an exact, iterative Riemann solver (Toro, 2009) by default. This is, however, computationally expensive as up to eight iterations are used to get close to the exact solution. An alternative is using approximate Riemann solvers, where we implemented a Roe solver (Roe, 1981), the HLL solver (Toro, 2009), and the HLLC (Toro, 2009) solver.

The strongest effect in runtime is present for strong shocks, where we find a speedup of up to 20 per cent in total. For more smooth problems, where less iterations of the exact solver are necessary, the speedup for the calculation of the fluxes itself is 20 per cent, resulting on an overall speedup of only up to 9 per cent for such problems dominated by hydrodynamical calculations. The effect becomes less important when using gravity and possibly even more extensions in cosmological applications. Already for the hydrostatic sphere, there is no significant difference in runtime, or even a slight increase.

As the Riemann solver introduces numerical diffusivity, the evolution will be different. This can be seen in various test problems, such as the Rayleigh-Taylor instability, shown in Fig. 5.25. While the instability evolved using the exact Riemann solver shows the most prominent secondary

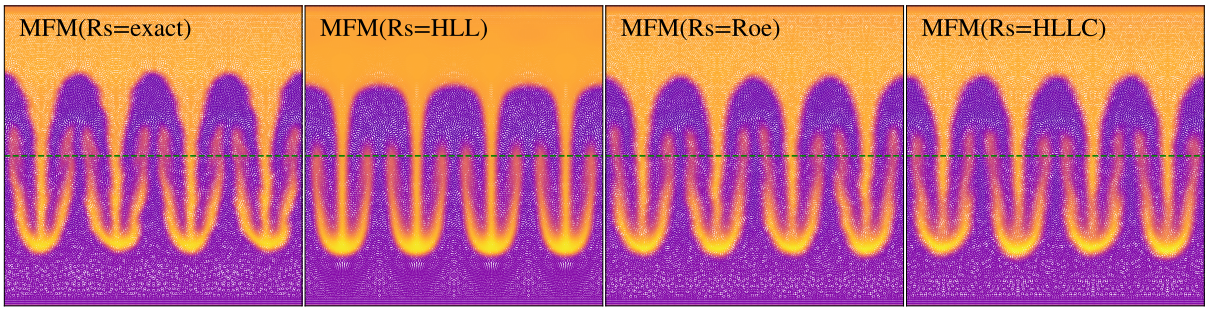

Figure 5.25: Rayleight-Taylor instability at time $t = 3.6$, evolved using different Riemann solvers. Secondary instabilities are more or less pronounced, depending on the solver used.

instabilities, closely followed by the Roe solver and the HLLC solver, the HLL Riemann solver leads to a suppression of any asymmetries in the final shape of the instability. This is a result of the additional numerical diffusivity introduced by the Riemann solver, as discussed in Sec. 5.2.5.

While for specific problems these alternative solvers could lead to faster results, we in general use the most accurate exact Riemann solver. The increase in runtime is compensated by the gain in accuracy.

5.5 Soundwave Convergence with Arepo

As described in Sec. 5.2.2, we would expect Arepo to have better convergence than observed. A first reason is the mesh regularization. If triggered, the positions of the cells are shifted, introducing a small numerical noise. In addition, small interfaces which contribute by less than 10^{-5} to the total interface are neglected. While this makes the code more stable in extreme environments, it introduces small errors (R. Pakmor, 2023, priv. comm.), which will be relevant for the very small deviations analyzed here.

Turning off the mesh regularization and only skipping interfaces which contribute by less than 10^{-8}, Arepo shows much better convergence behavior, close to what is expected from the analysis by Weinberger et al. (2020), as shown in Fig. 5.26. Especially, the scatter error drastically decreases, also making the determination of the other error components more reliable.

While these changes can lead to a better convergence behavior, they will cause other problems in cosmological simulations, such that in physical applications rather the non-optimized behavior would be observed.

5.6 Discussion and Conclusions

We presented a new MFM implementation into OpenGadget3 as an alternative hydro-solver to the currently used modern SPH. We verified its capabilities, both in idealized and more complex, cosmological test cases. Tests range from smooth, simple situations, mixing instabilities, shocks, tests including self-gravity, to the nifty cluster as cosmological example and decaying, subsonic

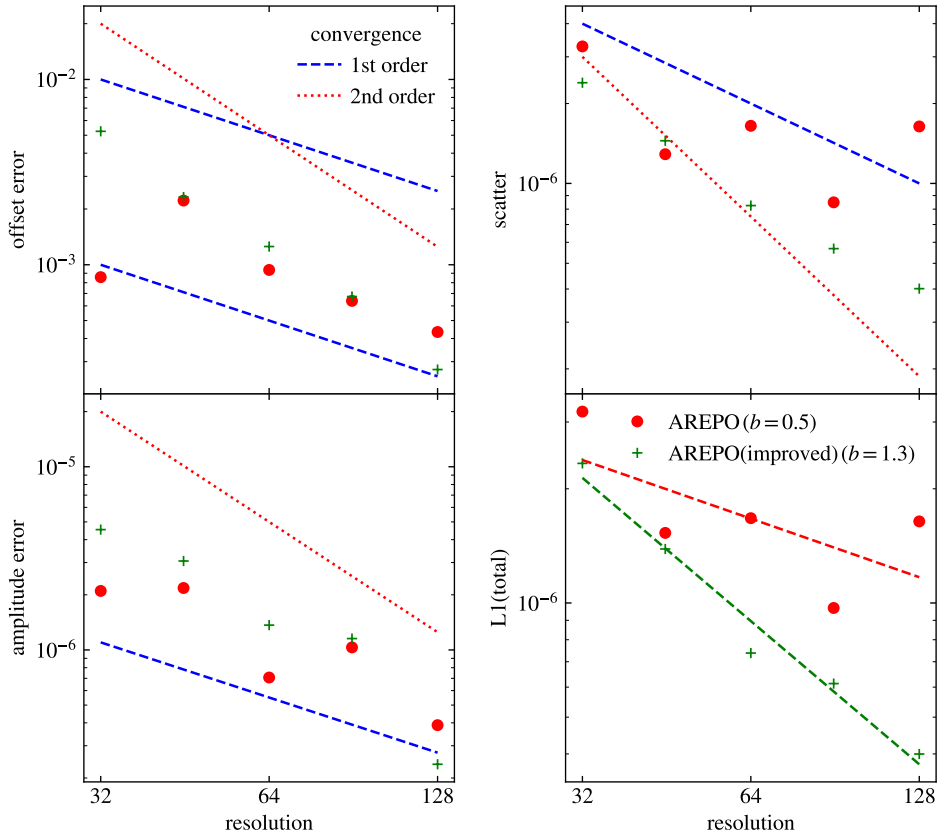

Figure 5.26: Offset-, amplitude-, scatter and total L1-errors of the density of a soundwave at $t = \frac{2}{c_s}$. Applying the changes described in the text reduces especially the scatter error, thus increasing the order of convergence and also making the determination of the other components more reliable. Thus, the overall order of convergence also increases.

turbulence. A comparison has been performed between MFM and SPH in OpenGadget3, the MFM implementation in GIZMO and the moving mesh code Arepo. In addition, two parameters have been analyzed in more detail.

Overall, we find very good agreement between the MFM implementation in OpenGadget3 and that in GIZMO. Minor differences are found in the precise appearance, while global properties are indistinguishable in most test cases. Even without further tuning, MFM reproduces the expected behavior in all test cases considered. The soundwave test is well suited for a convergence analysis, as an analytical solution exists. MFM shows a very good convergence behavior between first and second order for dispersion errors. Diffusion errors as well as the scatter converge second order. While the convergence is better than for SPH and a moving mesh, these methods show lower errors at low resolution, especially for the dispersion error.

An important advantage of MFM over SPH is the capability to accurately evolve mixing instabilities without additional artificial viscosity or conductivity as for SPH. In addition, a lower neighbor number compared to SPH is sufficient. MFM as well as a moving mesh even show secondary instabilities to occur. The blob test as combination between mixing and shocks emphasizes the ability of MFM to allow for more mixing. The decay rate of the cloud is similar to that of a moving mesh simulation and larger than for SPH. Compared to the more traditional SPH implementation shown by Hopkins (2015), the modern SPH implementation OpenGadget3 allows for more mixing and leads to a faster decay of the cloud. As this test is designed to mimic ram-pressure stripping, we expect this effect to be modeled more accurately using MFM compared to SPH. This should also lead to an overall more accurate evolution of galaxies in the environment of GCs. To fully understand and follow the evolution of such gas blob in cosmological contexts more physics such as cooling, and, depending on the context, star formation, is necessary. Gronke & Oh (2018, 2020, 2022) have analyzed this test in detail with such additional physics and found a great importance of the cooling.

In addition, MFM can model shocks for a wide range of Mach numbers. For the shock tube tests MFM performs especially well for lower Mach numbers, while effects of surface tension due to the choice of the slope-limiter are visible at higher Mach numbers. Nevertheless, it is still able to capture the main features of the shock including the position of the shock front, the contact discontinuity, and the rarefaction fan. Different methods lead to differences in the smoothing of the shock front. The lower neighbor number in MFM compared to SPH increases the effective spatial resolution by a factor of ≈ 2. For Arepo, the shock front is dominated by numerical artifacts due to difficulties in the mesh reconstruction in such highly anisotropic region.

The Sedov blast works well for all methods, verifying the capability of the wakeup scheme as non-local timestep criterion. Main differences are the smoothing and resulting lower amplitude of the density peak, revealing an even smaller smoothing for the moving mesh compared to MFM. The narrower shock front will help e.g. for shock detection in cosmological simulations (compare, e.g., Pfrommer et al., 2006; Beck et al., 2016a).

In general, MFM is able to preserve HE accurately, as well as preserving stable orbits. The better stability of the Kepler disk compared to SPH will improve results for simulations of e.g. isolated galaxies. For this case, a moving mesh leads to even better results, but requires additional boundary particles.

The hydrostatic sphere test showed that our MFM implementation coupled to gravity leads

to stable HE, as for SPH and a moving mesh. Depending on the details of the implementation, however, numerical diffusivity can be introduced. Thus, one could expect isolated galaxies or also the core of GCs to be more compact and cooler in the center. The timescales, on which these changes would happen, are, however, very long.

Also for the nifty GC we saw that there is no difference between MFM, Arepo, and modern SPH in the global structure. Numerical diffusivity introduced by the Riemann solver allows mixing of entropy into the core, thus decreasing the central density compared to traditional SPH, which suppresses any mixing. Modern SPH mimics the same effect by applying artificial conductivity, while a variation of the precise amount introduced can lead to significant changes in the structure. As observed GCs show a wide range of central entropy profiles (Cavagnolo et al., 2009), both results are consistent with observations. Especially, we expect a more complex interplay with cooling, as well as stellar and AGN feedback to influence the entropy-evolution of the core (compare, e.g. Pearce et al., 2000; Borgani et al., 2005; Rasia et al., 2015). These effects lead to the whole range of possible central profiles, dominating over effects of the hydro-solver. Thus, further studies including such processes would be necessary.

In the ICM, we expect turbulence at low Mach number to be seeded e.g. by mergers at large scales. It will then decay and build up a turbulent power spectrum. Such decaying, subsonic turbulence is a very challenging problem for many hydro-methods. MFM is able to recover the turbulent power spectrum best compared to SPH and a moving and stationary mesh, best visible at very low initial turbulent energy fractions. Only a small lack of energy at intermediate to small scales close to the resolution limit – similar to where this occurs also for Arepo – is present. This "dip" in energy moves to smaller scales for higher resolution, overall leading to fast convergence towards the expected Kolmogorov spectrum.

The decay rate of turbulent energy due to numerical dissipation is on the same order as for modern SPH, and decreases towards higher resolution. The results are consistent down to very small initial turbulent energy fractions $X_i = 0.0001$, corresponding to small Mach numbers $\mathcal{M} = 0.01$. For smaller $X_i < 0.0001$ numerical effects dominate and lead to unphysical increase in turbulent energy. Overall, the results are very promising for the accurate evolution of turbulence also within GCs.

An energy-entropy switch is of great importance to accurately evolve the temperature profile for the Zeldovich pancake. When it is included, MFM yields the best results, having a clear jump in the temperature. Comparing different possible values for such a switch, we found that careful tuning is required. In general, the switch based on potential energy produces more stable results.

Arepo misses the implementation of such a switch in the public version, such that the low-temperature region is entirely dominated by numerical noise. SPH also shows noise in the low-temperature region, originating from the amplification of noise present in the ICs, and also much broader wings around the peak. All methods show some punch-through in the temperature profile, indicating a too low viscosity.

In addition to comparing different methods, we used two tests to analyze the impact of the slope-limiter. Depending on the problem, different slope-limiters can be preferred. While the gizmo limiter performs best in most test cases, having a much lower numerical diffusivity, specific cases such as the hydrostatic square and also strong shocks work better using a more diffusive TVD-limiter. The Arepo limiter has an intermediate diffusivity and lies in between the two other

results. Also the choice of the Riemann solver can lead to additional numerical diffusivity, where the exact Riemann solver which we use as default has the lowest diffusivity.

In general, our implementation of MFM produces accurate results for the cases considered. It avoids some of the disadvantages of SPH, while requiring a similar computational cost per timestep. The total number of timesteps and thus the total runtime increases as a result of the smaller smoothing length and effectively higher spatial resolution. A faster, approximate Riemann solver can further decrease the computational costs in some cases, but has the drawback of introducing more numerical diffusivity. Compared to MFM, a moving mesh requires a very expensive tessellation to be performed, such that the required computational costs for many tests are drastically increased.

Overall, MFM is a promising alternative for cosmological simulations.

5.6.1 Outlook – Possible Extensions in the Future

To make use of the full advantages of OpenGadget3, it will be useful to couple MFM not only to gravity, but also to include more physical processes, such as cooling, star formation and stellar feedback, AGN feedback, physical conductivity and viscosity. For these, we can make use of already existing implementations in OpenGadget3. Finally, MFM can be expanded to an MHD method, including magnetic fields. This will also allow to include the existing implementation of CRs. For many of these extensions, coupling can be done in a similar way as for SPH, while others such as magnetic fields will require more significant changes including another Riemann solver.

In principle, also a general-relativistic (GR) extension would be possible, which has been implemented both for SPH (Liptai & Price, 2019; Rosswog & Diener, 2021) and a moving mesh (Chang & Etienne, 2020; Lioutas et al., 2024) and also exists for MFM within the gizmo code (Lupi, 2022). As GR is mainly important in extreme situations such as accretion discs around BHs, this would also make use of the fact that our MFM implementation is originally based on GANDALF, which itself was designed to deal with star and planet formation, and thus we would expect also our implementation to be well suited for calculations of disks.

6 | MFM Beyond Pure Hydrodynamics

6.1 MHD Implementation

To incorporate the effect of the magnetic field on the evolution of the fluid, several changes to the MFM implementation in the code OpenGadget3 are required. The implementation is still ongoing, the main equations relevant to the magneto-hydrodynamical evolution have already been implemented, but some changes such as the conversion between physical and comoving units or the incorporation of the magnetic vacuum permeability μ_0 have still to be done.

At first, the magnetic field must be added to the fluid vector as described in Sec. 2.2. The Riemann solver has to be changed to an HLLD Riemann solver (Miyoshi & Kusano, 2005). Our implementation is based on that in Athena (Stone et al., 2008). Cross-terms along directions occur in the governing equations, so the full fluid vector must always be used, even in lower dimensional tests. Gradients are still calculated in lower dimensions for one- or two-dimensional tests. For our implementation we mostly follow the descriptions by Gaburov & Nitadori (2011); Hopkins & Raives (2016).

Numerically, non-zero divergence of the magnetic field can arise. This requires a divergence cleaning strategy described in Sec. 6.1.1. We present a first test of this cleaning strategy in Sec. 6.2.

6.1.1 Divergence Cleaning

The correct advection of non-zero divergence is ensured by Powell et al. (1999) cleaning. An additional source term

$$\boldsymbol{S}_{\mathrm{Powell},i} = -\left(\nabla \cdot \boldsymbol{B}\right)_i \begin{pmatrix} 0 \\ \boldsymbol{B}_i \\ \boldsymbol{v}_i \cdot \boldsymbol{B}_i \\ \boldsymbol{v}_i \end{pmatrix} \tag{6.1}$$

is added to the main MFM equation (3.21). It ensures the method keeps the Lagrangian behavior, even if non-zero divergence is present. In the implementation, all source terms are applied after calculating the fluxes, and added to the $\frac{\mathrm{d}}{\mathrm{d}t}\left(\boldsymbol{V}\boldsymbol{U}\right)$ variable, before being converted from physical to comoving units.

The divergence is reduced using Dedner et al. (2002) cleaning. The field vector is extended by an additional component, the cleaning function ψ, such that the field vector becomes

$$\boldsymbol{U} = \begin{pmatrix} \rho \\ \rho \boldsymbol{v} \\ \rho e \\ \boldsymbol{B} \\ \rho \psi \end{pmatrix}. \tag{6.2}$$

Additional source terms

$$S_{\text{Dedner},i} = -\sigma_{\text{hyperbolic}} \begin{pmatrix} 0 \\ \mathbf{0} \\ (\nabla\psi)_i \cdot B_i \\ (\nabla\psi)_i \\ (\nabla \cdot \boldsymbol{B})_i \, \rho_i \left(0.5 c_{\max,i}\right)^2 \end{pmatrix} - \sigma_{\text{parabolic}} \begin{pmatrix} 0 \\ \mathbf{0} \\ 0 \\ \mathbf{0} \\ \rho\psi \frac{c_{\max,i}}{h_i} \end{pmatrix} \tag{6.3}$$

have to be added to Eqn. (3.21). The parabolic source term for the cleaning function is explicitly integrated, leading to an exponential decay with time. The discretized gradient and divergence terms in Eqn. (6.3) are calculated via

$$(V\nabla \cdot \boldsymbol{B})_i = -\sum_{j \in \text{Ngb}} \bar{B}_{x,ij} \left| \boldsymbol{A}_{ij} \right|, \tag{6.4}$$

$$(V\nabla\psi)_i = -\sum_{j \in \text{Ngb}} \bar{\psi}_{ij} \boldsymbol{A}_{ij}, \tag{6.5}$$

$$\bar{B}_{x,ij} = \frac{1}{2}\left(B_{x,L} + B_{x,R}\right) + \frac{1}{2\tilde{c}_{h,ij}}\left(\psi_R - \psi_R\right), \tag{6.6}$$

$$\bar{\psi}_{ij} = \frac{1}{2}\left(\psi_L + \psi_R\right) + \frac{\tilde{c}_{h,ij}}{2}\left(B_{x,L} - B_{x,R}\right). \tag{6.7}$$

The signal velocity $\tilde{c}_{h,ij}$ is the fastest speed in the local interaction. The left and right state values $B_{x,L/R}, \psi_{L,R}$ are the input values to the Riemann solver. They have been extrapolated to the interface using slope-limited gradients. Additional flux limiters as described by Hopkins & Raives (2016) ensure numerical stability of the cleaning. In addition, we also implement the two-wavespeed cleaning described by Hopkins & Raives (2016), which, however, did not lead to significant differences in our tests, as also discussed by Hopkins & Raives (2016). The corrected magnetic field $\bar{B}_{x,ij}$ is used in the Riemann solver replacing the x-component of the left and right magnetic field states.

The Riemann solver returns the total energy change. An additional term for the magnetic energy has to be added when converting it to internal energy. Based on the change of $\boldsymbol{B}V$, which is our primary variable in MFM, we add a second-order accurate magnetic energy correction,

similar to the kinetic energy correction in Eqn. (3.40):

$$\left(\frac{\mathrm{d}U}{\mathrm{d}t}\right)^n = \left(\frac{\mathrm{d}E_{\mathrm{tot}}}{\mathrm{d}t}\right)^n - \left(\frac{\mathrm{d}E_{\mathrm{kin}}}{\mathrm{d}t}\right)^n - \left(\frac{\mathrm{d}E_{\mathrm{mag}}}{\mathrm{d}t}\right)^n \tag{6.8}$$

$$\left(\frac{\mathrm{d}E_{\mathrm{mag}}}{\mathrm{d}t}\right)^n = \left(\frac{\mathrm{d}}{\mathrm{d}t}\left(\frac{1}{2}\boldsymbol{B}^2\right)\right)^n \tag{6.9}$$

$$\approx \left(\boldsymbol{B}^n + \frac{1}{2}\left(\frac{\mathrm{d}\left(\boldsymbol{B}V\right)}{\mathrm{d}t}\right)^n \frac{1}{V^n}\Delta t^n + \frac{1}{2}\boldsymbol{B}^n\left(\nabla\cdot\boldsymbol{v}\right)^n\Delta t^n\right)\cdot\left(\frac{\mathrm{d}\left(\boldsymbol{B}V\right)}{\mathrm{d}t}\right)^n\frac{1}{V^n}. \tag{6.10}$$

6.1.2 Comoving Integration

As described in Sec. 3.8, we use comoving units incorporating the effect of the cosmological background evolution. For the magnetic field and cleaning function variables, the transformation following Hopkins & Raives (2016) is

$$\boldsymbol{B}_c = a^2\boldsymbol{B}_p, \tag{6.11}$$

$$\psi_c = a^3\psi_p. \tag{6.12}$$

In principle, the ψ conversion depends on the timescale set by the fastest wavespeed. It is defined by either the sound speed or the Alfvén velocity, which give rise to different comoving evolution. Nevertheless, the decay time is short enough, such that in practical applications a single transformation is sufficient (Hopkins & Raives, 2016) and we use the scaling described above.

The magnetic field receives an additional decay term due to the cosmological expansion

$$\frac{\mathrm{d}\boldsymbol{B}}{\mathrm{d}t} = V\frac{\mathrm{d}\left(\boldsymbol{B}V\right)}{\mathrm{d}t} + \nabla\cdot\boldsymbol{v}B - H(t)B. \tag{6.13}$$

6.2 MHD Test Case

The implementation of MHD with MFM in OpenGadget3 is still preliminary. Nevertheless, we want to show a first test to study the properties of the implementation. Similarly to the hydrodynamical tests, we use a standardized setup for our test case, with the same general settings as for the hydrodynamical case described in Sec. 5.2.1.

The default Dedner cleaning parameters are set to $\sigma_{\mathrm{parabolic}} = 0.1$ and $\sigma_{\mathrm{hyperbolic}} = 1.0$. Magnetic field units are chosen such that the magnetic vacuum permeability is $\mu_0 = 1$.

6.2.1 Magnetic Monopole

In principle, the divergence of the magnetic field remains zero according to the MHD equations. To study the behavior of the code under numerically non-zero divergence, we set up an artificial magnetic monopole on an otherwise smooth background.

The ICs are set up as a regular grid of $128^2 \cdot 12$ particles in a box of size $l_x = l_y = 2$, $l_z = 0.1$, with density $\rho = 1$ and pressure $P = 6$. The initial magnetic field is

$$B_x = \begin{cases} \frac{1}{\sqrt{4\pi}} \left(\left(\frac{|\boldsymbol{r}-\boldsymbol{r}_0|}{d_0} \right)^8 - 2 \left(\frac{|\boldsymbol{r}-\boldsymbol{r}_0|}{d_0} \right)^4 + 1 \right) & |\boldsymbol{r} - \boldsymbol{r}_0| < d_0 \\ 0 & |\boldsymbol{r} - \boldsymbol{r}_0| \geq d_0 \end{cases} \tag{6.14}$$

$$B_y = 0.0 \tag{6.15}$$

$$B_z = \frac{1}{\sqrt{4\pi}} \tag{6.16}$$

where $\boldsymbol{r}_0 = (0.5, 0.5)$ and $d_0 = 1/\sqrt{8}$. Distances $|\boldsymbol{r} - \boldsymbol{r}_0|$ are calculated only in the xy-plane. The particles are initialized with a velocity $\boldsymbol{v} = (1, 1, 0)$.

We run the simulation with different settings for divergence cleaning shown in Fig. 6.1. Without Powell cleaning, the Lagrangian behavior of the method is lost, and the divergence is not advected with the flow. Instead, streams of non-zero divergence form in the direction of the flow from the edge of the monopole region. Including Powell cleaning fixes this non-Lagrangian behavior and properly advects the non-zero divergence.

Dedner cleaning reduces the divergence on short timescales. Depending on the parameters, the cleaning speed and pattern differ. With default parameters, the divergence is cleaned efficiently until $t \approx 0.3$. Without parabolic cleaning, the divergence is only spread out, but not damped. Even at $t = 1$ traces of high divergence are present throughout the simulation volume. Also, reduced hyperbolic cleaning leads to less efficient cleaning. This term is responsible for the spread-out of divergence, which is much reduced in this case. Thus, cleaning progresses more slowly, and the region of non-zero divergence is still visible at $t = 1$, confined roughly to the same region as for the simulation without Dedner cleaning.

Overall, this test shows that both Powell and Dedner cleaning are working properly. By choosing appropriate values for the Dedner cleaning parameters, the interplay of parabolic and hyperbolic cleaning efficiently reduces the divergence.

6.3 Coupling to Subgrid Models

OpenGadget3 contains various additional subgrid descriptions of physical processes. Models for artificial and physical viscosity and conductivity were originally written directly inside the SPH hydrodynamical calculation. The same is true for on-the-fly shock capturing or the calculation of turbulent velocity at the kernel scale. We moved these out of the hydro loop into separate functions that can be called both for the MFM and SPH hydro loop. Additional contributions to changes in hydrodynamical variables are stored in an additional variable to be compatible with conversion from physical units to code units at each timestep for MFM.

Other subgrid models such as star formation, stellar, and AGN feedback are carried out at each timestep in a separate function. Through feedback, these modules can affect the entropy and velocity changes. As implemented in OpenGadget3, all these changes are recalculated from the Riemann solver output at each kick and drift, to properly convert from comoving to physical

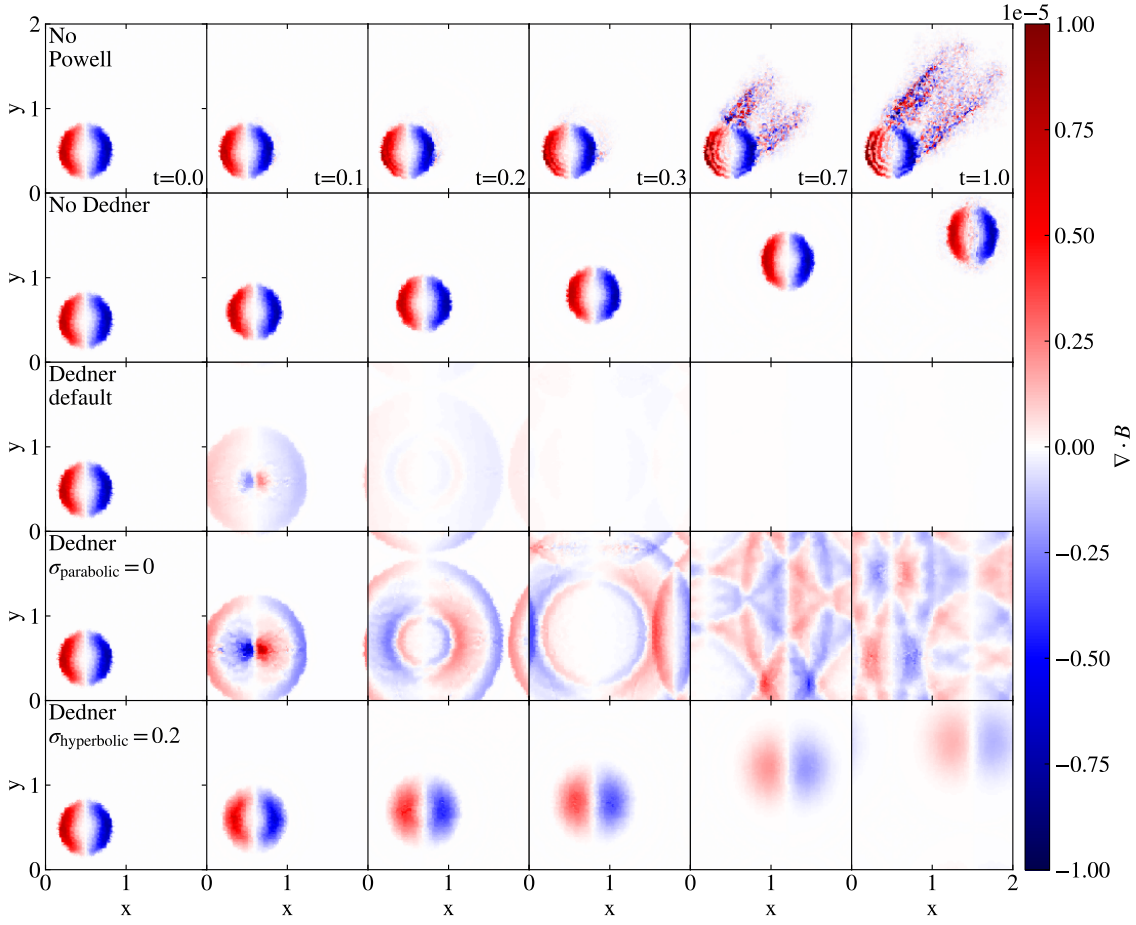

Figure 6.1: Magnetic monopole at $t = 0, 0.1, 0.2, 0.3, 0.7, 1.0$ (columns from left to right) evolved without any cleaning (top row), only including Powell cleaning (second row), with Dedner cleaning with default parameters $\sigma_{\text{hyperbolic}} = 1.0$, $\sigma_{\text{parabolic}} = 0.1$ (third row), without parabolic cleaning (fourth row), and with decreased $\sigma_{\text{hyperbolic}} = 0.2$ (bottom row).

units. To be compatible with this recalculation, the new entropy and velocity change have also to be assigned to the time derivative of conserved quantities $\frac{\mathrm{d}(V\boldsymbol{U})}{\mathrm{d}t}$ returned by the Riemann solver. Additionally, for MFM we evolve internal energy instead of entropy, which time derivative thus also has to be adjusted. The conversion is as follows:

$$\frac{\mathrm{d}u}{\mathrm{d}t} = u\left(\frac{\frac{\mathrm{d}A}{\mathrm{d}t}}{A} - (\gamma-1)\,\nabla\cdot\boldsymbol{v} - 3\,(\gamma-1)\,h\right), \tag{6.17}$$

$$\frac{\mathrm{d}\,(mu)_p}{\mathrm{d}t} = U\left(\frac{\frac{\mathrm{d}A}{\mathrm{d}t}}{A} - (\gamma-1)\,\nabla\cdot\boldsymbol{v}\right)hm. \tag{6.18}$$

The last term in the internal energy conversion in Eqn. (6.17) is the Hubble expansion correction and is only added for cosmological simulations. The Hubble parameter in Eqn. (6.18) is a result of the time integration scheme, and is set to $h = 1$ for non-comoving simulations.

Discrete mass changes can occur for star formation and accretion onto a BH. To ensure these changes do not affect the hydrodynamical evolution, the changes in conserved quantities are adjusted

$$\left.\frac{\mathrm{d}\,(V\boldsymbol{U})}{\mathrm{d}t}\right|_i = \left.\frac{\mathrm{d}\,(V\boldsymbol{U})}{\mathrm{d}t}\right|_{i,0} \cdot \frac{m_{i,0} + \Delta m}{m_{i,0}}. \tag{6.19}$$

The volume occupied by each particle and thus its number density does not change, leading to changes in the mass density

$$\rho_i = \rho_{i,0}\frac{m_{i,0} + \Delta m}{m_{i,0}}. \tag{6.20}$$

6.4 Test Cases for Subgrid Models

To test the coupling between subgrid models and MFM we perform several test simulations. Here, we want to focus on the coupling to cooling, star formation, and feedback models, which include all conversions described above. To this end, we run an isolated galaxy.

6.4.1 Isolated Galaxy

As a first, non-comoving test we simulate an isolated Milky Way-like galaxy, as described by Steinwandel et al. (2019). It has a total halo mass of $M_{200c} = 10^{12}\mathrm{M}_\odot$, and mass resolution of $M_\mathrm{DM} = 9.6 \cdot 10^5\mathrm{M}_\odot$, $M_\mathrm{gas} = 4.8 \cdot 10^4\mathrm{M}_\odot$, $M_* = M_\mathrm{gas}/3$. The gravitational softening length is $\epsilon_\mathrm{DM} = 218$ pc, $\epsilon_\mathrm{gas} = \epsilon_* = 50$ pc.

Simulations have been carried out with SPH and MFM, each using

- pure (non-radiative) hydrodynamics,
- star formation according to the Springel & Hernquist (2003) (SH03) model,

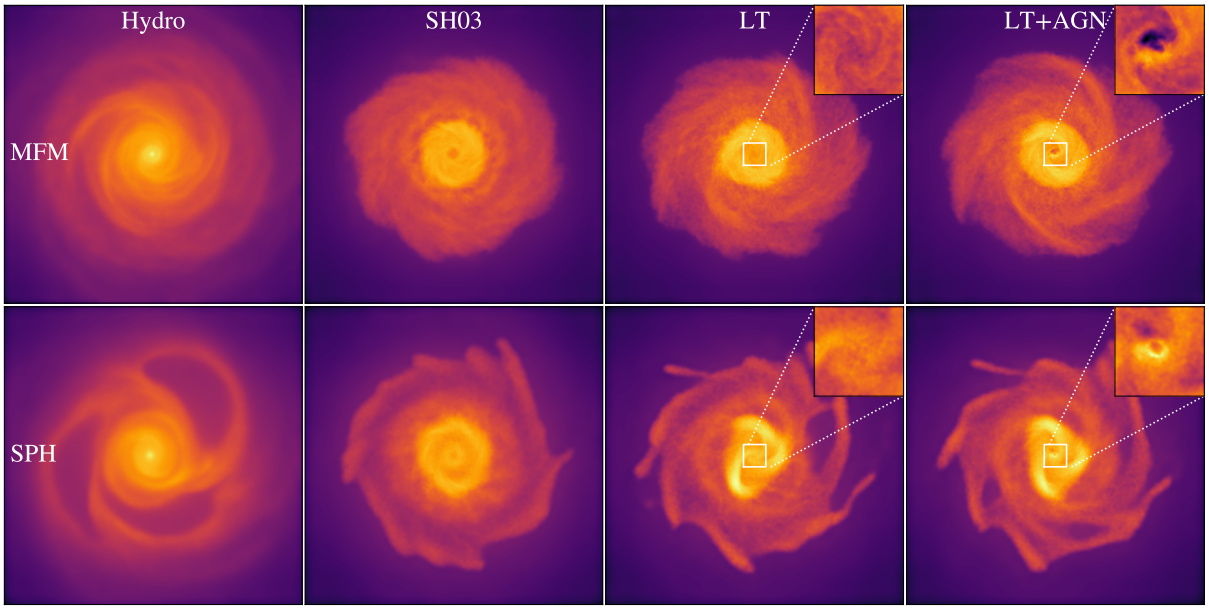

Figure 6.2: Isolated galaxy simulated with MFM (top row) and SPH (bottom row) with (from left to right) pure hydrodynamics, including SH03 star formation, including LT star formation, and LT star formation with additional AGN feedback. All simulations produce a spiral structure but with different small-scale features. The zoom regions focus on the impact of the central AGN with a narrower range for the color map.

- star formation according to Tornatore et al. (2003, 2004, 2007) (LT),
- star formation according to Tornatore et al. (2003, 2004, 2007) and additional AGN feedback.

For simulations that include AGN feedback, a BH of $M_{\mathrm{BH}} = 10^7\,\mathrm{M}_\odot$ was seeded in the center defined by the potential minimum following Sala et al. (2024).

The resulting surface density of the galaxy is shown in Fig. 6.2. Due to numerical perturbations in the initial particle distribution, a spiral structure starts to emerge. These spirals are visible for all simulations, independent of the additional physics, but different between MFM and SPH, as they are of numerical origin. Cooling in the radiative simulations compacts the disk. A simulation with only cooling would be unstable, heating by SN feedback is necessary to balance the cooling and prevent collapse of the gas. The global structure does not change between the different star formation models. AGN feedback mainly affects the center of the galaxy, heating the gas and reducing the central density. At the time shown this effect is stronger for MFM, it however strongly depends on the timing and generally appears stronger after a recent accretion and subsequent feedback event.

Additional insight into the coupling can be gained from the star formation rate shown in Fig. 6.3. Initially, a high peak in star formation occurs as the gas cools and compresses. The peak is even higher for MFM than for SPH due to the effectively smaller resolved scales due to

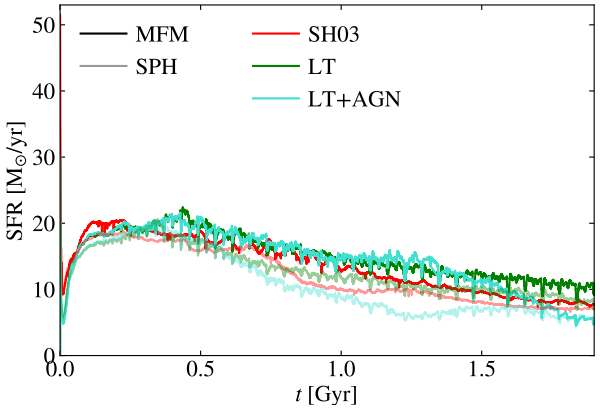

Figure 6.3: Star formation rate of the different simulations. Different colors indicate different star formation modes. Bright lines are simulations with SPH, dark lines with MFM. After a brief relaxation phase, all simulations reach a stable self-regulated state.

the smaller kernel size and thus higher resolved density peaks. It is followed by a strong burst of SN feedback, leading to a decrease in the star formation rate, and finally reaches a relaxed steady state. Self-regulation leads to an almost constant star formation rate at later times, which is consistent between all star formation models and hydro-methods. Additional small variations are visible because of the stochastic nature of the star formation subgrid model. These variations in the star formation history can explain the different small-scale structures visible in the surface density plots. As the gas reservoir gets depleted, the star formation rate decreases towards later times.

Overall, these simulations confirm the coupling between MFM and additional star formation models, as they reach a self-regulated equilibrium phase. The precise morphology changes due to small differences in the star formation history.

7 | Numerical Improvements in OpenGadget3

7.1 Pairwise Flux Calculation and Bitwise ProcessedFlag

In purely hydrodynamical simulations, the flux calculation including the Riemann solver can be the computationally most expensive part. We found its fraction to the total time to range between 10% for cosmological simulations up to 40% for the shock tube problem. Some speedup is achieved by assigning the fluxes, which are pairwise symmetric, not only to the active particle but also to its neighbor. The measured speedup of the hydro-calculation in a cosmological zoom-in simulation is $\approx 10\%$, so smaller than the theoretical maximum of factor 2, but still a substantial improvement. Differences can be explained by overhead and the timebin hierarchy.

Assigning pairwise fluxes requires some careful treatment in the parallelization strategy. To avoid the duplicate execution of a particle pair, only the particle on the smaller timebin is used as main particle. In the case of particles residing on the same timebin the degeneracy is broken by choosing the particle with the smaller ID. Information on the fluxes of neighboring particles is saved in the global particle structure, while the main particle fluxes are assigned to the local structure and added to the global values only after the neighbor loop has finished. OpenMP locks avoid race conditions in case of one particle being neighbor to several other particles executed at the same time.

In addition, this strategy requires careful bookkeeping of processed particles, especially if the buffer is not large enough to process all particles at once but requires several iterations. To this end, we extend the existing ProcessedFlag variable in a bit-wise manner, where some of the bits are used to store the information of the last neighbor loop a particle successfully finished.

7.2 C++ Classes

Some additional cleanup was achieved by moving code into functions and classes. A general slope limiter class with derived classes for each limiter is defined. The appropriate derived class is chosen once in the beginning and allows us to remove many pre-compilation checks in the actual slope limiter evaluation.

Different unit systems are used throughout the code. As discussed in Sec. 3.8, there are physical and comoving units. In addition, some units include a Hubble factor. Finally, there are

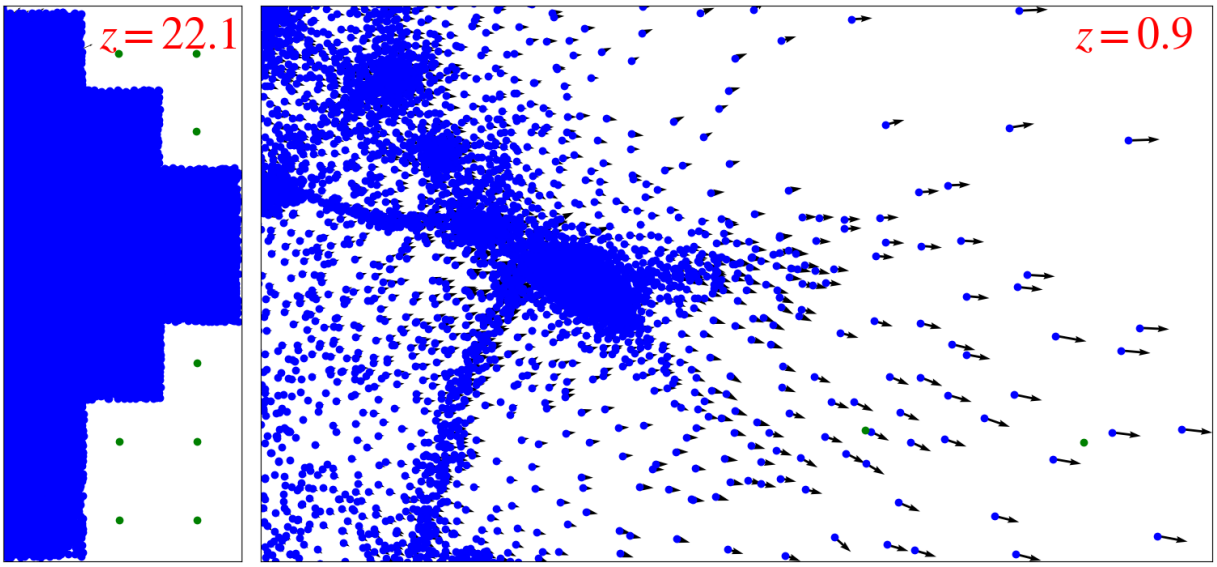

Figure 7.1: Thin slice through a zoom-in region at two different redshifts, showing gas particles in blue, and boundary particles in green. The left boundary of the two plots is located at the same relative position to the center of mass of all gas particles. Arrows indicate velocities for all particles at higher softening lengths than the median of all gas particles in the simulation volume.

physical cgs units compared to the internal unit system. All unit conversions have been done by hand at many places in the code. Changes in the time integration resulted in a few wrongly defined conversions. This led us to the definition of a unit class[1], containing all relevant factors and defining them in one place in the code. The appropriate derived class for non-comoving or comoving integration is assigned to a global variable, which can thus be accessed at all positions where needed. In addition to the resulting cleanup of the code, this leads to some minor speedup, as common pre-factors are evaluated only once per timestep.

7.3 Boundary Conditions

Zoom-in simulations designed for SPH often contain vacuum boundaries. An example of the setup for such a region has been shown in Sec. 4.2. The high-resolution gas region has a sharp boundary that includes corners and edges, as shown in more detail in Fig. 7.1. Everything outside this region is populated by low-resolution boundary particles that interact only gravitationally and contain information on the large-scale structure. This poses some challenges when running these regions, especially at higher resolution.

At first, the sharp edges can lead to an artificial collapse. No physical information is contained in the region close to the boundary, such that this effect can be ignored. A second problem is more specific to MFM simulations. Particles leaving the area populated with gas particles will see only one-sided fluxes, which results in a strong acceleration even further away from the center. The

[1]The implementation was done together with L. Böss.

velocity increases with time, as the particle moves away from the initial high-resolution domain. Ultimately, these particles will have very low timesteps. We identify these problematic particles either based on their very high velocities or on whether they leave the central high-resolution PM grid defined for the gravity solver. In both cases, we transform them into DM particles, re-using the function from the star formation model, which was used to convert gas into stellar or BH particles. This additional boundary condition makes high-resolution zoom-in simulations which would otherwise run into timestep issues much more stable.

Part III

Impact of the Hydrodynamical Solver on ICM Turbulence

8 | Turbulent Pressure Using Dianoga Regions[1]

Derived properties of ICM turbulence depend not only on the analysis method but also on the numerical setup. Detailed comparisons on different hydro-methods to simulate subsonic turbulence have been made mainly in idealized boxes (compare, e.g., Kitsionas et al., 2009; Price & Federrath, 2010; Padoan et al., 2007; Bauer & Springel, 2012; Price, 2012a). These works show that especially the power spectrum can be significantly impacted by the choice of the hydro scheme.

In cosmological simulations, several works studied the impact of individual numerical parameters. A too high artificial viscosity can significantly reduce the amount of turbulence (Dolag et al., 2005b). Also, artificial conductivity reduces turbulence, as a result of increased gas stripping (Biffi & Valdarnini, 2015).

In this work, we want to extend the comparison of different hydrodynamical methods from idealized simulations to cosmological environments. In particular, we want to study the differences between MFM (Lanson & Vila, 2008a,b) and SPH (Springel & Hernquist, 2002) as two different hydro methods on the resulting turbulence in the ICM. To this end, we use non-radiative, hydrodynamical zoom-in simulations of GCs to have a clean setup that allows us to produce robust results to compare MFM and SPH. In addition, we want to quantify the impact of the analysis method, as well as of the dynamical state of the cluster.

This chapter is organized as follows. In Sec. 8.1 we describe the code and simulation setup, followed by a description of the different methods used to analyze the simulations in Sec. 8.2. The general dynamical and thermodynamic properties of the clusters used in this work are described in Sec. 8.3. To gain insight into the turbulence, we start with a general analysis of the velocity structure in Sec. 8.4, and present the resulting turbulent pressure support in Sec. 8.5. An additional plot of the surface density of all clusters analyzed in this study is shown in Sec. 8.6. Our findings are discussed in Sec. 8.7.

[1]The content of this chapter has been submitted to Astronomy & Astrophysics and published as preprint by Groth et al. (2024). Some additions and adjustments have been made.

8.1 The Simulations

8.1.1 OpenGadget3

The simulations are performed with the hydrodynamical cosmological simulation code OpenGadget3. It is originally based on Gadget-2 (Springel et al., 2001; Springel, 2005). Gravity is calculated with an Oct-Tree-Particle Mesh (PM) approach (Xu, 1995; Springel, 2005; Springel et al., 2021). Hydrodynamical forces are calculated either using modern SPH (Springel & Hernquist, 2002) including artificial viscosity as formulated by Beck et al. (2016b) and artificial conductivity as formulated by Price (2008). Alternatively, the MFM hydro-solver is used, with the implementation presented by Groth et al. (2023).

295 neighbors are used for the SPH calculations with a Wendland C6 kernel (Wendland, 1995; Dehnen & Aly, 2012), while only 32 neighbors with a cubic spline kernel (Monaghan & Lattanzio, 1985) are best suited for MFM. This leads to an effectively higher spatial resolution for the hydrodynamical solver defined by the smoothing length h using MFM compared to SPH by a factor of ≈ 3.

The Subfind substructure finder (Springel et al., 2001; Dolag et al., 2009) and a shockfinder (Beck et al., 2016a) are run on-the-fly.

8.1.2 Dianoga Suite

We simulate seven massive GCs from the Dianoga suite of zoom-in regions (Bonafede et al., 2011a). The background cosmological evolution follows a flat ΛCDM cosmology with $\Omega_\mathrm{m} = 0.24$, $\Omega_\mathrm{b} = 0.04$, $h = 0.72$ and $\sigma_8 = 0.8$. The mass resolution is $M_\mathrm{DM} = 10^9 h^{-1}\ \mathrm{M}_\odot$, $M_\mathrm{gas} = 1.6 \cdot 10^8 h^{-1}\ \mathrm{M}_\odot$. The gravitational softening corresponds to 3.75 h^{-1}kpc for gas and 11.25 h^{-1}kpc for DM particles.

All selected clusters have a mass larger than $10^{15} h^{-1}\ \mathrm{M}_\odot$. Their names and masses are listed in Table 8.1. The selection includes active clusters with high merger activity and relaxed clusters that undergo mainly smooth accretion or minor mergers. This diversity allows us to study the effect of the dynamical state and compare results to other simulations and observations of populations of different clusters.

Every cluster was simulated twice, once with the MFM solver, and once with SPH. The main properties such as R_{200} and M_{200} quoted in Tab. 8.1 are consistent between the methods. Also the classification between active and relaxed systems including the fraction of their evolution they stay active or relaxed does not change when different hydro-solvers are used.

For each simulation, we create 46 snapshots from redshift $z = 0.43$ until redshift zero, which we use for time averaging and studying their evolution.

Cluster ID	M_{200} $[10^{15}h^{-1}\mathrm{M}_\odot]$	M_{200}^{gas}	R_{200}	R_{500} [Mpc]	R_{2500}	active/ relaxed
g1212639	1.9	0.28	3.2	2.2	0.5	61%/ 39%
g1483463	1.6	0.24	3.1	2.2	0.4	100%/ 0%
g1657050	1.9	0.29	3.2	2.1	0.5	47%/ 53%
g1680241	1.7	0.26	3.1	2.0	0.4	89%/ 11%
g1987669	1.9	0.29	3.2	2.3	0.5	96%/ 4%
g5503149	1.6	0.25	3.1	2.1	0.5	88%/ 12%
g6348555	1.7	0.28	3.1	2.1	0.5	0%/100%

Table 8.1: List of some general properties of the GCs analyzed in this study. The bold part of the identification number is used as an abbreviation in the text. The last column gives the fraction of the evolution time since $z = 0.43$ that the cluster is relaxed/active. The dynamical state was determined by the method described in Sec. 8.2.1.

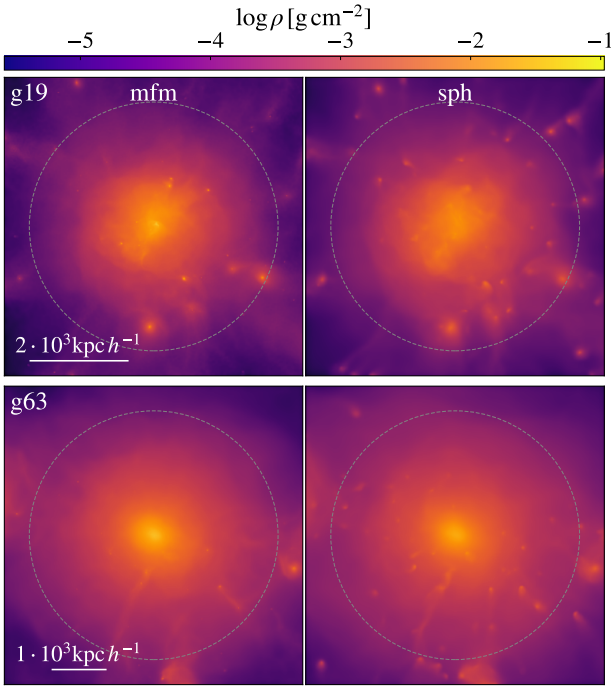

Figure 8.1: Projected gas density maps for g19 and g63 as examples of one more active and one more relaxed cluster analyzed in this work at redshift $z = 0$. The dashed circle denotes R_{vir}. The upper maps have a size of $\Delta x = \Delta y \approx 3064$ kpc h^{-1}, the lower maps $\Delta x = \Delta y \approx 2797$ kpc h^{-1}.

8.2 Analysis Methods

8.2.1 Dynamical States

To classify the dynamical state of a GC, we follow the method described by Cui et al. (2017, 2018). We use two complementary criteria, where clusters are classified as active if at least one of them is satisfied. The first criterion is based on the shift of the center of mass (com) with respect to the cluster center defined by the minimum potential, where active clusters have an offset of at least

$$\left|\boldsymbol{r}_{\text{min pot}} - \boldsymbol{r}_{\text{com}}\right| \geq 0.04\, R_{200}. \tag{8.1}$$

In addition, clusters for which the mass in substructures exceeds

$$M_{\text{sub}} \geq 0.1 M_{200} \tag{8.2}$$

are considered active. The cluster is classified as relaxed if none of the criteria are satisfied. The minimum potential, as well as the mass enclosed in substructures, is found using SUBFIND (Springel et al., 2001; Dolag et al., 2009). The center of mass is calculated for all gas and DM particles within R_{200}[2] from the SUBFIND center.

Both criteria are directly related to major mergers. The first one aims to capture the offset and sloshing of the gas within the DM potential shortly after the merger. Also massive substructures can offset the global mass distribution. The second criterion detects the infalling halo of an ongoing merger more directly.

Alternative criteria to classify the dynamical state would be possible, e.g. based on the virialization (compare, e.g., Cui et al., 2018). We found, however, that these closely follow the two criteria used in this work, such that they are sufficient to classify the dynamical state of the system.

8.2.2 Clump3d Analysis

The first option to calculate the non-thermal pressure contribution closely follows the method described by Sayers et al. (2021). In the first step, the ellipticity of the gas and total matter distribution is calculated according to the framework described by Fischer et al. (2022); Fischer & Valenzuela (2023) to account for deviations from spherical symmetry. The derived axes are used to define an elliptical radial coordinate used in all the fits.

The global density profile of gas plus DM is fit with a Navarro-Frenk-White (NFW) profile (Navarro et al., 1997). The gas density is fit with a modified beta-model, and its temperature with a modified broken power law (Vikhlinin et al., 2006). The total pressure is obtained from these fits using the HE equation:

$$\nabla P_{\text{tot}} = -\rho \nabla \Phi_{\text{mat}}. \tag{8.3}$$

[2]All quantities (R_{200}, M_{200}, etc) are defined with respect to to the mean mass density of the universe in this chapter.

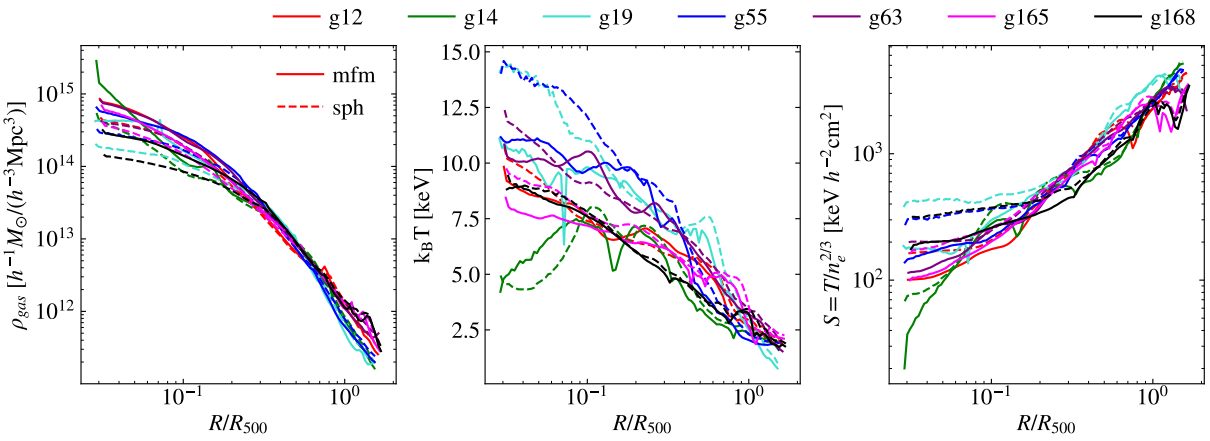

Figure 8.2: Radial gas density, temperature, and entropy profiles for the clusters analyzed in this work at redshift $z = 0$.

The thermal pressure is calculated directly from the gas density ρ_{gas} and internal energy u_{gas} of all particles as:

$$P_{\mathrm{therm}} = (\gamma - 1)\, \rho_{\mathrm{gas}} u_{\mathrm{gas}} \tag{8.4}$$

with adiabatic index $\gamma = 5/3$. We use 40 radial bins equally distributed in log space between $0.01\, R_{200}$ and $1.1\, R_{200}$ to compute these profiles, using a logarithmic mean over the particles within each bin. The non-thermal pressure is given by the deviation from the assumption of HE. It is computed as the difference between the total and thermal pressure $P_{\mathrm{nt}} = P_{\mathrm{tot}} - P_{\mathrm{therm}}$, limited to values greater than zero. Finally, the time and cluster-to-cluster average is computed with the radial coordinate normalized to R_{200}.

The non-thermal pressure derived from this method includes contributions from turbulence and bulk motions. Depending on which physics is included, it could also contain e.g. magnetic pressure. In addition, strong shocks after recent mergers could impact the derived non-thermal pressure.

8.2.3 Vortex Analysis – Helmholtz Decomposition

The second method to calculate the non-thermal pressure fraction uses the velocity data from the simulation more directly.

We use the VORTEX-P code developed by Vallés-Pérez et al. (2024) to perform a Helmholtz-decomposition (Vallés-Pérez et al., 2021b). The total gas velocity is split into compressive and solenoidal components which are derived via a scalar potential ϕ and vector potential $\boldsymbol{A}$, respectively, leading to a unique decomposition

$$\boldsymbol{v} = \boldsymbol{v}_{\mathrm{compressive}} + \boldsymbol{v}_{\mathrm{solenoidal}}, \tag{8.5}$$

$$\boldsymbol{v}_{\mathrm{compressive}} = -\nabla\phi, \quad \boldsymbol{v}_{\mathrm{solenoidal}} = \nabla \times \boldsymbol{A}. \tag{8.6}$$

The potentials are found as solutions to the elliptic partial differential equations

$$\nabla^2\phi = -\nabla\cdot\boldsymbol{v}, \quad \nabla^2\boldsymbol{A} = -\nabla\times\boldsymbol{v}. \tag{8.7}$$

The solenoidal component is associated with turbulence, while compressive motions are associated with shocks and bulk motion, following the results of Vazza et al. (2017) who find that the solenoidal component of turbulence dominates. In principle, the solenoidal component also contains components of motions at larger scales. Nevertheless, it tends to be more isotropic, thus behaving more like an additional pressure contribution compared to the compressive part (mainly radial; cf. figure 7 in Vallés-Pérez et al., 2021b).

Internally, VORTEX-P assigns the SPH data onto an ad-hoc set of nested AMR grids, with higher resolution in regions of higher particle number density, especially in the cluster center and within substructures.

We run the decomposition in a region of $50h^{-1}$Mpc sufficiently large to contain the virialized region of the main cluster and not be influenced by boundary effects. The base grid has a resolution of $N_x = 128$ and a maximum of $n_l = 6$ refinement levels. Cells at any refinement level containing more than $n_{\mathrm{part}}^{\mathrm{refine}} = 8$ particles are set to refine, thus producing a quasi-Lagrangian refinement. These settings result in a peak resolution of $\Delta x_6 \approx 6$kpc which is on the same order as the minimum smoothing length. A cubic spline kernel is used to interpolate the MFM simulations, while a Wendland C6 kernel is used for the SPH runs. Interpolations in the decomposition use the same neighbor number as in the cosmological simulation they are applied to. Further details on the setup of the cosmological simulations are provided in Sec. 8.1. The solenoidal velocity is then mapped back from the internal AMR grid to the original particle positions. This can introduce some smoothing and small errors, which are, however, on the same order as the errors involved in the initial grid assignment (see Vallés-Pérez et al., 2024, their figures 2 and 3).

The turbulent pressure within 40 elliptical shells is calculated directly from the particle-based velocity data:

$$P_{\mathrm{turb}} = \frac{1}{3}\rho v_{\mathrm{sol}}^2. \tag{8.8}$$

Also the thermal pressure is obtained directly from the gas properties according to Eqn. (8.4). The total pressure is the sum of both. All properties are calculated as mass-weighted mean.

8.2.4 Vortex Analysis – Multi-Scale Filtering

Finally, VORTEX-P can also perform a Reynolds decomposition to split the bulk component of the velocity field from the turbulent contribution. Following the initial idea by Vazza et al. (2012, 2017), we perform a multi-scale filtering approach. The details of the implementation and the extension of the method to AMR have been described by Vallés-Pérez et al. (2021a).

The outer scale of turbulence is constrained iteratively for each cell center. A lower bound $L_0 = 3\Delta x_l$ depends on the local resolution of the ad-hoc AMR grid (i.e., the refinement level l). Then, the filtering scale is iteratively increased until the turbulent velocity converges, indicating that longer spatial scales around the given point no longer contain more kinetic energy, and

hence the outer scale of the inertial range has been reached. To avoid divergent behavior at discontinuities, the iteration also stops if a shocked cell with Mach number $\mathcal{M} \geq 2.0$ enters the integration domain. The resulting filtered mean velocity corresponds to the bulk motion, such that the turbulent velocity remains as the difference between total and filtered mean velocity. As for the solenoidal velocity, the filtered velocities are mapped back to the particle position.

This decomposition offers the most direct way of measuring the turbulent velocity. The turbulent pressure is calculated according to Eqn. (8.8), replacing the solenoidal velocity with the filtered one.

8.3 Cluster Properties

To better understand the set of clusters, we first analyze some of their main properties. The projected gas density maps of two clusters representative of both more active and more relaxed clusters are shown in Fig. 8.1. Maps of the remaining clusters are shown in the Sec. 8.6. Overall, the GCs simulated with MFM have general properties which are similar to those of their analogous SPH version, by visual inspection. The same is true for the location of substructures, as the large-scale evolution is dominated by gravity. Also the accretion history of the gas is almost identical, with only minor timing differences.

Differences are visible on smaller scales. Small structures tend to be destroyed earlier for MFM, leading to less substructures in the cluster. We do not find a statistically significant difference in the subhalo gas mass function between MFM and SPH within R_{200} of the cluster, as it is highly dominated by uncertainties in the substructure finder for such small halos. For MFM, we even find an overall higher number of subhalos. Nevertheless, SUBFIND struggles to find the gas content and the differences are minor when manually calculating the mass of the gas enclosed within the substructure. However, the smaller number of substructures in MFM simulations appears to be a consistent trend by visual inspection of all surface density plots. This observation is a sign that MFM mixes gas more efficiently and is more dissipative, consistent with more idealized simulations shown by Groth et al. (2023). In addition, from visual inspection, the diffuse volume-filling ICM appears to have more turbulent density fluctuations, visible mainly in the active cluster g19.

Cluster g19, classified as an active cluster at almost all redshifts, has more and larger substructures and ongoing mergers. In contrast, more relaxed clusters, such as g63, have less substructures and undergo mainly smooth accretion. Their overall shape looks much smoother and rounder.

In contrast to the GC structure in the maps, the radial profiles, shown in Fig. 8.2, are consistent between MFM and SPH for all clusters. The first panel shows the gas density ρ_{gas}, the second panel the gas temperature in terms of $k_{\mathrm{B}}T$, and the third panel the entropy $S = T/n_e^{2/3}$ profile. The electron density n_e is calculated assuming full ionization. There are only minor differences between the two hydro-methods. In particular, MFM tends to produce slightly cooler and denser cores compared to SPH. This is a result of MFM having more mixing, resulting in a lower temperature in the core.

Most of the clusters have a hot core, visible both in temperature and in entropy. Only the g14 cluster has a cool core with a decrease in temperature in the center. This is most likely a

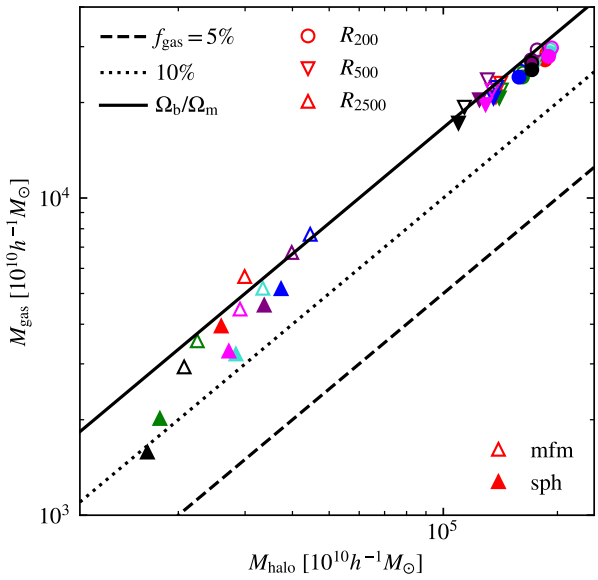

Figure 8.3: Gas mass to halo mass relation for the clusters evaluated inside different radii at redshift $z = 0$. Lines indicate constant gas fractions $f_{\rm gas}$. Same colors for each cluster as in Fig. 8.2.

transition state of the ongoing strong merger activity. In the surface density plot in Sec. 8.6, even two distinct density peaks in the center are visible as a result of a recent major merger. This can significantly impact all radial profiles for this particular cluster.

The gas mass to halo mass relation for the different clusters evaluated inside different radii R_{200}, R_{500}, and R_{2500} is shown in Fig. 8.3. MFM and SPH lead to almost identical results when evaluating the masses inside larger radii (i.e., R_{200} and R_{500}), as the global structure does not change. The gas content reaches roughly the cosmological one $\Omega_{\rm b}/\Omega_{\rm m} \approx 16.7\%$. Strong clustering in the cluster center can lead to gas contents even above the cosmological value observed for a few clusters.

Slight differences appear in the innermost region inside R_{2500}, where MFM generally leads to larger masses, consistent with the increase in density found in the radial profiles. The gas content ranges from 10% to approximately the cosmological value of 16.7%. While this is slightly larger than typical observation results around $5 - 13\%$ (Vikhlinin et al., 2006; David et al., 2012), differences can be explained by the absence of AGN feedback processes, which would reduce the gas fraction, especially at smaller radii (McNamara et al., 2000; Churazov et al., 2000; Eckert et al., 2021), and also star formation which reduces the gas as it is transformed into stars.

The clusters show a variety of dynamical states as shown in Fig. 8.4. As described in Sec. 8.2.1, clusters are classified as relaxed if both, offset of the center of mass and mass enclosed in substructures, are below the threshold marked by the gray-shaded region, while they are classified as active otherwise. Sloshing can make the center of mass approach the center defined by the minimum potential at some reshifts, but still have a non-zero relative velocity. Our second

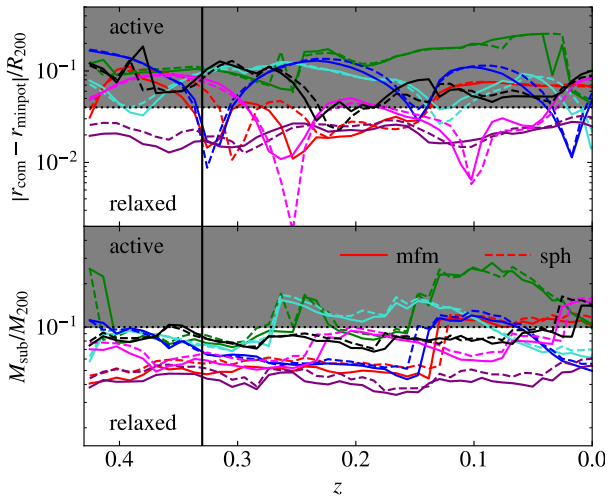

Figure 8.4: Evolution of the center offset and substructure-mass over time of all clusters analyzed in this work. As described in Sec. 8.2.1, a cluster is classified as relaxed only if both lines are below the two dotted thresholds, and otherwise as active. Same colors for each cluster as in Fig. 8.2.

criterion of the mass enclosed in substructures ensures that the clusters can also be classified as active under such a condition.

Some clusters such as g14 (green) or g63 (purple) remain active or relaxed, respectively, at all redshifts. Other clusters such as g55 (dark blue) can change their dynamical state over time, becoming active after larger mergers, but becoming relaxed again soon after.

There are only minor differences between the two hydro-methods. In particular, the mass enclosed in substructures is slightly smaller for MFM compared to that of SPH, but this does not change the dynamical state classification. Overall, using two criteria allows for a stable classification of the dynamical state.

8.4 Velocity Structure

A more turbulent structure of the ICM for MFM compared to SPH is already visible from the surface density fluctuations. A more direct tracer is the velocity structure. In the upper part of Fig. 8.5 we show the solenoidal velocity component in a slice through the g55 cluster. As expected, the global structure is qualitatively very similar between MFM and SPH. A strong increase can be found within a small region at the lower left. The total velocity shows that this region also has a very high infall velocity in general.

Quantitatively MFM leads to higher velocities on average, and regions of large velocities are more extended. In addition, MFM has finer structures in the central region, which can be a result of more turbulent structure and also the effectively higher resolution due to the smaller neighbor number.

The even more direct tracer for turbulence is the filtered velocity, shown in lower panels of Fig. 8.5. The patterns are similar to the solenoidal component, especially in the center. Nevertheless, the filtered velocity has a much lower maximum and does not show a strong increase within the accreting region. These differences persist and become clearer when averaging the absolute value within spherical shells, as shown in Fig. 8.6. Differences between MFM and SPH are small, but a slight increase for MFM in the solenoidal and filtered components is visible.

While turbulence is mainly solenoidal (compare, e.g., Vazza et al., 2017), also other solenoidal motions can be present in the ICM. Thus, the solenoidal component is a possible tracer of turbulence, but it tends to overestimate the turbulent velocity compared to the filtered one for almost every cluster.

8.5 Turbulent Pressure Fractions

Finally, we can use the methods described in Sec. 8.2 to derive non-thermal/turbulent pressure fractions. We start by showing values at two individual redshifts, i.e. at $z = 0$ and $z = 0.33$, in Fig. 8.7, to better compare to observations that typically cover a narrow redshift range.

A strong scatter is present as the number of clusters used for averaging is small. Only two of the clusters are relaxed at redshift $z = 0$, and five of them are active. Single outliers and timings of ongoing mergers can significantly influence the value. We find an increase in non-thermal pressure towards the outskirts, where the cluster is not in equilibrium but dominated by bulk, turbulent motions, and the presence of a larger number of substructures.

All the methods predict a non-zero turbulent pressure fraction with only a few exceptions. Due to the strong scatter, no clear differences are visible between the individual analysis methods. In addition, there are no clear trends for the turbulent pressure fraction with redshift. We find some increase in turbulent pressure for active clusters compared to relaxed ones, where this seems to be even stronger for MFM compared to SPH. Relaxed clusters have on average only a few percent of turbulent pressure support, while active ones can have up to $\approx 20\%$. Nevertheless, these trends are not significant and all non-thermal pressure profiles are consistent within the strong scatter among individual clusters.

A clearer picture arises when averaging over redshifts $0.43 \geq z \geq 0$, as shown in Fig. 8.8. We include different data from the literature as a comparison, including X-ray observations in the Perseus cluster (Hitomi Collaboration et al., 2016, 2018), averages from the X-COP sample (Eckert et al., 2019), as well as the observations and "The 300 simulations" (Cui et al., 2018) analyzed by Sayers et al. (2021). These span a wide range of possible turbulent pressure fractions from $P_{\rm nt}/P_{\rm tot} = 0$ up to ≈ 0.13.

All the methods predict an increase in the outskirts consistent with the observations by Sayers et al. (2021), but stronger than for their simulation results. We typically find pressure values greater than zero, but still consistent with zero within the cluster-to-cluster and redshift-to-redshift scatter, which is typically around 0.08. The average 1σ scatter within $0.1\,R_{200}$ for each method is indicated by a bar on the left of each panel.

For the relaxed clusters, we find turbulent pressure values smaller than "The 300 simulations" analyzed by Sayers et al. (2021) within the central region. Differences can be attributed to not

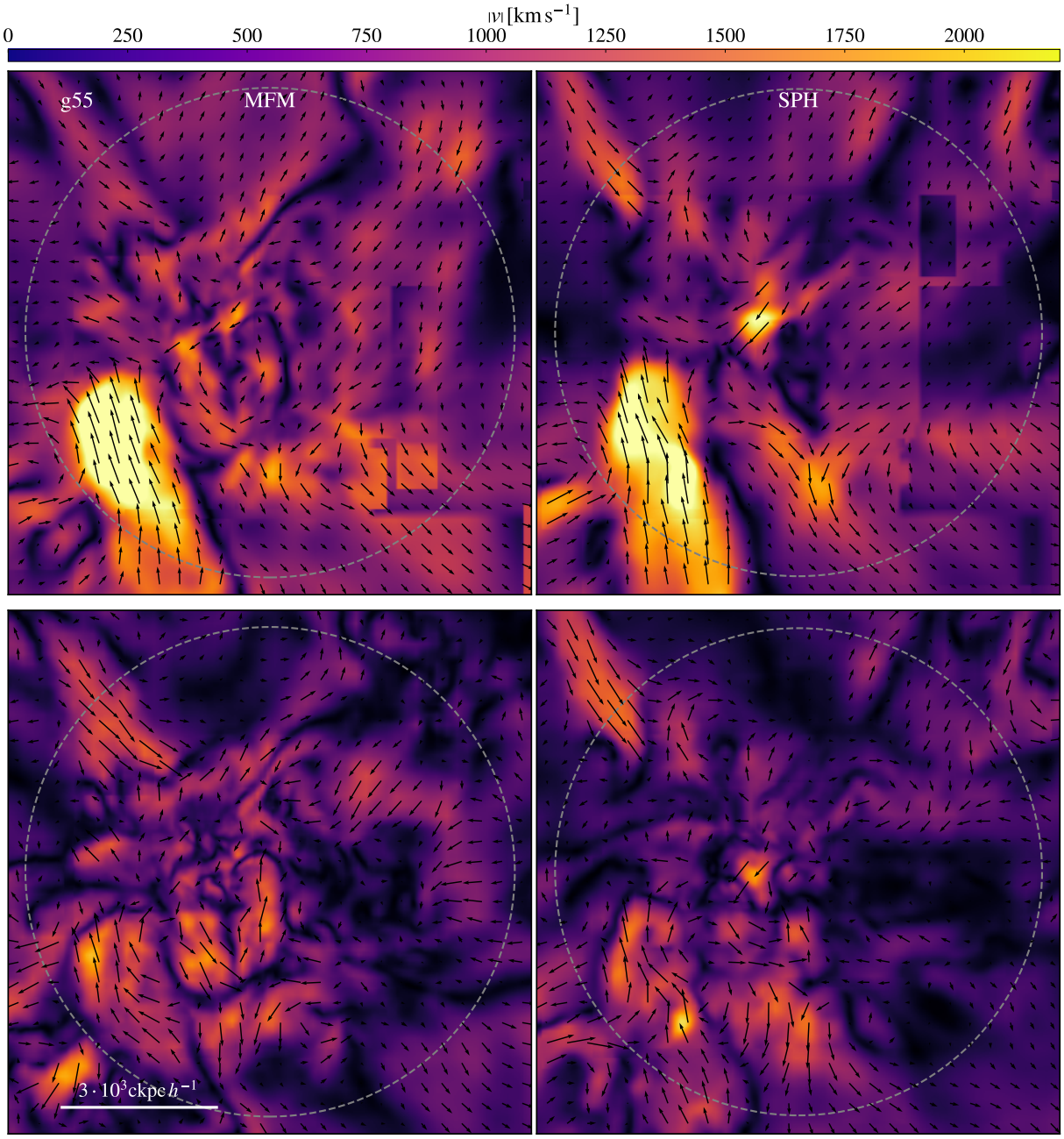

Figure 8.5: Slice through the g55 cluster at redshift $z = 0$, showing the rotational component of the velocity in the upper panel and the multi-scale filtered velocity in the lower panel, each comparing MFM and SPH. The color indicates the absolute value of the solenoidal/filtered velocity, while the quivers show the direction. The dashed circle marks R_{vir}.

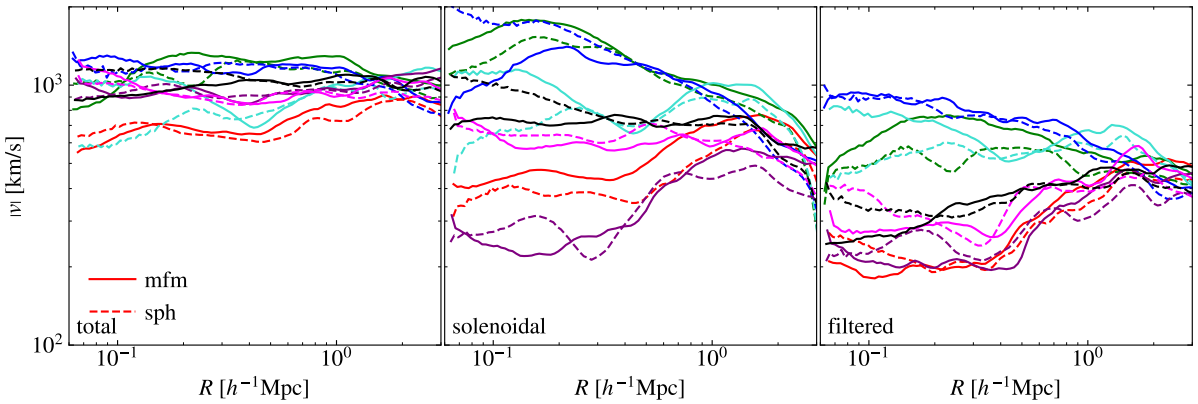

Figure 8.6: Velocity profiles of all the simulated GCs, at redshift $z = 0$. Same colors for each cluster as in Fig. 8.2.

including feedback processes in our simulations, which could potentially increase the amount of turbulence. Our results should thus be considered as lower limits. We find that the relaxed subsample is consistent with the spectral observations in the Perseus cluster (Hitomi Collaboration et al., 2016, 2018), which is often assumed to be relaxed in the center, even though showing tracers of activity in the outskirts.

Active clusters yield higher turbulent pressure values, more consistent with the simulations of the active clusters by Sayers et al. (2021). In general, our predictions, even though not including feedback processes, lie within the expected range of values found by other simulations and observations.

The Clump3d method analyzing the deviation from HE predicts a non-thermal pressure around $\lesssim 10\%$. It does not lie above the other two methods: rather, it lies below their predictions for MFM. This is opposed to the aim of the technique, which should indicate an upper limit for turbulence, as it also includes the non-thermal pressure contribution from bulk motions. A mild increase for active clusters compared to relaxed ones is present both for MFM and even stronger for SPH. Overall, the differences between hydro-methods are very small.

In contrast, the velocity-based methods show much clearer trends with the hydro-method and dynamical state. Interestingly, despite the radial velocity profiles showing a higher solenoidal velocity than the filtered one, we find the opposite trend for the pressure evaluated from the squared velocity. Nevertheless, the two methods produce very similar results. Relaxed clusters have a turbulent pressure fraction in the center of $2 - 4\%$. We find a strong increase in turbulent pressure for active clusters to $8 - 9\%$ for SPH, and even higher up to $9 - 13\%$ for the MFM simulation.

Overall, we find small, but non-negligible turbulent pressure fractions in all simulations, which are consistent with previous results.

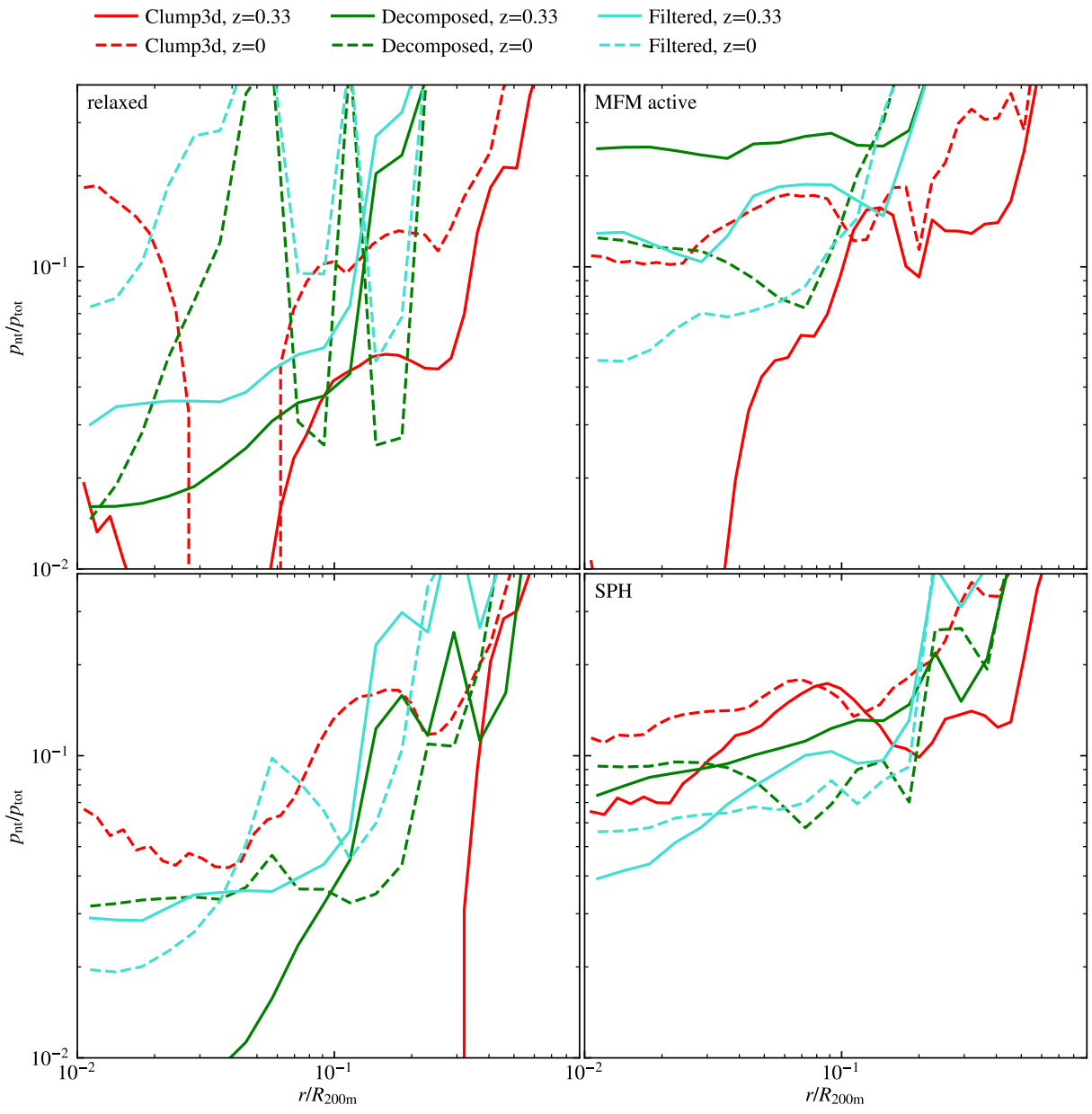

Figure 8.7: Turbulent pressure profile averaged over all clusters at redshift $z = 0.33$ and $z = 0$, comparing the three analysis methods: the Clump3d method, the solenoidal velocity component, and the multi-scale filtered velocity. The sample is split between dynamical states (left column: relaxed, right column: active) and hydro-methods (top row: MFM, bottom row: SPH) used for the simulation. The linestyle indicates the redshift, the color the analysis method. As only seven clusters are used for averaging, a strong scatter between individual clusters dominates the uncertainty.

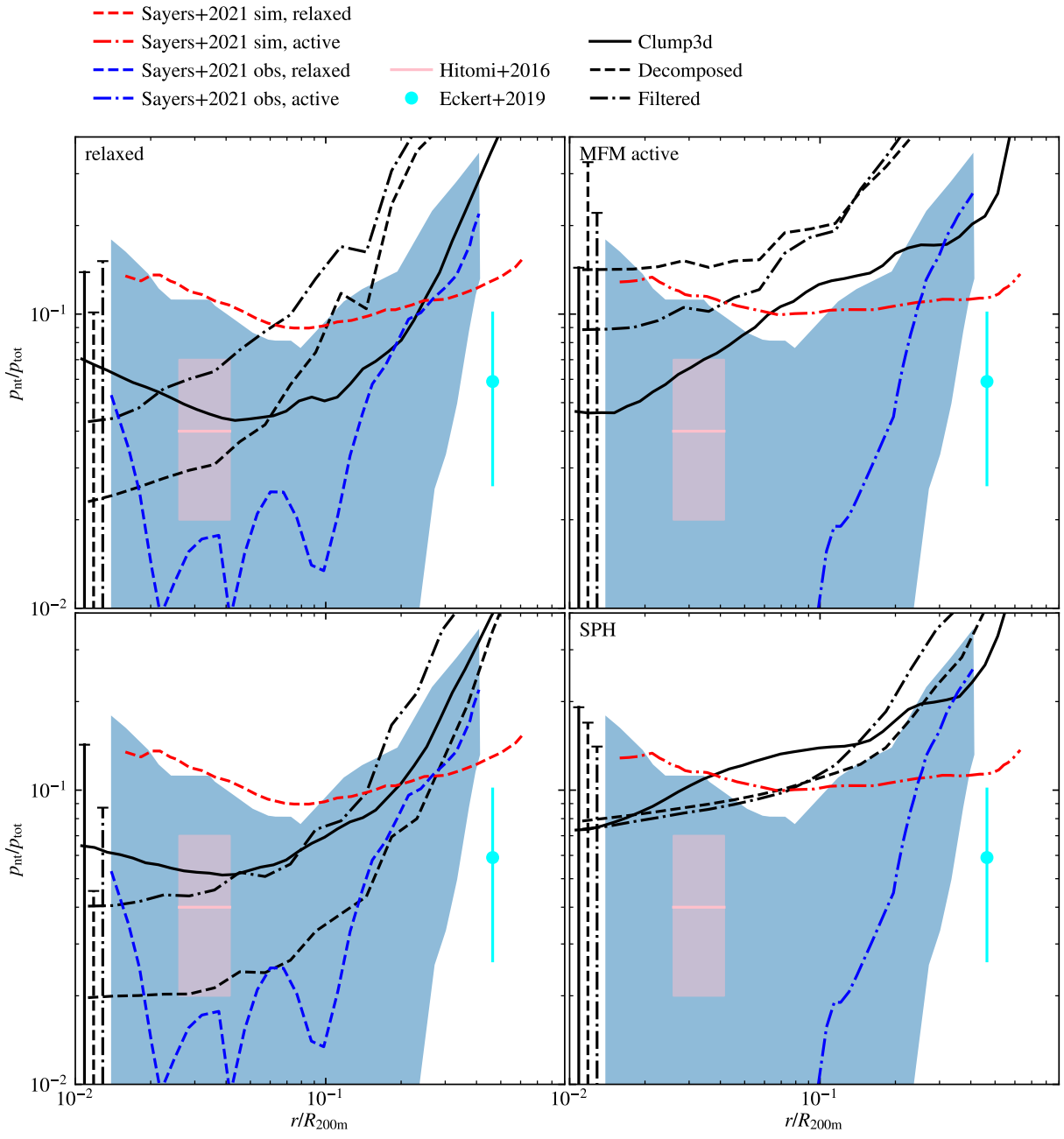

Figure 8.8: Turbulent pressure profile averaged over all clusters and redshifts $0.43 \geq z \geq 0$. The sample is split between dynamical states and hydro-methods used for the simulation, shown in the different panels. The solid line shows the results for the Clump3d analysis, the dashed line the pressure resulting from the solenoidal velocity component using the Helmholtz-decomposed velocity, and the dash-dotted line results from the multi-scale filtering.
The typical uncertainty is on the order of $\sigma = 0.08$ and indicated for each method with an errorbar on the left of each panel.

8.5.1 Velocity Distributions via Line Profiles

An alternative method to analyze the distribution of velocities is via line profiles, which also offers a more direct comparison to observational results. We follow a simplified approach, as described by Dolag et al. (2005b). When evaluating the line profile, the thermal broadening is ignored, and we focus purely on Doppler broadening due to velocity.

We assume a constant iron abundance and emissivity proportional to the density, independent of temperature

$$\epsilon \sim n_e^2 \Delta V \sim \rho. \tag{8.9}$$

The total emission is computed as the sum of all particles i within the virial radius and a cylinder in the direction of the sightline in z-direction with radius $r = 150\ h^{-1}\mathrm{kpc}$

$$I(\Delta E) = \sum_{i \in V} \epsilon_i \delta(\Delta E_i), \tag{8.10}$$

$$\Delta E_i = E_0 \frac{\sqrt{1-\beta_i^2}}{(1+\beta_i \cos\phi_i)}. \tag{8.11}$$

The energy of the line is shifted due to the relativistic Doppler shift with $\beta_i = |\boldsymbol{v}_i|/c$ and angle of the velocity with respect to the line of sight $\cos\phi_i = \left|\boldsymbol{v}_{\mathrm{los},i}\right|/|\boldsymbol{v}_i|$. As we neglect any thermal broadening, each individual line is described by a Dirac delta function δ. The impact parameter is varied between 0, 250 h^{-1}kpc and 500 h^{-1}kpc along the x-direction.

In Fig. 8.9, we show the corresponding profiles binned at a resolution of 1 eV for a 6.702 keV iron line for all our clusters. As the density is highest in the center, the intensity of the line profile looking through the cluster center is the highest, and it decreases as the profile is evaluated moving further from the GC center.

All line profiles are significantly broadened due to bulk- and turbulent motions by several 10 eV. Their shape can vary between close to Gaussian to highly irregular profiles, depending on the velocity structure. Clusters g14, g19, and g55, which have the highest turbulent velocities in the radial profiles shown in Fig. 8.6, also show the broadest and most irregular line profiles compared to more relaxed clusters.

Comparing the ratio of emissivity with MFM to SPH, we find that for many clusters, this ratio increases towards the wings of the line, which indicates that the distribution is broader for MFM compared to SPH. For several cases, this can be seen even from the line profile itself. An exception is cluster g63, where a secondary maximum appears for SPH, but not MFM. This is most likely connected to a substructure at that position. Also Dolag et al. (2005b) argue that this method is highly sensitive to the timing and position of substructures.

Overall, the line profiles confirm the previous findings that more turbulence is present for MFM compared to SPH. Even if the line profile includes information not only on the turbulent motion but also on bulk velocities, it is a good tracer of turbulence.

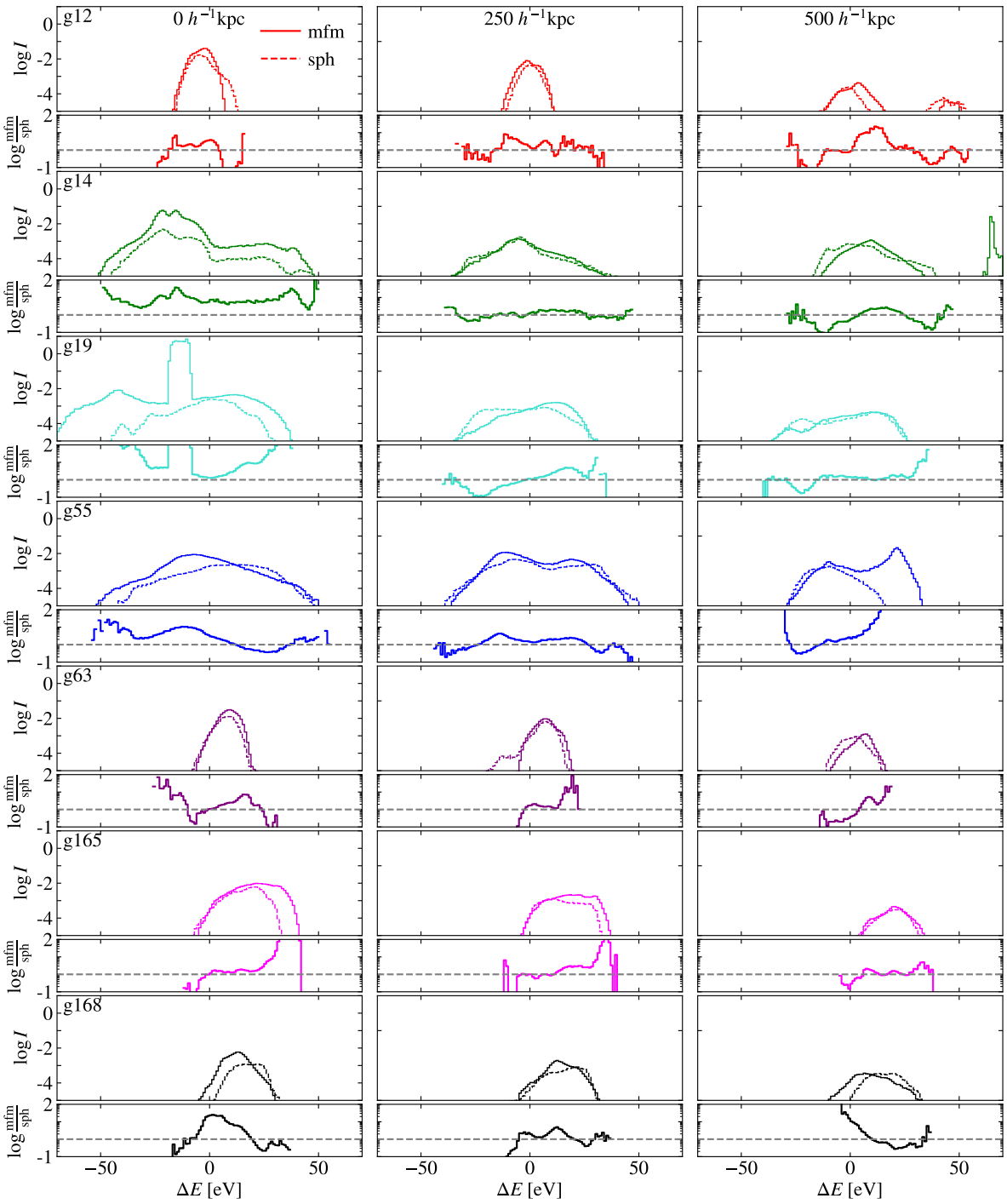

Figure 8.9: Line profiles of a 6.702 keV iron line for the different clusters at different distances from the cluster center (as written in each of the top panels). The intensity is in arbitrary units. For each panel, we also calculate the ratio between intensity for MFM and SPH to emphasize smaller differences.

8.6 Surface Density

In Fig. 8.10 we show the surface density of all clusters. More active clusters such as g14 or g19 show a lot of substructure, while more relaxed clusters such as g63 show much less substructure. In g14 even two distinct cores in the center are visible as tracers of a recent major merger.

8.7 Conclusions

We have analyzed the turbulent pressure support in GCs simulated with different hydro-methods, where the turbulence has been estimated in three different ways. Our set of zoom-in regions includes clusters at various dynamical states so that even using few clusters we can get meaningful results.

The amount of turbulent pressure can vary significantly depending on the analysis method which is employed. The multi-scale filtering is the most direct approach, as it filters out bulk motions depending on the local structure. Like the filtered velocity, also the solenoidal velocity is a tracer of the turbulent velocity. Compared to the filtered velocity, it is slightly less direct and shows some differences in radial velocity profiles and derived turbulent pressure. While the Clump3d method should predict an upper limit for the turbulence as it includes the effect of bulk motions, we find values similar to or even lower than those of the velocity-based methods. Possible explanations are limitations of the Clump3d method, which relies on several assumptions, or that not all solenoidal or small-scale motion acts as an actual source of pressure for the HE equation. To unquestionably assess the reason for this discrepancy, a more detailed analysis beyond the scope of this work is necessary.

Our setup allows us to compare hydro-methods for simulating turbulence in the ICM beyond idealized simulations, for the first time. The global structure is very similar between MFM and SPH, with differences on smaller scales. Visual inspection of the projected surface density reveals more small-scale density fluctuations for MFM compared to SPH. This can partly be explained by the effectively higher resolution for MFM, but also the better capturing of subsonic turbulence via the MFM scheme. Even though the reduced amount of small substructures for MFM is not statistically significant, this indicates more numerical dissipation and consequently more mixing for MFM.

Higher turbulent velocities are present for MFM than for SPH. Consistent with more idealized simulations, MFM predicts more turbulence for the velocity-based methods. For the Clump3d method, only minor differences are present.

Finally, we analyzed the impact of the dynamical state. By exploiting velocity-based methods, we find that active clusters have more turbulence than relaxed ones, in contrast to Sayers et al. (2021). Some differences with respect to their work can be attributed to feedback processes, which are not present in our simulations as we instead preferred to have a clearer setup. Stellar and AGN feedback can drive feedback on small scales, increasing the overall amount of turbulence. While AGN feedback affects the cluster mainly in the center, the effect of stellar feedback can be more widespread. Although not including feedback processes, the amount of turbulence we find in our simulations is consistent with the range of values found in previous works between a few

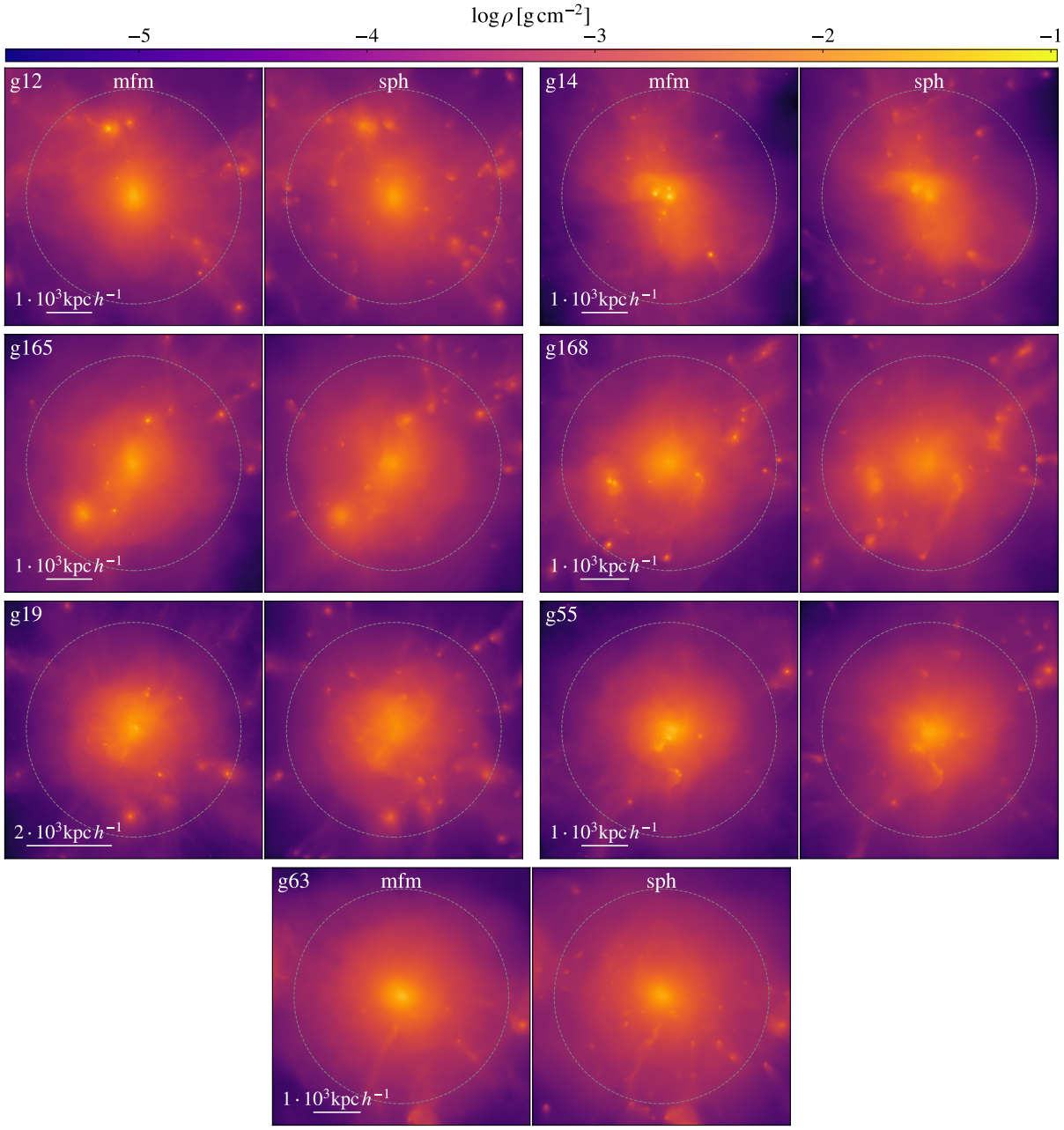

Figure 8.10: Projected gas density maps for all clusters analyzed in this work at redshift $z = 0$. The dashed circle denotes R_{vir}.

percent for relaxed clusters and up to $\approx 13\%$ in the center for active clusters.

As the turbulent pressure increases towards the outskirts, the hydrostatic bias at the X-ray boundary around $R_{500} \approx 0.7R_{200}$, where the signal is obtained by observations, is small, but non-negligible. We don't expect this result to change due to feedback processes.

As a final remark, we stress that it is key to quantify which are the discrepancies among different simulations and analysis techniques, and why they arise: this allows us to understand their (possibly different) predicted non-thermal or turbulent pressure support.

8.7.1 Outlook

While this work focused on a clean setup using purely hydrodynamical simulations, the inclusion of additional physical processes might partly change the picture. Especially, cooling would act as a sink for energy. Star formation, stellar, and AGN feedback in contrast would act as small-scale drivers of turbulence. As feedback processes self-regulate, they might also reduce differences between hydro-methods. More studies including feedback processes would be necessary to confirm our findings beyond non-radiative simulations. In addition, this could give further insight into the expected amount of turbulence in real GCs.

Also the inclusion of magnetic fields would provide an additional channel to study turbulence, as they closely couple via the dynamo effect. In addition, they can change the shape of turbulence and leave an imprint on the power spectrum.

9 | Turbulence in Local Universe Clusters

A new class of ICs for simulations are constrained ICs. They are designed to reproduce our Universe not only statistically, but to include specific objects with their particular formation history as described in Sec. 4.1. One example are the Simulating the LOcal Web (SLOW) simulations by Dolag et al. (2023). Recently, also ICs for zoom-in simulations of several local GCs have been extracted (Seidel et al. in prep.).

For our analysis, we use simulations at a mass resolution of $M_{\rm gas} = 5.77 \cdot 10^7 h^{-1}{\rm M}_\odot$, $M_{\rm DM} = 3.10 \cdot 10^8 h^{-1}{\rm M}_\odot$, and gravitational softening length $\epsilon_{\rm gas} = 1.5\, h^{-1}$kpc, $\epsilon_{\rm DM} = 4.5\, h^{-1}$kpc. The background cosmology is based on Planck Collaboration et al. (2014) with $h = 0.6777$, $\Omega_{\rm m} = 0.307115$, $\Omega_{\rm b} = 0.0480217$, $\Omega_\Lambda = 0.692885$, and $\sigma_8 = 0.829$.

Simulations have been carried out with OpenGadget3 using modern SPH with time- and spatially dependent artificial viscosity (Beck et al., 2016b) and physical conduction (Arth et al., 2014), using a Wendland C6 kernel (Wendland, 1995; Dehnen & Aly, 2012) with 295 neighbors.

9.1 Turbulent Pressure

We use these simulated clusters to perform the multi-scale filtering analysis described in Sec. 8.2.4 and by Groth et al. (2024). Being the most direct analysis based on velocity data, this allows for a more direct comparison to the measured values of real clusters, in particular with the spectrally resolved observations by XRISM and previous Hitomi Collaboration et al. (2016, 2018).

In Fig. 9.1, we show the resulting turbulent pressure profile of 14 local universe clusters with a focus on Virgo, Coma, and Perseus. Most clusters in the sample are active, including Coma and Perseus. Virgo is considered relaxed. As our criteria of relaxation are based on larger scales, Perseus is also considered active, even if it shows some evidence of being relaxed in the center in observations. The general turbulent pressure fractions are consistent with the mean and (1σ) scatter of the Dianoga analysis shown as black line (Sec. 8.5, and Groth et al., 2024).

Even if the simulations do not include feedback processes, the turbulent pressure of Perseus is consistent with the Hitomi results. Virgo is even more relaxed, with a central turbulent pressure support below 1%. Coma is the most active cluster of the three.

Overall, these results will allow for a close comparison with the observations by XRISM.

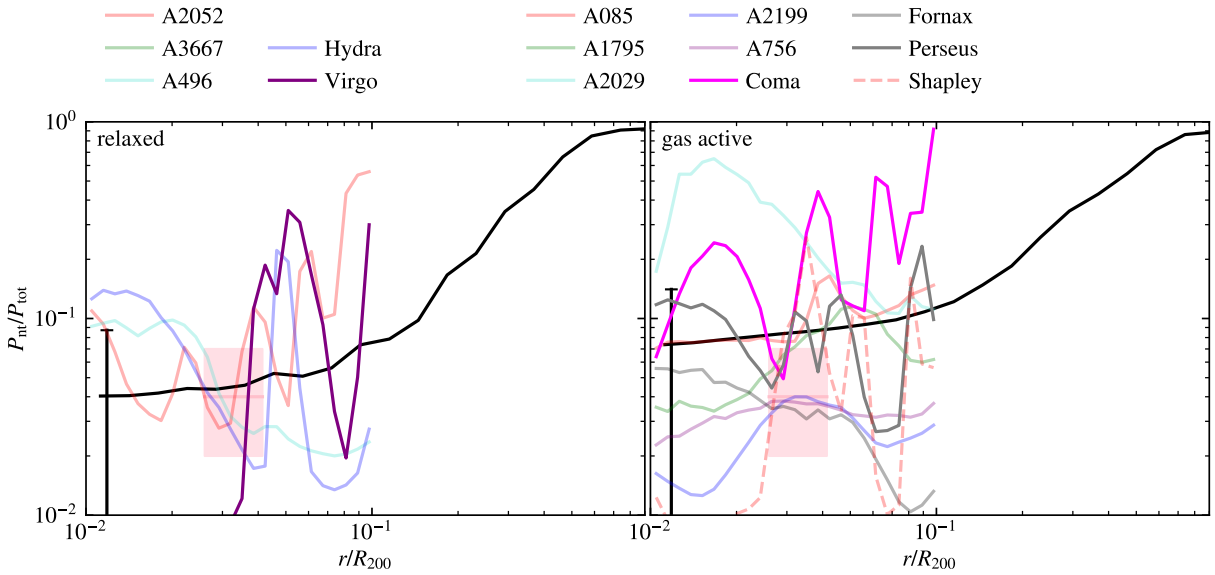

Figure 9.1: Turbulent pressure fraction of GCs in the local universe from the SLOW zoom-in regions (Seidel et al. in prep) with a focus on Virgo, Coma, and Perseus. The clusters are divided into relaxed (left) and active (right) clusters. As a comparison, the mean non-thermal pressure support of the Dianoga clusters simulated with SPH by Groth et al. (2024) (black line) is shown.

9.2 Line Profiles

As for the Dianoga clusters, we generate line profiles for the simulated clusters in the local universe. We follow the method described in Sec. 8.5.1 and by Groth et al. (2024), focusing on only a single central beam of radius 150 h^{-1}kpc.

The resulting line profiles are shown in Fig. 9.2. Significant turbulent broadening of several 10 eV can be observed for most of the clusters, mostly consistent with the turbulent pressure fractions. Out of the three clusters discussed above, Virgo has the most peaked line profile, though the broadening can be seen in the wings, followed by Perseus. Coma has the strongest broadening due to multiple substructures in the central region.

These results can give first expectations for observations, but an analysis beyond the simplified calculation of the profiles, including thermal broadening, emissivities, and correct pre-factors would be necessary for a direct comparison.

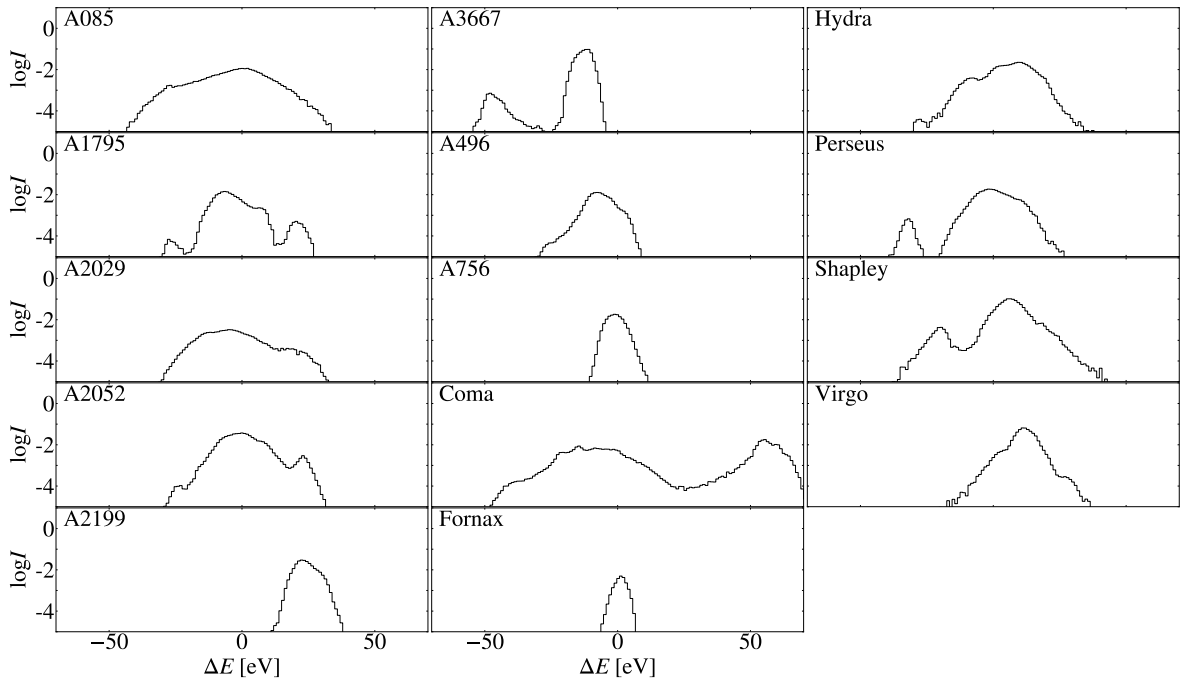

Figure 9.2: Line profiles calculated for a 150 kpch^{-1} beam through the center for simulated local-universe clusters.

Part IV

Outlook & Conclusion

10 | Conclusion

In this work, we presented a new implementation of MFM in the code OpenGadget3 as an alternative to the previously implemented SPH. Our implementation produces stable results in idealized simulations, as well as zoom-in simulations of GCs.

In Sec. 5 (also published by Groth et al., 2023) extensive tests have been carried out to probe the capabilities of the new implementation. In addition, we performed a detailed and fair comparison with other hydrodynamical methods, including SPH in OpenGadget3, moving mesh code Arepo, and another MFM implementation in gizmo. General agreement is found with gizmo, with minor differences due to the different Riemann solver and other details of the implementation.

The convergence is between first and second order, and better than for SPH. At fixed mass resolution it runs at similar computational costs as SPH. The more expensive iterative, exact Riemann solver is compensated by requiring less neighbors. Compared to a moving mesh, the main advantage is not having to calculate the mesh reconstruction, making MFM much cheaper in comparison.

The incorporation of a Riemann solver allows accurate capture of mixing instabilities without additional parameters such as artificial viscosity or conductivity. This will improve the simulation of galaxies in the environment of GCs, where ram pressure stripping occurs in the interaction between ISM and ICM. An effectively higher spatial resolution due to the smaller neighbor number and kernel size further improves results. MFM produces good results for shocks at various Mach numbers. Due to the effectively higher resolution, the shock front is narrower. This should result in better shock capturing for MFM. At very high Mach numbers, effects of surface tension due to the slope limiter become visible.

MFM performs very well on decaying subsonic turbulence. The turbulent cascade is captured accurately down to a very small Mach number $\mathcal{M} = 0.01$, and is the best among all other hydro-methods compared to in this work. This will be of great importance to study turbulence in the ICM.

In Sec. 6 we presented a preliminary MHD implementation. Divergence cleaning already works very well, but some additional work is required for full usage. Also different sub-resolution models have been coupled and lead to consistent results with SPH. Overall, the incorporation of additional physics in simulations will allow one to obtain more realistic systems.

Additional improvements have been summarized in Sec. 7. Some of them lead to a cleanup of the codebase of OpenGadget3, but other improvements such as the pairwise flux calculation also lead to a speedup. The measured improvement in runtime in realistic simulations is $\approx 10\%$,

smaller than the theoretical maximum of factor 2, but still significant. The improved implementation allows to make efficient use of hybrid MPI-OpenMP parallelization in OpenGadget3. New boundary conditions make MFM zoom-in simulations more stable at high resolution.

We applied the newly implemented MFM to zoom-in simulations of GCs in Sec. 8 (also published by Groth et al., 2024) to study turbulent pressure support in the ICM. A comparison between MFM and SPH underlines the importance of the hydrodynamical method. For the first time, this work allows us to assess the differences beyond idealized simulations. Many findings from visual inspection such as increased mixing agree with results from idealized simulations. More turbulence is found in simulations with MFM compared to SPH, consistent with the better capturing of the turbulent cascade in turbulent box simulations.

Our work also shows the importance of understanding the differences between various analysis methods. The Clump3d method returns a non-thermal pressure, while the velocity-based methods return a turbulent pressure. Thus, they can lead to different results. In our analysis, the non-thermal pressure can be even lower than the turbulent pressure. This can be explained by the fact that not all small-scale motions act as pressure or by limitations of the Clump3d method. Further analysis will be necessary to fully understand the differences. The multi-scale filtered velocity is the most direct approach. We found that the solenoidal component is on average a very good approximation, which is computationally cheaper to calculate. Nevertheless, differences can be observed in specific regions of the ICM.

We find an influence of the dynamical state on the turbulent pressure support. The amount of turbulence is higher for more active clusters compared to more relaxed ones in contrast to some previous results (e.g., Sayers et al., 2021). Including feedback processes might reduce differences between dynamical states and hydrodynamical methods as they act as additional turbulence drivers on smaller scales. The turbulent pressure support ranges between a few percent in relaxed clusters up to $\approx$ 13% for active clusters. As it increases towards the outskirts, the hydrostatic bias, typically measured within $R_{500} \approx 0.7 R_{200}$, is small but non-negligible.

The increased turbulence for more active clusters compared to more relaxed ones as well as MFM compared to SPH also manifests in the broadening of the line profiles. Overall, it is important to understand the differences between simulations and analysis methods when comparing different predictions of turbulent or non-thermal pressure fractions.

In Sec. 9 we extended the analysis to simulated clusters from the local universe. Measured values are consistent with results from the Dianoga set. Studying local universe clusters gives the unique opportunity to compare more directly to observations. We find astonishing agreement between our simulated Perseus cluster with observations of the real Perseus cluster from our Universe, even if our simulations miss additional physical processes.

Overall, MFM is a very useful method to model a variety of systems and scales, and subsonic turbulence in particular. Thus, it will be a valuable addition to the OpenGadget3 code for many future applications.

11 | Outlook

11.1 Coupling to Subgrid Models

Many of the subgrid models have already been coupled to MFM and are ready to use. Nevertheless, some additional physics is still remaining. As presented in Sec. 6.1, the MHD implementation in OpenGadget3 is still preliminary, and more work will be necessary to allow its full usage.

Hydrodynamical tests show that MFM can accurately capture mixing instabilities. Thus, we expect a similar performance on MHD instabilities such as the magnetothermal or heat-flux-driven buoyancy instability (McCourt et al., 2012) that play a role in the weakly magnetized plasma of the ICM on small scales. Even though not resolved in current simulations, with increasing resolution this could become more important. In addition, AGN jets are prone to several hydrodynamical and MHD instabilities. Heating by AGN feedback can lead to convective instabilities and rising AGN bubbles (Chandran, 2004, 2005). Thus, the correct handling of these is of great importance for small-scale simulations of these systems and to better understand AGN feedback. These can ultimately be used to inform sub-resolution models for simulations at larger scales.

The star formation model by Tornatore et al. (2003, 2004, 2007) also includes chemical evolution. If only used as passive tracers, the model should work by default, even though some testing would be desirable. With changing chemical composition also the adiabatic index γ and with it the equation of state would change on a particle-to-particle base. As implemented now, γ is a constant, and some restructuring of the code will be necessary to make it more flexible.

Finally, OpenGadget3 contains the flexible spectral CR model CRESCENDO (Böss et al., 2023). As for the chemical evolution, CRs as passive tracers should work without problems. Additional work is required to allow the usage with full physical implications. CRs change the adiabatic index and exert additional pressure on their surroundings. The former can be coupled in the same way as the chemical evolution. Coupling of the latter could be done in two different ways. At first, an approach similar to SPH can be chosen. The evolution of CRs is decoupled from the gas following an operator splitting approach. The CR pressure is added as an additional term to the MHD equations. As an alternative, a CR Riemann solver can be utilized, evolving CRs and gas together. Such solvers have already been developed (e.g., Pfrommer et al., 2006; Kudoh & Hanawa, 2016). Nevertheless, these are only designed for gray CR models. The spectral distribution could be translated into effective gray CR values, translating it back to obtain changes in the CR spectrum. This is most likely more complex and could cause some loss of information in the process of translating to gray values. Thus, the first method would be preferred as a first attempt.

11.2 Further Numerical Improvements

In addition to improvements to the code described in this work, many more improvements are possible. The shockfinder used in OpenGadget3 is based on the description by Beck et al. (2016a). For MFM, a more direct approach is conceivable. Each interaction is based on a Riemann solver, which internally relies on assuming a shock structure. The effective Mach number of interactions could be used as an indicator for shocks and their Mach number, with the direction derived from the neighbor distribution.

With modern computer architectures relying more and more on GPUs, MFM should be included in the modules executable on GPUs. Challenges are mainly the parallelization approach, which is slightly different to the paradigms of CPU parallelization, and memory management, as less memory is available on a typical GPU compared to CPU infrastructures. A general OpenACC implementation within OpenGadget3 has been described by Ragagnin et al. (2020). This should be extendable rather directly to the MFM module in the same way as done for SPH. An Intel-compatible OpenMP GPU implementation is still in development, so far only for the gravity calculation. A GPU implementation will likely not work with the pairwise flux calculation, as the local particle data is used as input only, and output data is stored and communicated separately. Also the usage of OpenMP locks is not compatible with GPU parallelization approaches. Nevertheless, the expected speedup by $\gtrsim 3$ (Ragagnin et al., 2020) is higher than the effect of the previous improvement.

11.3 Turbulence Beyond Pure Hydrodynamics

Our analysis of ICM turbulence is so far based on purely hydrodynamical simulations. While this provides the cleanest setup, additional physics is required to obtain more realistic systems. SN and AGN feedback should drive up turbulence while cooling acts as an energy sink. Overall, we expect the inclusion of these processes to reduce differences between hydro-methods, as self-regulation of star formation occurs. The overall amount of turbulence should increase, especially in the center if AGN feedback is active. In combination with more extended SN feedback, this could potentially reduce differences to "The 300 simulations" analyzed by Sayers et al. (2021).

Studying the turbulent power spectrum could provide more information on the turbulent cascade, including the injection scale and the (numerical) dissipation range. As the power at large scales is dominated by bulk motions, the solenoidal or multi-scale filtered velocity should be used as a more unbiased tracer of turbulence.

Magnetic fields will change the power spectrum of turbulence. In addition, turbulence couples to magnetic fields via the turbulent dynamo, which should thus be more effective with MFM. Overall, magnetic fields should be included to obtain a more realistic environment.

A final goal for the simulations would be to include all available subgrid models in OpenGadget3 that can potentially affect turbulence, including the previously mentioned ones, physical anisotropic viscosity (Sijacki & Springel, 2006; Marin-Gilabert et al., 2022, 2024), and CRs.

In addition to including more physics, simulations at higher resolution can open possibilities of a convergence study of the results. We don't expect strong changes as most of the turbulence

power is on larger scales and we did not see hints of systematic changes from the local universe simulations compared to the Dianoga ones, which increased the resolution by ≈ 3. As these are different clusters and also a different background cosmology was chosen, a more sophisticated analysis of the same system at different resolution will be required.

With modern X-ray telescopes such as eROSITA (Bulbul et al., 2024) or the upcoming Athena (Barret et al., 2018), sensitivity is high enough to also resolve galaxy groups. Also potential telescopes that are still in the proposal stage such as AXIS (Reynolds et al., 2023) or LEM (Kraft et al., 2022) can be used for observations of galaxy groups if one of them gets accepted for construction. Information on gas dynamics can be extracted from spectral information using Athena even for systems at a group scale. In addition to the different mass scales, the ratio between AGN and SN feedback does change. Within the shallower gravitational potential of the intra-group medium (IGM) AGN feedback becomes more important, such that the combination of clusters and groups will be an ideal testbed for studying the individual effects of each feedback process.

11.4 Results in (X-ray) Light of Upcoming XRISM Results

We live in a time of rapid development, both of numerical and observational capabilities. New X-ray observations and the current X-ray Imaging and Spectroscopy Mission (XRISM) in particular will give valuable insight into gas dynamics, in combination with numerical studies such as our analysis of turbulence in the ICM.

So far, most observational approaches have relied on rather indirect methods to determine the turbulent or non-thermal pressure. One example is the study by Churazov et al. (2008), who studied the non-thermal pressure in the central galaxy of the Fornax cluster based on the potential derived from optical and X-ray observations. The upper limit of the non-thermal pressure is around 10% and is even consistent with zero within the uncertainty. It is consistent with many other results previously cited in Sec. 1.2.4. The non-thermal pressure includes effects of turbulence, but also magnetic fields, bulk motions, and CRs such that it provides an upper limit for the turbulent pressure.

One exception was the study by Hitomi Collaboration et al. (2016, 2018). Exploiting spectrally resolved lines allowed them to study the ICM gas dynamics more directly and with much improved accuracy. However, due to technical problems, they could only perform a single observation in the Perseus clusters, finding very low turbulent velocities on the order of 187 ± 13 km/s in the core and 164 ± 10 km/s in the outer region, leading to pressure fractions in the center of only $\approx 4\%$ compared to the thermal pressure.

It showcased the amazing resolution possible with the instruments. The XRISM instrument (XRISM Science Team, 2022; Sato et al., 2023) was built and began to take first observations to continue the great scientific success. The technology is similar to the one included in Hitomi, yet with some modifications and improvements.

XRISM contains two instruments: The X-ray CCD "Xtend" and the micro calorimeter "Resolve". "Xtend" provides an angular resolution of 1.7 arcmin a wide field of view of 38×38 arcmin^2. In addition, it has a spectroscopic capability reaching a medium energy resolution

$E/\Delta E \approx 35@6\,\mathrm{keV}$.

The "Resolve" spectrometer has a much smaller field of view of only 3×3 arcmin^2 consisting of 6×6 pixels, including one calibration pixel. As for Xtend, the angular resolution is limited by 1.7 arcmin. The core strength of this instrument is the high spectral resolution. It was designed to achieve a full-width-half-maximum line resolution of $< 7\,\mathrm{eV}$ within the $0.3 - 12\,\mathrm{keV}$ range, and an absolute energy scale below 2 eV. When starting operation, the gate valve did not open, blocking light in the soft X-ray band and leading to a loss of capabilities in the low-energy part of the spectrum. The range is effectively restricted to $\geq 1800\,\mathrm{eV}$ (Kazmierczak, 2024). In contrast, at higher energies first tests showed that the instrument even outperforms the requirements at a spectral resolution of 5 eV.

The scientific objectives of the mission (XRISM Science Team, 2022) include the line emission from AGN winds to investigate feedback processes, and SN remnants to understand their progenitors better and use them as laboratories for collisionless shocks and radiative processes. Most relevant to our work are planned observations of GCs, studying AGN-ICM interactions and the non-thermal pressure support. Turbulent line broadening observed using the Resolve instrument gives direct insight into small-scale turbulent velocities.

As showcased in Sec. 8.5.1 and 9.2 for simulated clusters, this resolution will allow for a precise determination of small-scale velocities. Even if our assumed resolution is higher than the real resolution by XRISM, the broadening of several 10 eV for most clusters to about 100 eV for Coma is sufficiently larger than the 5 eV resolution.

Compared to our multi-scale filtering approach, derived velocities from the line broadening correspond to a constant filtering length analysis, which can lead to differences in the resulting turbulent pressure values. At the distance of the clusters, the (half) angular resolution of 1.7/2 arcmin= 0.85 arcmin corresponds to a beam size of 250 kpc ($z = 0.023997$) for Coma, 190 kpc ($z = 0.01767$) for Perseus, and 47 kpc ($z = 0.04283$) for Virgo[1]. Thus, Virgo has a much smaller resolved scale than the beam size in our analysis ($150\,h^{-1}$kpc$\approx$ 220 kpc), while Coma and Perseus have a similar resolution. The strongest difference is expected for Virgo, which is the closest cluster to us. In general, due to the smaller filtering scale Perseus and Virgo should have a smaller broadening because more motion on larger scales is filtered out, while Coma should have an even larger broadening.

Also for the turbulent pressure analysis some differences would be expected. The multi-scale filtering length in the central region is between $30\,h^{-1}$kpc and $1700\,h^{-1}$kpc for the three clusters. Thus, the XRISM resolution is within the range of filtering lengths. Some bulk motions of smaller structures at scales smaller than the XRISM resolution might still be contained in the measured velocities, while other larger-scale turbulent motions are filtered out. The overall effect on the measured turbulent pressure is unclear. A more detailed analysis of our results also with a constant filtering length of comparable size would be necessary for an even closer comparison.

Several clusters that are included in our sample of simulated clusters from the local universe presented in Sec. 9 will also be covered by XRISM. Already the performance verification targets[2]

[1] Redshift from NASA/IPAC Extragalactic Database `http://ned.ipac.caltech.edu/`. Retrieved 2024-09-18.

[2] Published at `https://xrism.isas.jaxa.jp/research/proposer/approved/pv/index.html`, accessed 2024-09-14

include several pointings within Coma, Virgo, and Perseus. Even more are yet to come in the first observation phase[3].

The first results presented at conferences are consistent with previous upper limits such as the one by Churazov et al. (2008) and confirm the general findings summarized in Sec. 1.2.4. Differences in the structure of different GCs can now be interpreted in terms of measured velocities.

Our work lays the foundation for the correct interpretation of these results and a proper comparison with previous findings. In addition, upcoming observations can be used as validation for numerical studies, giving more direct access to the small scales via the turbulence. We can look forward to exciting times, with increasing synergies between simulations and observations.

[3]Published at `https://xrism.isas.jaxa.jp/research/proposer/approved/ao1/index_0801b.html`, accessed 2024-09-14.

A | Appendix

A.1 Flowchart of the OpenGadget3 Code Structure

We present a flowchart diagram of the structure of OpenGadget3 in Fig. A.1.1.

The two central functions called within CodeBase/main.c are begrun and run. The former is responsible for the initial setup, the latter performs the actual simulation via the iteration over all timesteps. The main variables that are updated within each function are shown next to the function name.

Depending on whether MFM or SPH is used for a simulation, different hydrodynamical functions are called. The gradient calculation is shared between the two, calculating SPH-like gradients together with the MFM ones directly after the smoothing length iteration. For SPH, it follows the calculation of hydrodynamical accelerations. For MFM, the limiter calculation is necessary as an intermediate step, before the fluxes can be calculated. As the GIZMO limiter does not require an additional neighbor loop, overall no additional neighbor loop is necessary for MFM compared to the SPH implementation.

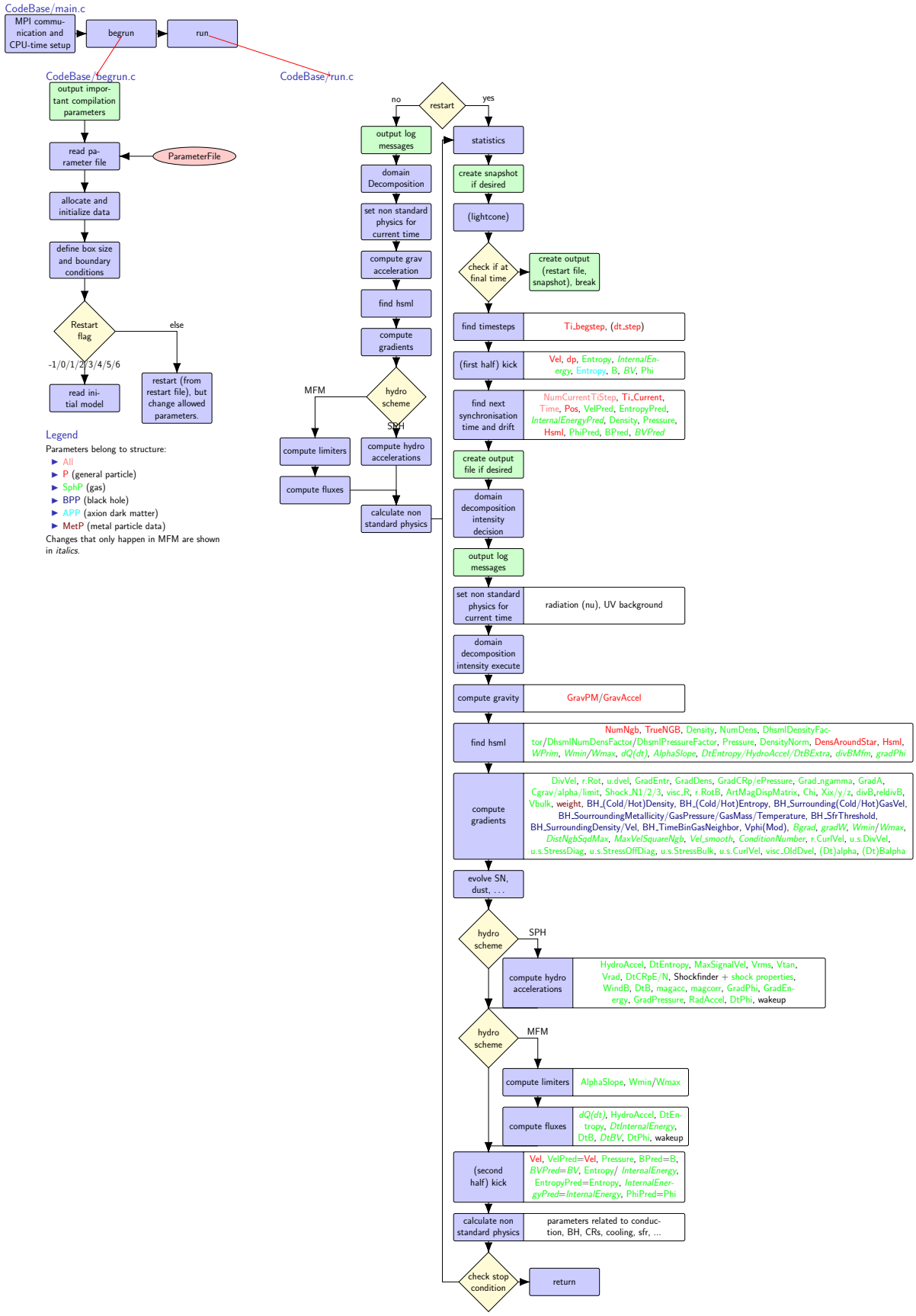

Figure A.1.1: Flowchart of the structure of OpenGadget3. The main.c file contains two functions, the begrun function pointing to begrun.c, and the run function pointing to run.c, each shown in more detail.

Bibliography

Abdalla, E., Abellán, G. F., Aboubrahim, A., et al. (2022), *Cosmology Intertwined: A Review of the Particle Physics, Astrophysics, and Cosmology Associated with the Cosmological Tensions and Anomalies*, Journal of High Energy Astrophysics, 34, 49

Abell, G. O. (1958), *The Distribution of Rich Clusters of Galaxies.*, The Astrophysical Journal Supplement Series, 3, 211

Agertz, O., Moore, B., Stadel, J., et al. (2007), *Fundamental Differences between SPH and Grid Methods*, Monthly Notices of the Royal Astronomical Society, 380, 963

Alam, S., Aubert, M., Avila, S., et al. (2021), *Completed SDSS-IV Extended Baryon Oscillation Spectroscopic Survey: Cosmological Implications from Two Decades of Spectroscopic Surveys at the Apache Point Observatory*, Physical Review D, 103, 083533

Alonso Asensio, I., Dalla Vecchia, C., Potter, D., and Stadel, J. (2023), *Mesh-Free Hydrodynamics in PKDGRAV3 for Galaxy Formation Simulations*, Monthly Notices of the Royal Astronomical Society, 519, 300

Alpher, R. A., Bethe, H., and Gamow, G. (1948), *The Origin of Chemical Elements*, Physical Review, 73, 803

Alpher, R. A. and Herman, R. (1948), *Evolution of the Universe*, Nature, 162(4124), 774

Angulo, R. E., Springel, V., White, S. D. M., et al. (2012), *Scaling Relations for Galaxy Clusters in the Millennium-XXL Simulation*, Monthly Notices of the Royal Astronomical Society, 426, 2046

Appel, A. W. (1985), *An Efficient Program for Many-Body Simulation*, SIAM Journal on Scientific and Statistical Computing, 6, 85

Arbey, A. and Mahmoudi, F. (2021), *Dark Matter and the Early Universe: A Review*, Progress in Particle and Nuclear Physics, 119, 103865

Arth, A., Dolag, K., Beck, A. M., et al. (2014), *Anisotropic Thermal Conduction in Galaxy Clusters with MHD in Gadget*

Balsara, D. S. (1998), *Total Variation Diminishing Scheme for Adiabatic and Isothermal Magnetohydrodynamics*, The Astrophysical Journal Supplement Series, 116, 133

Balsara, D. S. (2004), *Second-Order-accurate Schemes for Magnetohydrodynamics with Divergence-free Reconstruction*, The Astrophysical Journal Supplement Series, 151, 149

Barnes, J. and Hut, P. (1986), *A Hierarchical O(N Log N) Force-Calculation Algorithm*, Nature, 324, 446

Barret, D., Lam Trong, T., den Herder, J.-W., et al. (2018), *The ATHENA X-ray Integral Field Unit (X-IFU)*, in *Proceedings of the SPIE*, volume 10699, 106991G, eprint: arXiv:1807.06092

Barth, T. and Jespersen, D. (1989), *The Design and Application of Upwind Schemes on Unstructured Meshes*, in *27th Aerospace Sciences Meeting*, American Institute of Aeronautics and Astronautics

Bauer, A. and Springel, V. (2012), *Subsonic Turbulence in Smoothed Particle Hydrodynamics and Moving-Mesh Simulations*, Monthly Notices of the Royal Astronomical Society, 423(3), 2558

Beck, A. M., Dolag, K., and Donnert, J. M. F. (2016a), *Geometrical On-the-Fly Shock Detection in Smoothed Particle Hydrodynamics*, Monthly Notices of the Royal Astronomical Society, 458(2), 2080

Beck, A. M., Murante, G., Arth, A., et al. (2016b), *An Improved SPH Scheme for Cosmological Simulations*, Monthly Notices of the Royal Astronomical Society, 455, 2110

Berger, M. J. and Colella, P. (1989), *Local Adaptive Mesh Refinement for Shock Hydrodynamics*, Journal of Computational Physics, 82, 64

Berger, M. J. and Oliger, J. (1984), *Adaptive Mesh Refinement for Hyperbolic Partial Differential Equations*, Journal of Computational Physics, 53, 484

Berlok, T. (2022), *Hydromagnetic Waves in an Expanding Universe – Cosmological MHD Code Tests Using Analytic Solutions*, arXiv:2203.11887 [astro-ph]

Bezanson, J., Edelman, A., Karpinski, S., and Shah, V. B. (2014), *Julia: A Fresh Approach to Numerical Computing*

Biffi, V., Borgani, S., Murante, G., et al. (2016), *On the Nature of Hydrostatic Equilibrium in Galaxy Clusters*, The Astrophysical Journal, 827, 112

Biffi, V., Dolag, K., and Böhringer, H. (2011), *Velocity Structure Diagnostics of Simulated Galaxy Clusters*, Monthly Notices of the Royal Astronomical Society, 413, 573

Biffi, V., Planelles, S., Borgani, S., et al. (2017), *The History of Chemical Enrichment in the Intracluster Medium from Cosmological Simulations*, Monthly Notices of the Royal Astronomical Society, 468, 531

Biffi, V., Sembolini, F., De Petris, M., et al. (2014), *The MUSIC of Galaxy Clusters - II. X-ray Global Properties and Scaling Relations*, Monthly Notices of the Royal Astronomical Society, 439, 588

Biffi, V. and Valdarnini, R. (2015), *The Role of the Artificial Conductivity in SPH Simulations of Galaxy Clusters: Effects on the ICM Properties*, Monthly Notices of the Royal Astronomical Society, 446, 2802

Biron, L. (2024), *First Results from DESI Make the Most Precise Measurement of Our Expanding Universe*, https://newscenter.lbl.gov/2024/04/04/desi-first-results-make-most-precise-measurement-of-expanding-universe/

Bode, P., Ostriker, J. P., and Xu, G. (2000), *The Tree Particle-Mesh N-Body Gravity Solver*, The Astrophysical Journal Supplement Series, 128, 561

Boggess, N. W., Mather, J. C., Weiss, R., et al. (1992), *The COBE Mission: Its Design and Performance Two Years after Launch*, The Astrophysical Journal, 397, 420

Böhringer, H. and Werner, N. (2010), *X-Ray Spectroscopy of Galaxy Clusters: Studying Astrophysical Processes in the Largest Celestial Laboratories*, Astronomy and Astrophysics Review, 18, 127

Bonafede, A., Dolag, K., Stasyszyn, F., et al. (2011a), *A Non-Ideal Magnetohydrodynamic GADGET: Simulating Massive Galaxy Clusters*, Monthly Notices of the Royal Astronomical Society, 418, 2234

Bonafede, A., Govoni, F., Feretti, L., et al. (2011b), *Magnetic Field in Galaxy Clusters from Depolarization of Radio Sources.*, Memorie della Societa Astronomica Italiana, 82, 654

Bonafede, A., Vazza, F., Brüggen, M., et al. (2013), *Measurements and Simulation of Faraday Rotation across the Coma Radio Relic*, Monthly Notices of the Royal Astronomical Society, 433, 3208

Borgani, S., Finoguenov, A., Kay, S. T., et al. (2005), *Entropy Amplification from Energy Feedback in Simulated Galaxy Groups and Clusters*, Monthly Notices of the Royal Astronomical Society, 361, 233

Böss, L. M. (2023), *LudwigBoess/SPHtoGrid.Jl: V0.4.5*, Zenodo

Böss, L. M., Steinwandel, U. P., Dolag, K., and Lesch, H. (2023), *CRESCENDO: An on-the-Fly Fokker-Planck Solver for Spectral Cosmic Rays in Cosmological Simulations*, Monthly Notices of the Royal Astronomical Society, 519, 548

Böss, L. M. and Valenzuela, L. M. (2022), *LudwigBoess/GadgetIO.Jl: V0.6.2*, Zenodo

Bournaud, F. and Duc, P. A. (2006), *From Tidal Dwarf Galaxies to Satellite Galaxies*, Astronomy and Astrophysics, 456, 481

Bowyer, A. (1981), *Computing Dirichlet Tessellations**, The Computer Journal, 24(2), 162

Bryan, G. L., Norman, M. L., O'Shea, B. W., et al. (2014), *ENZO: An Adaptive Mesh Refinement Code for Astrophysics*, The Astrophysical Journal Supplement Series, 211, 19

Bryan, G. L., Norman, M. L., Stone, J. M., et al. (1995), *A Piecewise Parabolic Method for Cosmological Hydrodynamics*, Computer Physics Communications, 89(1), 149

Bulbul, E., Liu, A., Kluge, M., et al. (2024), *The SRG/eROSITA All-Sky Survey - The First Catalog of Galaxy Clusters and Groups in the Western Galactic Hemisphere*, Astronomy & Astrophysics, 685, A106

Bullock, J. (2013), *Notes on the Missing Satellites Problem*, in *Local Group Cosmology*, edited by D. Martínez-Delgado, Canary Islands Winter School of Astrophysics, 95–122, Cambridge University Press, Cambridge

Burgers, J. M. (1948), *A Mathematical Model Illustrating the Theory of Turbulence*, in *Advances in Applied Mechanics*, edited by R. Von Mises, T. Von Kármán, volume 1, 171–199, Elsevier

Carilli, C. L. and Taylor, G. B. (2002), *Cluster Magnetic Fields*, Annual Review of Astronomy and Astrophysics, 40, 319

Cassano, R., Ettori, S., Giacintucci, S., et al. (2010), *On the Connection Between Giant Radio Halos and Cluster Mergers*, The Astrophysical Journal, 721, L82

Cavagnolo, K. W., Donahue, M., Voit, G. M., and Sun, M. (2009), *Intracluster Medium Entropy Profiles for a Chandra Archival Sample of Galaxy Clusters*, The Astrophysical Journal Supplement Series, 182, 12

Cha, S. H. and Whitworth, A. P. (2003), *Implementations and Tests of Godunov-type Particle Hydrodynamics*, Monthly Notices of the Royal Astronomical Society, 340, 73

Chandran, B. D. G. (2004), *Convection in Galaxy-Cluster Plasmas Driven by Active Galactic Nuclei and Cosmic-Ray Buoyancy*, The Astrophysical Journal, 616, 169

Chandran, B. D. G. (2005), *AGN-driven Convection in Galaxy-Cluster Plasmas*, The Astrophysical Journal, 632, 809

Chang, P. and Etienne, Z. B. (2020), *General Relativistic Hydrodynamics on a Moving-Mesh I: Static Space-Times*, Monthly Notices of the Royal Astronomical Society, 496, 206

Churazov, E., Forman, W., Jones, C., and Böhringer, H. (2000), *Asymmetric, Arc Minute Scale Structures around NGC 1275*, Astronomy and Astrophysics, 356, 788

Churazov, E., Forman, W., Vikhlinin, A., et al. (2008), *Measuring the Non-Thermal Pressure in Early-Type Galaxy Atmospheres: A Comparison of X-ray and Optical Potential Profiles in M87 and NGC 1399*, Monthly Notices of the Royal Astronomical Society, 388, 1062

Clarke, C. and Carswell, B. (2007), *Principles of Astrophysical Fluid Dynamics*, Cambridge University Press, Cambridge

Cockburn, B. and Shu, C.-W. (1998), *The Local Discontinuous Galerkin Method for Time-Dependent Convection-Diffusion Systems*, SIAM Journal on Numerical Analysis, 35(6), 2440

Couchman, H. M. P. (1991), *Mesh-Refined P 3M: A Fast Adaptive N-Body Algorithm*, The Astrophysical Journal, 368, L23

Crocce, M., Pueblas, S., and Scoccimarro, R. (2006), *Transients from Initial Conditions in Cosmological Simulations*, Monthly Notices of the Royal Astronomical Society, 373(1), 369

Cuciti, V., Cassano, R., Brunetti, G., et al. (2021), *Radio Halos in a Mass-Selected Sample of 75 Galaxy Clusters. II. Statistical Analysis*, Astronomy & Astrophysics, 647, A51

Cuciti, V., Cassano, R., Brunetti, G., et al. (2015), *On the Occurrence of Radio Halos in Galaxy Clusters - Insight from a Mass-Selected Sample*, Astronomy & Astrophysics, 580, A97

Cui, W., Knebe, A., Yepes, G., et al. (2018), *The Three Hundred Project: A Large Catalogue of Theoretically Modelled Galaxy Clusters for Cosmological and Astrophysical Applications*, Monthly Notices of the Royal Astronomical Society, 480, 2898

Cui, W., Liu, L., Yang, X., et al. (2008), *An Ideal Mass Assignment Scheme for Measuring the Power Spectrum with FFTs*, The Astrophysical Journal, 687(2), 738

Cui, W., Power, C., Borgani, S., et al. (2017), *On the Dynamical State of Galaxy Clusters: Insights from Cosmological Simulations - II.*, Monthly Notices of the Royal Astronomical Society, 464, 2502

Damiano, A., Valentini, M., Borgani, S., et al. (2024), *Dynamical Friction and Evolution of Black Holes in Cosmological Simulations: A New Implementation in OpenGadget3*

Davé, R., Anglés-Alcázar, D., Narayanan, D., et al. (2019), *Simba: Cosmological Simulations with Black Hole Growth and Feedback*, Monthly Notices of the Royal Astronomical Society, 486(2), 2827

David, L. P., Jones, C., and Forman, W. (2012), *THE UNIVERSAL GAS MASS FRACTION IN CLUSTERS OF GALAXIES*, The Astrophysical Journal, 748(2), 120

de Berg, M., Cheong, O., van Kreveld, M., and Overmars, M. (2008), *Delaunay Triangulations*, in *Computational Geometry: Algorithms and Applications*, 191–218, Springer, Berlin, Heidelberg

de Gasperin, F., Intema, H. T., Shimwell, T. W., et al. (2017), *Gentle Reenergization of Electrons in Merging Galaxy Clusters*, Science Advances, 3, e1701634

Dedner, A., Kemm, F., Kröner, D., et al. (2002), *Hyperbolic Divergence Cleaning for the MHD Equations*, Journal of Computational Physics, 175(2), 645

Dehnen, W. and Aly, H. (2012), *Improving Convergence in Smoothed Particle Hydrodynamics Simulations without Pairing Instability*, Monthly Notices of the Royal Astronomical Society, 425, 1068

Del Popolo, A. and Le Delliou, M. (2021), *Review of Solutions to the Cusp-Core Problem of the ΛCDM Model*, Galaxies, 9(4), 123

den Herder, J. W., Brinkman, A. C., Kahn, S. M., et al. (2001), *The Reflection Grating Spectrometer on Board XMM-Newton*, Astronomy and Astrophysics, 365, L7

Deng, Y., Li, H., Liu, B., et al. (2024), *RIGEL: Simulating Dwarf Galaxies at Solar Mass Resolution with Radiative Transfer and Feedback from Individual Massive Stars*

DES Collaboration, Abbott, T. M. C., Aguena, M., et al. (2022), *Dark Energy Survey Year 3 Results: Cosmological Constraints from Galaxy Clustering and Weak Lensing*, Physical Review D, 105(2), 023520

DESI Collaboration, Adame, A. G., Aguilar, J., et al. (2024), *DESI 2024 VI: Cosmological Constraints from the Measurements of Baryon Acoustic Oscillations*

Dolag, K. (2015), *The Magneticum Simulations, from Galaxies to Galaxy Clusters*, in *IAU General Assembly*, volume 29, 2250156

Dolag, K., Borgani, S., Murante, G., and Springel, V. (2009), *Substructures in Hydrodynamical Cluster Simulations*, Monthly Notices of the Royal Astronomical Society, 399(2), 497

Dolag, K., Hansen, F. K., Roncarelli, M., and Moscardini, L. (2005a), *The Imprints of Local Superclusters on the Sunyaev-Zel'dovich Signals and Their Detectability with Planck*, Monthly Notices of the Royal Astronomical Society, 363(1), 29

Dolag, K., Jubelgas, M., Springel, V., et al. (2004), *Thermal Conduction in Simulated Galaxy Clusters*, The Astrophysical Journal, 606(2), L97

Dolag, K., Komatsu, E., and Sunyaev, R. (2016), *SZ Effects in the Magneticum Pathfinder Simulation: Comparison with the Planck, SPT, and ACT Results*, Monthly Notices of the Royal Astronomical Society, 463, 1797

Dolag, K., Sorce, J. G., Pilipenko, S., et al. (2023), *Simulating the LOcal Web (SLOW): I. Anomalies in the Local Density Field*, Astronomy & Astrophysics, 677, A169

Dolag, K. and Stasyszyn, F. (2009), *An MHD GADGET for Cosmological Simulations*, Monthly Notices of the Royal Astronomical Society, 398, 1678

Dolag, K., Vazza, F., Brunetti, G., and Tormen, G. (2005b), *Turbulent Gas Motions in Galaxy Cluster Simulations: The Role of Smoothed Particle Hydrodynamics Viscosity*, Monthly Notices of the Royal Astronomical Society, 364, 753

Donnert, J., Vazza, F., Brüggen, M., and ZuHone, J. (2018), *Magnetic Field Amplification in Galaxy Clusters and Its Simulation*, Space Science Reviews, 214, 122

Doroshkevich, A. G. and Novikov, I. D. (1964), *Mean Density of Radiation in the Metagalaxy and Certain Problems in Relativistic Cosmology*, Soviet Physics Doklady, 9, 111

Dubois, Y., Pichon, C., Welker, C., et al. (2014), *Dancing in the Dark: Galactic Properties Trace Spin Swings along the Cosmic Web*, Monthly Notices of the Royal Astronomical Society, 444, 1453

Duffell, P. C. and MacFadyen, A. I. (2011), *TESS: A RELATIVISTIC HYDRODYNAMICS CODE ON A MOVING VORONOI MESH*, The Astrophysical Journal Supplement Series, 197(2), 15

Eastwood, J. W. and Hockney, R. W. (1974), *Shaping the Force Law in Two-Dimensional Particle-Mesh Models*, Journal of Computational Physics, 16(4), 342

Eckert, D., Gaspari, M., Gastaldello, F., et al. (2021), *Feedback from Active Galactic Nuclei in Galaxy Groups*, Universe, 7, 142

Eckert, D., Ghirardini, V., Ettori, S., et al. (2019), *Non-Thermal Pressure Support in X-COP Galaxy Clusters*, Astronomy and Astrophysics, 621, A40

Einfeldt, B. (1988), *On Godunov-Type Methods for Gas Dynamics*, SIAM Journal on Numerical Analysis, 25, 294

Einstein, A. (1916), *Die Grundlage Der Allgemeinen Relativitätstheorie*, Annalen der Physik, 354, 769

Ettori, S., Baldi, A., Balestra, I., et al. (2015), *The Evolution of the Spatially Resolved Metal Abundance in Galaxy Clusters up to $z = 1.4$*, Astronomy and Astrophysics, 578, A46

Falkovich, G. (1994), *Bottleneck Phenomenon in Developed Turbulence*, Physics of Fluids, 6, 1411

Fedeli, C. (2012), *The Effects of Baryonic Cooling on the Concentration-Mass Relation*, Monthly Notices of the Royal Astronomical Society, 424, 1244

Federrath, C., Klessen, R. S., Iapichino, L., and Beattie, J. R. (2021), *The Sonic Scale of Interstellar Turbulence*, Nature Astronomy, 5, 365

Federrath, C., Klessen, R. S., and Schmidt, W. (2008), *The Density Probability Distribution in Compressible Isothermal Turbulence: Solenoidal versus Compressive Forcing*, The Astrophysical Journal, 688(2), L79

Federrath, C., Klessen, R. S., and Schmidt, W. (2009), *The Fractal Density Structure in Supersonic Isothermal Turbulence: Solenoidal Versus Compressive Energy Injection*, The Astrophysical Journal, 692, 364

Federrath, C., Roman-Duval, J., Klessen, R. S., et al. (2010), *Comparing the Statistics of Interstellar Turbulence in Simulations and Observations. Solenoidal versus Compressive Turbulence Forcing*, Astronomy & Astrophysics, 512, A81

Feldmeier, A. (2019), *Theoretical Fluid Dynamics*, Theoretical and Mathematical Physics, Springer International Publishing, Cham

Fischer, M. S., Brüggen, M., Schmidt-Hoberg, K., et al. (2022), *Cosmological Simulations with Rare and Frequent Dark Matter Self-Interactions*, arXiv:2205.02243 [astro-ph, physics:hep-ph]

Fischer, M. S. and Valenzuela, L. M. (2023), *Sensitivity of Halo Shape Measurements*, Astronomy and Astrophysics, 670, A120

Friedmann, A. (1922), *Über Die Krümmung Des Raumes*, Zeitschrift fur Physik, 10, 377

Friedmann, A. (1924), *Über Die Möglichkeit Einer Welt Mit Konstanter Negativer Krümmung Des Raumes*, Zeitschrift fur Physik, 21, 326

Frigo, M. and Johnson, S. G. (2005), *The Design and Implementation of FFTW3*, Proceedings of the IEEE, 93(2), 216

Fryxell, B., Olson, K., Ricker, P., et al. (2000), *FLASH: An Adaptive Mesh Hydrodynamics Code for Modeling Astrophysical Thermonuclear Flashes*, The Astrophysical Journal Supplement Series, 131, 273

Gaburov, E. and Nitadori, K. (2011), *Astrophysical Weighted Particle Magnetohydrodynamics*, Monthly Notices of the Royal Astronomical Society, 414(1), 129

Ghirardini, V., Eckert, D., Ettori, S., et al. (2019), *Universal Thermodynamic Properties of the Intracluster Medium over Two Decades in Radius in the X-COP Sample*, Astronomy and Astrophysics, 621, A41

Gingold, R. A. and Monaghan, J. J. (1977), *Smoothed Particle Hydrodynamics: Theory and Application to Non-Spherical Stars.*, Monthly Notices of the Royal Astronomical Society, 181, 375

Gnedin, N. Y. (1995), *Softened Lagrangian Hydrodynamics for Cosmology*, The Astrophysical Journal Supplement Series, 97, 231

Godunov, S. (1959), *A difference method for numerical calculation of discontinuous solutions of the equations of hydrodynamics*, Matematicheski\u ı Sbornik. Novaya Seriya, 47(89)(3), 271

Goldreich, P. and Sridhar, S. (1995), *Toward a Theory of Interstellar Turbulence. II. Strong Alfvenic Turbulence*, The Astrophysical Journal, 438, 763

Gronke, M. and Oh, S. P. (2018), *The Growth and Entrainment of Cold Gas in a Hot Wind*, Monthly Notices of the Royal Astronomical Society, 480, L111

Gronke, M. and Oh, S. P. (2020), *Is Multiphase Gas Cloudy or Misty?*, Monthly Notices of the Royal Astronomical Society, 494, L27

Gronke, M. and Oh, S. P. (2022), *Cooling Driven Coagulation*

Groth, F., Steinwandel, U. P., Valentini, M., and Dolag, K. (2023), *The Cosmological Simulation Code OpenGadget3 – Implementation of Meshless Finite Mass*, Monthly Notices of the Royal Astronomical Society, 526(1), 616

Groth, F., Valentini, M., Steinwandel, U. P., et al. (2024), *Turbulent Pressure Support in Galaxy Clusters – Impact of the Hydrodynamical Solver*

Harten, A., Lax, P. D., and van Leer, B. (1983), *On Upstream Differencing and Godunov-Type Schemes for Hyperbolic Conservation Laws.*, Society for Industrial and Applied Mathematics Review, 25(1), 35

Heitmann, K., Lukić, Z., Fasel, P., et al. (2008), *The Cosmic Code Comparison Project*, Computational Science and Discovery, 1, 015003

Hernández-Martínez, E., Dolag, K., Seidel, B., et al. (2024), *Simulating the LOcal Web (SLOW). II. Properties of Local Galaxy Clusters*, Astronomy & Astrophysics, 687, A253

Hernquist, L. and Katz, N. (1989), *TREESPH: A Unification of SPH with the Hierarchical Tree Method*, The Astrophysical Journal Supplement Series, 70, 419

Hess, S. and Springel, V. (2010), *Particle Hydrodynamics with Tessellation Techniques*, Monthly Notices of the Royal Astronomical Society, 406(4), 2289

Hirschmann, M., Dolag, K., Saro, A., et al. (2014), *Cosmological Simulations of Black Hole Growth: AGN Luminosities and Downsizing*, Monthly Notices of the Royal Astronomical Society, 442, 2304

Hitomi Collaboration, Aharonian, F., Akamatsu, H., et al. (2016), *The Quiescent Intracluster Medium in the Core of the Perseus Cluster*, Nature, 535, 117

Hitomi Collaboration, Aharonian, F., Akamatsu, H., et al. (2018), *Atmospheric Gas Dynamics in the Perseus Cluster Observed with Hitomi*, Publications of the Astronomical Society of Japan, 70, 9

Hoekstra, H., Bartelmann, M., Dahle, H., et al. (2013), *Masses of Galaxy Clusters from Gravitational Lensing*, Space Science Reviews, 177, 75

Hopkins, P. F. (2013), *A General Class of Lagrangian Smoothed Particle Hydrodynamics Methods and Implications for Fluid Mixing Problems*, Monthly Notices of the Royal Astronomical Society, 428, 2840

Hopkins, P. F. (2015), *GIZMO: A New Class of Accurate, Mesh-Free Hydrodynamic Simulation Methods*, Monthly Notices of the Royal Astronomical Society, 450(1), 53

Hopkins, P. F. and Raives, M. J. (2016), *Accurate, Meshless Methods for Magneto-Hydrodynamics*, Monthly Notices of the Royal Astronomical Society, 455(1), 51

Hu, C.-Y., Naab, T., Walch, S., et al. (2014), *SPHGal: Smoothed Particle Hydrodynamics with Improved Accuracy for Galaxy Simulations*, Monthly Notices of the Royal Astronomical Society, 443, 1173

Hubber, D. A., Rosotti, G. P., and Booth, R. A. (2018), *GANDALF - Graphical Astrophysics Code for N-body Dynamics And Lagrangian Fluids*, Monthly Notices of the Royal Astronomical Society, 473(2), 1603

Hubble, E. (1929), *A Relation between Distance and Radial Velocity among Extra-Galactic Nebulae*, Proceedings of the National Academy of Science, 15, 168

Iapichino, L., Federrath, C., and Klessen, R. S. (2017), *Adaptive Mesh Refinement Simulations of a Galaxy Cluster Merger - I. Resolving and Modelling the Turbulent Flow in the Cluster Outskirts*, Monthly Notices of the Royal Astronomical Society, 469, 3641

Iapichino, L. and Niemeyer, J. C. (2008), *Hydrodynamical Adaptive Mesh Refinement Simulations of Turbulent Flows - II. Cosmological Simulations of Galaxy Clusters*, Monthly Notices of the Royal Astronomical Society, 388, 1089

Idelsohn, S. R., Oñate, E., Calvo, N., and Del Pin, F. (2003), *The Meshless Finite Element Method*, International Journal for Numerical Methods in Engineering, 58, 893

Inutsuka, S.-I. (2002), *Reformulation of Smoothed Particle Hydrodynamics with Riemann Solver*, Journal of Computational Physics, 179, 238

Ivleva, A., Remus, R.-S., Valenzuela, L. M., and Dolag, K. (2024), *Merge and Strip: Dark Matter-Free Dwarf Galaxies in Clusters Can Be Formed by Galaxy Mergers*, Astronomy and Astrophysics, 687, A105

Junk, V., Walch, S., Heitsch, F., et al. (2010), *Modelling Shear Flows with Smoothed Particle Hydrodynamics and Grid-Based Methods*, Monthly Notices of the Royal Astronomical Society, 407, 1933

Kazmierczak, J. (2024), *NASA/JAXA XRISM Mission Reveals Its First Look at X-ray Cosmos - NASA Science*, https://science.nasa.gov/missions/xrism/nasa-jaxa-xrism-mission-reveals-its-first-look-at-x-ray-cosmos/

Kim, C.-G. and Ostriker, E. C. (2015), *Momentum Injection by Supernovae in the Interstellar Medium*, The Astrophysical Journal, 802, 99

Kitsionas, S., Federrath, C., Klessen, R. S., et al. (2009), *Algorithmic Comparisons of Decaying, Isothermal, Supersonic Turbulence*, Astronomy and Astrophysics, Volume 508, Issue 1, 2009, pp.541-560, 508(1), 541

Kolmogorov, A. N. (1941), *Dissipation of Energy in Locally Isotropic Turbulence*, Akademiia Nauk SSSR Doklady, 32, 16

Komatsu, E., Smith, K. M., Dunkley, J., et al. (2011), *Seven-Year Wilkinson Microwave Anisotropy Probe (WMAP) Observations: Cosmological Interpretation*, The Astrophysical Journal Supplement Series, 192, 18

Kraft, R., Markevitch, M., Kilbourne, C., et al. (2022), *Line Emission Mapper (LEM): Probing the Physics of Cosmic Ecosystems*

Kraichnan, R. H. (1965), *Inertial-Range Spectrum of Hydromagnetic Turbulence*, Physics of Fluids, 8, 1385

Kravtsov, A. V. and Borgani, S. (2012), *Formation of Galaxy Clusters*, Annual Review of Astronomy and Astrophysics, 50, 353

Kravtsov, A. V., Klypin, A. A., and Khokhlov, A. M. (1997), *Adaptive Refinement Tree: A New High-Resolution N-Body Code for Cosmological Simulations*, The Astrophysical Journal Supplement Series, 111, 73

Kritsuk, A. G., Yee, H. C., Sjögreen, B., and Kotov, D. (2020), *Comparative Study of High Order Methods for Subsonic Turbulence Simulation with Stochastic Forcing*, Journal of Physics: Conference Series, 1623(1), 012010

Kudoh, Y. and Hanawa, T. (2016), *Approximate Riemann Solvers for the Cosmic Ray Magnetohydrodynamical Equations*, Monthly Notices of the Royal Astronomical Society, 462(4), 4517

Kulsrud, R. M. and Zweibel, E. G. (2008), *On the Origin of Cosmic Magnetic Fields*, Reports on Progress in Physics, 71, 046901

Landau, L. D. and Lifshitz, E. M. (1959), *Fluid Mechanics*, volume 6 of *Course of Theoretical Physics*, Pergamon, Oxford, first edition

Lanson, N. and Vila, J.-P. (2008a), *Renormalized Meshfree Schemes I: Consistency, Stability, and Hybrid Methods for Conservation Laws*, SIAM Journal on Numerical Analysis, 46(4), 1912

Lanson, N. and Vila, J.-P. (2008b), *Renormalized Meshfree Schemes II: Convergence for Scalar Conservation Laws*, SIAM Journal on Numerical Analysis, 46(4), 1935

Lau, E. T., Kravtsov, A. V., and Nagai, D. (2009), *Residual Gas Motions in the Intracluster Medium and Bias in Hydrostatic Measurements of Mass Profiles of Clusters*, The Astrophysical Journal, 705, 1129

Lemaître, G. (1927), *Un Univers Homogène de Masse Constante et de Rayon Croissant Rendant Compte de La Vitesse Radiale Des Nébuleuses Extra-Galactiques*, Annales de la Société Scientifique de Bruxelles, 47, 49

Lemaître, G. (1931), *A Homogeneous Universe of Constant Mass and Increasing Radius Accounting for the Radial Velocity of Extra-Galactic Nebulae*, Monthly Notices of the Royal Astronomical Society, 91, 483

Lemaître, G. (1933), *L'Univers En Expansion*, Annales de la Société Scientifique de Bruxelles, 53, 51

Lioutas, G., Bauswein, A., Soultanis, T., et al. (2024), *General Relativistic Moving-Mesh Hydrodynamic Simulations with AREPO and Applications to Neutron Star Mergers*, Monthly Notices of the Royal Astronomical Society, 528, 1906

Liptai, D. and Price, D. J. (2019), *General Relativistic Smoothed Particle Hydrodynamics*, Monthly Notices of the Royal Astronomical Society, 485, 819

Liu, X.-D., Osher, S., and Chan, T. (1994), *Weighted Essentially Non-oscillatory Schemes*, Journal of Computational Physics, 115(1), 200

Lodato, G. and Price, D. J. (2010), *On the Diffusive Propagation of Warps in Thin Accretion Discs*, Monthly Notices of the Royal Astronomical Society, 405, 1212

Lucy, L. B. (1977), *A Numerical Approach to the Testing of the Fission Hypothesis.*, The Astronomical Journal, 82, 1013

Lupi, A. (2022), *A General Relativistic Extension to Mesh-Free Methods for Hydrodynamics*, Monthly Notices of the Royal Astronomical Society, 519(1), 1115

Maier, A., Iapichino, L., Schmidt, W., and Niemeyer, J. C. (2009), *Adaptively Refined Large Eddy Simulations of a Galaxy Cluster: Turbulence Modeling and the Physics of the Intracluster Medium*, The Astrophysical Journal, 707, 40

Marin-Gilabert, T., Steinwandel, U. P., Valentini, M., et al. (2024), *Density Fluctuations in the Intracluster Medium: An Attempt to Constrain Viscosity with Cosmological Simulations*

Marin-Gilabert, T., Valentini, M., Steinwandel, U. P., and Dolag, K. (2022), *The Role of Physical and Numerical Viscosity in Hydrodynamical Instabilities*

Marinacci, F., Vogelsberger, M., Pakmor, R., et al. (2018), *First Results from the IllustrisTNG Simulations: Radio Haloes and Magnetic Fields*, Monthly Notices of the Royal Astronomical Society, 480, 5113

Martel, H. and Shapiro, P. R. (1998), *A Convenient Set of Comoving Cosmological Variables and Their Application*, Monthly Notices of the Royal Astronomical Society, 297, 467

Mavriplis, D. J. (1997), *Unstructured Grid Techniques*, Annual Review of Fluid Mechanics, 29, 473

May, S. and Berger, M. (2013), *Two-Dimensional Slope Limiters for Finite Volume Schemes on Non-Coordinate-Aligned Meshes*, SIAM Journal on Scientific Computing, 35(5), A2163

McCourt, M., Sharma, P., Quataert, E., and Parrish, I. J. (2012), *Thermal Instability in Gravitationally Stratified Plasmas: Implications for Multiphase Structure in Clusters and Galaxy Haloes*, Monthly Notices of the Royal Astronomical Society, 419, 3319

McNally, C. P., Lyra, W., and Passy, J.-C. (2012), *A Well-posed Kelvin-Helmholtz Instability Test and Comparison*, The Astrophysical Journal Supplement Series, 201, 18

McNamara, B. R., Wise, M., Nulsen, P. E. J., et al. (2000), *Chandra X-Ray Observations of the Hydra A Cluster: An Interaction between the Radio Source and the X-Ray-emitting Gas*, The Astrophysical Journal, 534, L135

Medvedev, M. V. and Loeb, A. (1999), *Generation of Magnetic Fields in the Relativistic Shock of Gamma-Ray Burst Sources*, The Astrophysical Journal, 526, 697

Miniati, F. (2014), *The Matryoshka Run: A Eulerian Refinement Strategy to Study the Statistics of Turbulence in Virialized Cosmic Structures*, The Astrophysical Journal, 782, 21

Miniati, F. (2015), *The Matryoshka Run. II. Time-dependent Turbulence Statistics, Stochastic Particle Acceleration, and Microphysics Impact in a Massive Galaxy Cluster*, The Astrophysical Journal, 800, 60

Miyoshi, T. and Kusano, K. (2005), *A Multi-State HLL Approximate Riemann Solver for Ideal Magnetohydrodynamics*, Journal of Computational Physics, 208(1), 315

Mohapatra, R., Federrath, C., and Sharma, P. (2020), *Turbulence in Stratified Atmospheres: Implications for the Intracluster Medium*, Monthly Notices of the Royal Astronomical Society, 493(4), 5838

Mohapatra, R., Federrath, C., and Sharma, P. (2021), *Turbulent Density and Pressure Fluctuations in the Stratified Intracluster Medium*, Monthly Notices of the Royal Astronomical Society, 500, 5072

Mohapatra, R., Jetti, M., Sharma, P., and Federrath, C. (2022), *Velocity Structure Functions in Multiphase Turbulence: Interpreting Kinematics of Hα Filaments in Cool-Core Clusters*, Monthly Notices of the Royal Astronomical Society, 510, 2327

Monaghan, J. J. and Lattanzio, J. C. (1985), *A Refined Particle Method for Astrophysical Problems*, Astronomy and Astrophysics, 149(1), 135

Morris, J. P. (1996), *A Study of the Stability Properties of Smooth Particle Hydrodynamics*, Publications of the Astronomical Society of Australia, 13, 97

Murante, G., Monaco, P., Borgani, S., et al. (2015), *Simulating Realistic Disc Galaxies with a Novel Sub-Resolution ISM Model*, Monthly Notices of the Royal Astronomical Society, 447, 178

Murante, G., Monaco, P., Giovalli, M., et al. (2010), *A Subresolution Multiphase Interstellar Medium Model of Star Formation and Supernova Energy Feedback*, Monthly Notices of the Royal Astronomical Society, 405, 1491

Naiman, J. P., Pillepich, A., Springel, V., et al. (2018), *First Results from the IllustrisTNG Simulations: A Tale of Two Elements - Chemical Evolution of Magnesium and Europium*, Monthly Notices of the Royal Astronomical Society, 477, 1206

Navarro, J. F., Frenk, C. S., and White, S. D. M. (1997), *A Universal Density Profile from Hierarchical Clustering*, The Astrophysical Journal, 490, 493

Nelson, D., Pillepich, A., Ayromlou, M., et al. (2024), *Introducing the TNG-Cluster Simulation: Overview and the Physical Properties of the Gaseous Intracluster Medium*, Astronomy and Astrophysics, 686, A157

Nelson, D., Pillepich, A., Springel, V., et al. (2019), *First Results from the TNG50 Simulation: Galactic Outflows Driven by Supernovae and Black Hole Feedback*, Monthly Notices of the Royal Astronomical Society, 490, 3234

Nelson, D., Pillepich, A., Springel, V., et al. (2018), *First Results from the IllustrisTNG Simulations: The Galaxy Colour Bimodality*, Monthly Notices of the Royal Astronomical Society, 475, 624

Obukhov, A. M. (1962), *Some Specific Features of Atmospheric Turbulence*, Journal of Geophysical Research, 67, 3011

O'Shea, B. W., Nagamine, K., Springel, V., et al. (2005), *Comparing AMR and SPH Cosmological Simulations. I. Dark Matter and Adiabatic Simulations*, The Astrophysical Journal Supplement Series, 160, 1

Padoan, P., Jones, B. J. T., and Nordlund, Aa. (1997), *Supersonic Turbulence in the ISM: Stellar Extinction Determinations as Probes of the Structure and Dynamics of Dark Clouds*, The Astrophysical Journal, 474(2), 730

Padoan, P., Nordlund, Å., Kritsuk, A. G., et al. (2007), *Two Regimes of Turbulent Fragmentation and the Stellar Initial Mass Function from Primordial to Present-Day Star Formation*, The Astrophysical Journal, 661, 972

Pakmor, R., Edelmann, P., Röpke, F. K., and Hillebrandt, W. (2012), *Stellar GADGET: A Smoothed Particle Hydrodynamics Code for Stellar Astrophysics and Its Application to Type Ia Supernovae from White Dwarf Mergers*, Monthly Notices of the Royal Astronomical Society, 424, 2222

Pakmor, R. M. (2010), *Progenitor Systems of Type Ia Supernovae: Mergers of White Dwarfs and Constraints on Hydrogen-Accreting White Dwarfs*, Ph.D. thesis, Technical University of Munich

Passot, T. and Vázquez-Semadeni, E. (1998), *Density Probability Distribution in One-Dimensional Polytropic Gas Dynamics*, Physical Review E, 58, 4501

Pearce, F. R., Thomas, P. A., Couchman, H. M. P., and Edge, A. C. (2000), *The Effect of Radiative Cooling on the X-ray Properties of Galaxy Clusters*, Monthly Notices of the Royal Astronomical Society, 317, 1029

Pen, U.-L. (1998), *A High-Resolution Adaptive Moving Mesh Hydrodynamic Algorithm*, The Astrophysical Journal Supplement Series, 115, 19

Penzias, A. A. and Wilson, R. W. (1965), *A Measurement of Excess Antenna Temperature at 4080 Mc/s.*, The Astrophysical Journal, 142, 419

Pfrommer, C., Springel, V., Enßlin, T. A., and Jubelgas, M. (2006), *Detecting Shock Waves in Cosmological Smoothed Particle Hydrodynamics Simulations*, Monthly Notices of the Royal Astronomical Society, 367, 113

Pillepich, A., Nelson, D., Hernquist, L., et al. (2018), *First Results from the IllustrisTNG Simulations: The Stellar Mass Content of Groups and Clusters of Galaxies*, Monthly Notices of the Royal Astronomical Society, 475, 648

Pillepich, A., Nelson, D., Springel, V., et al. (2019), *First Results from the TNG50 Simulation: The Evolution of Stellar and Gaseous Discs across Cosmic Time*, Monthly Notices of the Royal Astronomical Society, 490, 3196

Planck Collaboration, Ade, P. A. R., Aghanim, N., et al. (2014), *Planck 2013 Results. XVI. Cosmological Parameters*, Astronomy and Astrophysics, 571, A16

Planck Collaboration, Aghanim, N., Akrami, Y., et al. (2020), *Planck 2018 Results. VI. Cosmological Parameters*, Astronomy & Astrophysics, 641, A6

Powell, K. G., Roe, P. L., Linde, T. J., et al. (1999), *A Solution-Adaptive Upwind Scheme for Ideal Magnetohydrodynamics*, Journal of Computational Physics, 154(2), 284

Prada, F., Klypin, A. A., Cuesta, A. J., et al. (2012), *Halo Concentrations in the Standard LCDM Cosmology*, Monthly Notices of the Royal Astronomical Society, 423(4), 3018

Press, W. H. and Schechter, P. (1974), *Formation of Galaxies and Clusters of Galaxies by Self-Similar Gravitational Condensation*, The Astrophysical Journal, 187, 425

Price, D. J. (2008), *Modelling Discontinuities and Kelvin Helmholtz Instabilities in SPH*, Journal of Computational Physics, 227, 10040

Price, D. J. (2012a), *Resolving High Reynolds Numbers in Smoothed Particle Hydrodynamics Simulations of Subsonic Turbulence*, Monthly Notices of the Royal Astronomical Society, 420, L33

Price, D. J. (2012b), *Smoothed Particle Hydrodynamics: Things I Wish My Mother Taught Me*, ASP Conference Proceedings, 453, 249

Price, D. J. and Federrath, C. (2010), *A Comparison between Grid and Particle Methods on the Statistics of Driven, Supersonic, Isothermal Turbulence*, Monthly Notices of the Royal Astronomical Society, 406, 1659

Price, D. J., Wurster, J., Tricco, T. S., et al. (2018), *Phantom: A Smoothed Particle Hydrodynamics and Magnetohydrodynamics Code for Astrophysics*, Publications of the Astronomical Society of Australia, 35, e031

Ragagnin, A., Dolag, K., Wagner, M., et al. (2020), *Gadget3 on GPUs with OpenACC*

Rasia, E., Borgani, S., Murante, G., et al. (2015), *Cool Core Clusters from Cosmological Simulations*, The Astrophysical Journal, 813, L17

Reynolds, C. S., Kara, E. A., Mushotzky, R. F., et al. (2023), *Overview of the Advanced X-ray Imaging Satellite (AXIS)*, in *UV, X-Ray, and Gamma-Ray Space Instrumentation for Astronomy XXIII*, 49

Riess, A. G., Casertano, S., Yuan, W., et al. (2019), *Large Magellanic Cloud Cepheid Standards Provide a 1% Foundation for the Determination of the Hubble Constant and Stronger Evidence for Physics beyond ΛCDM*, The Astrophysical Journal, 876(1), 85

Riess, A. G., Nugent, P. E., Gilliland, R. L., et al. (2001), *The Farthest Known Supernova: Support for an Accelerating Universe and a Glimpse of the Epoch of Deceleration*, The Astrophysical Journal, 560, 49

Robertson, H. P. (1935), *Kinematics and World-Structure*, The Astrophysical Journal, 82, 284

Robertson, H. P. (1936a), *Kinematics and World-Structure II.*, The Astrophysical Journal, 83, 187

Robertson, H. P. (1936b), *Kinematics and World-Structure III.*, The Astrophysical Journal, 83, 257

Roe, P. L. (1981), *Approximate Riemann Solvers, Parameter Vectors, and Difference Schemes*, Journal of Computational Physics, 43(2), 357

Roettiger, K. and Burns, J. O. (1999), *Radio Halo Formation and Evolution in the Galaxy Cluster Merger Environment*, in *American Astronomical Society Meeting Abstracts*, volume 195, 13.04

Rosswog, S. (2015), *SPH Methods in the Modelling of Compact Objects*, Living Reviews in Computational Astrophysics, 1(1), 1

Rosswog, S. (2020), *The Lagrangian Hydrodynamics Code MAGMA2*, Monthly Notices of the Royal Astronomical Society, 498, 4230

Rosswog, S. and Diener, P. (2021), *SPHINCS_BSSN: A General Relativistic Smooth Particle Hydrodynamics Code for Dynamical Spacetimes*, Classical and Quantum Gravity, 38, 115002

Ruszkowski, M. and Pfrommer, C. (2023), *Cosmic Ray Feedback in Galaxies and Galaxy Clusters*, Astronomy and Astrophysics Review, 31, 4

Ryu, D., Miniati, F., Jones, T. W., and Frank, A. (1998), *A Divergence-free Upwind Code for Multidimensional Magnetohydrodynamic Flows*, The Astrophysical Journal, 509, 244

Ryu, D., Ostriker, J. P., Kang, H., and Cen, R. (1993), *A Cosmological Hydrodynamic Code Based on the Total Variation Diminishing Scheme*, The Astrophysical Journal, 414, 1

Saitoh, T. R. and Makino, J. (2009), *A NECESSARY CONDITION FOR INDIVIDUAL TIME STEPS IN SPH SIMULATIONS*, The Astrophysical Journal, 697(2), L99

Sala, L., Valentini, M., Biffi, V., and Dolag, K. (2024), *Supermassive Black Hole Spin Evolution in Cosmological Simulations with OPENGADGET3*, Astronomy and Astrophysics, 685, A92

Sánchez, A. G. (2020), *Arguments against Using ${h}^{\ensuremath{-}1}\text{ }\mathrm{Mpc}$ Units in Observational Cosmology*, Physical Review D, 102(12), 123511

Sarazin, C. L. (1986), *X-Ray Emission from Clusters of Galaxies*, Reviews of Modern Physics, 58, 1

Sato, K., Uchida, Y., and Ishikawa, K. (2023), *Hitomi/XRISM Micro-Calorimeter*

Sayers, J., Sereno, M., Ettori, S., et al. (2021), *CLUMP-3D: The Lack of Non-Thermal Motions in Galaxy Cluster Cores*, Monthly Notices of the Royal Astronomical Society, 505, 4338

Schekochihin, A., Cowley, S., Maron, J., and Malyshkin, L. (2001), *Structure of Small-Scale Magnetic Fields in the Kinematic Dynamo Theory*, Physical Review E, 65, 016305

Schekochihin, A. A. (2022), *MHD Turbulence: A Biased Review*, Journal of Plasma Physics, 88, 155880501

Schekochihin, A. A. and Cowley, S. C. (2006), *Turbulence, Magnetic Fields, and Plasma Physics in Clusters of Galaxies*, Physics of Plasmas, 13, 056501

Schekochihin, A. A., Cowley, S. C., Taylor, S. F., et al. (2004), *Simulations of the Small-Scale Turbulent Dynamo*, The Astrophysical Journal, 612, 276

Schuecker, P., Finoguenov, A., Miniati, F., et al. (2004), *Probing Turbulence in the Coma Galaxy Cluster*, Astronomy and Astrophysics, v.426, p.387-397 (2004), 426, 387

Sedov, L. I. (1946), *Propagation of Strong Shock Waves*, Journal of Applied Mathematics and Mechanics, 10, 241

Sedov, L. I. (1959), *Similarity and Dimensional Methods in Mechanics*, New York: Academic Press

Sembolini, F., De Petris, M., Yepes, G., et al. (2014), *The MUSIC of Galaxy Clusters - III. Properties, Evolution and Y-M Scaling Relation of Protoclusters of Galaxies*, Monthly Notices of the Royal Astronomical Society, 440, 3520

Sembolini, F., Yepes, G., De Petris, M., et al. (2013), *The MUSIC of Galaxy Clusters - I. Baryon Properties and Scaling Relations of the Thermal Sunyaev-Zel'dovich Effect*, Monthly Notices of the Royal Astronomical Society, 429, 323

Sembolini, F., Yepes, G., Pearce, F. R., et al. (2016), *nIFTy Galaxy Cluster Simulations I: Dark Matter & Non-Radiative Models*, Monthly Notices of the Royal Astronomical Society, 457(4), 4063

Sijacki, D. and Springel, V. (2006), *Physical Viscosity in Smoothed Particle Hydrodynamics Simulations of Galaxy Clusters*, Monthly Notices of the Royal Astronomical Society, 371, 1025

Sod, G. A. (1978), *A Survey of Several Finite Difference Methods for Systems of Nonlinear Hyperbolic Conservation Laws*, Journal of Computational Physics, 27(1), 1

Sorce, J. G. (2018), *Galaxy Clusters in Local Universe Simulations without Density Constraints: A Long Uphill Struggle*, Monthly Notices of the Royal Astronomical Society, 478(4), 5199

Sorce, J. G. and Tempel, E. (2018), *Galaxy Clusters in Simulations of the Local Universe: A Matter of Constraints*, Monthly Notices of the Royal Astronomical Society, 476(4), 4362

Spitzer, L. (1956), *Physics of Fully Ionized Gases*, Interscience Publishers, New York

Springel, V. (2005), *The Cosmological Simulation Code GADGET-2*, Monthly Notices of the Royal Astronomical Society, 364(4), 1105

Springel, V. (2010), *E Pur Si Muove: Galiliean-invariant Cosmological Hydrodynamical Simulations on a Moving Mesh*, Monthly Notices of the Royal Astronomical Society, 401(2), 791

Springel, V. and Hernquist, L. (2002), *Cosmological Smoothed Particle Hydrodynamics Simulations: The Entropy Equation*, Monthly Notices of the Royal Astronomical Society, 333, 649

Springel, V. and Hernquist, L. (2003), *Cosmological Smoothed Particle Hydrodynamics Simulations: A Hybrid Multiphase Model for Star Formation*, Monthly Notices of the Royal Astronomical Society, 339, 289

Springel, V., Pakmor, R., Pillepich, A., et al. (2018), *First Results from the IllustrisTNG Simulations: Matter and Galaxy Clustering*, Monthly Notices of the Royal Astronomical Society, 475, 676

Springel, V., Pakmor, R., Zier, O., and Reinecke, M. (2021), *Simulating Cosmic Structure Formation with the GADGET-4 Code*, Monthly Notices of the Royal Astronomical Society, 506(2), 2871

Springel, V., Wang, J., Vogelsberger, M., et al. (2008), *The Aquarius Project: The Subhaloes of Galactic Haloes*, Monthly Notices of the Royal Astronomical Society, 391, 1685

Springel, V., White, S. D. M., Jenkins, A., et al. (2005), *Simulations of the Formation, Evolution and Clustering of Galaxies and Quasars*, Nature, 435, 629

Springel, V., Yoshida, N., and White, S. D. M. (2001), *GADGET: A Code for Collisionless and Gasdynamical Cosmological Simulations*, New Astronomy, 6(2), 79

Stasyszyn, F. A., Dolag, K., and Beck, A. M. (2013), *A Divergence-Cleaning Scheme for Cosmological SPMHD Simulations*, Monthly Notices of the Royal Astronomical Society, 428, 13

Steinborn, L. K., Dolag, K., Hirschmann, M., et al. (2015), *A Refined Sub-Grid Model for Black Hole Accretion and AGN Feedback in Large Cosmological Simulations*, Monthly Notices of the Royal Astronomical Society, 448, 1504

Steinwandel, U. P., Beck, M. C., Arth, A., et al. (2019), *Magnetic Buoyancy in Simulated Galactic Discs with a Realistic Circumgalactic Medium*, Monthly Notices of the Royal Astronomical Society, 483, 1008

Steinwandel, U. P., Boess, L. M., Dolag, K., and Lesch, H. (2021), *On the Small Scale Turbulent Dynamo in the Intracluster Medium: A Comparison to Dynamo Theory*, arXiv:2108.07822 [astro-ph]

Steinwandel, U. P., Dolag, K., Böss, L. M., and Marin-Gilabert, T. (2024a), *Toward Cosmological Simulations of the Magnetized Intracluster Medium with Resolved Coulomb Collision Scale*, The Astrophysical Journal, 967, 125

Steinwandel, U. P., Moster, B. P., Naab, T., et al. (2020), *Hot Phase Generation by Supernovae in ISM Simulations: Resolution, Chemistry, and Thermal Conduction*, Monthly Notices of the Royal Astronomical Society, 495, 1035

Steinwandel, U. P., Rennehan, D., Orr, M. E., et al. (2024b), *Pumping Iron: How Turbulent Metal Diffusion Impacts Multiphase Galactic Outflows*, arXiv e-prints, arXiv:2407.14599

Stone, J. M., Gardiner, T. A., Teuben, P., et al. (2008), *Athena: A New Code for Astrophysical MHD*, The Astrophysical Journal Supplement Series, 178, 137

Stone, J. M. and Norman, M. L. (1992), *ZEUS-2D: A Radiation Magnetohydrodynamics Code for Astrophysical Flows in Two Space Dimensions. I. The Hydrodynamic Algorithms and Tests*, The Astrophysical Journal Supplement Series, 80, 753

Stone, J. M., Tomida, K., White, C. J., and Felker, K. G. (2020), *The Athena++ Adaptive Mesh Refinement Framework: Design and Magnetohydrodynamic Solvers*, The Astrophysical Journal Supplement Series, 249, 4

Subramanian, K., Shukurov, A., and Haugen, N. E. L. (2006), *Evolving Turbulence and Magnetic Fields in Galaxy Clusters*, Monthly Notices of the Royal Astronomical Society, 366, 1437

Sunyaev, R. A. and Zeldovich, Ya. B. (1972), *The Observations of Relic Radiation as a Test of the Nature of X-Ray Radiation from the Clusters of Galaxies*, Comments on Astrophysics and Space Physics, 4, 173

Taylor, G. (1950), *The Formation of a Blast Wave by a Very Intense Explosion. I. Theoretical Discussion*, Proceedings of the Royal Society of London Series A, 201, 159

Teyssier, R. (2002), *Cosmological Hydrodynamics with Adaptive Mesh Refinement. A New High Resolution Code Called RAMSES*, Astronomy and Astrophysics, 385, 337

Toomre, A. and Toomre, J. (1972), *Galactic Bridges and Tails*, The Astrophysical Journal, 178, 623

Tormen, G., Bouchet, F. R., and White, S. D. M. (1997), *The Structure and Dynamical Evolution of Dark Matter Haloes*, Monthly Notices of the Royal Astronomical Society, 286, 865

Tornatore, L., Borgani, S., Dolag, K., and Matteucci, F. (2007), *Chemical Enrichment of Galaxy Clusters from Hydrodynamical Simulations*, Monthly Notices of the Royal Astronomical Society, 382(3), 1050

Tornatore, L., Borgani, S., Matteucci, F., et al. (2004), *Simulating the Metal Enrichment of the ICM*, Monthly Notices of the Royal Astronomical Society, 349(1), L19

Tornatore, L., Borgani, S., Springel, V., et al. (2003), *Cooling and Heating the ICM in Hydrodynamical Simulations*, Monthly Notices of the Royal Astronomical Society, 342(4), 1025

Toro, E. F. (2009), *Riemann Solvers and Numerical Methods for Fluid Dynamics: A Practical Introduction*, Springer, Dordrecht ; New York, third edition

Toro, E. F., Spruce, M., and Speares, W. (1994), *Restoration of the Contact Surface in the HLL-Riemann Solver*, Shock Waves, 4(1), 25

Tricco, T. and Price, D. (2013), *A Switch for Artificial Resistivity and Other Dissipation Terms*

Valentini, M., Murante, G., Borgani, S., et al. (2020), *Impact of AGN Feedback on Galaxies and Their Multiphase ISM across Cosmic Time*, Monthly Notices of the Royal Astronomical Society, 491, 2779

Valentini, M., Murante, G., Borgani, S., et al. (2017), *On the Effect of Galactic Outflows in Cosmological Simulations of Disc Galaxies*, Monthly Notices of the Royal Astronomical Society, 470, 3167

Valentino, E. D., Mena, O., Pan, S., et al. (2021), *In the Realm of the Hubble Tension—a Review of Solutions**, Classical and Quantum Gravity, 38(15), 153001

Vallés-Pérez, D., Planelles, S., and Quilis, V. (2021a), *Troubled Cosmic Flows: Turbulence, Enstrophy, and Helicity from the Assembly History of the Intracluster Medium*, Monthly Notices of the Royal Astronomical Society, 504(1), 510

Vallés-Pérez, D., Planelles, S., and Quilis, V. (2021b), *Unravelling Cosmic Velocity Flows: A Helmholtz–Hodge Decomposition Algorithm for Cosmological Simulations*, Computer Physics Communications, 263, 107892

Vallés-Pérez, D., Planelles, S., Quilis, V., et al. (2024), *Vortex-p: A Helmholtz-Hodge and Reynolds Decomposition Algorithm for Particle-Based Simulations*, Computer Physics Communications, 304, 109305

van Daalen, M. P., Schaye, J., Booth, C. M., and Dalla Vecchia, C. (2011), *The Effects of Galaxy Formation on the Matter Power Spectrum: A Challenge for Precision Cosmology*, Monthly Notices of the Royal Astronomical Society, 415, 3649

Vandenbroucke, B. and De Rijcke, S. (2016), *The Moving Mesh Code Shadowfax*, Astronomy and Computing, 16, 109

Vazza, F., Angelinelli, M., Jones, T. W., et al. (2018a), *The Turbulent Pressure Support in Galaxy Clusters Revisited*, Monthly Notices of the Royal Astronomical Society, 481, L120

Vazza, F., Brunetti, G., Brüggen, M., and Bonafede, A. (2018b), *Resolved Magnetic Dynamo Action in the Simulated Intracluster Medium*, Monthly Notices of the Royal Astronomical Society, 474, 1672

Vazza, F., Brunetti, G., Kritsuk, A., et al. (2009), *Turbulent Motions and Shocks Waves in Galaxy Clusters Simulated with Adaptive Mesh Refinement*, Astronomy & Astrophysics, 504(1), 33

Vazza, F., Jones, T. W., Brüggen, M., et al. (2017), *Turbulence and Vorticity in Galaxy Clusters Generated by Structure Formation*, Monthly Notices of the Royal Astronomical Society, 464, 210

Vazza, F., Roediger, E., and Brüggen, M. (2012), *Turbulence in the ICM from Mergers, Cool-Core Sloshing, and Jets: Results from a New Multi-Scale Filtering Approach*, Astronomy and Astrophysics, 544, A103

Verlet, L. (1967), *Computer "Experiments" on Classical Fluids. I. Thermodynamical Properties of Lennard-Jones Molecules*, Physical Review, 159(1), 98

Vikhlinin, A., Kravtsov, A., Forman, W., et al. (2006), *Chandra Sample of Nearby Relaxed Galaxy Clusters: Mass, Gas Fraction, and Mass-Temperature Relation*, The Astrophysical Journal, 640, 691

Vila, J. P. (1999), *On Particle Weighted Methods and SPH*, Mathematical Models & Methods in Applied Sciences - M3AS, 09, 161

Viola, M., Monaco, P., Borgani, S., et al. (2008), *How Does Gas Cool in Dark Matter Haloes?*, Monthly Notices of the Royal Astronomical Society, 383, 777

Voit, G. M., Kay, S. T., and Bryan, G. L. (2005), *The Baseline Intracluster Entropy Profile from Gravitational Structure Formation*, Monthly Notices of the Royal Astronomical Society, 364, 909

von Neumann, J. (1961), *Collected Works*, Pergamon, Oxford

Wadsley, J. W., Keller, B. W., and Quinn, T. R. (2017), *Gasoline2: A Modern Smoothed Particle Hydrodynamics Code*, Monthly Notices of the Royal Astronomical Society, 471, 2357

Wadsley, J. W., Stadel, J., and Quinn, T. (2004), *Gasoline: A Flexible, Parallel Implementation of TreeSPH*, New Astronomy, 9, 137

Walker, A. G. (1937), *On Milne's Theory of World-Structure*, Proceedings of the London Mathematical Society, 42, 90

Wang, Q. H. S., Giacintucci, S., and Markevitch, M. (2018), *Bow Shock in Merging Cluster A520: The Edge of the Radio Halo and the Electron-Proton Equilibration Timescale*, The Astrophysical Journal, 856, 162

Watson, D. F. (1981), *Computing the N-Dimensional Delaunay Tessellation with Application to Voronoi Polytopes**, The Computer Journal, 24(2), 167

Weibel, E. S. (1959), *Spontaneously Growing Transverse Waves in a Plasma Due to an Anisotropic Velocity Distribution*, Physical Review Letters, 2, 83

Weinberger, R., Springel, V., and Pakmor, R. (2020), *The Arepo Public Code Release*, The Astrophysical Journal Supplement Series, 248(2), 32

Wendland, H. (1995), *Piecewise Polynomial, Positive Definite and Compactly Supported Radial Functions of Minimal Degree*, Advances in Computational Mathematics, 4(1), 389

Whitehurst, R. (1995), *A Free Lagrange Method for Gas Dynamics*, Monthly Notices of the Royal Astronomical Society, 277, 655

XRISM Science Team (2022), *XRISM Quick Reference*

Xu, G. (1995), *A New Parallel N-Body Gravity Solver: TPM*, The Astrophysical Journal Supplement Series, 98, 355

Xu, G. (1997), *Hydrodynamic and N-body Schemes on an Unstructured, Adaptive Mesh with Applications to Cosmological Simulations*, Monthly Notices of the Royal Astronomical Society, 288, 903

Zel'dovich, Y. B. (1970a), *Gravitational Instability: An Approximate Theory for Large Density Perturbations.*, Astronomy and Astrophysics, 5, 84

Zel'dovich, Ya. B. (1970b), *The Hypothesis of Cosmological Magnetic Inhomogeneity.*, Soviet Astronomy, 13, 608

Zeldovich, Ya. B. and Sunyaev, R. A. (1969), *The Interaction of Matter and Radiation in a Hot-Model Universe*, Astrophysics and Space Science, 4, 301

Zhuravleva, I., Churazov, E., Kravtsov, A., et al. (2013), *Quantifying Properties of ICM Inhomogeneities*, Monthly Notices of the Royal Astronomical Society, 428, 3274

Zhuravleva, I., Churazov, E., Schekochihin, A. A., et al. (2019), *Suppressed Effective Viscosity in the Bulk Intergalactic Plasma*, Nature Astronomy, 3, 832

Zwicky, F. (1933), *Die Rotverschiebung von Extragalaktischen Nebeln*, Helvetica Physica Acta, 6, 110

Zwicky, F., Herzog, E., and Wild, P. (1968), *Catalogue of Galaxies and of Clusters of Galaxies*, California Institute of Technology (CIT), Pasadena

Acknowledgements

First of all, I want to thank my PhD advisor Prof. Dr. Klaus Dolag for the great supervision. Thank you Klaus for always being available for questions and discussions and the great mentorship throughout the time of my thesis.

Also, I want to thank Ulrich Steinwandel for the countless discussions on the code and numerics. Thank you also for the P-Gadget version, you initially gave me, the tests you calculated as comparisons, and examples you provided to me.

I want to thank Milena Valentini for all the discssusions. Thank you for the detailed and careful proofreading of my papers and my thesis, and your help with improving formulations.

I want to thank all my PhD and Postdoc colleagues and all members of the CAST group for the scientific and not-so-scientific discussions during the group meetings, coffee, and lunch. Thank you all for the discussions and exchange, which gave me new input and new ideas.

In particular, I want to thank Tirso Marin Gilabert for many discussions on the hydrodynamics part of the code. I thank Ludwig Böss for the discussions on the general code infrastructure and the common cleanup we did, it was a lot of fun working together. I thank Stephan Vladutescu-Zopp for the discussions during the writing process and the common struggles we went through when writing simultaneously.

I want to thank Ludwig Böss, Luca Sala, Tirso Marin Gilabert, Laura di Federico, Lucas Valenzuela, and Benjamin Seidel for proofreading my final manuscript and for your useful comments.

I acknowledge support by the COMPLEX project from the European Research Council (ERC) under the European Union's Horizon 2020 research and innovation program grant agreement ERC-2019-AdG 882679. I acknowledge support by the Deutsche Forschungsgemeinschaft (DFG, German Research Foundation) under Germany's Excellence Strategy - EXC-2094 - 390783311. I am especially grateful for the support by M. Petkova through the Computational Center for Particle and Astrophysics (C2PAP) under the project pn68va. Some simulations were carried out at the Leibniz Supercomputer Center (LRZ) under the project pr86re (SuperCast).

The analysis was performed mainly in julia (Bezanson et al., 2014), including the package GadgetIO by Böss & Valenzuela (2022). The surface density of the nifty cluster was calculated using Smac (Dolag et al., 2005a). Other surface density plots have been created using SPHtoGrid (Böss, 2023).

I thank the developers of GIZMO and AREPO for making the codes publicly available. I thank David Hubber for initial discussions on the MFM implementation in GANDALF which was used as a base for the implementation in OPENGADGET3. I thank Christian Alig for a turbulence AREPO setup and Ludwig Böss for providing ICs for the shock-tubes. I thank Rüdiger Pakmor for the help in analyzing and improving the convergence of the soundwave with AREPO. I thank L. Sala for setting up the isolated galaxy with a BH in the center.